Rhenium and Manganese α-diimine tricarbonyls as CO$_2$ reduction catalysts: Insights from novel ligand design

Steven J. P. Spall

Department of Chemistry – The University of Sheffield

Supervisor: Professor Julia Weinstein

Thesis submitted for the degree of Doctor of Philosophy

"Carrying out a systematic series of electrolyses to evaluate a catalyst, determine the best conditions of its use, avoiding side phenomena such as ohmic losses, self-inhibition, deactivation, etc.…is an exhaustive task."

– Professor Cyrille Costentin

Abstract

Concerns over climate change and energy security combined with the commercial application of carbon capture technologies has led to increased interest in the use of CO_2 reduction catalysts as a means to convert this captured waste into fuel. In order to accomplish this photocatalytic or electrocatalytic systems must be employed of which the Lehn type catalyst based on the original $[ReCl(CO)_3(bpy)]$ complex is highly suitable due its selective CO formation and high efficiency.

The purpose of this project was to develop new understanding of Lehn type CO_2 reduction catalysis and, in particular, to develop new families of catalysts integrating manganese in place of rhenium. Much of the research has focussed on the concept of decoupling – either decoupling electron withdrawing groups from the α-diimine or decoupling the electronic effects from the steric effects.

A variety of rhenium and manganese complexes have been synthesised and studied using a variety electrochemical and spectroscopic methods. Initial research focussed upon developing our understanding of the photodecomposition of the manganese based Lehn type catalysts and it was determined that the complexes decay via CO elimination giving a large variety of decomposition products. This research led to the investigation of the electrocatalytic and photocatalytic properties of three rhenium bis(mestiylimino)-acenaphthene complexes which exhibited electrocatalytic activity but not photocatalytic activity. The major family of ligands studied were asymmetric imino pyridine ligands which due to the break of symmetry between the phenyl moiety and the diimine allow for sterically demanding groups to be incorporated into the complexes without changing the electronic properties of the complex. These complexes are ideal for 'lab mouse' investigations of systems that show sensitivity to both steric and electronic factors. It was observed that while the rhenium imino pyridine complexes behaved in a manner similar to bipyridine complexes the manganese variants exhibited behaviour more akin to what has been observed in manganese diazabutadiene catalysts.

Attempts to provide quantitative analysis of catalyst performance led to the employment of many different techniques ranging from gas chromatography to line shape analysis of voltammograms, however, no satisfactory method of performing quantitative analysis could be found.

The overall conclusion is that the manganese based Lehn type catalysts can be used effectively as homogeneous electrocatalysts but the photosensitivity prohibits practical use in photocatalytic systems. The asymmetric imino pyridine ligands have shown great potential for systematic investigation of CO_2 reduction catalysts and offer enormous scope for further development, however it is necessary for the community to adopt and publicise standards for benchmarking new catalysts as the methods employed today are not ideal.

Acknowledgements

Abbreviations

Abs	Absorption
BOC	Tert-Butyl-Dicarbonate
bpy	Bipyridine
CCS	Carbon Capture and Storage
CCU	Carbon Capture and Utilisation
$CDCl_3$	Deuterated chloroform
cm	Centimetre
CV	Cyclic Voltammetry
DAB	Diazabutadiene
dmbpy	Dimethyl Bipyridine
DMF	Dimethylformamide
E	Potential
ECE	Electrochemical Chemical Electrochemical
EEC	Electrochemical Electrochemical Chemical
Em	Emission
Fc	Ferrocene
FTIR	Fourier Transform Infrared
HOMO	Highest Occupied Molecular Orbital
HPIB	N-ethyl-6-{6-[ethyl(4-hexylphenyl)carbamoyl] pyridin-2-yl}-N-(4-hexylphenyl)pyridine-2-carboxamide
i	Current
IEP	Imino Ethyl Pyridine
IMP	Imino Methyl Pyridine
iPr	Iso Propyl
LUMO	Lowest Unoccupied Molecular Orbital
M	Molar
Mb	Myoglobin

MeCN	Acetonitrile
Mes	Dimesityl Bipyridine
mesBIAN	Bis(mestiylimino)-acenaphthene
mesbpy	6,6'-dimesityl-2,2'-bipyridine
mg	Milligram
MLCT	Metal to ligand charge transfer
MS	Mass Spectrometry
mV	Millivolts
mW	Milliwatt
nm	Nanometres
NMR	Nuclear Magnetic Resonance
OTf	Trifluoromethanesulphonate
OTTLE	Optically Transparent Thin Layer Electrode
Red	Reduction
s	Seconds
SCE	Standard Calomel Electrode
SEC	Spectroelectrochemistry
tBu	Tertiary Butyl
TCD	Thermal Conductivity Detector
TEOA	Triethanolamine
THF	Tetrahydrofuran
TOF	Turn Over Frequency
TON	Turn Over Number
TRIR	Time Resolved Infrared
UV	Ultra Violet
X	Halide
XLCT	Halide to Ligand Charge Transfer
λ	Wavelength
$\tilde{\upsilon}$	Wavenumbers
φ	Quantum Yield

Table of Contents

This thesis contains images and excerpts from copyrighted material. These uses fall well within the copyright doctrine of Fair Use.

Figures reprinted (adapted) with permission from The American Chemical Society, John Wiley & Sons, Elsevier and the RSC where appropriate. Please follow references for journal details.
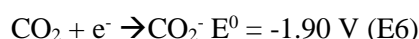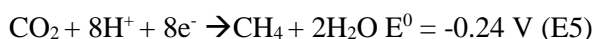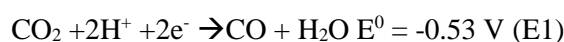
1. Introduction

1.1 [Mn(X)(CO)₃(α-diimine)] as a catalyst for CO₂ reduction, past studies based on [Re(X)(CO)₃(α-diimine)]'s and current developments

The reduction of CO_2 into useable fuels has been of great interest in recent years due to the concerns over climate change and the desire to provide energy security[1]. This has led to a remarkable diversity of photo[2] and electro[3,4] catalytic systems for CO_2 reduction. Outside of semiconductor and nanoparticle research[5,6,7,8] probably the most studied and employed system is that based on rhenium tricarbonyl alpha diimines. Although there is no doubt that this catalyst is effective (*vide infra*) it does suffer from the high cost and low abundance of rhenium (abundance ratio 0.7 mg t⁻¹)[9]. Recently it has become apparent that manganese analogues may provide a low cost and effective alternative to rhenium catalysts. Manganese alpha diimines are well categorised complexes[10,11] which can be prepared via simple synthetic routes,[12] however, it has become apparent that they are photosensitive, potentially limiting their application as photocatalysts and electrocatalysts if such a system required exposure to light (see chapter 2).

This chapter will serve to discuss the known state of CO_2 catalysis with rhenium tricarbonyl alpha diimines and explore the emergence of their manganese analogues.

1.1.1 The need for a catalyst

The first question to be addressed when discussing CO_2 reduction catalysts is why is a catalyst required for CO_2 reduction at all? Although the one electron reduction of CO_2 is indeed possible using an electrode, it requires an extremely negative voltage and does not produce any useful or stable products, only CO_2-anion. However, the proton coupled multi-electron reduction of CO_2 takes place at substantially less negative thermodynamic potentials than the single electron reduction (see figure 1.1) due to the thermodynamically more stable species being produced.[13]

$$CO_2 + 2H^+ + 2e^- \rightarrow CO + H_2O \quad E^0 = -0.53 \text{ V (E1)}$$
$$CO_2 + 2H^+ + 2e^- \rightarrow HCO_2H \quad E^0 = -0.61 \text{ V (E2)}$$
$$CO_2 + 4H^+ + 4e^- \rightarrow HCHO + H_2O \quad E^0 = -0.48 \text{ V (E3)}$$
$$CO_2 + 6H^+ + 6e^- \rightarrow CH_3OH + H_2O \quad E^0 = -0.38 \text{ V (E4)}$$
$$CO_2 + 8H^+ + 8e^- \rightarrow CH_4 + 2H_2O \quad E^0 = -0.24 \text{ V (E5)}$$
$$CO_2 + e^- \rightarrow CO_2^- \quad E^0 = -1.90 \text{ V (E6)}$$

Figure 1.1 Thermodynamics of catalytic CO₂ reduction at 25 °C in pH 7 aqueous solution with voltage measured against the normal hydrogen electrode.

A reduction catalyst acts as an electron transfer agent which ideally operates near the thermodynamic potential of the reaction ($E^0_{(products/substrates)}$), though usually the application of an over potential is required to drive the reaction. Overpotential is defined as the potential that must be applied to induce

catalysis minus the equilibrium potential (E^0) and minimizing the over potential allows for increased conversion efficiency.

1.2 The use of rhenium tricarbonyls as CO$_2$ reduction catalysts

The use of [Mn(X)(CO)$_3$(α-diimine)] catalysts for CO_2 reduction is a relatively recent development born out of the use of analogous rhenium tricarbonyls and the desire to replace them with a cheaper more abundant metal. The first reported use of a rhenium based catalyst for CO_2 reduction was made by Hawecker and Lehn *et al*. in 1983 who employed [ReX(CO)$_3$(bpy)] (where X is Cl or Br) as a photocatalyst in the presence of a sacrificial electron donor to produce CO.[14]

Their results showed that [ReX(CO)$_3$(bpy)] was highly selective towards CO production, with no H_2 or formate generation observed (an aspect that had been noted for some other catalysts[4,15,16]) and exhibited reasonable turn over numbers of up to 11 (1 hour of illumination in the presence of NEt$_4$Cl), though kinetic experiments showed that the catalytic activity reduced over time. This loss of activity, however, could be remedied by the addition of surplus halide ions into the solution. The general motif of a group 7 metal tricarbonyl complex with a diimine ligand used for CO_2 reduction (either electrocatalytically or photocatalytically), such as the type employed by Hawecker and Lehn *et al*., is here after referred to as a "Lehn type" catalyst or a Lehn catalyst. A generalised structure of a Lehn type catalyst can be seen in figure 1.2.

1.2.1 Rhenium tricarbonyls as photocatalysts

Rhenium tricarbonyl diimine complexes have many properties that make them ideal as photocatalysts, not least of which is the high degree of photostability they exhibit, which has been noted in experiments we have conducted using high power lasers during which no degradation was observed.[17]

In addition to photostability a good photocatalyst must have the ability to absorb photons of sufficient energy to excite a ground state electron into a higher energy orbital (typically a π^* antibonding orbital in the case of transition metal catalysts). The complexes must then be efficiently reductively quenched by a sacrificial electron donor and undergo further chemistry. This entire process must occur with sufficient rapidity in order to get an efficient turnover rate and do so with an absolute minimum of side reactions and deactivation processes, and with (ideally) no upper limit to the number of times the catalyst can turn over (turnover number TON).
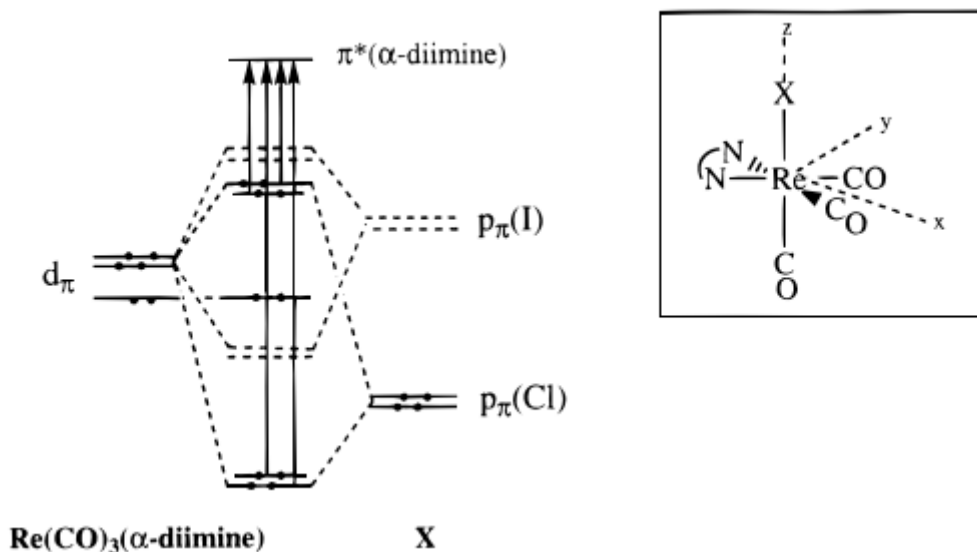
Figure 1.2 Qualitative MO Scheme for [Re(X)(CO)$_3$ (R-diimine)]. The dπ(Re) orbitals (d$_{xz}$ and d$_{yz}$) of the Re(CO)$_3$(R-diimine) unit interact with the pπ(X) (p$_x$ and p$_y$) orbitals, resulting in π-bonding (dπ(Re) + pπ(X)) and π-antibonding (dπ(Re) - pπ(X)) combinations. The d$_{xy}$(Re) orbital is nonbonding with respect to the halide. The solid lines show the orbital diagram for X =Cl; the dashed lines, the situation for X = I. Figure reproduced from reference 20.

This stability is due to the presence of the carbonyl ligands and the low oxidation state of the rhenium in these Lehn catalyst (+1) resulting in a large degree of ligand field splitting. This property, combined with the low energy of the π* system on the bipyridine, due to the large conjugated π system, means that the MLCT transition is usually the lowest energy transition. This facilitates stability because the $\pi\pi$* and MLCT transitions are the dominant transitions and take place with great ease due to their being both allowed and possessing of large transition dipole moments. Dissociation of a CO ligand, though, does not proceed from the ^{3}MLCT state but rather from higher energy states which could be populated with < 330nm light (> 3 eV), such as vibrationally hot ^{1}MLCT states.[18] The major transition in the visible region do not lead to a population of metal ligand antibonding orbitals,[19] though in reality there is a high degree of mixing between the dπ(Re) and the pπ (X) orbitals.

Complexes that use Cl$^-$ or Br$^-$ exhibit MLCT lowest excited state but complexes with I$^-$ show XLCT transitions (transitions involving the donation of electrons from the halide group into the alpha diimine) due to the increase of the HOMO energy in the X ligand[20,21]. When rhenium tricarbonyls are being used as an electrocatalyst, CO_2 reduction takes place usually through a 2-electron reduced species (*vide infra*). However, in the photocatalytic system this is not the case.[22] Although there is much contention as to the most accurate description of the catalytic cycle, a general outline of the reaction can be described as follows[23]:

1) The starting rhenium complex is excited by photo irradiation into the ^{3}MLCT state.

2) Because the ^{3}MLCT excited state of the rhenium complex is more oxidising than the ground state rhenium complex (E$_{1/2}^{red}$ of + 1.15 V vs SCE for excited state [ReCl(CO)$_3$(bpy)])

reduction by a sacrificial electron donor (such as triethanolamine (TEOA) $E_{1/2}^{red} = + 0.80$ vs SCE[19]) can occur.

3) The X ligand is eliminated from the one electron reduced species and replaced by a solvent molecule.

4) The one electron reduced solvent coordinated species undergoes electrophilic attack by CO_2 along with protonation to form the CO_2 adduct shown in figure 1.3.

5) The CO_2 adduct accepts another electron, probably from the one-electron-reduced form of the starting complex or solvated species[24] and evolves CO, regenerating the solvated species.

6) The solvent-coordinated rhenium complex absorbs UV light to form the one-electron-reduced solvent-coordinated Re complex driving the continuous reaction cycle.
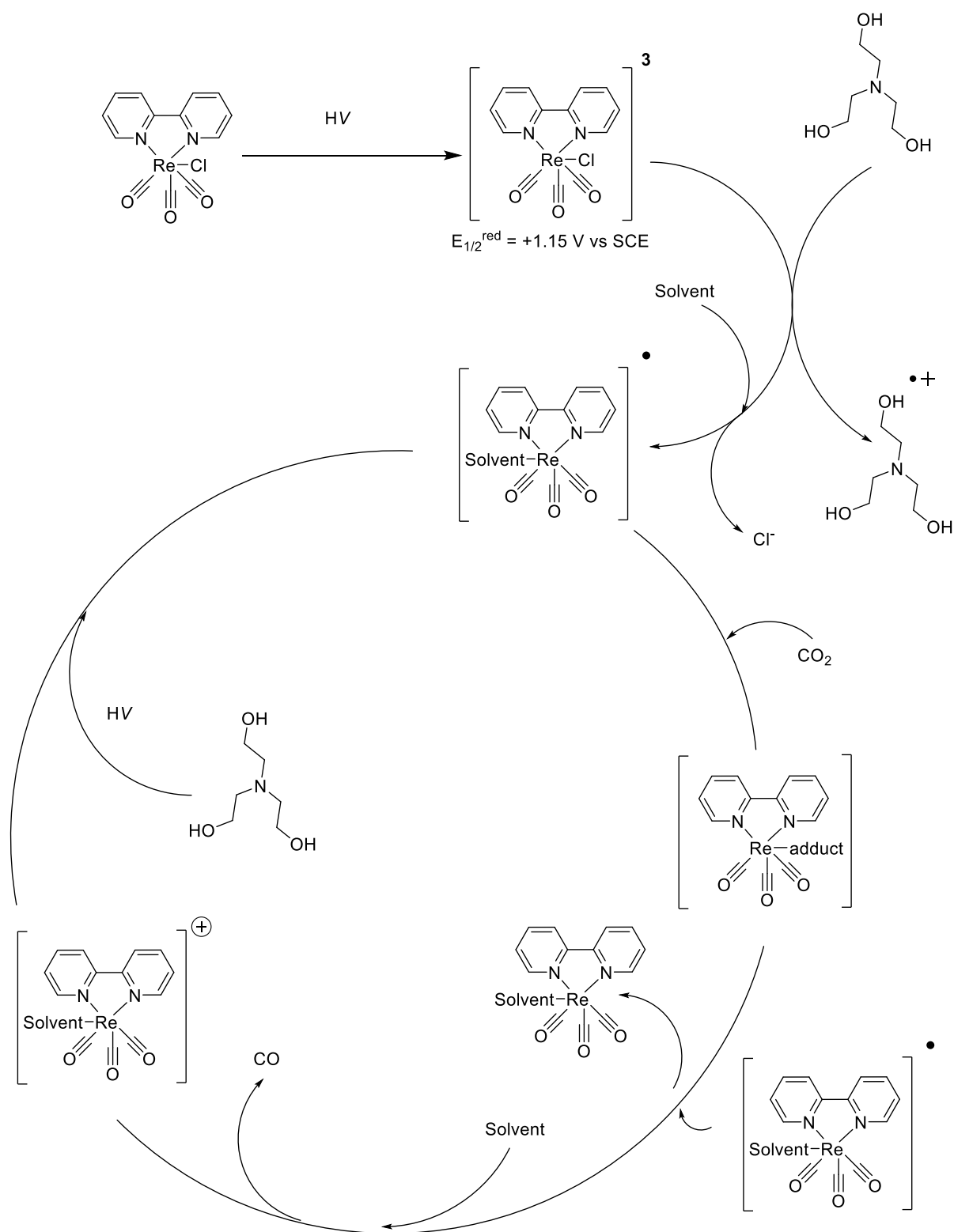
Figure 1.3 Photocatalytic cycle of a typical rhenium tricarbonyl alpha diimine system using triethanolamine (TEOA) as a sacrificial electron donor.

Of great importance to the photogeneration of CO using this system is lability of the X ligand. X ligands which bind to the rhenium centre forming unlabile complexes, such as X = CN, do not produce CO because none of the X ligand is able to dissociate. As such there will not be a vacant

coordination site for the CO_2 to bind to the metal centre. This is not to say that the most labile X ligand will offer superior catalytic performance as compared with less labile ligands, however, as many factors play a role. X = CNS, for example, is intermediately stable in its binding to rhenium between CN and Cl meaning that a significant population of the one electron reduced species can accumulate. Unlike the CN ligand however, a small amount of $[Re(CO)_3(bpy)]^{\bullet-}$ does form allowing CO_2 to coordinate and form the CO_2 adduct. This adduct has a greater chance to come in contact and be reduced by the now relatively abundant one electron reduced species. This process proceeds with a quantum yield for CO formation of 0.30. The Cl ligand, in contrast, dissociates with comparative ease and a much lower population of the one electron reduced species can accumulate resulting in reduced activity for photocatalytic CO generation and a quantum yield of 0.16.[24] Therefore, for efficient photocatalytic CO production a large population of the one electron reduced species is desirable.

Because the first and second reduction of CO_2 are carried out by a different species there is room to optimise each process. Work conducted by Takeda *et al.* has yielded some very interesting results in this respect. They employed $[Re(CO)_3(4,4'-(MeO)_2bpy)(P(OEt)_3)]^+$ as a photosensitizer to generate the one electron reduced species with high efficiency. The Re complex was combined in a 25:1 ratio, which was found to be optimal, with $[Re(CO)_3(bpy)(CH_3CN)]^+$, which by itself showed no catalytic activity but is able to easily form the 17 e^- species, to which the CO_2 can coordinate. This optimised bicatalytic system showed a remarkably high quantum yield for CO production of 0.59, which, at the time of writing, is the highest reported amongst homogeneous photocatalysts.

An important part of the systems described above is the "CO_2 adduct" in which both the nucleophilic catalyst species and the CO_2 come together to form the reactive intermediate. Exactly what this CO_2 adduct is has remained mysterious with several unconfirmed proposals made.[25,26,27]

However, a recent study by Kou *et al.* has confirmed the presence of several key reaction intermediates allowing the scheme shown in figure 1.4 to be proposed.[23] In this scheme the presence of intermediates, **2, 3** and **3'** was confirmed using FTIR and mass spectrometry methods. The detection intermediate **3'** is highly significant as there was no detection or evidence of a dimer or similar species as had been postulated by some. This mechanism indicates that reduction from the one electron reduced species occurs via an outer sphere electron transfer process.
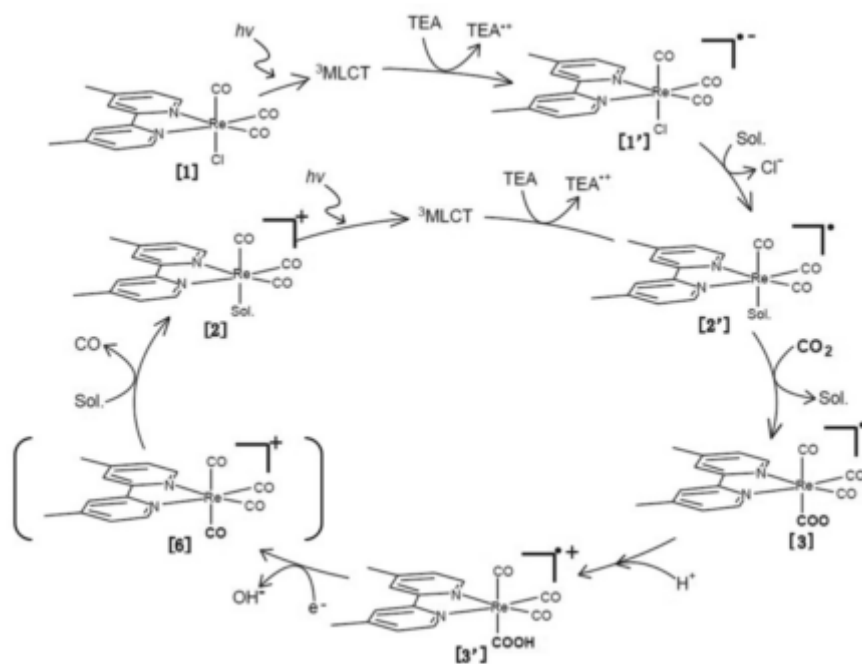
Figure 1.4 Photochemical CO₂ Reduction Cycle Sensitized by [ReCl(CO)₃(dmbpy)]. Figure reproduced from reference 23.

Although mononuclear rhenium tricarbonyls are effective photocatalysts they do suffer from their poor absorption in the regions of peak solar output. Figure 1.5 shows a comparison of the absorption spectra of [ReCl(CO)₃(bpy)] and [ReCl(CO)₃(dmbpy)] with the standard solar spectrum. Although not to the same scale, it can clearly be seen that neither rhenium complex exhibits any absorption at all in the region 500-700 nm where peak solar radiation lies.
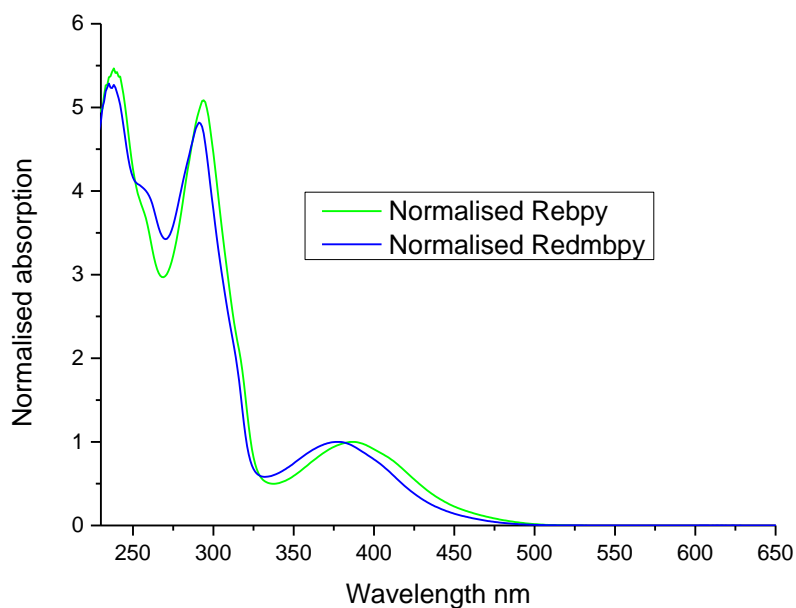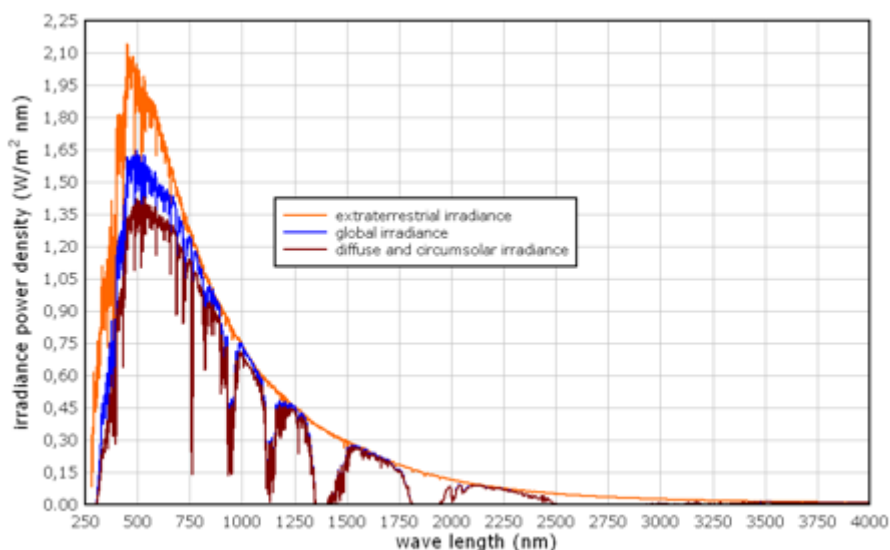
ASTM G173-03 Reference Solar Spectral Irradiance
(credit: Renewable Resource Data Center (RReDC): Standard Solar Spectra*)*

Figure 1.5 Comparison of the absorption spectrum of [ReCl(CO)₃(bpy)][28] and [ReCl(CO)₃(dmbpy)] with the solar spectrum.

One possibility to increase the efficiency of solar harvesting by capturing more of the solar spectrum is to vary either the X ligands or the diimine ligands. An example of such study performed by Kurz *et al*.[29] (table 1.1) showed, however, that altering the X ligand has little effect on the maximum absorption wavelength, and therefore this approach will not allow one to shift λ_{max} into the area of peak solar output. There is thus little opportunity to tune light harvesting of the complex by altering the X ligand. By contrast, variation of the α-diimine ligand shows much greater potential to shift the absorption wavelength into the more intense regions of solar output. The diimine ligands used in these experiments are shown in figure 1.6. (The nomenclature of Kurz *et al*. is used for the discussion of their complexes). Since the HOMO is largerly localised on the Re center, and the LUMO – on the diimine (albeit with some contribution from the Re center) this is not surprising that varying "X" has little effect on the lowest, MLCT, absorption band.

**Table 1.1 spectroscopic and electrochemical properties of [Re(bpy)(CO)₃X] complexes[29].**

Ligand X	λ_{max} Abs nm[a]	λ_{max} Em nm[a]	$\ddot{v}_{CO}$ cm^{-1} [b]	$E_{1/2\ red}$ [mV][c]
Cl⁻ (1)	370	580	2019, 1883	-1130
Br⁻ (2)	370	575	2019, 1905	-1190
H₂O (4)	350	540	2036, 1918	-1000
SCN⁻ (5)	375	580	2020, 1928	-1015
CN⁻(6)	355	540	2006, 1878	-1125
M-CN-Re (7)	365	535	2025, 1910	-1050

[a] In DMF, [b] KBr pellets, [c] In DMF with 0.1 M TBAPF₆, Volts vs Ag/AgCl

Table 1.2 spectroscopic and electrochemical properties of [Re(bpy)(CO)₃X] complexes[29].

| Ligand diimine	λ_{max} Abs nm[a]	λ_{max} Em nm[a]	$\ddot{v}_{CO}$ cm^{-1} [b]	$E_{1/2\ red}$ [mV][c]
bpy (2)	370	575	2019, 1905	-1190
phen (8)	370	570	2018, 1933	-1090
dqp (9)	ca. 375[d]	585	2025, 1948	-975
dppz (10)	ca. 425[d]	520	2018, 1918	-705
biq (11)	435	[c]	2014, 1895	-735
Hdcbpy (12)	360	540	2024, 1896	-1250[f]
bpm (13)	385	[e]	2030, 1931	-860
phd (14)	375[d]	[e]	2033, 1943	-15, -755
abpy (15)	550, 360[d]	[e]	2020, 1924	+50

[a] In DMF, [b] KBr pellets, [c] In DMF with 0.1 M TBAPF₆, Volts vs Ag/AgCl, [d] Absorption shoulder, [e] No fluorescence observed at room temperatures, [f] Irreversible reduction.
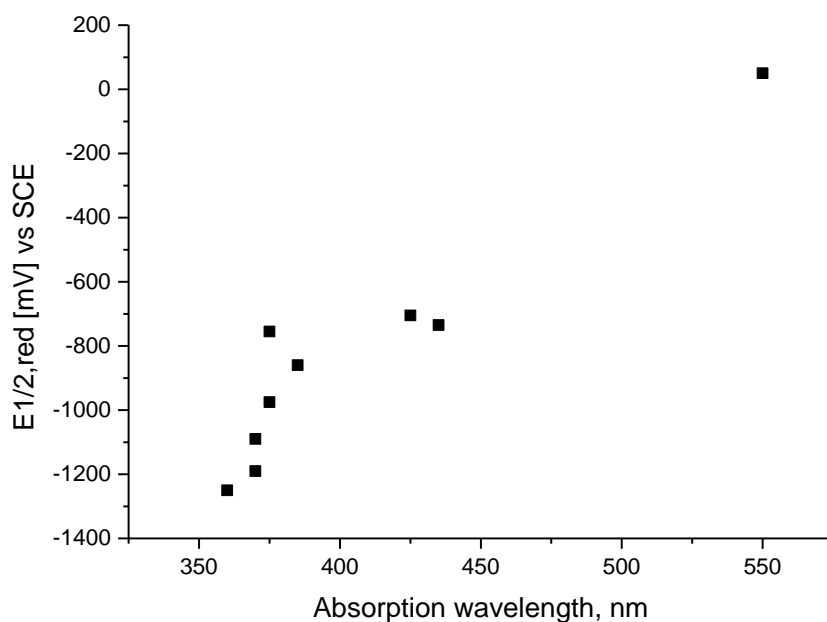
Figure 1.5 $E^{1/2}_{red}$ potentials of the complexes shown in table 1.2 against their absorption maximum. Absorption spectra were recorded in DMF and voltammograms were recorded in DMF in the presence of 0.1 M TBAPF$_6$ with voltages reported against a Ag/AgCl reference.

As can be seen in table 1.2, there is a significant shift to lower energies of absorption λ_{max} where unusual coordination geometries (such as complex **11**) are present or where low-lying stabilised LUMO's are present (such as complex **15**). However, the shift to lower energy comes at the expense of photocatalytic activity towards CO_2 reduction. Figure 1.5 shows that shifting the absorption band to longer wavelengths i.e., lowering the HOMO-LUMO energy gap, comes at the expense of the reduction potential being less negative. As a consequence complexes **11, 13, 14** and **15** show no catalytic activity towards CO generation, as the strong electron accepting nature of the diimine ligands in these complexes leads to the energy of the LUMO being less than the energy of the vacant orbital on CO_2, the LUMO does not have the energy to reduce CO_2. The reduction of the energy level of the LUMO will result in the reduction of the efficiency of photocatalytic CO_2 reduction (*vide infra*). This link between the absorption maximum to harvest light energy, and the need to keep the energy of the LUMO sufficiently high, presents a dilemma that the majority of complexes that are able to effectively harvest visible light photons are not suitable as photocatalysts and although complex **10** is active, it is active at a lower rate than the bpy and phen based complexes.
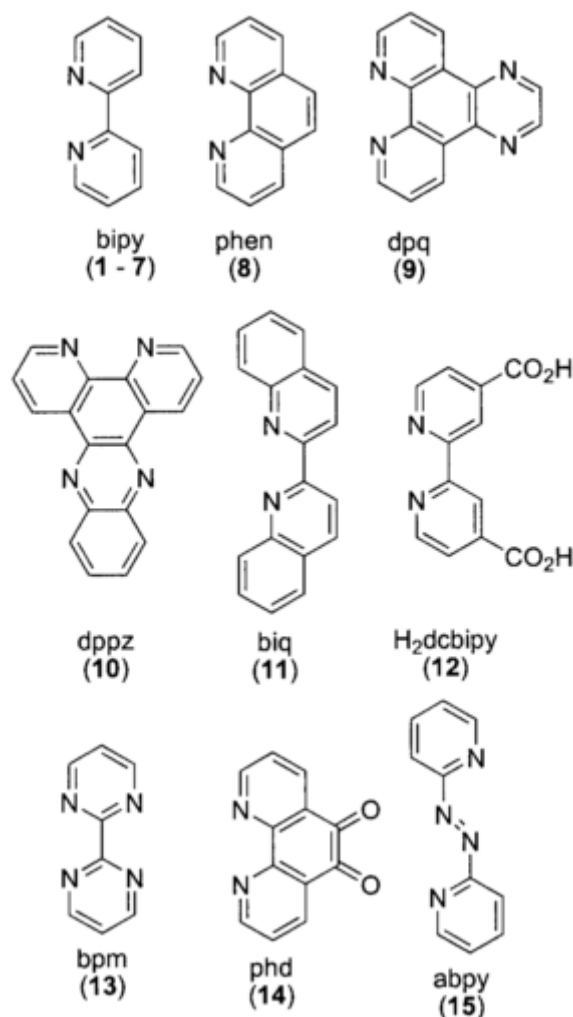
Figure 1.6 Diimine ligands used for the synthesis of [ReBr(di imine)(CO)₃] complexes with the numbering of the corresponding complexes in brackets: 2,2'-bipyridine (bpy) (1–7); 1,10-phenanthroline (phen) (8); dipyrido[3,2-f:2',3'-h] quinoxaline (dpq) (9); dipyrido [3,2-a:2',3' -c] phenazine (dppz) (10); 2,2'-biquinoline (biq) (11); 2,2'-bipyridine-4,4'-dicarboxylic acid (H₂dcbipy) (12); 2,2'-bipyrimidine (bpm) (13); 1,10-phenanthroline-5,6-dione (phd) (14); 2,2'-azobispyridine (abpy) (15).[29]

The results above show that overall modifications to the rhenium tricarbonyl complex itself can have only limited effects on the useful light harvesting capability of the catalyst. Another option to increase the light harvesting range of rhenium complexes is to bind the rhenium catalyst to a separate light harvesting moiety, which once promoted to its excited state, reduces the rhenium catalyst moiety[15] (see figure 1.7). This method was investigated by Gholamkhass *et al*. who synthesised a range of supramolecular complexes incorporating a ruthenium polypyridine bridged to a rhenium tricarbonyl through a decorated bpy ligand.[30] The complexes synthesised are shown in figure 1.8 and comprise a range of unconjugated binuclear and tetranuclear complexes as well as complexes joined through a conjugated imidazole group.
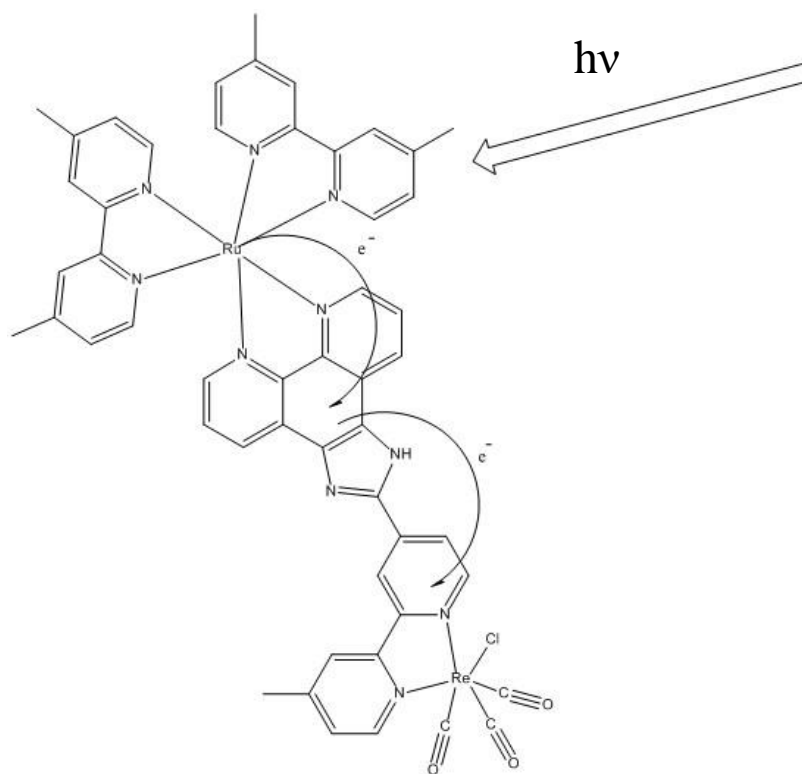
Figure 1.7 Electron transfer from light harvesting moiety (in this case, a Ru(II) complex) to the catalytic rhenium moiety.

All of the complexes shown in figure 1.8 show MLCT absorption bands in the range 442– 478 nm. Of these, the most effective catalysts were $d_2Ru - Re$ and $RuRe_3$ with the other complexes showing either greatly reduced or no catalytic activity.
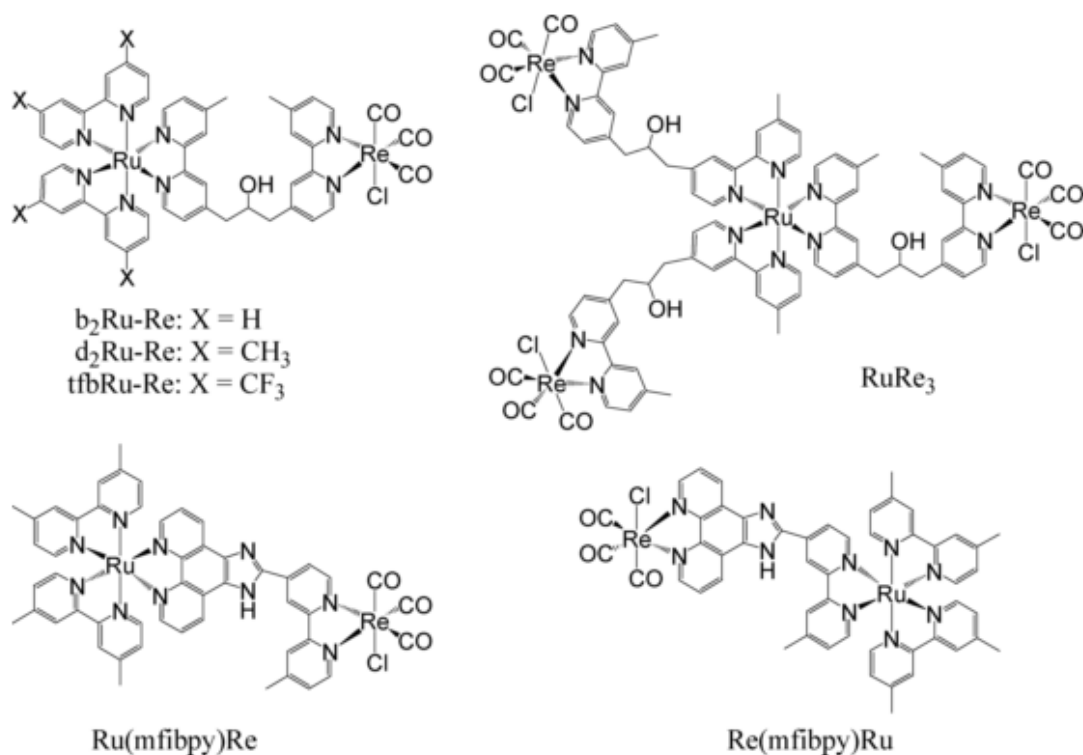
Figure 1.8 Schematic representation of the metal complexes and their abbreviations. Figure reproduced from reference 30.

Figure 1.9 shows the turnover numbers for the different complexes described by Gholamkhass *et al*. Not shown in figure 1.9 are the tfbRu-Re complex that exhibited the lowest turnover number (TON$_{co}$ of 3) followed by complexes containing the mfibpy moiety.

The tfb (tfbRu-Re) moiety and that containing undecorated bpy (b$_2$Ru-Re) seem to be catalytically inactive because reduction of the rhenium moiety is an endothermic process with a ΔG of +0.55 and +0.05 eV respectively, with electron density located predominantly on the peripheral ligands of the ruthenium moiety and are therefore incapable of reducing the catalyst. The free energy of electron transfer in the next two complexes, d$_2$Ru-Re and RuRe$_3$, is approximately 0. Time-resolved spectroscopy reveals that while being a relatively slow process taking from several hundred milliseconds to a second, the Ru-photosensitiser in these complexes is nonetheless capable of reducing the rhenium moiety. Clearly electron transfer is a significant factor in the activity of these forms of photocatalyst and one would assume that facilitating the electron transfer process would increase the activity. However, inspection of figure 1.9 reveals this is not the case and one is led to the rather counter intuitive conclusion: that the inclusion of conjugation into the bridge results in less effective catalysis, a statement which was reiterated by Perutz at the 2nd solar fuels symposium in Liverpool (14th of January 2014). On the face of it, this does not make sense; after all, shouldn't a more conjugated the central bridging unit facilitate faster electron transfer?[31].

However, the energy level of π^* diimine orbitals in the conjugated system are lower than those of the non-conjugated systems. Thus inclusion of conjugation into the bridging structure lowered the overall reducing power of the complexes and hence their photocatalytic ability. In addition to which intramolecular electron transfer in the supramolecular complexes does not require diffusion controlled collision between electron acceptor and donor in solution. However, reduction of the CO_2 is highly dependent upon the rate of collision between the reduced rhenium moiety and the CO_2. This means that electron transfer is not the rate limiting step but rather the lifetime of charge separated state and CO_2 reduction itself is and the slower rate of electron transfer in the d_2Ru-Re and RuRe$_3$ is sufficient to ensure effective catalysis. The conjugated bridge promotes both forward electron transfer, generating Re-anion, but also the back electron transfer, which returns the system to the ground state.
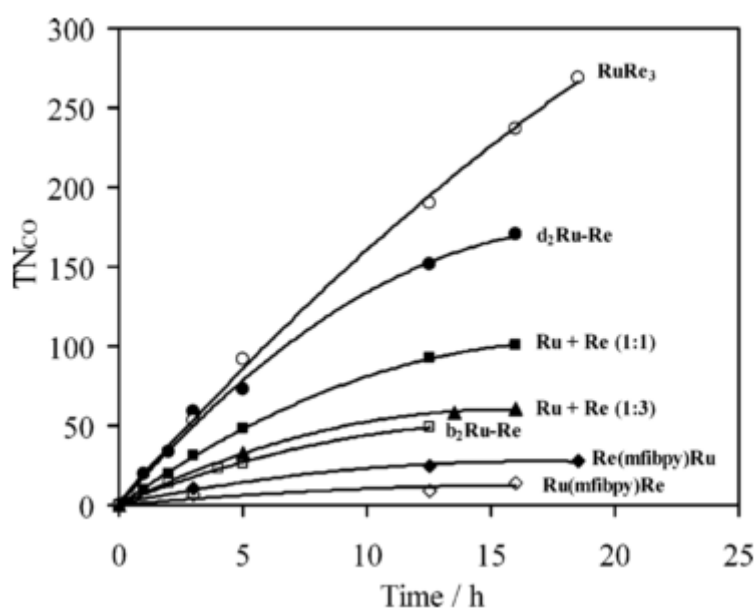
Figure 1.9 Turnover number for production of CO from CO_2 as a function of irradiation time. For selective excitation of the ruthenium moiety, solutions were irradiated at $\lambda \geq 500$ nm using a high-pressure Hg lamp, in a merry-go-round irradiation apparatus, combined with a uranyl glass and a K_2CrO_4 (30% w, d = 1 cm) solution filter. The concentration of the photocatalysts used is 0.05 mM, in a CO_2-saturated DMF/TEOA (5:1) solution containing 0.1 M of the sacrificial reagent BNAH.[30] Figure reproduced from reference 30.

Since conjugation appeared to limit the effectiveness of the catalyst it was decided to investigate the distance dependence of the bridge on the effectiveness of catalysis. For this purposes the compounds shown in figure 1.10 were synthesised. The results showed that the RuC$_2$Re complex was by far the most effective catalyst, even more so than the d_2Ru-Re complex. All complexes shown in figure 1.10 showed absorption peaks at 459 nm, reduction peaks around -1.72 mV vs Ag/AgNO$_3$ and φ_{CO} of 0.11 or 0.13 (for n = 4/6 and n = 2 respectively). The turn over numbers were much improved for the n = 2 complex however, attaining a TON$_{CO}$ of 180 against a TON $_{CO}$ of 120 for the other two complexes[32].
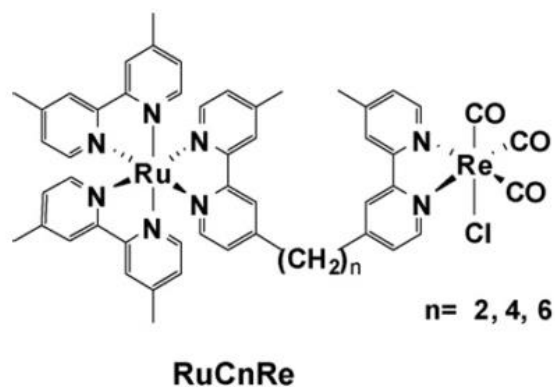
Figure 1.10 Ruthenium-bridge-dimer complexes synthesised to investigate the effect of bridge length on catalysis. Figure reproduced from reference 32.

Although the results shown by Koike *et al.*[32] seem fairly conclusive it is worth taking an element of caution into consideration when dealing with bridge length as optimisation may have much to do with the mechanism of electron transfer. A comparison can be made with a similar photosensitiser-spacer-catalyst system using a zinc porphyrin photosensitiser coupled to a rhenium bipyridine catalyst via a methoxy-benzamide spacer[33], which shows broad absorption in the region 500 - 650 nm. Figure 1.11 shows the complexes studied.
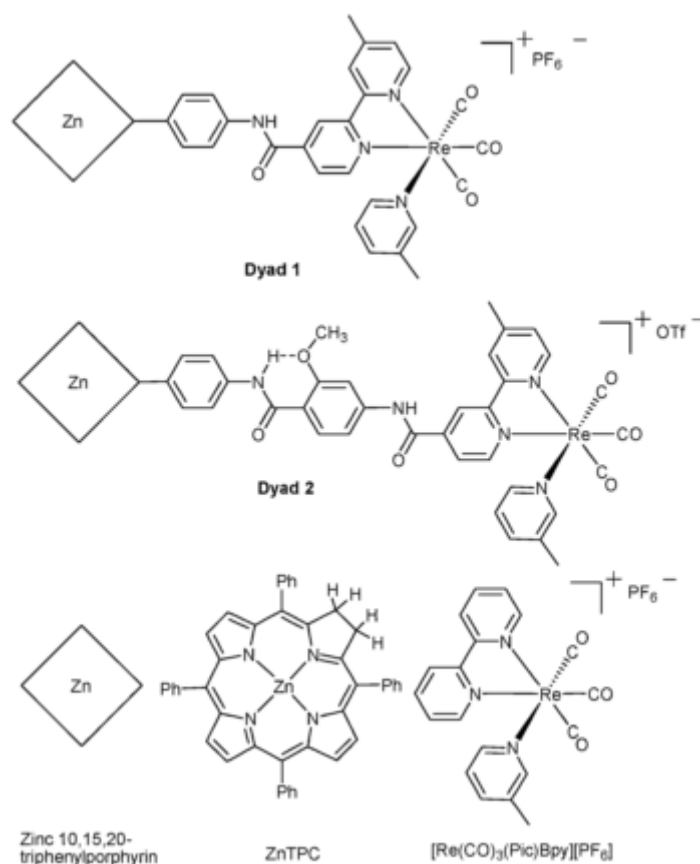
Figure 1.11 Dyad 1, Dyad 2 and monomeric components. Figure reproduced from reference 33.

While the shorter spacer showed the most effective catalysis in the Ru-Re complexes, the zinc porphyrin-rhenium complexes exhibited the opposite trend, with the monomers outperforming the dyads and the longer chained dyad outperforming the shorter chained dyad. In decreasing order:

zinc porphyrin + Re > long spacer dyad > zinc chlorin (ZnTPC) + Re > short spacer dyad.

It has been speculated that this is because the dyad with greater sensitizer-rhenium separation results in a longer-lived charge separated state although an alternative hypothesis is that the monomers and long spacer variants are better able to adopt a geometry in which effective orbital overlap and electron transfer could be achieved. It may be that in the case of the of the Zn – Re complexes charge separation is more rapid than in the Ru-Re complexes but this is contrary to what has been seen elsewhere (*vide supra*). A separate study involving a palladium analogue of Dyad 1 also found that monomers were more effective catalysts than dyads although the turn over numbers were an order of magnitude smaller[34].
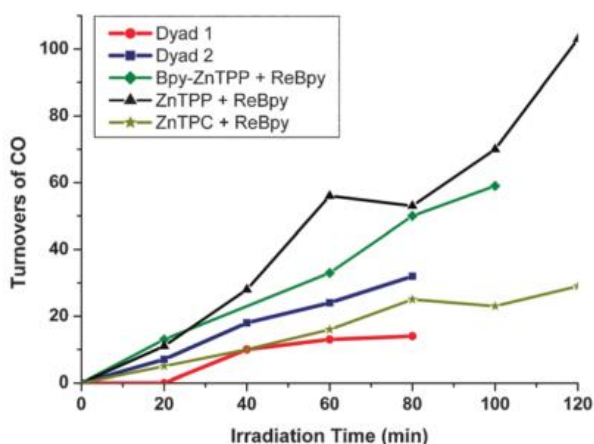
Figure 1.12: Turnovers of CO generated on irradiation ($\lambda > 520$ nm) of photocatalysts under 1 atm CO_2 in DMF/TEOA (5:1) 0.05 mM catalyst. Figure reproduced from reference 33.

1.2.2 Rhenium diimine tricarbonyl complexes as electrocatalysts

The first publication by Hawecker *et al.* on rhenium catalysis for CO_2 reduction described the rhenium catalyst which acted as both the photon harvester and the reduction catalyst. However it was quickly discovered that $[ReX(CO)_3(bpy)]$ can also be employed successfully purely as an electrocatalyst,[35] allowing for greater versatility in its manner of deployment and improvement from the slow photocatalytic process with 5-12 TON per hour[36] to tens to hundreds TON per second.[37] When Hawecker *et al.* used a glassy carbon electrode to feed electrons to the catalyst, they found that under electrocatalytic conditions current efficiencies as high as 98% with turnover numbers approaching 300 could be achieved in a solvent of DMF-H_2O (10%) with NBu_4ClO_4 (supporting electrolyte), with sustained performance over the course of 14 hours. It was discovered that the

addition of 10% water to the solvent provided optimal efficiency, as at higher concnetrations of water traces of H_2 were generated whilst in the absence of water coulomb consumption and CO production were much slower, levelling off after a few hours (vide infra).

Electrochemical characterisation of $[ReCl(CO)_3(dmbpy)]$ concluded that the complex can undergo a reversible one-electron reduction to the radical anion as well as a further irreversible reduction to the dianion. In the absence of CO_2[38] the former can dimerise to give a metal-metal bonded dimer and the latter undergoes rapid loss of chloride and incorporation of acetonitrile.[39]

The photocatalytic route involves CO_2 coordination to a one electron reduced species followed by further reduction via a CO_2 adduct and a second one electron reduced species (*vide supra*) which is similar to the one electron route proposed by Sullivan *et al*. in 1985[40]. Two routes were proposed in this paper: a slower one electron pathway and a faster two electron pathway going through a 5-coordinate radical and a 5-coordinate anion respectively[38].
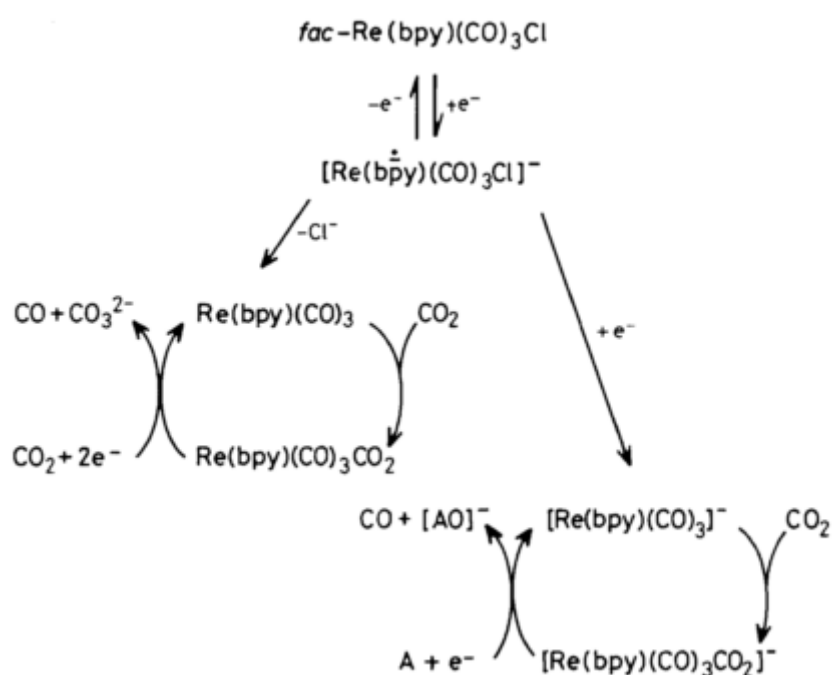
Figure 1.13: One and two electron pathway, one electron pathway on the left and two electron pathway on the right. Figure reproduced from reference 40.

A thorough investigation into these pathways was conducted by Johnson *et al*. who, using IR spectroelectrochemistry, concluded that the two electron pathway was facilitated by a coordinating solvent such as CH_3CN, which is able to coordinate to the radical $[Re(CO)_3(bpy)]^•$, producing a solvated species $[Re(CO)_3(bpy)(CH_3CN)]^•$. This solvated species is then reduced, forming the active 5-coordinate anion, as can be seen in figure 1.14. In contrast, in a solvent with much weaker coordination properties, such as THF, no solvated radical was observed until higher potentials were

applied. This was because the radical [Re(CO)$_3$(bpy)]$^{\bullet}$ was able to dimerise because the THF was unable to occupy the vacant coordination site, and while the reduction potential of the solvated complex is comparable to the starting material, the reduction potential of the dimer is significantly higher (table 1.3) providing a driving force for its formation. Thus, coordinating solvent facilitates the two electron pathway by providing a lower energy pathway to the reduced 5-coordinate anion.

It is this two electron pathway that will be discussed in detail as it is the dominant pathway in the systems discussed.

Table 1.3 reduction potentials of intermediates in the two electron process recorded in acetonitrile (potentials in V vs Fc/Fc$^+$)

Complex	E$_{1/2}$
[ReCl(CO)$_3$(bpy)]	-1.86
[Re(CO)$_3$(bpy)]$_2$	-2.03
[Re(CO)$_3$(bpy)(CH$_3$CN)]$^+$	-1.58
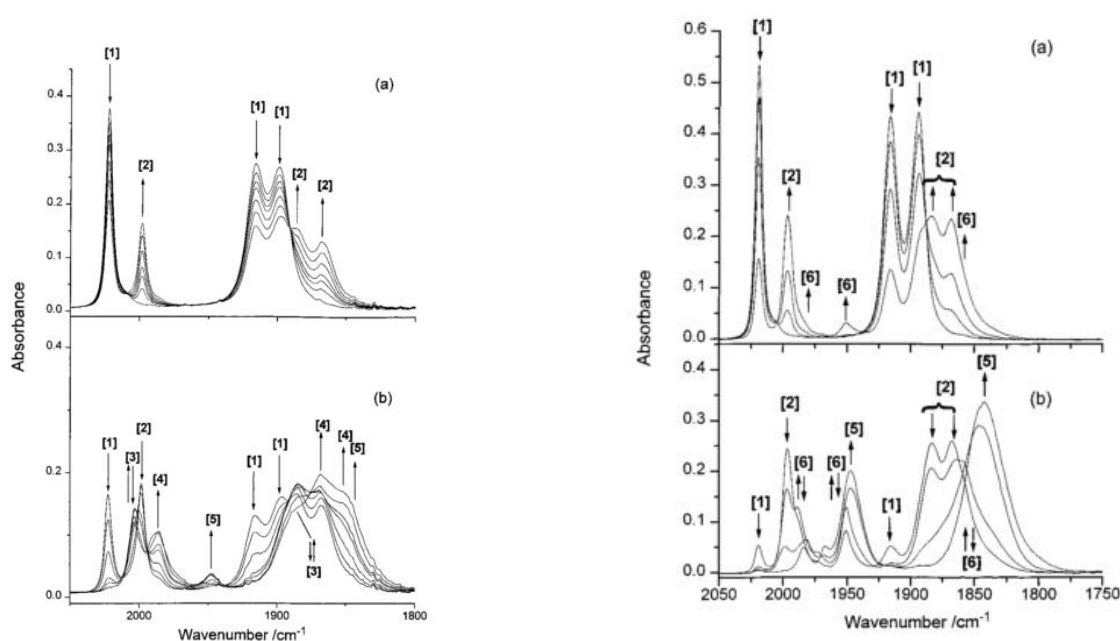
Figure 1.14: Left: ν(CO) IR spectral changes following OTTLE cell reduction of [ReCl(CO)$_3$(bpy)] (1) in acetonitrile solution containing excess Et$_4$NCl as electrolyte (arrows indicate whether the bands decrease ↓ or increase ↑): (a) Initial reduction of [ReCl(CO)$_3$(bpy)] (1) leading to the growth of the one-electron reduced radical anion [ReCl(CO)$_3$(bpy)]$^{\cdot-}$ (2); (b) the three ν(CO) bands assigned to [ReCl(CO)$_3$(bpy)] (1) continuing to decrease. The radical anion [ReCl(CO)$_3$(bpy)]$^{\cdot-}$ (2) is unstable and decays to produce the solvent coordinated radical complex [Re(CO)$_3$(bpy)(CH$_3$CN)]$^{\cdot}$ (3), which is reduced at a similar potential to [ReCl(CO)$_3$(bpy)] (1)to give the two-electron reduced anions, [Re(CO)$_3$(bpy)(CH$_3$CN)]$^-$ (4) and [Re(CO)$_3$(bpy)]$^-$ (5). Figure reproduced from reference 38.

Right: ν(CO) IR spectral changes following OTTLE cell reduction of [ReCl(CO)$_3$(bpy)] (1)in THF solution containing excess Et$_4$NCl as electrolyte. Initial reduction of [ReCl(CO)$_3$(bpy)] (1) leading to the growth of the one-electron reduced radical anion [ReCl(CO)$_3$(bpy)]$^{\cdot-}$ (2). Small features due to the dimer [Re(CO)$_3$(bpy)]$_2$ (6) can been seen to appear as the unstable radical anion 2 begins to decay. (b) The starting complex [ReCl(CO)$_3$(bpy)] (1) is further reduced. The three ν(CO) bands of 2 decrease with a concomitant increase in the intensity of the ν(CO) bands assigned to the dimer 6. As the potential is shifted more negatively, the dimer is reduced leading to the appearance of two new bands assigned to the two-electron reduced, five-coordinate anion [Re(CO)$_3$(bpy)]$^-$ (5). Figure reproduced from reference 38

Discussion of the electrocatalytic rhenium complexes can be divided effectively into three areas; effect of functionalization on the bipyridine, mechanistic aspects and selectivity. Although all three of these areas are heavily interlinked it serves greatly to simplify discussion if they are treated in isolation to some degree.

The original catalyst used by Haweker *et al*. incorporated 2,2'-bipyridine as the diimine, however, other experiments have shown the use of some other bipyridine derivatives lead to more efficient catalysts. One of the first variations of bipyridine employed was 4,4'-dimethyl-2,2'-bipyridine which has been employed in electrocatalytic studies since at least 1996[38]. The definitive work on this compound is probably Smeija *et al*.'s 2010 Inorganic Chemistry paper, in which Re(I) tricarbonyl chloride complexes with numerous bpy-derivatives as ligands were tested for electrocatalytic activity. This study showed that 4,4'-tBu-2,2'-bipyridine (tBu = tertiary butyl) the most electron-donating bpy-derivatives used, was "the best electrocatalyst of the series"[41]. This term is somewhat misleading however as the "best" catalyst of any series depends entirely upon what metric one is using. In this case, the best catalyst was the one that gave the greatest current enhancement and hence turn over frequency. However, this is not a fair comparison as the over potential used was necessarily much greater in the case of the 4,4'-tBu-2,2'-bipyridine complex, as compared with, for instance, bpy. This concept is explored further in chapter 8, but it is important to be sure when talking about the "best" of any catalyst that we are comparing like with like and the metrics we use are well defined.

Although many rhenium tricarbonyl complexes had been reported, relatively few had been tested for catalytic activity regarding CO_2 reduction[42,43]. In this work [ReCl(CO)$_3$(bpy-COOH)] (bpy- COOH = 4,4'-dicarboxyl-2,2'-bipyridine), [ReCl(CO)$_3$(bpy)], [ReCl(CO)$_3$(dmbpy)] (dmbpy = 4,4'-dimethyl-2,2'-bipyridine), [ReCl(CO)$_3$(bpy-tBu)] (bpy-tBu = 4,4'-di-tert-butyl-2,2'- bipyridine) and [ReCl(CO)$_3$(bpy-OMe)] (bpy-OMe = 4,4'-dimethoxy-2,2'-bipyridine) (electron donating ability in the order COOH <H <Me <tBu <OCH_3) were synthesised and tested for catalytic efficacy.

Solutions of the proposed rhenium based catalyst were tested via cyclic voltammetry in CO_2 saturated and argon saturated acetonitrile. Where current enhancement was observed under the CO_2 saturated solution catalytic activity could be assigned, figure 1.15. [ReCl(CO)$_3$(bpy-COOH)] and [ReCl(CO)$_3$(bpy-OMe)] showed little to no current enhancement indicating that they are not catalytically active. [ReCl(CO)$_3$(bpy)] showed a 3.4-fold current increase at -1.73 V vs SCE, [ReCl(CO)$_3$(dmbpy)] showed a current enhancement that was slightly larger while [ReCl(CO)$_3$(bpy-tBu)] showed the largest catalytic current with an 18.4 fold increase in peak current at a scan rate of 100 mV s^{-1}.
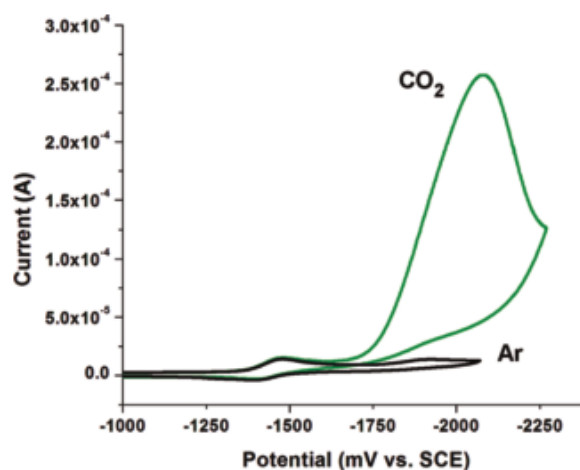
Figure 1.15 figure showing current enhancement of [ReCl(CO)₃(bpy-tBu)] under CO₂ as compared to argon. Figure reproduced from reference 41.

Further testing showed that [ReCl(CO)₃(bpy-tBu)] displayed a 3.5 times increase in catalytic current compared with [ReCl(CO)₃(bpy)] with turnover frequencies greater than 200 s⁻¹, faradaic efficiency of ca. 100% and no loss of performance over 5 hours[41]. This increase in efficiency came at the expense of more negative reduction potentials (the implications of this phenomenon for our results are discussed in chapter 8) as more electron-donating bpy-ligands were employed.

Table 1.4: Reduction potentials for the rhenium bipyridine complexes investigated by Smeija *et al*.[41]

Complex	1st reduction potential (mV vs SCE)	2nd reduction potential (mV vs SCE)
[ReCl(CO)₃(bpy-COOH)]	-940	-1725
[ReCl(CO)₃(bpy)]	-1340	-1725
[ReCl(CO)₃(dmbpy)]	-1430	-1765
[ReCl(CO)₃(bpy-tBu)]	-1445	-1830
[ReCl(CO)₃(bpy-COOH)]	-1485	-1860

Rhenium catalysed CO₂ reduction has been the subject of intense study[44] with an aim to understand it and hence improve efficiency of catalysis. The rhenium species discussed in this chapter are characterised by a two one electron reductions, an often reversible one electron reduction in the region -1.4 V vs SCE and an irreversible reduction at ca. 1.7 V vs SCE[45].

The reactivity of the rhenium complexes upon reduction is determined by the π-accepting ability of the bpy ligand, with more π-accepting bipyridines being able to lower the energy gap between the Re and the π* orbitals and thus the reduction potential of the complex[46]. However, bpy π* orbitals of

higher relative energy polarize the Re-X bond[47], resulting in more facile dissociation. This partially helps to account for the increased reactivity of the complexes with electron donating groups on the bpy ring[41]. The initial reduction is localised predominantly on the bpy[48] with dissociation of the chloride ligand taking place slowly there after[38], in a solvent such as acetonitrile the 5-coordinate radical will be stabilised by the association of a solvent molecule. The complex is then reduced again resulting in loss of the solvent molecule and formation of the 5-coordinate anion. CO_2 coordinates directly with this resulting in $[Re(CO)_3(bpy)(CO_2)]^-$ which is rapidly protonated to form $[Re(CO)_3(bpy)(CO_2H)]^{[49]}$ in a non-rate limiting step. Protonation occurs even in the absence of a Brönsted acid and has been speculated to arise from the extraction of a proton from solvent acetonitrile.[48]

It has been found that the $[Re(CO)_3(bpy-tBu)]^-$ reacts approximately ten times faster with CO_2 than the similar $[Re(CO)_3(bpy)]^-$ most likely due to the higher over potentials which provides a greater driving force for the reaction. The complex is then reduced again and protonated resulting in loss of water. Experiments involving the substitution of available H^+ with D^+ show a kinetic isotope effect, as the first reduction is facile and rapid (*vide supra*) it is believed that the second reduction is a rate determining step[48]. A further reduction then takes place releasing $CO^{[37]}$, which Grice *et al*. have suggested may be facilitated by electron transfer from a catalytic quantity of reduced solvated species $[Re(CO)_3(bpy-R)(CH_3CN)]^\bullet$, as shown in figure 1.16.
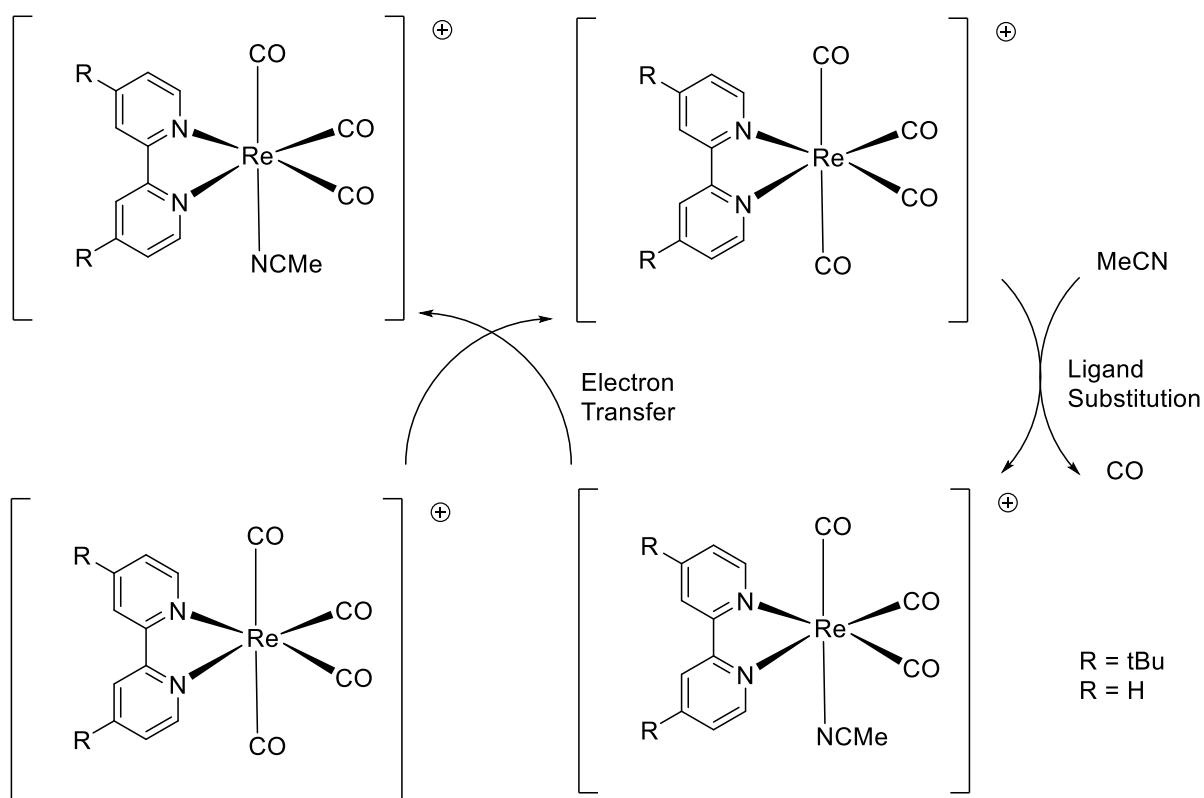
Figure 1.16 Electron transfer catalysed ligand substitution, Figure reproduced from reference 37.

A cursory reading of the literature shows that while it is agreed that 1) a 2 electron reduction of the [Re Cl(CO)$_3$(bpy)] leads to the catalytically active 5-coordinate anion [Re(CO)$_3$(bpy)]$^-$; 2) a 2 electron reduction takes place after CO_2 coordinates to the rhenium; and 3) this involves the presence of protons and that CO is produced, there is some debate as to the actual path taken. To this end, Keith *et al.*[37] performed a combined experimental and computational study to determine the most likely pathway of CO_2 reduction. These pathways are shown in figure 1.17, with reaction coordinates in figure 1.18 illustrating the most likely pathways to operate. Significantly, the presence of a counter ion (modelled as K$^+$) proved crucial, in their calculations, to facilitate the most thermodynamically favourable pathway (i.e. that with the most negative Gibbs free energy).
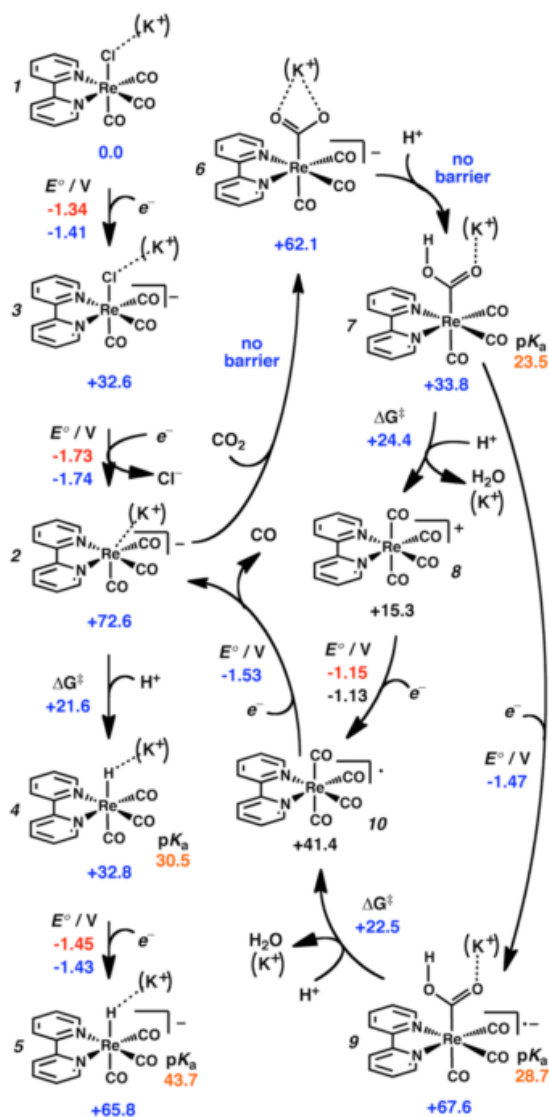
Figure 1.17: [a]**Reaction free energies (labelled below each complex and referenced to complex 1-K) and barrier heights (ΔG‡) are reported in kcal/mol. Data colours: red = experimentally obtained reduction potentials; black = calculated data with no counter ion present; blue = calculated data involving an explicit K$^+$ counter ion interacting with the Re complex; orange = calculated pK$_a$s obtained after applying a linear correction to reduce systematic errors in acetonitrile pK$_a$s. Figure reproduced from reference 37.**

In the lowest energy pathway the [ReCl(CO)$_3$(bpy)] is reduced and Cl$^-$ is lost with help of stabilisation of a counter ion, the complex is then reduced again to form **2**, CO$_2$ binds to **2** forming **6** which is then protonated to **7**. At catalytic over potentials (below -1.25 V vs SCE) **7** can be reduced to **9** which is then protonated causing loss of water and reduced to **10**, **10** is likely a highly transient species since it has not been observed spectroscopically from the reduction of **8** +e$^-$ →**10** and hence rapidly decays to **2**.
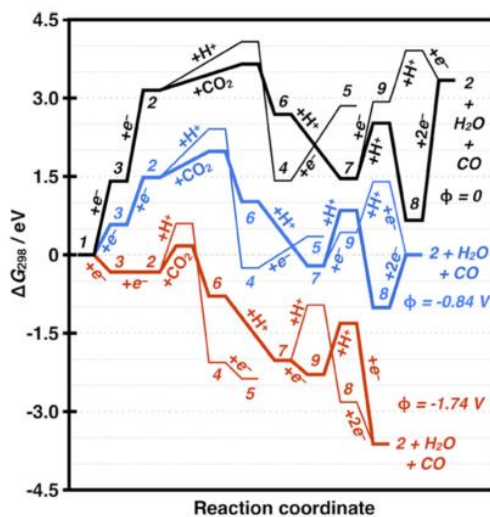
Figure 1.18: A mechanistic summary depicting overall reaction free energies and their dependencies on applied electrode potential. Numbers represent Re complexes shown in Scheme 2. Energetically preferred pathways at each potential are denoted with the thick lines. Figure reproduced from reference 37.

Rhenium tricarbonyls are highly selective for CO generation over hydrogen reduction. This selectivity most likely arises due to orbital overlap, kinetics and activation barriers. It has been speculated that the mixed metal ligand character of the catalyst HOMO provides better overlap with the σ+π orbitals of CO$_2$ compared with the purely σ orbitals of the H$^+$.[48] Reaction of the catalyst with CO$_2$ is significantly faster than with water or methanol as a reactant; rate constants of the order of ca. 1 s^{-1} were observed with water and methanol. However, a rate constant of 35 s^{-1} was seen with CO$_2$ showing that there is a significant kinetic preference for reaction CO$_2$. This kinetic preference appears to be due to a higher activation energy for the binding of H$^+$. Even though the protonated species (**4** in figure 1.18) is 4.2 kJ mol^{-1} more stable than the CO$_2$ bound species the barrier for protonation is 42.3 kJ mol^{-1} higher than the barrier for CO$_2$ binding when MeOH is used as the Brönsted acid. This higher activation barrier appears to be due to the stability of the conjugate base, for methanol in acetonitrile a counter ion is needed to stabilise the conjugate base and a relatively high pK$_a$ is observed (calculated pK$_a$ ≈ 37). However, calculations with HCl (calculated pK$_a$ ≈ 11) show that the protonation barrier would be greatly reduced and hydrogen production would occur. Thus it appears the stability of the

conjugate base decides the reaction mechanism indeed when ammonium was used as the Brönsted acid ($pK_a \approx 16.5$) H_2 was produced[50].

1.3 Manganese tricarbonyls as CO_2 reduction catalysts

Although rhenium catalysts for CO_2 reduction have been known for some time, there has been remarkably little effort to substitute the expensive and rare rhenium metal centre. This may be due in part to findings indicating that $[Mn(X)(CO)_3(\alpha\text{-diimine})]$s were not catalytically active.[38] This was largely believed be due to the greater electron density and less diffuse orbital structure of the manganese metal centre stabilising the 5-coordinate intermediate and preventing CO_2 from binding. However, in 2011, Bourrez *et al.* reported the successful employment of $[MnBr(CO)_3(bpy)]$ and $[MnBr(CO)_3(dmbpy)]$ for the electrocatalytic reduction of CO_2 to CO in acetonitrile at reduction potentials of -1.8 V and -1.89 V vs Ag/Ag^+ respectively.[51]

When the complexes are subjected to cyclic voltammetry, two irreversible reduction peaks are observed at -1.56 V and -1.8 V vs Ag/Ag^+ for $[MnBr(CO)_3(bpy)]$ and at -1.64 V and -1.89 V vs Ag/Ag^+ for $[MnBr(CO)_3(dmbpy)]$. It is believed that the first reduction results in the labialisation of the bromide ligand which instantly dissociates, leaving the $[Mn(CO)_3(L)]^{\bullet}$ radical, which then forms the dimer $[Mn(CO)_3(diimine)]_2$. The second reduction results in splitting of the Mn-Mn bond and forms the catalytically active 5-coordinate species $[Mn(CO)_3(diimine)]^{-}$ (vide infra). This is very similar to the proposed mechanisms for CO_2 reduction involving the rhenium analogues (*vide supra*).

The manganese dimer ($[Mn(CO)_3(diimine)]_2$) was identified by UV-Vis spectroscopy during bulk reductive electrolysis. The reduced species $[MnBr(CO)_3(diimine^{\bullet-})]^{-}$ was not observed, though, suggesting that elimination of the Br^{-} is rapid upon reduction. This is in contrast to rhenium analogue where the reduced intermediate is stable and observable[38]. The results displayed in table 1.5 also show that the dimer is formed in solution, as the second reduction potential clearly matches the first reduction potential of the corresponding dimer species.

Table 1.5 Redox potentials[a] and UV/Vis data of manganese carbonyl complexes in CH₃CN with 0.1 M TBAP.[51]

Complexes	1st reduction potential (mV vs Ag/Ag$^+$)	2nd reduction potential (mV vs Ag/Ag$^+$)	λ_{max} Abs nm
$[MnBr(CO)_3(bpy)]$	-1560	-1800	366(sh), 416
$[MnBr(CO)_3(CH_3CN)]$[a]	-1420	-1800	376
$[MnBr(CO)_3(dmbpy)]$	-1640	-1890	360(sh), 412
$[MnBr(CO)_3(CH_3CN)]$[a]	-1500	-1890	375
$[Mn(CO)_3(bpy)]_2$	-1800	-	394, 461, 633, 806
$[Mn(CO)_3(dmbpy)]_2$	-1890	-	404, 445, 538(sh), 638, 817
$[Mn(CO)_3(bpy)]^-$	-	-	370, 560, 626(sh)
$[Mn(CO)_3(dmbpy)]^-$	-	-	374, 561

[a] Synthesised complexes

When a solution of [MnBr(CO)$_3$(diimine)] in acetonitrile was saturated with CO$_2$, no catalytic current was observed at any voltage until the addition of water to the solution, which resulted in the emergence of a catalytic current on the second reduction peak (see figure 1.19). Also seen was the formation of a new reduction peak at a potential 150 mV less negative that the first reduction of the complex, attributed to reduction of [Mn(diimine)(CO)$_3$(solvent)]$^+$ which is formed from the partial solvolysis of [MnBr(CO)$_3$(dmbpy)]. These results indicate that a proton source is necessary for manganese catalysed CO$_2$ reduction, in contrast to the rhenium analogues where catalysis still occurs even in the absence of added Brönsted acids. In the case of rhenium, it appears that acetonitrile[52] is able to act as a proton donor while the endergonic CO$_2$ binding free energy prevents protonation by acetonitrile in the case of the manganese analogue.[53]
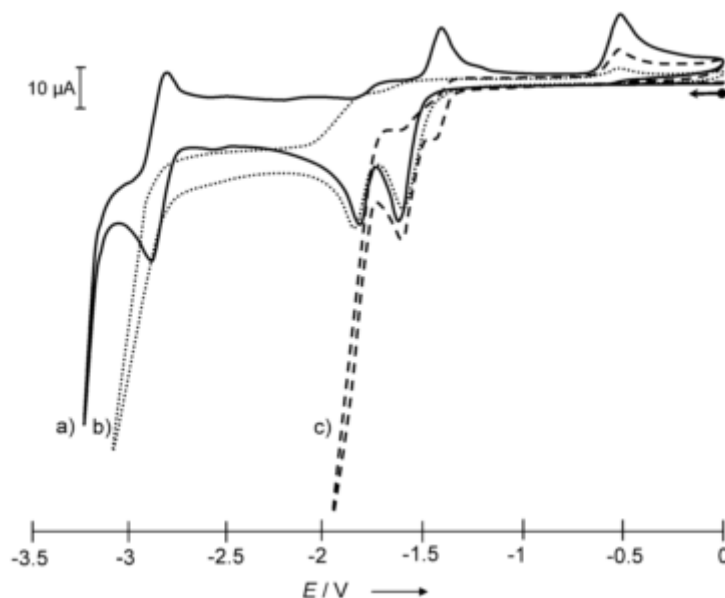
Figure 1.19 CV's of [MnBr(CO)$_3$(bpy)] at a concentration of 1 mM in CH$_3$CN with 0.1 M TBAP versus a vitreous carbon electrode of 3 mm diameter, $v = 100 mVs^{-1}$ at room temperature a) under Ar and under CO$_2$, b) without and c) with 5% of H$_2$O. Figure reproduced from reference 51.

This idea has been developed further by Kubiak *et al.*, whose 2013 paper discussing the importance of acids in manganese catalysed CO$_2$ reduction revealed many interesting differences between the manganese and rhenium analogues.[52] Their findings showed clearly that the addition of a proton source of some nature was crucial in order to facilitate the turnover of the manganese catalyst, and that the addition of more or stronger Brönsted acids also resulted in stronger catalytic current, even rivalling those of the rhenium catalysts.
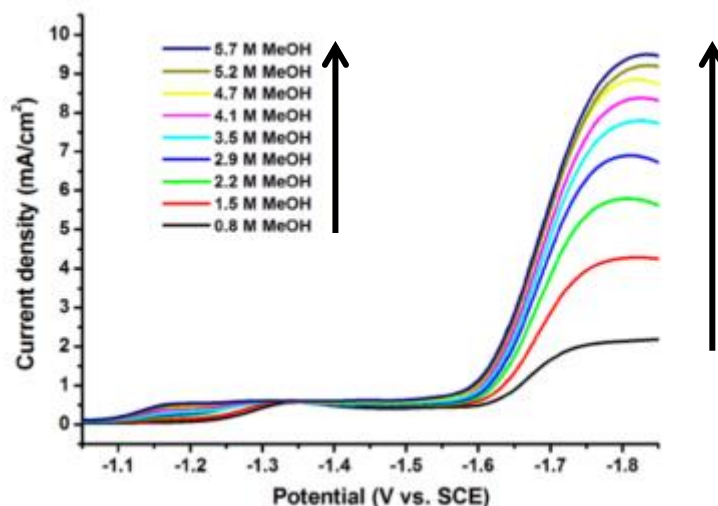
Figure 1.20 Linear scan voltammograms showing the electrocatalytic reduction of CO_2 to CO by 1 mM [MnBr(CO)$_3$(bpy-tBu)] in acetonitrile with addition of MeOH. The solution is under an atmosphere of, and saturated with (ca. 0.28 M), carbon dioxide. Electrochemical conditions were 0.1 M TBAH as supporting electrolyte, 1 mm diameter glassy carbon working electrode, Pt wire counter electrode, and Ag wire reference electrode separated from the bulk solution by a Vycor tip. Figure reproduced from reference 52.

Table 1.6 Comparison of Peak i_{cat}/i_p Values for both Mn(bpy-tBu)(CO)$_3$Br and [Re(bpy-tBu)(CO)$_3$(CH$_3$CN)](OTf) in CH$_3$CN (1 mM in Each Catalyst). Solutions Are Saturated with (ca. 0.19−0.28 M)ᵃ and under an Atmosphere of CO2 with Added Brönsted Acids.[52]

	[MnBr(CO)$_3$(bpy-tBu)]			**[Re(CO)$_3$(bpy-tBu)(CH$_3$CN)](OTf)**			
Brönsted acid	**[acid]** **M**	**i_{cat}/i_{peak}**	**TOF** **(s⁻¹)**	**[acid]** **M**	**i_{cat}/i_{peak}**	**TOF** **(s⁻¹)**	**TOF$_{Mn}$/ TOF$_{Re}$**
None	0.0	1.0	0	0.0	3.3	2.1	
H$_2$O	3.1	25	120	10	9.0	16	7.5
MeOH	5.8	26	130	9.9	42	340	0.38
TFE	1.4	42	340	1.6	54	570	0.60

[CO$_2$] is ca. 0.28 M in dry CH$_3$CN, 0.19 M in 10 M H$_2$O, 0.22 M in 9.9 M MeOH and 0.27 M in 1.6 M TFE

Table 1.6 shows a comparison between [MnBr(CO)$_3$(bpy-tBu)] and a [Re(CO)$_3$(bpy-tBu)(CH$_3$CN)] (OTf) analogue. The manganese catalyst clearly outperforms the rhenium one in water with both a higher turnover frequency and a higher catalytic current. This situation is reversed when MeOH or TFE (2,2,2-trifluoroethanol) are used. In the paper no explanation as to why manganese should be more active than rhenium in water but not in stronger acids is offered. It may be that while the water coordinates to rhenium in a competitive equilibrium with CO_2 inhibiting binding and reduction of the CO_2[54] the same competitive coordination serves to stabilise the 5-coordinate manganese intermediate.

What is also clearly significant is that the reduction of CO_2 occurs at a significantly smaller overpotential for the manganese catalyst as compared to the rhenium analogue, with reduction occurring at -1.39 V vs SCE and -1.57 V vs SCE for [MnBr(CO)$_3$(bpy-tBu)] and -1.45 V vs SCE and -1.83 V vs SCE for [ReCl(CO)$_3$(bpy-tBu)].[41] This means that under aqueous conditions the manganese out performs it rhenium counterpart in terms of reduced over potential, catalytic current and turn over frequencies.

1.3.1 Mechanism of Mn(CO)$_3$(alpha-diimine)(X) CO_2 catalysis

Using [MnBr(CO)$_3$(bpy)] the first reduction results in the dissociation of the bromide ligand and dimerization with neither the [MnBr(CO)$_3$(bpy$^-$)]$^{\bullet-}$ or [Mn(CO)$_3$(bpy)]$^{\bullet}$ intermediates being visible by either UV-Vis or IR spectroscopy[51,52]. Rather the associated growth of characteristic [Mn(CO)$_3$(bpy)]$_2$ CO vibrational bands at 1973, 1928, 1878, and 1850 cm^{-1} and UV absorption bands at 394, 461, 633, 806 nm shows that bromide dissociation and dimerization occurs rapidly upon first reduction. Time resolved infrared (TRIR) studies reveal that no solvent binds into the vacant coordination site before dimerisation, instead a 5 coordinate radical species is produced which rapidly dimerises ($2k_{dim}$ = (1.3 $\pm$ 0.1) X 10^9 M^{-1} s^{-1})[55]. This is in contrast to rhenium analogues in which [ReCl(CO)$_3$(bpy$^-$)]$^{\bullet-}$ can be observed using IR spectroscopy and identified by the ca. 20 cm^{-1} bathochromic shift of the carbonyl peaks.[41] This difference arises because in the case of the rhenium analogue the first reduction is predominantly based upon the bpy ligand inhibiting chloride loss. Upon the loss of the halogen ligand the binding of a new sixth ligand to the metal centre is more favourable in the case of the rhenium analogue than the manganese complex. This is because the 5d electrons of the rhenium complex are bound less strongly metal centre than the 3d electrons of the manganese complex. Thus upon reduction the electron density is located upon the metal centre more so than the bpy ligand. As such, binding of sixth ligand to the one electron reduced manganese complex would lead to transfer of electron density from the metal centre to the bpy ligand which is energetically costly.[56]

Post dimerization, two pathways have been proposed which I shall refer to as the anionic and oxidative pathways respectively. The anionic pathway involves a reduction of the dimer generating a third species. The anionic pathway is broadly similar to the 2 electron pathway observed in rhenium complexes. Kubiak *et al*. showed an example with ν(CO) stretching vibrations at 1907 and 1807 cm^{-1},[52] corresponding to the 5-coordinate anion [Mn(CO)$_3$(bpy-*t*Bu)]$^-$ which was identified by comparison with the CO bands detected in the IR spectrum of [Mn(CO)$_3$(bpy-*t*Bu)][k(18-crown-6)] (1905 and 1805 cm^{-1}). Bond length alterations of the bpy ring obtained by DFT calculations indicated that significant electron density was located on the ring but the very low energy CO stretching frequencies revealed strong M-CO back bonding indicating that the manganese metal centre is comparatively electron dense.

By contrast, the oxidative pathway was identified by Bourez *et al.* using pulsed EPR studies and found a low spin Mn^{II} complex generated by the addition of water and CO_2 in a collaborative pathway. In this path, CO was only released after a 2 electron reduction after a Mn-COOH intermediate had been formed, figure 1.22.[57]
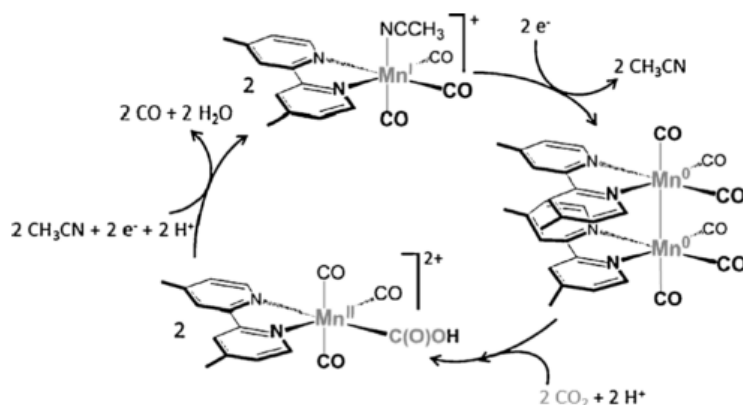
Figure 1.22 Proposed oxidative pathway for CO₂ reduction by Mn(diimine)(CO)₃X catalyst. Figure reproduced from reference 57.

Upon the second reduction the dimer breaks along the Mn-Mn bond producing the catalytically active $[Mn(CO)_3(bpy)]^-$ anion upon which CO_2 binds forming $[Mn(CO)_3(bpy)(CO_2)]^-$. This intermediate is stabilised by the binding of H^+ to an oxygen atom on the CO_2, facilitating the cleavage of one of the carbon oxygen bonds. From here, computational investigations show that reduction can take place in a manner similar to that described for the rhenium analogues (reduction-first pathway) or via a pathway which involves protonation of the CO_2 bound species (protonation-first pathway) which is energetically unfavourable for the rhenium catalyst, allowing the manganese catalysts to reduce CO_2 at significantly lower potentials than the rhenium catalysts.[56]
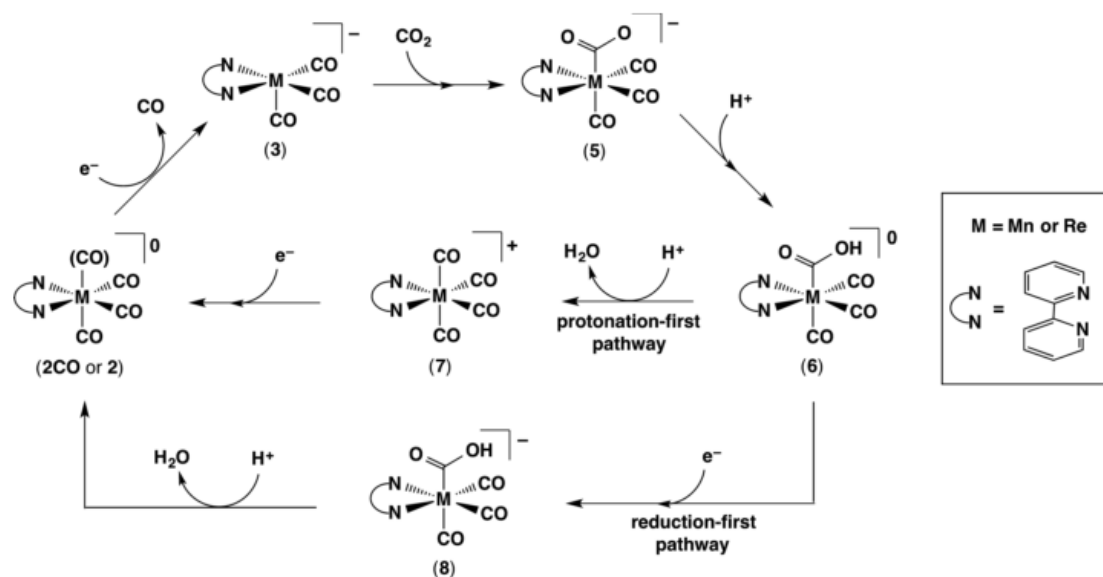
Figure 1.23 Schematic catalytic reaction mechanism of CO₂ reduction by the active catalysts [Mn(CO)₃(bpy)]⁻ and [Re(CO)₃(bpy)]⁻. Figure reproduced from reference 56.

1.3.2 Direct formation of the 5-coordinate anion

Since the active catalytic species is the 5-coordiante anion efforts have been made to attempt to generate the 5-cooridnate anion directly upon first reduction in the hope of reducing the catlaytic overpotaential neccisary to induce CO₂ reduction. The first such effort was made by Kubiak *et al*. who reported a study in which the complex [MnBr(CO)₃(mesbpy)] (where mesbpy is 6,6'-dimesityl-2,2'-bipyridine) was investigated. The bpy moiety utilised contained bulky mesityl groups which inhibited the dimerization of the complex upon first reduction.[58] In the observed mechanism, only a single reversible two electron reduction wave was observed at –1.55 V vs. Fc⁺/Fc, indicating that the first and second reduction took place at the same potential. This is close to the first reduction potential observed for [MnBr(CO)₃(bpy)] of -1.6 V vs. Fc⁺/Fc as can be seen in figure 1.16, however, IR studies have shown that singly reduced species grows in first with stretches later being observed for the two electron reduced species suggesting two single electron reductions in an EEC or ECE mechanism rather than a concerted two electron reduction.
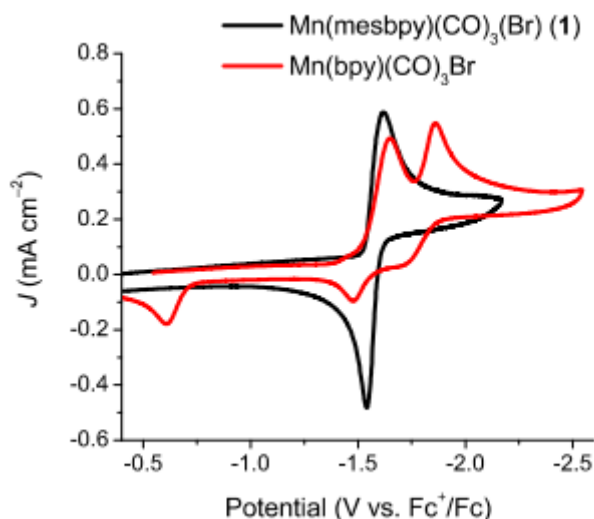
Figure 1.24 Comparison of the cyclic voltammograms of [MnBr(CO)₃(mesbpy)] and [MnBr(CO)₃(bpy)]under identical conditions (1 mM complex). Each experiment is performed in CH₃CN with 0.1 M TBAPF₆ as the supporting electrolyte, under an atmosphere of N₂, at a scan rate of 100 mV s⁻¹, with a glassy carbon working electrode (3 mm diameter), with a platinum wire counter electrode, and with a Ag/AgCl wire pseudo-reference, and with Fc added as an internal reference. Figure reproduced from reference 58

At the applied potential the catalyst was observed to bind CO_2 but would not release the resultant CO in order to turn over catalytically. Catalytic CO generation could only be achieved after the application of a further 300 mV of overpotential was applied, indicating that the CO bound complex is more stable than the halogen coordinated parent complex. Interestingly in methanol or TFE, the bulky catalyst was observed to be more active than the previously reported most active catalyst [MnBr(CO)₃(tBu-bpy)], however this was the case when using water as the Brönsted acid, exhibiting TOF of 700 s⁻¹ at 3.5 M H_2O, TOF = 2000 s⁻¹ at 3.2 M MeOH and TOF = 5000 s⁻¹ at 1.4 M TFE. Under Identical conditions [MnBr(CO)₃(mesbpy)] is ca. 1.2 times more active than [MnBr(CO)₃(tBu-bpy)].

The same rationale has also led the utilisation of [Mn(CO)₃(iPr-DAB)]⁻ (DAB = 1,4- diazabuta-1,3-diene, iPr = isopropyl) as it too forms the 5-coordinate anion directly upon reduction of the parent complex without the added complication of incorporating a large amount of steric bulk in the vicinity of the vacant coordination site.[59,60,61] Unfortunately the results were almost identical to what was observed for the Mn-mesbpy complex and CO_2 was able to bind with the 5-coordinate anion at lower potentials but required the application of even more negative potentials in order to induce catalytic turn over and CO release.

1.3.3 Photocatalysis using a Mn(CO)₃(alpha-diimine)(X) complex

Development of a photocatalytic system for a [Mn(CO)₃(alpha-diimine)(X)] has proven difficult due to the photo instability of this class of compounds[12] which decay via photo induced dimerisation[62] and

as a result the above studies have concentrated their efforts on using [MnBr(CO)$_3$(L)] (L = bpy derivative) as electrocatalysts. Although this is a sensible avenue of inquiry it does limit the applications of the manganese catalyst somewhat as many desire to develop a 'wireless' solar fuel cell in which light harvesting and CO$_2$ reduction take place via a discreet photochemical reaction.

Thus far the only progress that has been made on this is by Takeda *et al*. who published a paper in 2014 in which [Ru(dmb)$_3$]$^{2+}$ was used as a photosensitiser for *fac*-[MnBr(CO)$_3$(bpy)] in a bimolecular system.[63] In a typical run, a 4:1 (v/v) mixed solution of N,N'-dimethyl-formamide (DMF) and triethanolamine (TEOA) was used as solvent with 1-benzyl-1,4- dihydronicotinamide (BNAH) as a sacrificial electron donor. In order to prevent decomposition of the manganese catalyst photo excitation was by a 480 nm monochromatic light which was only absorbed by the ruthenium based photosensitiser and not absorbed by the catalyst, see figure 1.21.
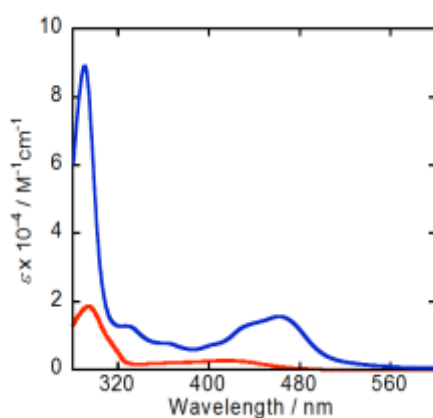
Figure 1.25 UV-Vis absorption spectra of [MnBr(CO)$_3$(bpy)] (red) and [Ru(dmb)$_3$](PF$_6$)$_2$ (blue) in DMF, reproduced from supplementary information. Figure reproduced from reference 63.

Outside of the novelty of applying photo sensitisation to a [Mn(CO)$_3$(alpha-diimine)(X)] catalyst this paper also reports that the major product of the reaction was formic acid with a selectivity of 85% and smaller quantities of carbon monoxide and hydrogen also being formed. This contrasts with other papers for both the manganese catalyst and its rhenium analogue which report CO as the major product with little and usually no other products formed. [51,52,35] What is especially interesting that when the DMF-TEOA mixture was replaced with CH$_3$CN -TEOA the distribution of products shifted so that formic acid was still the major product but with significantly more CO production. This suggests that altering the solvent used in the reaction may allow a degree of tuneability in the product, perhaps allowing more reduced products (*vide supra*) to be formed if the right solvent mixture were found, although this seems a distant prospect at present.

Table 1.7 Photocatalytic reactions of the Ru-Re complexes under differing solvent and irradiation conditions. Figure reproduced from reference 63.

Entry	Mn complex	Ru complex	Solvent	Irradn time/min	TON		
					HCOOH	CO	H_2
1	fac-Mn(bpy)(CO)$_3$Br	[Ru(dmb)$_3$]$^{2+}$	DMF–TEOA	10	4	2	0
				120	67	8	1
				720	149	12	14
2[b]	fac-Mn(bpy)(CO)$_3$Br	[Ru(dmb)$_3$]$^{2+}$	DMF–TEOA	720	4	2	49
3	—	[Ru(dmb)$_3$]$^{2+}$	DMF–TEOA	120	8	1	4
				720	25	3	11
4	fac-Mn(bpy)(CO)$_3$Br	—	DMF–TEOA	720	1	3	0
5	fac-Mn(bpy)(CO)$_3$Br	[Ru(dmb)$_3$]$^{2+}$	DMA–TEOA	720	98	9	14
6	—	[Ru(dmb)$_3$]$^{2+}$	DMA–TEOA	720	19	3	7
7	fac-Mn(bpy)(CO)$_3$Br	[Ru(dmb)$_3$]$^{2+}$	MeCN–TEOA	720	78	40	17
8	—	[Ru(dmb)$_3$]$^{2+}$	MeCN–TEOA	720	14	2	12
9	fac-Mn(bpy)(CO)$_3$Br	[Ru(bpy)$_3$]$^{2+}$	DMF–TEOA	720	157	12	8

[a] Irradiation with 480 nm monochromatic light (intensity, 4.3×10^{-8} einstein s^{-1}) conducted on a solution containing a Mn complex (0.05 mM), a Ru complex (0.05 mM), BNAH (0.1 M) and TEOA (25 v%) under a CO_2 atmosphere. [b] Under an Ar atmosphere.

While this represents a hugely interesting proof of concept for photocatalysis by [Mn(CO)$_3$(alpha-diimine)(L)]'s it is not a viable method of solar energy harvesting and provides ample scope for development.

1.4 Conclusions

The discussion above shows that there is high scope for development of manganese complexes as CO_2 reduction catalysts. Manganese-based catalysts typically exhibit a lower catalytic over potential, higher activity in water and lower cost to manufacture than the rhenium analogues; however, the photosensitivity may prove to be a significant hindrance to its further development and will probably limit manganese tricarbonyls to electrocatalytic uses.

Prior work with rhenium tricarbonyls has shown that photocatalytic CO_2 reduction with the complexes of group VII elements with alpha-diimines is possible. Further, it has been shown that sensitisation of the catalyst with a separate photon harvesting moiety is possible and has been successfully applied to sensitize manganese complexes. However, such work requires the use of a sacrificial electron donor in all cases and the reduction process is slow compared with electrocatalytic methods.

Both rhenium and manganese tricarbonyl alpha diimine complexes show catalytic activity toward CO_2 reduction. In the case of rhenium, this usually involved a one-electron reduction, elimination of the halogen and coordination of a solvent molecule, reduction of the solvated species and elimination of the solvent molecule, coordination of the CO_2 and its reduction. Manganese complexes incorporating bipyridine ligands do not form a solvated species upon reduction and instead dimerise upon first reduction, though this can be inhibited both through ligand design and incorporating steric bulk. The active species of CO_2 reduction by Mn diimines is almost certainly the 5-coordinate anion having been observed with IR spectroscopy.

Inhibition of dimerisation via incorporation of greater steric bulk allows CO_2 to bind to the manganese metal centre at a lower over potential, however, application of greater over potentials are required to

release CO from the sterically hindered manganese centre. This was also the case when the 5-cooridnate anion was generated directly upon first reduction when using manganese catalysts incorporating DAB ligands as the diimine.

From a reading of the literature, the initial direction of the project solidified around two aims. The first aim being to conduct investigation aimed on finding out the nature of photo degradation (in particular determining if this actually inhibits catalysis and what the products of photo degradation are) including the degree to which structural modification can prevent or hinder degradation. The second aim being to investigate refinements to the Lehn type catalyst/catalytic system utilising decorated alpha diimines with the aim to inhibit dimerisation, lower over potentials and hopefully increase stability. It is from these initial concepts that the research in this thesis has sprung.

1.5 References

(1)   Roy, S. C.; Varghese, O. K.; Paulose, M.; Grimes, C. A. *ACS Nano* **2010**, *4*, 1259.

(2)   Habisreutinger, S. N.; Schmidt-Mende, L.; Stolarczyk, J. K. *Angew. Chem. Int. Ed. Engl.* **2013**, *52*, 7372.

(3)   Angamuthu, R.; Byers, P.; Lutz, M.; Spek, A. L.; Bouwman, E. *Science* **2010**, *327*, 313.

(4)   Qiao, J.; Liu, Y.; Hong, F.; Zhang, J. *A review of catalysts for the electroreduction of carbon dioxide to produce low-carbon fuels.*; 2013.

(5)   Sohn, Y.; Huang, W.; Taghipour, F. *Appl. Surf. Sci.* **2017**, *396*, 1696.

(6)   Li, X.; Yu, J.; Wageh, S.; Al-Ghamdi, A. A.; Xie, J. *Small* **2016**, *48*, 6640.

(7)   Huang, C.; Li, Z.; Zou, Z. *MRS Commun.* **2016**, *6*, 216.

(8)   Li, K.; Peng, B.; Peng, T. *ACS Catal.* **2016**, *6*, 7485.

(9)   Lavrov, O. B.; Kuleshevich, L. V. *Dokl. Earth Sci.* **2010**, *432*, 598.

(10)   Stufkens, D. J.; van der Graaf, T. Van; Stor, G. J.; Oskam, A. *Coord. Chem. Rev.* **1991**, 331.

(11)   Rossenaar, B. D.; Stufkens, D. J.; Oskam, A.; Fraanje, J.; Goubitz, K. *Inorganica Chim. Acta* **1996**, *247*, 215.

(12)   Staal, L. H.; Oskam, A.; Vrieze, K. *J. Organomet. Chem.* **1979**, *170*, 235.

(13)   Benson, E. E.; Kubiak, C. P.; Sathrum, A. J.; Smieja, J. M. *Chem. Soc. Rev.* **2009**, *38*, 89.

(14)   Hawecker, J.; Lehn, J.; Ziessel, R. *J. Chem. Soc., Chem. Commun.* **1983**, 536.

(15)   Takeda, H.; Ishitani, O. *Coord. Chem. Rev.* **2010**, *254*, 346.

(16)   Froehlich, J. D.; Kubiak, C. P. *Inorg. Chem.* **2012**, *51*, 3932.

(17)   Delor, M.; Sazanovich, I. V; Towrie, M.; Spall, S. J.; Keane, T.; Blake, A. J.; Wilson, C.; Meijer, A. J. H. M.; Weinstein, J. A. *J. Phys. Chem. B* **2014**, *118*, 11781.

(18)   Sato, S.; Sekine, A.; Ohashi, Y.; Ishitani, O.; Blanco-Rodríguez, A. M.; Vlcek, A.; Unno, T.; Koike, K. *Inorg. Chem.* **2007**, *46*, 3531.

(19)   Takeda, H.; Koike, K.; Morimoto, T.; Inumaru, H.; Ishitani, O. *Adv. Inorg. Chem.* **2011**, *63*, 137.

(20)   Rossenaar, B. D.; Stufkens, D. J.; Vlcek, A. J. *Inorg. Chem.* **1996**, *35*, 2902.

(21)   Rossenaar, B. D.; Stufkens, D. J.; Vleek, A. *Inorganica Chim. Acta* **1996**, *247*, 247.

(22)   Morris, A. J.; Meyer, G. J.; Fujita, E. *Acc. Chem. Res.* **2009**, *42*, 1983.

(23)   Kou, Y.; Nabetani, Y.; Masui, D.; Shimada, T.; Takagi, S.; Tachibana, H.; Inoue, H. *J. Am. Chem. Soc.* **2014**, *136*, 6021.

(24)   Takeda, H.; Koike, K.; Inoue, H.; Ishitani, O. *J. Am. Chem. Soc.* **2008**, *130*, 6708.

(25)   Gibson, D. H.; Yin, X. *J. Am. Chem. Soc.* **1998**, *120*, 11200.

(26)   Agarwal, J.; Sanders, B. C.; Fujita, E.; Schaefer, H. F.; Harrop, T. C.; Muckerman, J. T. *Chem. Commun. (Camb).* **2012**, *48*, 6797.

(27)   Agarwal, J.; Fujita, E.; Schaefer, H. F.; Muckerman, J. T. *J. Am. Chem. Soc.* **2012**, *134*, 5180.

(28)   Zhao, L.; Odaka, H.; Ono, H.; Kajimoto, S.; Hatanaka, K.; Hobley, J.; Fukumura, H. *Photochem. Photobiol. Sci.* **2005**, *4*, 113.

(29)   Kurz, P.; Probst, B.; Spingler, B.; Alberto, R. *Eur. J. Inorg. Chem.* **2006**, 2966.

(30)   Gholamkhass, B.; Mametsuka, H.; Koike, K.; Tanabe, T.; Furue, M.; Ishitani, O. *Inorg. Chem.* **2005**, *44*, 2326.

(31)   Wenger, O. S. *Acc. Chem. Res.* **2011**, *44*, 25.

(32)   Koike, K.; Naito, S.; Sato, S.; Tamaki, Y.; Ishitani, O. *J. Photochem. Photobiol. A Chem.* **2009**, *207*, 109.

(33)   Windle, C. D.; Câmpian, M. V.; Duhme-Klair, A.-K.; Gibson, E. a.; Perutz, R. N.; Schneider, J. *Chem. Commun.* **2012**, *48*, 8189.

(34)   Schneider, J.; Vuong, K. Q.; Calladine, J. a; Sun, X.-Z.; Whitwood, A. C.; George, M. W.; Perutz, R. N. *Inorg. Chem.* **2011**, *50*, 11877.

(35)   Hawecker, J.; Lehn, J.-M.; Ziessel, R. *J. Chem. Soc, Chem. Commun.* **1984**, 328.

(36)   Hori, H.; Johnson, F. P. A.; Koike, K.; Ishitani, O.; Ibusuki, T. *J. Photochem. Photobiol. A Chem.* **1996**, *96*, 171.

(37)   Keith, J. A.; Grice, K. A.; Kubiak, P.; Carter, E. A. *J. Am. Chem. Soc.* **2013**, *135*, 15823.

(38)   Johnson, F. P. A.; George, M. W.; Hartl, F.; Turner, J. J. *Organometallics* **1996**, *15*, 3374.

(39)   Breikss, I.; Abruna, D. *J. Electroanl. Chem.* **1986**, *201*, 347.

(40)   Sullivan, B. P.; Bolinger, C. M.; Conrad, D.; Vining, W. J.; Meyer, T. J. *J. Chem. Soc., Chem. Commun.* **1985**, 1414.

(41)   Smieja, J. M.; Kubiak, C. P. *Inorg. Chem.* **2010**, *49*, 9283.

(42)   Yam, V. W.; Lau, V. C.; Cheung, K.; Chichester, H. **1996**, 2749.

(43)   Gibson, D. H.; Yin, X.; He, H.; Mashuta, M. S. *Organometallics* **2003**, *22*, 337.

(44)   Rossenaar, B. D. Remarkable influence of L on the excited state and redox properties of M(L)(CO)3(alpha diimine)complexes (M= Mn, Re; L= Alkyl, halide, metal fragment), 1995.

(45)   Stor, G. J.; Hartl, F.; Outersterp, J. W. M. Van; Stufkens, D. J. *Organometallics* **1995**, *14*, 1115.

(46)   Rossenaar, B. D.; Lindsay, E.; Stufkens, D. J.; Vlcek, A. *Inorganica Chim. Acta* **1996**, *250*, 5.

(47)   Rossenaar, B. D.; Kleverlaan, C. J.; Ven, M. C. E. van de; Stufkens, D. J.; Oskam, A.; Fraanje, J.; Goubitz, K. *J. Organomet. Chem.* **1995**, *493*, 153.

(48)   Smieja, J. M.; Benson, E. E.; Kumar, B.; Grice, K. A.; Seu, C. S.; Miller, A. J. M.; Mayer, J. M.; Kubiak, C. P. *Proc. Natl. Acad. Sci. USA* **2012**, *109*, 15646.

(49)   Sampson, M. D.; Froehlich, J. D.; Smieja, J. M.; Benson, E. E.; Sharp, I. D.; Kubiak, C. P. *Energy*

Environ. Sci. **2013**, *6*, 3748.

(50)   Hawecker, J.; Lehn, J.-M.; Ziessel, R. *Helv. Chim. Acta* **1986**, *69*, 1990.

(51)   Bourrez, M.; Molton, F.; Chardon-Noblat, S.; Deronzier, A. *Angew. Chem. Int. Ed. Engl.* **2011**, *50*, 9903.

(52)   Smieja, J. M.; Sampson, M. D.; Grice, K. A.; Benson, E. E.; Froehlich, J. D.; Kubiak, C. P. *Inorg. Chem.* **2013**, *52*, 2484.

(53)   Riplinger, C.; Carter, E. A. *ACS Catal.* **2015**, *5*, 900.

(54)   Wong, K.; Chung, W.; Lau, C. *Jounal Electroanal. Chem.* **1998**, *453*, 161.

(55)   Grills, D. C.; Farrington, J. A.; Layne, B. H.; Lymar, S. V; Mello, B. A.; Preses, J. M.; Wishart, J. F. *J. Am. Chem. Soc.* **2014**, *136*, 5563.

(56)   Riplinger, C.; Sampson, M. D.; Ritzmann, A. M.; Kubiak, C. P.; Carter, E. A. *J. Am. Chem. Soc.* **2014**, *136*, 16285.

(57)   Bourrez, M.; Orio, M.; Molton, F.; Vezin, H.; Duboc, C.; Deronzier, A.; Chardon-Noblat, S. *Angew. Chem. Int. Ed. Engl.* **2014**, *53*, 240.

(58)   Sampson, M. D.; Nguyen, A. D.; Grice, K. A.; Moore, C. E.; Rheingold, A. L.; Kubiak, C. P. *J. Am. Chem. Soc.* **2014**, *136*, 5460.

(59)   Zeng, Q.; Tory, J.; Hartl, F. *Organometallics* **2014**, *33*, 5002.

(60)   Rossenaar, B. D.; Hartl, F.; Stufkens, D. J.; Amatore, C.; Maisonhaute, E.; Verpeaux, J.-N. *Organometallics* **1997**, *16*, 4675.

(61)   Vollmer, M. V; Machan, C. W.; Clark, M. L.; Antholine, W. E.; Agarwal, J.; Schaefer, H. F.; Kubiak, P.; Walensky, J. R. *Organometallics* **2014**, *34*, 3.

(62)   Floch, P. Le; Mathey, F.; Ricard, L.; Rosa, P.; Heyro, J. V. *Inorg. Chem.* **2003**, *42*, 5724.

(63)   Takeda, H.; Koizumi, H.; Okamoto, K.; Ishitani, O. *Chem. Commun. (Camb).* **2014**, *50*, 1491.

2. Exploration of the complex [MnBr(CO)₃(4,4'-methylphosphonate-diethylester-2,2'-bipyridine] as a CO₂ reduction catalyst.

2.1.1 Introduction

Although mononuclear rhenium tricarbonyls (see chapter 1) are effective photocatalysts they do suffer from poor absorption in the regions of peak solar output (the peak MLCT absorption of [ReCl(CO)₃(bpy)] is at 370 nm[1], whereas peak global irradiance lies in the 500-700 nm range)[2].

As was discussed in chapter 1, modifications to the rhenium tricarbonyl complex itself have only limited effects on the useful light harvesting capability of the catalyst and a separate light harvesting moiety can be bound to the rhenium to increase the light harvesting range[3,4]. It was with this aim that the ligand shown in scheme 2.1 was developed by previous group members.[5,6]
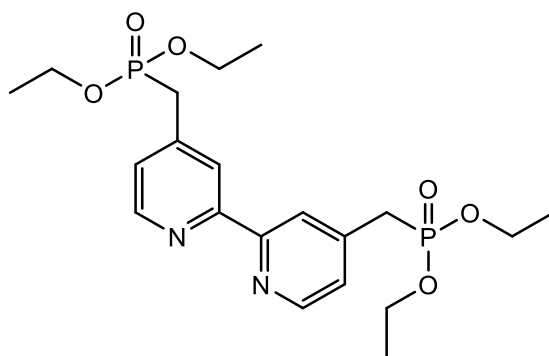
Scheme 2.1. 4,4'-methylphosphonate-diethyl-2,2'-bipyridine (ligand 1).

The overall intention was to hydrolyse the ester to form a phosphonic acid, the bpy would then be bound to [ReCl(CO)₅] forming [ReCl(CO)₃(4,4'-methyl-phosphonic-acid], this could then be anchored to either an electrode or photon harvesting semi-conductor such as titanium dioxide or tantalum pentoxide,[7,8] which could act to feed electrons into the catalyst[9] in a manner similar to [Ru(bpy)₃]²⁺ or zinc porphyrin.[10] In order to achieve this goal, an anchoring group must be incorporated into the bipyridine. The first choice for this was the phosphonate ester moiety which has subsequently been used with success in similar complexes[11]. However, there were concerns that direct functionalisation (i.e. attaching the phosphorus directly to one of the aromatic carbon atoms) would affect the electronic properties of the bipyridine. This would be a problem because the reactivity of manganese and rhenium tricarbonyl α-diimine complexes upon reduction is determined by the π acceptability of the bpy ligand[12], with more π accepting bipyridines being able to lower the energy gap between the metal and the π* orbitals and thus the reduction potential of the complex inhibiting catalytic activity.[13,1,14,15,16] In

turn, bpy π^* orbitals of higher energy polarize the Metal-X bond[17] resulting in more facile dissociation and increased reactivity of the complexes with electron donating groups on the bpy ring at the expense of greater catalytic overpotential,[13] The effects of electron withdrawing or donating groups on the HOMO-LUMO[18,19,20,15,21] can result in substantial variation in the reactivity of the complex. In order to circumvent these potential issues, a CH_2 spacer was introduced to the ligand acting to effectively decouple the electron withdrawing effects of the phosphonate.[6]

Although this project had been reasonably successful in its aims, rhenium catalysts for CO_2 reduction had been known and studied for some time.[22,23] Thus it was felt that in order to advance the use of group 7 metals as serious CO_2 reduction catalysts, it was necessary to substitute the expensive and rare rhenium metal centre with a more abundant metal. Until 2011, it was widely believed that $[Mn(X)(CO)_3(\alpha\text{-diimine})]$ complexes were not catalytically active with respect to CO_2 reduction[24], due to the greater electron density and less diffuse orbital structure of the manganese metal centre stabilising the five coordinate intermediate, and in theory, preventing CO_2 from binding.

However, in 2011 Bourrez *et al*. reported the successful employment of $[MnBr(CO)_3(bpy)]$ and $[MnBr(CO)_3(dmbpy)]$ for the electrocatalytic reduction of CO_2 to CO in acetonitrile at reduction potentials of -1.46 and -1.55 vs Ag/Ag^+ respectively[25].

2.1.2 Aims

The aims of this project were to investigate whether the incorporation of the CH_2 spacer unit had any effect on decoupling the electron withdrawing phosphonate moiety from the bipyridine moiety by comparing the phosphonate complex with $[MnBr(CO)_3(bpy)]$ and $[MnBr(CO)_3(dmbpy)]$ and more significantly to investigate the potential to use $[MnBr(CO)_3(4,4'\text{-methylphosphonate-diethylester-}2,2'\text{-bipyridine})]$ (here after referred to as **Mn-Phos**) as a photocatalyst.

2.2 Experimental Methods

2.2.1 Materials and General Procedures

Commercially available starting materials and reagents were obtained from Sigma-Aldrich, Apollo Scientific and STREM and used as received with the exception of tetrabutylammonium hexafluorophosphate (Sigma-Aldrich) which was recrystallized from hot ethanol and dried overnight in a vacuum oven. All solvents (Fisher Scientific, Sigma-Aldrich, VWR) were of HPLC grade or higher and were used without further purification unless otherwise stated. Dry solvents were obtained from a Grubbs solvent drying system.

The phosphonate ligands were prepared by Stuart Archer according to previously published methods[5].

2.2.2 Instrumentation and Analysis

2.2.2.1 Nuclear Magnetic Resonance (NMR) Spectroscopy

^1H and ^{13}C NMR spectra were recorded using Bruker Avance 400 (DPX-400), Bruker Avance 400, Bruker Avance III HD 400, Bruker Avance III 400 and Bruker Avance III HD 500 spectrometers. Deuterated solvents were purchased from Sigma-Aldrich and were of spectroscopic grade.

2.2.2.2 Mass Spectrometry

High resolution mass spectrometry samples were collected using direct infusion Na^+ ionisation and analysed using time of flight.

Multiple attempts were made to gather mass spectra of the photo decayed product using both solar light and 455 nm diode as irradiation sources and acetonitrile and DCM as solvent during preparation. Samples were run using matrix assisted laser desorption ionisation (MALDI) and analysed with time of flight (TOF) mass spectrometry.

2.2.2.3 UV-Visible Absorption Spectroscopy

UV-Visible absorption spectra were recorded on either a Cary 50 Bio spectrophotometer or Cary 5000 UV-VIS-NIR spectrophotometer utilising 1 cm path length quartz curvettes.

2.2.2.4 Cyclic Voltammetry

Cyclic voltammetry was performed on either an Electrochemie Autolab potentiostat or a Princeton Applied Research VersaSTAT 3 potentiostat.

Before experiments the solutions were purged with bottled N_2 (British Oxygen Company) and an atmosphere of acetonitrile saturated N_2 was maintained over the sample. The cell set up was composed of a glassy carbon working electrode, platinum wire counter electrode and a Ag/AgCl (0.1 M KCl solution) reference electrode in 6 cm^3 of Grubbs dried acetonitrile with NBu_4PF_6 (0.2 mol dm^{-3}) as supporting electrolyte. A solution concentration of 0.002 M Mn-Phos was used during all CV experiments. Ferrocene was added as an internal reference; the redox couple was observed at +0.428 V.

2.2.2.5 Bulk electrolysis and Gas Chromatography

Bulk electrolysis was performed in a single compartment cell with a stirrer bar. A large surface area platinum mesh electrode was used as the working electrode and platinum bar

separated from the bulk solution by a frosted glass end was used as the counter electrode. A silver wire in a glass electrode casing with a semi permeable tip in 0.1 M KCl solution was used a reference electrode.

In order to confirm that the complex was reducing CO_2, 0.1 g of **Mn-Phos** in 100 ml of 94.4% acetonitrile to 5.6% H_2O (0.0015 M) was subjected to controlled potential electrolysis (-1.8 V vs silver wire reference electrode) in a single compartment cell under stirring. Gas samples from the head space were taken at regular intervals using a gas tight syringe and analysed using gas chromatography (H_2 carrier gas) fitted with a thermal conductivity detector.

2.2.2.6 Photocatalysis

In order to determine the photocatalytic activity of **Mn-Phos**, 2.13 mg (0.11 mmol dm^{-3}) of the complex was dissolved in 24 cm^3 acetonitrile with 4.5 cm^3 triethanolamine (TEOA), added as a sacrificial electron donor. The solution was bubbled thoroughly with either CO_2 or N_2 in order to saturate the solution with the appropriate gas. The solution was then irradiated with an Xe lamp (1cm diameter, 76 mW) in a specially designed cell with a path length of 10 cm. Gas samples from the head space were taken at regular intervals using a gas tight syringe and analysed using gas chromatography (H_2 carrier gas) fitted with a thermal conductivity detector.

2.2.2.7 Spectroelectrochemistry (SEC)

In a typical experiment, infrared spectroelectrochemistry was performed using an EmStat3 potentiostat (PalmSens, The Netherlands). A 4 mmol dm^{-3} solution of **Mn-Phos** in presence of 0.3 mol dm^{-3} of [Bu$_4$N][PF$_6$] was prepared in dry acetonitrile and analysed in an optically transparent thin-layer spectroelectrochmeical cell (OTTLE cell) equipped with Pt minigrid working electrodes, a Ag microwire psudoreference electrode and CaF$_2$ windows. Samples were prepared under argon atmosphere and samples for catalytic measurements were prepared by bubbling the electrolyte with CO_2 for 15 minutes. IR spectroscopy was performed on Bruker Vertex 70v FT-IR spectrometer and thin-layer voltammograms were recorded in the course of the experiment.

2.2.2.8 X-Ray diffraction

Crystals suitable for X-ray diffraction were grown by slow vapour diffusion crystallisation utilising diethyl ether anti-solvent into a solution utilising a DCM solvent. A specimen of $C_{23}H_{30}BrMnN_2O_9P_2$, approximate dimensions 0.400 mm x 0.500 mm x 0.500 mm, was used for the X-ray crystallographic analysis. The X-ray intensity data were measured.

The integration of the data using a triclinic unit cell yielded a total of 22074 reflections to a maximum θ angle of 27.55° (0.77 Å resolution), of which 6307 were independent (average redundancy 3.500, completeness = 97.2%, R_{int} = 6.21%, R_{sig} = 5.80%) and 5238 (83.05%)

were greater than $2\sigma(F^2)$. The final cell constants of $\underline{a} = 11.2728(5)$ Å, $\underline{b} = 12.1366(6)$ Å, $\underline{c} = 12.4282(6)$ Å, $\alpha = 61.173(2)°$, $\beta = 72.144(2)°$, $\gamma = 74.311(2)°$, volume $= 1402.48(12)$ Å^3, are based upon the refinement of the XYZ-centroids of reflections above 20 $\sigma(I)$. The calculated minimum and maximum transmission coefficients (based on crystal size) are 0.4255 and 0.4927.

The structure was solved and refined using the Bruker SHELXTL Software Package, using the space group P -1, with Z = 2 for the formula unit, $C_{23}H_{30}BrMnN_2O_9P_2$. The final anisotropic full-matrix least-squares refinement on F^2 with 347 variables converged at R1 = 3.78%, for the observed data and wR2 = 9.80% for all data. The goodness-of-fit was 1.028. The largest peak in the final difference electron density synthesis was 1.211 e$^-$/Å^3 and the largest hole was -0.785 e$^-$/Å^3 with an RMS deviation of 0.099 e$^-$/Å^3. On the basis of the final model, the calculated density was 1.599 g/cm^3 and F(000), 688 e$^-$.

2.2.3 Synthesis

2.2.3.1 4,4'-methylphosphonate-diethyl-2,2'-bipyridine

Ligand 1 (4,4'-methylphosphonate-diethyl-2,2'-bipyridine) was synthesised by Dr Stuart Archer.[5] Chloroform (10 mL) was mixed with diethyl phosphite (15 mL) and sparged with dry nitrogen for 30 min. This mixture was transferred to a flask containing 4,4'-bis(bromomethyl)-2,2'-bipyridine (842 mg, 2.46 mmol) and refluxed at 85°C for 6 hours. After cooling to room temperature the chloroform and diethyl phosphite were removed under vacuum leaving a pale pink solid. The crude product was purified using silica gel column chromatography (80:20 v/v Ethyl Acetate:Methanol eluent) to give a pale yellow oil, which crystallized overnight to an off-white solid. Yield = 942 mg (64%).

^{1}H NMR (250 MHz, CDCl$_3$) δ 8.60 (d, J = 5.0 Hz, 2H), 8.33 (s, 2H), 7.42 – 7.28 (m, 2H), 4.07 (dq, J = 8.1, 7.1 Hz, 8H), 3.23 (d, J = 22.2 Hz, 4H), 1.27 (t, J = 7.1 Hz, 12H). ^{31}P NMR (101 MHz, CDCl$_3$) δ 24.30 (s). MS (ESI, +ve): m/z 457.2 (MH$^+$)
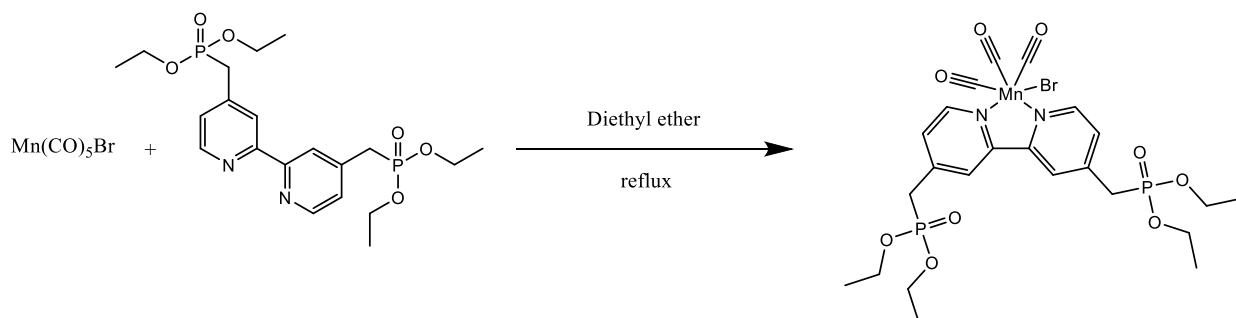
2.2.3.2 [MnBr(CO)₃(4,4'-methylphosphonate-diethyl-2,2'-bipyridine)]

Mn-Phos was synthesised according to an established procedure.[26] During reaction and work up the complex was protected from light due the photosensitivity of the manganese complexes.

Manganese pentacarbonyl bromide 0.3 g (1.09 mmols) was refluxed for 4 hours with 4,4'-methylphosphonate-diethylester-2,2'-bipyridine 0.465 g (1.02 mmols) in aerobic conditions in diethyl ether (50 cm^3). The reaction vessel was left to cool to room temperature then further cooled to 0°C in an ice water bath and the precipitate removed via filtration. The material was

then washed with chilled diethyl ether giving the product as a yellow powder that could be extracted via filtering. Yield = 79%.

^{1}H NMR (d-DMSO) δ 9.13 (d, 2H, 6 and 6'), δ 8.44 (s, 2H, 3 and 3'), δ 7.63 (d, 2H, 5 and 5'), δ 4.03 (m, 10 CH$_2$), δ 3.59 (d, 5, CH$_2$), δ 1.19 (t, 15, CH$_3$). HRMS (TOF-ES, +ve): m/z (HRMS M+Na$^+$) Calcd for C$_{23}$H$_{30}$N$_2$O$_9$NaP$_2$BrMn 696.9908; Found 696.9888.


Scheme 2.2 Synthesis of Mn-Phos.
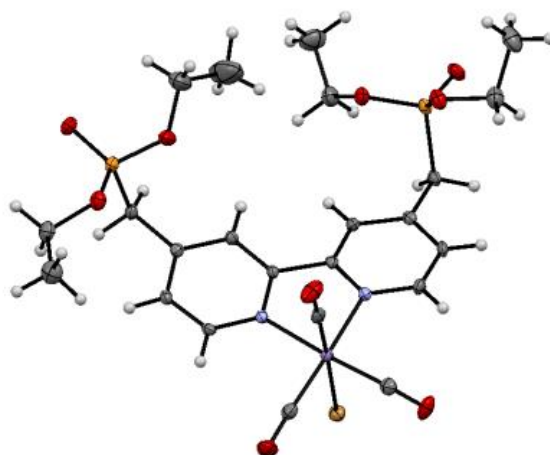
Figure 2.1 X-ray crystal structure [MnBr(CO)$_3$(4,4'-methylphosphonate-diethylester-2,2'-bipyridine].

The Electronic absorption spectrum was measured in dichloromethane (DCM) at room temperature. The absorption coefficient was calculated by sequentially adding 20 μl of a stock solution (6.71 x 10^{-4} mols dm^{-3}) to an initial volume of 2 cm^3 DCM and recording the UV spectrum. The absorption coefficient was then calculated for all points simultaneously using a spread sheet and the Beer-Lambert law.

Emission spectra were recorded in DCM, however, no emission was observed for this complex. No emission spectra have reported for similar manganese complexes reported in the literature.
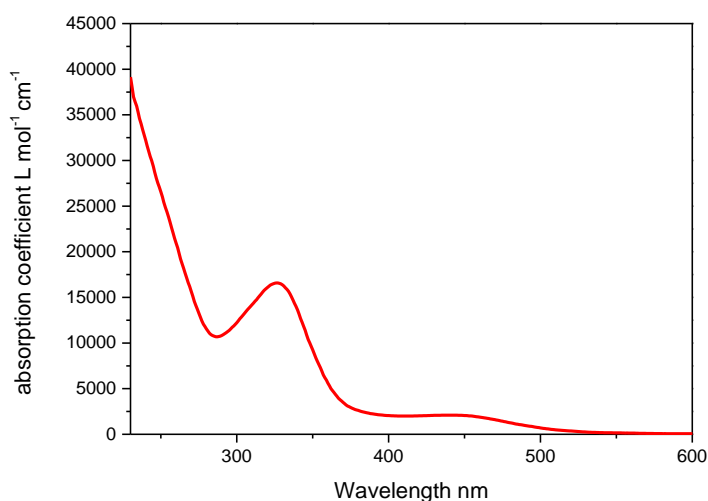
Figure 2.2 Absorption spectrum of Mn-Phos in DCM.

2.2.3.3 [MnBr(CO)$_3$(4,4'-methyl-2,2'-bipyridine)] (Mn-dmbpy)

Mn-dmbpy was synthesised for use a reference allowing **Mn-Phos** to be compared to a previously reported complex.

Manganese pentacarbonyl bromide 0.1010 g (0.37 mmols) was refluxed for 2 hours with 4,4'-methyl-2,2'-bipyridine 0.0648 g (0.352 mmols) in aerobic conditions in diethyl ether (20 cm^3). The reaction vessel was left to cool to room temperature then further cooled to -78 $^{\circ}$C in a dry ice acetone bath and the precipitate removed via vacuum filtration. The material was then washed with chilled diethyl ether giving the product as a yellow powder that could be extracted via filtering. Yield = 94%. During reaction and work up the complex was protected from light due the photosensitivity of the manganese complexes.

^{1}H NMR (400 MHz, CDCl$_3$) δ 8.55 (d, J = 5.0 Hz, 1H), 8.24 (s, 1H), 7.14 (d, J = 5.8 Hz, 1H), 2.45 (s, 3H) corresponding to literature data.

2.2.3.4 [MnBr(CO)$_3$(2,2'-bipyridine)] (Mn-bpy)

Mn-bpy was synthesised for use a reference allowing **Mn-Phos** to be compared to a previously reported complex.

Manganese pentacarbonyl bromide 0.35 g (1.27 mmols) was refluxed for 2 hours with 2,2'-bipyridine 0.2 g (1.28 mmols) in aerobic conditions in diethyl ether (20 cm^3). The reaction vessel was left to cool to room temperature and the precipitate removed via centrifugation. Yield = 80%. During reaction and work up the complex was protected from light due the photosensitivity of the manganese complexes.

^{1}H NMR (500 MHz, CDCl$_3$) δ 9.27 (d, J = 4.3 Hz, 1H), 8.12 (d, J = 6.5 Hz, 1H), 7.99 (s, 1H), 7.53 (s, 1H). HRMS (TOF-ESI, +ve): m/z (M+Na$^+$) Calcd for C$_{13}$H$_8$N$_2$O$_3$NaBrMn 396.8991; Found 396.8988.

## 2.3 Results and Discussion

2.3.1 Electrocatalytic activity of Mn-Phos

In order to determine whether **Mn-Phos** would be suitable as a CO$_2$ reduction catalyst, it was necessary to test its electrocatalytic activity.

In order to look for evidence of CO$_2$ reduction, cyclic voltammetry (CV) is performed in solutions saturated with N$_2$ under which no catalysis should occur. The solution is then saturated with CO$_2$; under CO$_2$ if catalysis is possible, certain peaks should grow in intensity as electrons flow from the glassy carbon cathode into the catalyst and ultimately into the CO$_2$. In practice, it may be necessary to add a Brönsted acid such as water in order to facilitate catalysis, in which case current enhancement will not be observed until this is added.[27,28,29]

Under N$_2$, three irreversible reduction waves in the cyclic voltammetry traces of **Mn-Phos** could be seen at -1.20 V, -1.64 V and -1.92 V vs Fc/Fc$^+$. Bubbling with CO$_2$ did not result in large current enhancements, although some slight current enhancement was observed, most likely due to the presence of water in the CO$_2$ gas used to saturate the solution. Upon the addition of 0.5 ml of H$_2$O, substantial current enhancement of all peaks was observed. This matches what has been reported for similar [MnX(CO)$_3$(un/substituted-bipyridine)] complexes:[25] although acetonitrile can act as an initial proton donor for rhenium based catalysts, this is not possible for manganese based catalysts and the presence of a Brönsted acid is required for catalysis to occur.[30,31] The current enhancement is strong and good evidence of catalysis; however, in order to prove that current enhancement was due to the reduction of CO$_2$ and not the result of the addition of water to the solution the CV was repeated using a solvent of 91.66% acetonitrile to 8.33% water, all other conditions kept the same. As can be seen, current enhancement does not occur until the solution is saturated with CO$_2$.
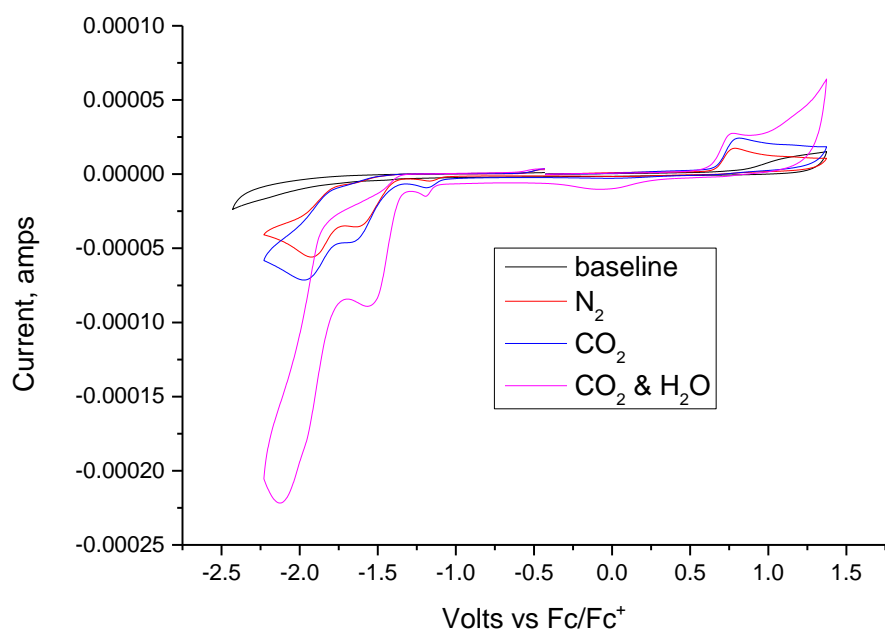
**Figure 2.3 Cyclic voltammograms of Mn-Phos in acetonitrile, scan rate 0.1 Vs^{-1}, 0.2 M electrolyte NBu$_4$PF$_6$.**
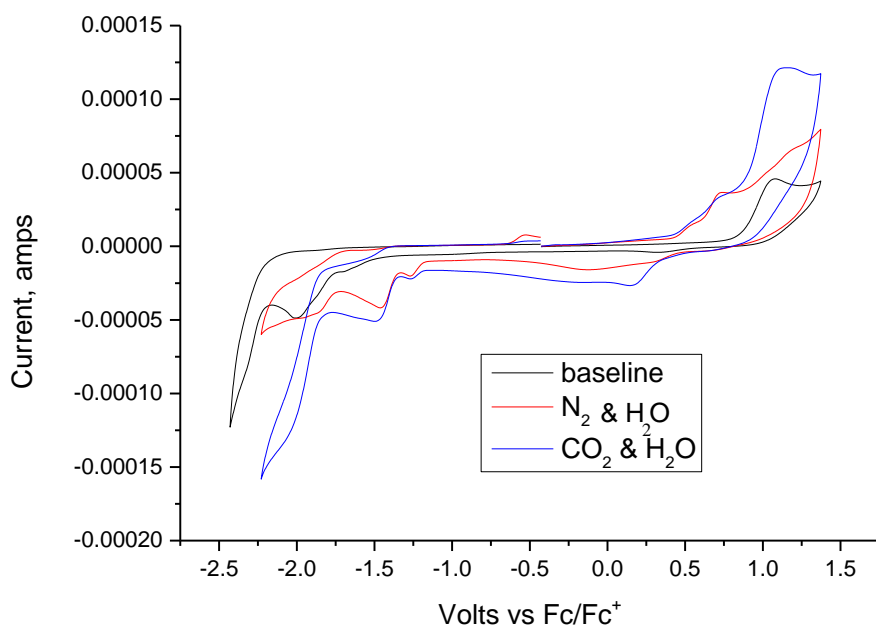
Figure 2.4 Cyclic voltammograms of Mn-Phos in 91.66% acetonitrile to 8.33% water, scan rate 0.1 Vs^{-1}, 0.2 M electrolyte NBu$_4$PF$_6$

In order to verify that the current enhancement observed was the result of CO_2 being reduced to CO, bulk electrolysis was performed and head space gas samples were taken with gas chromatography being performed on those samples. Analysis revealed that carbon monoxide was successfully produced during the electrolysis. No other products were observed in the GC

traces; however, due to limitations with the equipment used it was not possible to observe hydrogen or carbon dioxide. After 40 minutes, CO production seemed to have stopped and the solvent had begun to break down. The results of the GC experiments were not suitable for quantification (See chapter 8).

It is possible that some or all of the CO observed in the experiment was due to the breakdown of the complex due to the applied potentials, however, this is unlikely as the applied potentials were not excessive relative to the potentials utilised in the cyclic voltammetry experiments. Experiments under identical conditions in which the acetonitrile solution was saturated with nitrogen did not show the formation of CO. However, these results should be taken with some caution. In order to confirm the origin of the CO in the head space, isotopic labelling of the manganese complex could have been performed with gas samples analysed by mass spectrometry. However, these resources were not available when the experiments were performed.
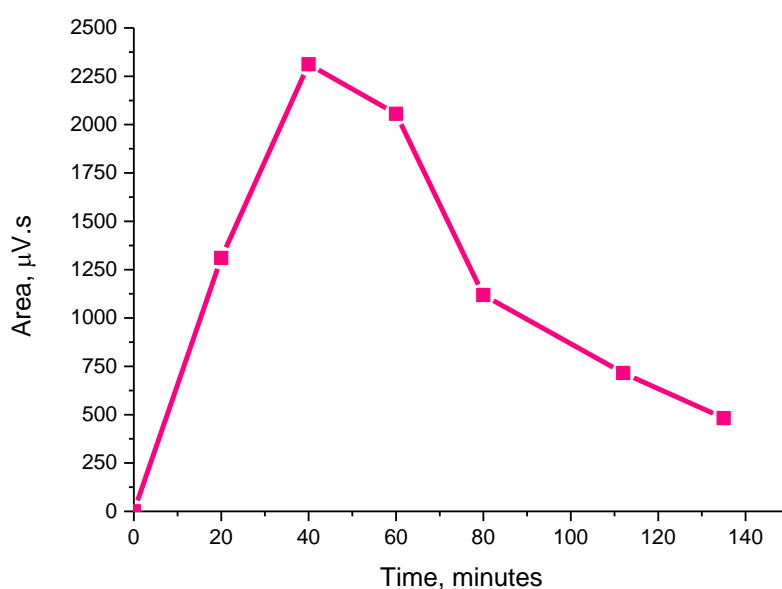
Figure 2.5 GC analysis of fixed potential electrolysis of Mn-Phos in CO_2 saturated 94.4% acetonitrile / 5.6% H_2O (-1.8 V vs silver wire psreference electrode/-2.15 V vs Fc/Fc$^+$). The area observed (reported in μVs^{-1}) is proportional to the concentration of CO see chapter 8.

Most significantly, IR-SEC was performed on **Mn-Phos**, and initial IR spectra showed peaks at 2027, 1934 and 1923 cm^{-1}, which matches FTIR measurements of the parent complex. Upon initial reduction, bands are observed at 1975, 1932, 1880 and 1855 cm^{-1} and these peaks can be assigned to the Mn^0-Mn^0 dimer[32]. Under CO_2 no evidence of catalysis was observed when only dimer was present. The second reduction generates the catalytically active 5-coordinate anion and can be seen via the growth of broad peaks at 1912 and 1812 cm^{-1} which is characteristic of this manner of 5-coordinate complex.[33] Under CO_2, the 5-coordinate anion

reacts with CO_2 and peaks are observed to grow in the region of 1600 to 1700 cm^{-1}, which are indicative of CO_2 reduction to CO. It has been proposed in the literature by Johnson *et al.*[24] that these peaks correspond to free bicarbonate and subordinate formate which are formed in the course of CO_2 reduction and are indicative of CO_2 reduction to CO.[33,34] From this data, we therefore assign the characteristic triad to a mixture of free bicarbonate and subordinate formate. It should be noted that the appearance of the triad occurs concurrently with the loss of the IR stretching bands at 2255 cm^{-1} (which corresponds to dissolved $^{13}CO_2$) as well as the large band at ca. 2340 cm^{-1} (corresponding to dissolved $^{12}CO_2$) as well as the rapid formation of bubbles upon the working electrode. Crucially it has been observed both in our own work as well as that of others that the diimine ligand is able to be displaced under these conditions forming $[Mn(CO)_5]^-$ proving that in the thin film CO is being formed. As such the appearance of the triad is solid evidence for the reduction of CO_2 into CO. However, no attempt will be made to assign the stretching frequency definitively in this thesis.

Although not observed in these experiments, it has been seen in other chapters (*vide infra*) that upon formation of the 5-coordinate anion in CO_2 saturated solution, a band of energy intermediate between the two higher energy bands of the triad is formed before reduction of the bound CO_2 takes place. This has been determined by Zeng *et al.* to be a bicarbonate species.[33] The assignment of a bicarbonate complex made by Zeng *et al.* was made via the synthesis of a complex $[Mn(CO)_3(iPr\text{-}DAB)(\eta^1\text{-}OCO_2H)]$ from $[Mn(CO)_3(iPr\text{-}DAB)(OTf)]$ and $NH_4[OCO_2H]$. The yellow product was characterized by ^1H NMR (CDCl$_3$: δ 1.49 (d, 12H, CH(CH$_3$)$_2$), 4.27 (sept, 2H, CH(CH$_3$)$_2$), 8.38 (s, 2H, N=CH); the expected broad OH signal was not observed below 10 ppm) and IR spectroscopy (THF: v(C≡O) at 2032 and 1934 (br) cm^{-1}; v(C=O) at 1646 cm^{-1}).

The electrochemical reduction of $[Mn(CO)_3(iPr\text{-}DAB)(\eta^1\text{-}OCO_2H)]$ in THF containing Br$^-$ ions resulted in the facile formation of $[Mn(CO)_3(iPr\text{-}DAB)Br]$ (v(C≡O) at 2024, 1936, and 1918 cm^{-1}), meaning that the bicarbonate ligand is only weakly coordinated to the manganese and the complex is reduced at less negative potentials than the bromide complex.

As such, the bicarbonate complex cannot be assigned as the intermediate observed in electrochemical reduction. However, electrochemical reduction of $[Mn(CO)_3(iPr\text{-}DAB)(\eta^1\text{-}OCO_2H)]$ in the absence of CO_2 led to the formation of a product (v(C≡O) at 2024 and 1922 (br) cm^{-1}) which was very close to the intermediate in its electrochemical behaviour (its cathodic wave is shifted to ca. -2.2 V vs Fc/ Fc$^+$ and the corresponding reduction generated the five-coordinate anion at 1920, 1816, and 1800 (sh) cm^{-1}). This cathodic behaviour was consistent with the electrochemical reduction of the parent complex in the CO_2 saturated THF electrolyte. Importantly the (likely bicarbonate-bearing intermediate) could not be identified with a tricarbonyl Mn complex bearing an axial hydroxycarbonyl or formate ligand as these complexes exhibited a much smaller C≡O stretching frequency.[33]

Although we do not believe we have sufficient evidence to definitively assign this intermediate, we believe that there is sufficient evidence to suggest it may be due to the formation of a bicarbonate bearing intermediate. This shows that it is the 5-coordinate anion which is the active species for CO_2 reduction, as is typical for this type of catalyst (*vide supra*).
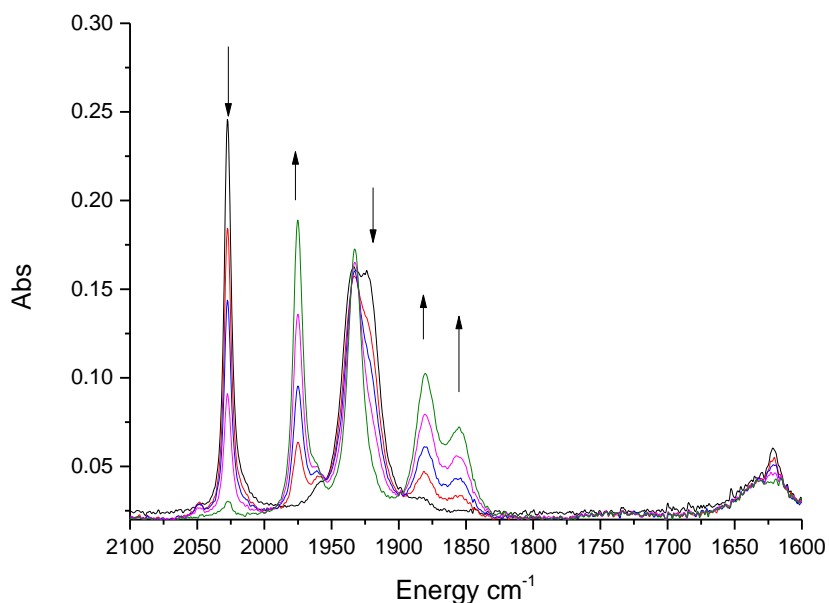
Figure 2.6 IR-SEC of Mn-Phos in CO_2 saturated acetonitrile. Showing the first reduction of the parent complex and the growth of the Mn^0-Mn^0 dimer. As can be seen there is no growth in the free bicarbonate triad region (1700 to 1600 cm^{-1}).
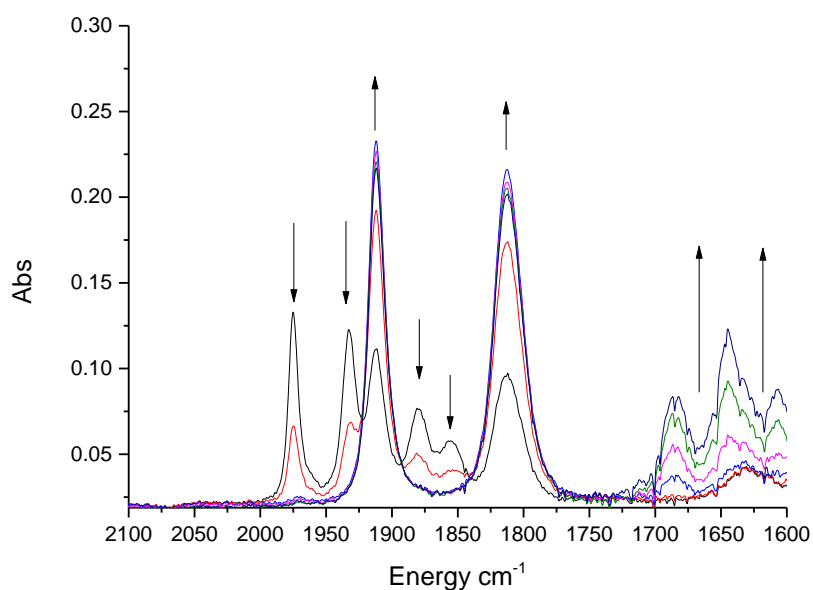
Figure 2.7 IR-SEC of the second reduction of Mn-Phos in CO_2 saturated acetonitrile showing reduction of the Mn^0-Mn^0 dimer into the 5-coordinate anion which proceeds to react with CO_2 to form CO.

2.3.2 Evidence for decoupling between the phosphonate and bipyridine moieties.

Although investigating the effect of the CH_2 moiety towards decoupling the electron withdrawing phosphonate from the π-π* system of the bipyridine ring was not the primary aim of this particular project[6], we felt it was still worth commenting upon. Indeed, a thorough study of electron donating and withdrawing moieties on bipyridine ligands and their effect on rhenium analogues was conducted by Smieja *et al*.[13] and it can be assumed that the manganese complexes should show the similar effects towards such substituents. The study shows the importance of maintaining a suitable HOMO-LUMO energy gap and how functionalization with an electron withdrawing moiety (such as a phosphonate) will lower the HOMO-LUMO energy gap, decreasing both the reduction potential and hence peak catalytic activity, while electron donating moieties (such as a methyl) will result in increased overpotential and hence increased .

With this in mind, table 2.1 shows a comparison of the catalytic reduction potentials of **Mn-Phos** to two previously reported complexes $Mn(bpy)(CO)_3Br$ and $Mn(dmbpy)(CO_3)Br$.

Table 2.1 Comparison of reduction potential of Mn-Phos with previously reported complexes

Complex	Reduction potential V vs Fc/Fc$^+$
$[MnBr(CO)_3(bpy)]$[25]	-1.91
$[MnBr(CO)_3(methylphosphonate-diethylester-bpy)]$	-1.92
$[MnBr(CO)_3(dmbpy)]$[25]	-2.00

As can be seen in table 2.1, **Mn-Phos** exhibits an intermediate reduction potential between Mn-bpy and Mn-dmbpy. Based on the work of Smieja *et al*.[13], one would assume that a phosphonate complex without any decoupling between the phosphonate and the bipyridine moiety would exhibit a less negative reduction potential than Mn-bpy. However, as is shown in table 2.1, **Mn-Phos** does not have a reduction potential that is less negative than Mn-bpy but is instead reduced at *more* negative potentials. Although this is certainly not total decoupling, this catalyst demonstrates that it is possible to 'insulate' the bipyridine from the electron withdrawing effects of the phosphonate by incorporation of a CH_2 spacer.

2.3.3 Light sensitivity

Shortly after synthesising **Mn-Phos**, it became obvious that the complex was sensitive to light. This was discovered when an NMR of **Mn-Phos** was submitted onto an automatic carousel loader in a transparent NMR tube; initially the sample was a yellow colour but upon collection

the sample had turned dark brown. The sample was rerun immediately and smaller peaks at δ 8.60, δ 8.36, δ 7.36, δ 7.12 and δ 3.43 could be seen in the 1H NMR spectrum while depletion of the parent peaks was also observed (figure 2.8).
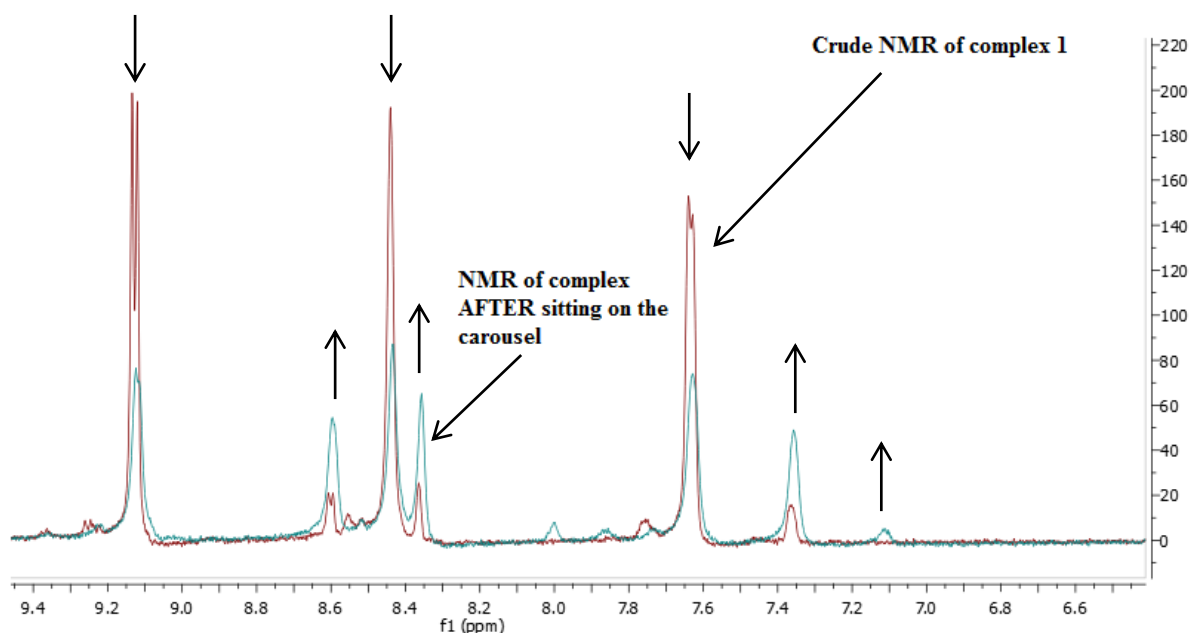

Figure 2.8 Overlay of the NMR spectra of Mn-Phos showing the growth of peaks associated with decomposition of Mn-Phos. See section 2.2.3.1 for assignment of parent NMR peaks.

In order to confirm that the decomposition was due to light, solutions of **Mn-Phos** were prepared using Grubbs dried DCM (to eliminate the possibility that water was the cause of the degradation) and analysed by UV spectroscopy, one sample was left exposed to light and the other was kept in darkness (figure 2.9). As can be seen, exposure to light resulted in the loss of the MLCT-XLCT band[15,35,36] and weakening of the intra ligand band. Although some loss of the MLCT-XLCT and IL bands could be seen in the sample that was kept in the dark at the very end of the experiment the cause of this has not been determined it may be that the time the sample was exposed to light during transfer to the UV spectrophotometer, or indeed the UV irradiation itself, was the cause of the degradation observed.

In order to confirm that this was due to light and not solvent a similar experiment was performed using DMSO and acetonitrile as the solvent. Both solutions exhibited the same behaviour.
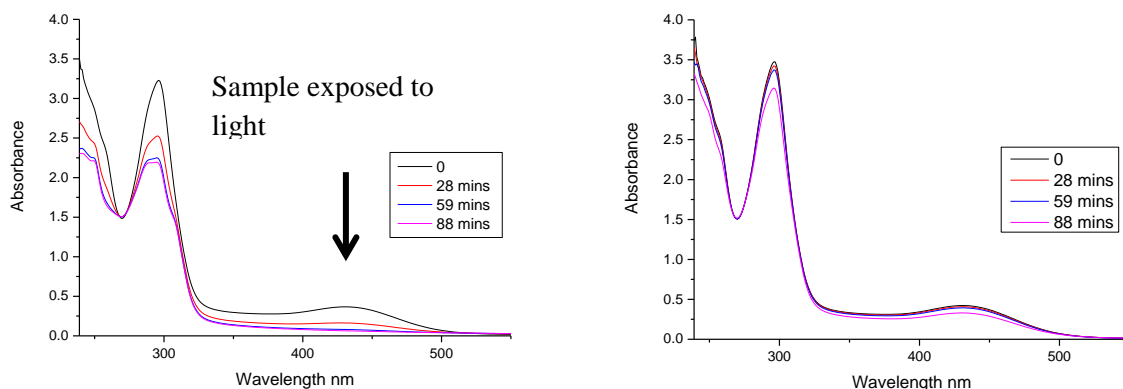
Figure 2.9 UV spectra of samples of Mn-Phos in Grubbs dried DCM after exposure of ambient light (left) and kept in darkness (right).

It may come across as obvious to those who regularly work with $[MnX(CO)_3(diimine)]$ complexes that they exhibit photosensitivity; however, this is a message that is not well communicated in the literature regarding manganese tricarbonyl α-diimines as CO_2 reduction catalysts. To illustrate this point a SciFinder search (accessed 13:15, 18-Oct-2016) of Mn-bpy (CAS numbers 38173-71-6, 14881-42-6, 66068-93-7 and 1637314-32-9) and Mn-dmbpy (CAS numbers 122219-96-3 and 210919-96-3) revealed 56 references but when the search was refined to search for "photo degradation" and "photo decomposition" no references were found. Indeed, at the time of writing, we have only discovered one publication in which the photosensitivity of the manganese complexes is mentioned.[26] With this in mind it was decided to conduct some investigations into the photodegradation of the manganese complexes to see if the pathway of degradation and the resulting products could be uncovered.

2.3.3.1 IR experiments following irradiation

In the first experiment, IR spectra of **Mn-Phos** were collected before exposure to ambient sunlight and after the solution had become colourless due to ambient light exposure. As can be seen in figure 2.10, following photodegradation peaks at 1975, 1961, 1933, 1882 and 1856, cm^{-1} were observed to grow in while the parent peaks were depleted. As can be seen these are very similar to the absorption bands seen in the IR-SEC spectrum (figure 2.6) at 1975, 1932, 1880 and 1855 cm^{-1}, which were assigned to a dimer. In addition, because the lowest lying absorption band observed in the UV absorption spectrum is to a high degree defined as being an XLCT absorption band centred on the metal-halide bond, the depletion of this band in figure 2.9 indicates that upon irradiation, the halide is being liberated and so it would make sense to assume that the resultant $[Mn(CO)_3(diimine)]^{\bullet}$ complex would dimerise.

Another possibility is that upon exposure to light the complex is undergoing Fac to Mer isomerisation, which has been noted under certain conditions.[37,38,39] The pathway of isomerisation is varied, with the normal route being via the oxidation of the fac Mn^I complex to an Mn^{II} complex which then isomerises into a mer complex. However photochemical and thermal isomerisation have been observed.[40,41]
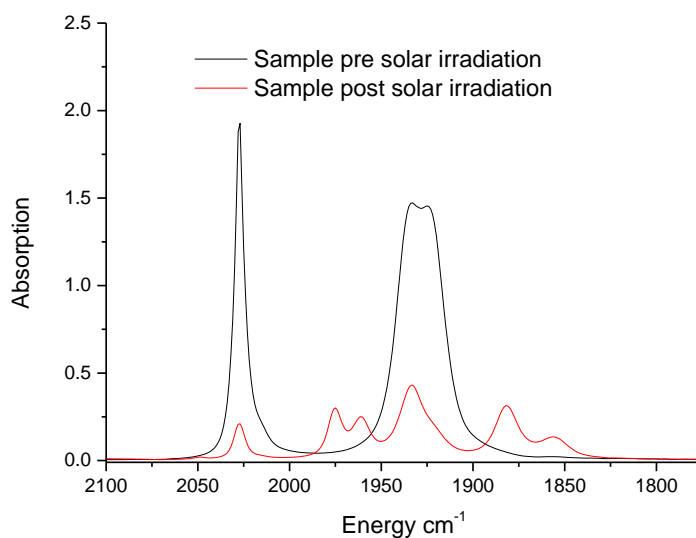
Figure 2.10 Overlay of the normalised IR absorption spectra of Mn-Phos before and after photo degradation due to exposure to ambient sunlight.

The experiment was repeating using a 455 nm diode with IR measurements taken periodically so as to establish if there was any difference between broad spectrum and well defined irradiation. As can be seen in figure 2.11, targeting the MLCT-XLCT band exclusively resulted in an apparently entirely different complex being formed upon photodegradation as compared with ambient solar radiation. These experiments were repeated multiple times and the same result was obtained each time.

The loss of the parent carbonyl bands combined with the only very modest growth of the band at 1958 cm^{-1} would seem to suggest that the carbonyls are being eliminated from the complex when irradiation is limited to 455 nm.
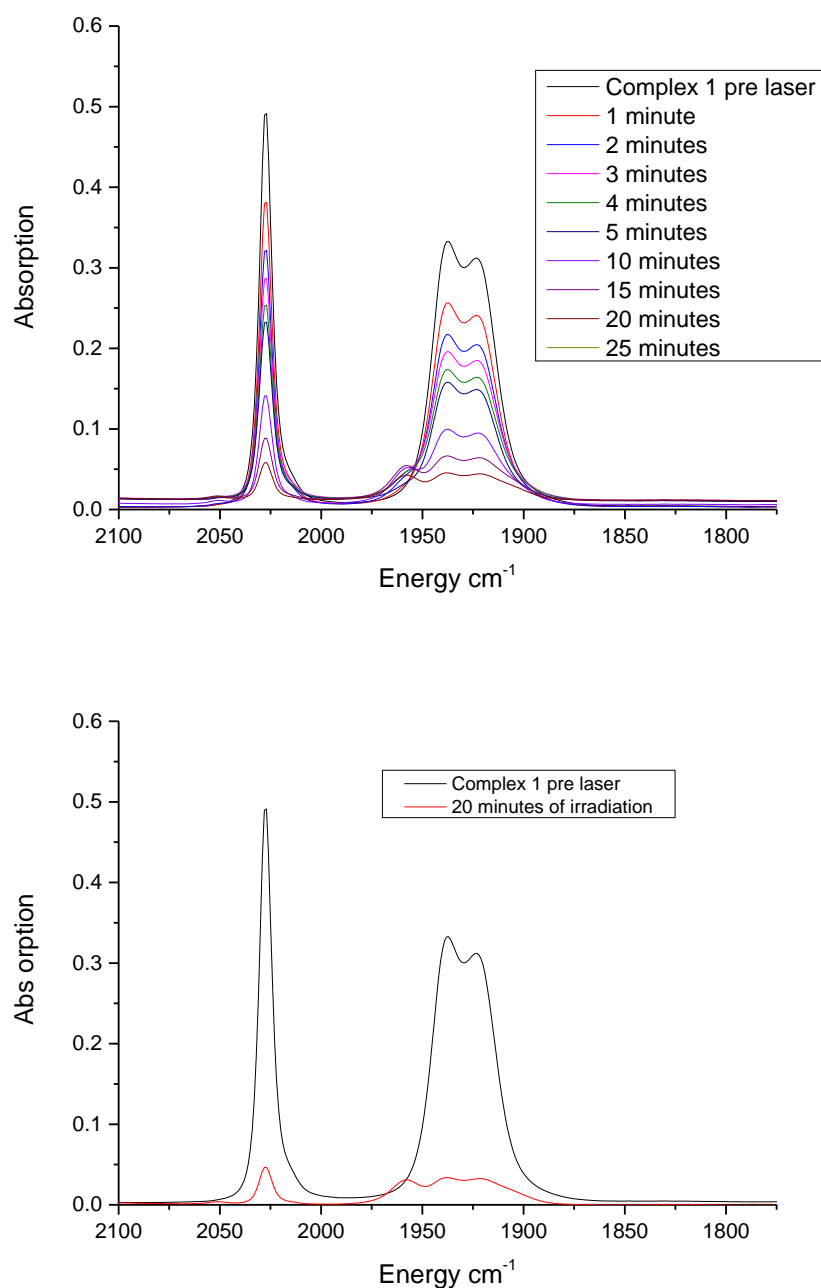
Figure 2.11 IR spectra of Mn-Phos after irradiation at 455 nm with a diode laser in acetonitrile

2.3.3.2 Mass spectrometry experiments

Unfortunately analysis by mass spectrometry did not prove to be very conclusive, with only two of the observed peaks in any of the experiments being positively identified. The first of these (seen on pages 6 and 7 of appendix 1), centred at 592.1 AMU, appears to correspond to a complex with a formula of $C_{20}H_{30}BrMnN_2O_6P_2$ [MnBr(methylphosphonate-diethylester-bpy)]. This sample was prepared in acetonitrile via irradiation with a 455 nm diode. A similar experiment prepared in CDCl$_3$ via irradiation with the 455 nm diode revealed a mass peak

centred around 1013.3 AMU that seemed to correspond to a complex with a formula $C_{40}H_{60}BrMn_2N_4O_{12}P_4$. From these results it appears that irradiation at 455 nm results in the elimination of CO from **Mn-Phos. T**his is in line with what has been reported for manganese based CO releasing molecules.[42,43,44]

Table 2.2 detected mass fragments from mass spectra shown in appendix 1.

Mn decomp	Mn Phos ester break down	Mn Phos decomp	Mn phos dimer in acetontirile
548.2	474.4	441.4	590.1
555.2	484.5	444.3	591.1
557.2	492.4	629.4	592.1
576.5	500.4	630.5	593.1
601.1	522.5	631.4	594.1
650.5	532.5		594.8
688.5	543.5		599.1
689.5	558.6		601
690.5	561.5		1002.3
1002.4	576.5		1003.4
1003.3	580.5		1004.3
1004.4	625.6		1005.3
1005.3	637.6		1046.3
1011.3	650.6		1047.3
1012.3	665.6		1048.3
1013.3	668.6		1049.3
1014.3	688.6		1050.3
1015.3			1171.1
1046.3			1173.2
1047.48			1175.1
1048.9			1215.1
1057.2			1216.1
1059.3			1217.1
			1218.1
			1219.1
			1220.1
			1221.1
			1259
			1261.1
			1262.1
			1263.1
			1264.1
			1265.1
			1266.1

Although none of the other mass peaks from these experiments were able to be identified, it can be seen that several peaks are observed in multiple mas spectra suggesting there might be some common degradation pathway.

2.3.3.3 Cyclic voltammetry experiments

From the IR spectroscopy and mass spectrometry data, it appeared that using broad band irradiation resulted in a different degradation pathway to simply exciting the absorption band at 455 nm, and hence different degradation products. If we were correct that using broad band irradiation resulted in formation of a dimer, and since one of the observed intermediates in the electrocatalytic cycle is a dimer (*vide supra*), it was wondered if the photosensitivity would actually be an issue for the use of manganese based Lehn type catalysts in real world (i.e. exposed to broad band solar light) and their application as CO_2 reduction catalysts. Indeed if photodegradation were to result in formation of a dimer, could this dimer not be formed photochemically and then reduced electrochemically? Although the evidence was certainly tentative at best it was felt that this was a pathway worth exploring.

In order to test for any evidence of CO_2 reduction, a CV sample of the photodecayed product was prepared by leaving a prepared CV sample of **Mn-Phos** (prepared according to the procedure outlined in the section 2.2.2.4) exposed to sunlight for 2 hours. When the sample was examined, brown-black flocks had settled to the bottom suggesting that bromine had been eliminated, reacted with something in the CV sample (acetonitrile, tetrabutyl ammonium hexafluorophosphate or **Mn-Phos**) and flocculated out of solution. The flocks were filtered out using a pipette with a cotton bud filter and the filtered solution returned to the electrochemical cell. A normal CV experiment was then performed under N_2, CO_2 and CO_2 with H_2O. As can be seen in figure 2.12, no current enhancement was observed under these conditions meaning electrocatalytic CO_2 reduction was not taking place.

Attempts to repeat the CV runs proved to be unsuccessful with no flocculation being observed and the working electrode quickly becoming fouled. In line with what has been observed in the mass spectra, it is clear that there are multiple products that can be formed from photo degradation.
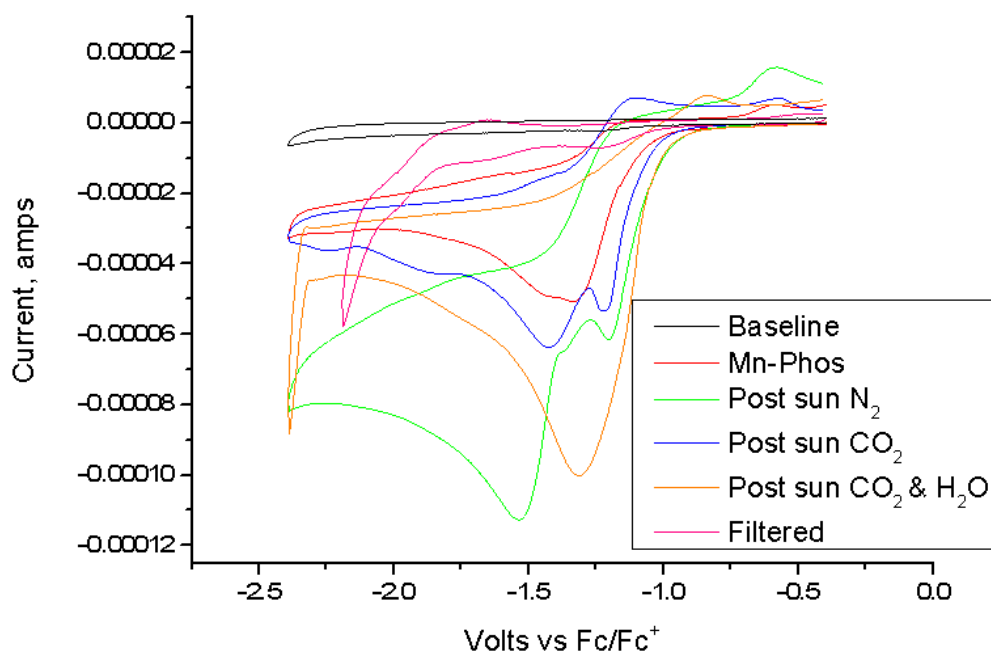
**Figure 2.12 Cyclic voltammograms of complex 2 in acetonitrile, scan rate 0.1 Vs^{-1}, 0.2 M electrolyte NBu_4PF_6.**

2.3.4 Photocatalytic CO_2 reduction by Mn-Phos

Following a discussion with Professor Michael R. Wasielewski at the First International Solar Fuel conference (ISF-1) in Uppsala 2015, a potentially simple method for applying manganese as a photocatalyst was identified.

From the experiments above it appeared at the time that **Mn-Phos** photosensitive, from the IR spectra of the solar irradiated product it looked as if a dimer was forming and that this product was not an electrocatalytically active species. It stands to reason that if the solar irradiated product is formed by elimination of bromide in MeCN or DCM solvent, then that complex must be an oxidised species. If this is the case, could the photodegradation pathway be quenched if a sacrificial electron donor were present in the solvent mixture to reduce the excited state **Mn-Phos**? If so, could this reduced complex be able to go on to photo-catalytically reduce CO_2 in a manner similar to $[ReCl(CO)_3(bpy)]$[45] without becoming deactivated?

Figure 2.13 shows that CO was detected when the solution was saturated with either CO_2 or N_2. The experiment was repeated using Mn-dmbpy with the same results. This means that the observed CO is not the product of photocatalysis but rather the carbonyl ligands being released from the complex upon photodegradation (in line with the identified products in the mass spectra). As a result it can be said with some confidence that photodegradation remains an issue for application of **Mn-Phos**, and if manganese complexes are to be used for CO_2

reduction they must be protected from light. This limitation rules out their use as photocatalysts with direct photo excitation, meaning that applying manganese complexes for CO_2 reduction will depend upon electrocatalytic techniques.
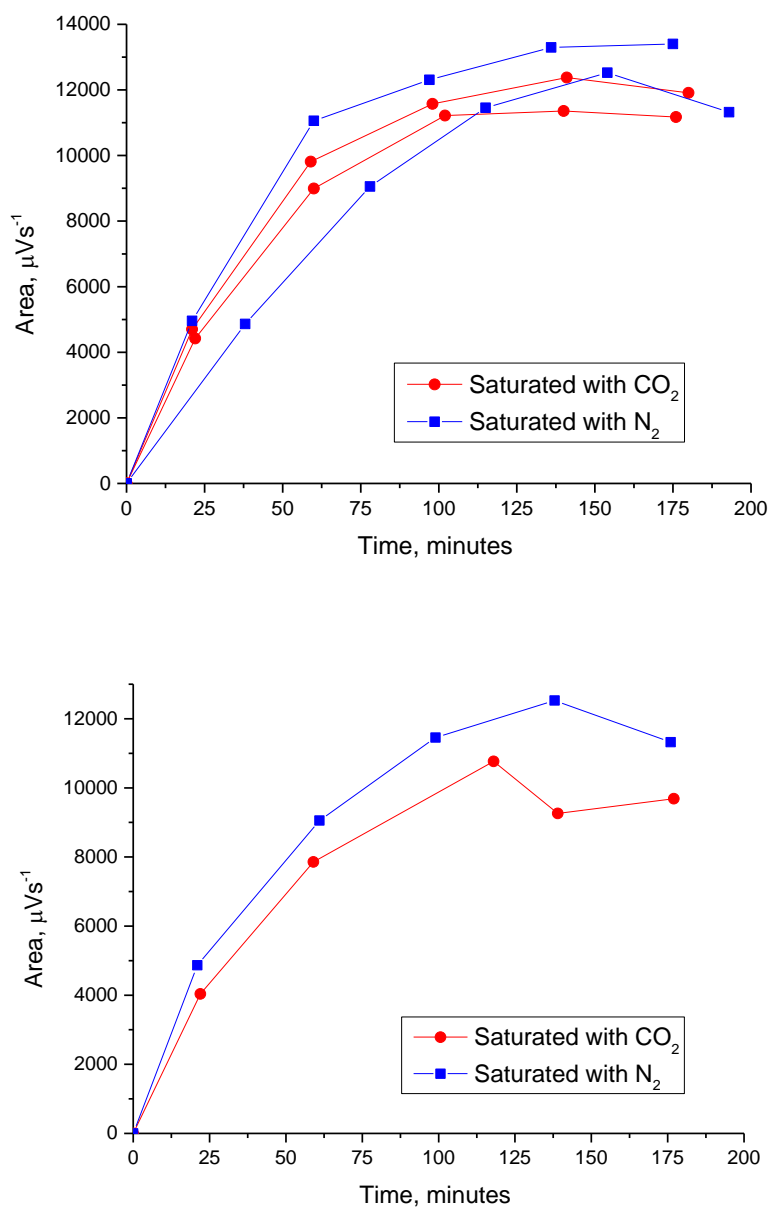
Figure 2.13 GC analysis of Mn-Phos (top) and Mn-dmbpy (bottom) in CO_2 and N_2 saturated acetonitrile in the presence of 16% TEOA after irradiation with a broad band Xe lamp.

2.4 Conclusions

From the cyclic voltammetry data, we can say that there is indeed some element of decoupling between the phosphonate moiety and the bipyridine moiety due to the reduction potential lying intermediate between [MnBr(CO)$_3$(bpy)] and [MnBr(CO)$_3$(dmbpy)]. Whilst this has not been

investigated thoroughly, it is clear that the reduction potential has not been affected to the detriment of catalysis, as has been observed with rhenium bipyridine complexes that had similar electron withdrawing moieties.[13] However, as was stated in the introduction, it was not the intention of this particular work to thoroughly investigate this effect; that remit belongs to a prior work.[6]

Electrochemical experiments revealed that **Mn-Phos** is able to reduce CO_2 to CO and behaves like [MnBr(CO)$_3$(bpy)], forming a dimer upon first reduction which is then further reduced to form a 5-coordinate anion, this 5-coordinate anion then reacts with the CO_2 in solution producing free CO.

Multiple attempts were made to utilise the photodegradation product of **Mn-Phos** for CO_2 reduction, both photochemically and electrochemically. Unfortunately, the cyclic voltammetry results revealed that the photodegradation complex (**complex 2**) does not electrochemically reduce CO_2 nor is it possible to "quench" the photodegradation pathway by using a sacrificial electron donor to reduce the photo excited complex. Rather, upon photo excitation, the carbonyl ligands are eliminated from the manganese centre forming a variety of products. Interestingly, according to the mass spectra, it appears that the bromide is not eliminated despite prior research suggesting that the lowest lying absorption band belongs to a mixed MLCT-XLCT[35,36,46] transition.

From these results, it appears that it is not possible to utilize [MnBr(CO)$_3$(R-bpy)] complexes as catalysts where there is a danger of photodegradation, and without having a more concrete understanding of the cause and pathway of the photodegradation applications appear to be limited to electrocatalysis.

Addendum: Following the conclusion of the experiments in this chapter the author became aware of the use of Mn carbonyl complexes as CORM's (CO releasing molecules). Such complexes with similar or identical structures and moieties as those studied in this chapter are used to release CO upon irradiation, usually with the intention that the CO will kill nearby pathogens or diseased tissues. The fact there is a wealth of research upon Mn complexes as CORM's yet no discussion of the photosensitivity of Mn complexes when employed as catalysts for CO_2 reduction must come as a warning of the need to properly communicate across research areas.[42,43,44,47,48,49]

2.5 Bibliography

(1)   Kurz, P.; Probst, B.; Spingler, B.; Alberto, R. *Eur. J. Inorg. Chem.* **2006**, 2966–2974.

(2)   Bird, R. E.; Hulstrom, R. L.; Lewis, L. J. *Sol. Energy* **1983**, *30* (6), 563–573.

(3)   Takeda, H.; Ishitani, O. *Coord. Chem. Rev.* **2010**, *254*, 346–354.

(4)   Nakada, A.; Koike, K.; Maeda, K.; Ishitani, O. *Green Chem.* **2016**.

(5)   Archer, S. The Synthesis and Photophysical Properties of Light-Harvesting Platinum (II) Diimine Acetylides, 2015.

(6)   Parker, S. Anchored photo-electro-catalysts for CO2 reduction based on transition metal complexes, 2014.

(7)   Habisreutinger, S. N.; Schmidt-Mende, L.; Stolarczyk, J. K. *Angew. Chem. Int. Ed. Engl.* **2013**, *52* (29), 7372–7408.

(8)   Kumar, B.; Smieja, J. M.; Kubiak, C. P. *J. Phys. Chem. C* **2010**, *114*, 14220–14223.

(9)   Takeda, H.; Koizumi, H.; Okamoto, K.; Ishitani, O. *Chem. Commun. (Camb).* **2014**, *50* (12), 1491–1493.

(10)   Windle, C. D.; Câmpian, M. V.; Duhme-Klair, A.-K.; Gibson, E. a.; Perutz, R. N.; Schneider, J. *Chem. Commun.* **2012**, *48* (66), 8189–8191.

(11)   Windle, C. D.; Pastor, E.; Reynal, A.; Whitwood, A. C.; Vaynzof, Y.; Durrant, J. R.; Perutz, R. N.; Reisner, E. *Chem. - A Eur. J.* **2015**, *21*, 3746–3754.

(12)   Takeda, H.; Koike, K.; Morimoto, T.; Inumaru, H.; Ishitani, O. *Adv. Inorg. Chem.* **2011**, *63*, 137–186.

(13)   Smieja, J. M.; Kubiak, C. P. *Inorg. Chem.* **2010**, *49* (20), 9283–9289.

(14)   Hartl, F.; Rosa, P.; Ricard, L.; Le Floch, P.; Záliš, S. *Coord. Chem. Rev.* **2007**, *251*, 557–576.

(15)   Rossenaar, B. D.; Lindsay, E.; Stufkens, D. J.; Vlcek, A. *Inorganica Chim. Acta* **1996**, *250*, 5–14.

(16)   Stufkens, D. J.; Aarnts, M. P.; Nijhoff, J.; Rossenaar, B. D.; Vleek, A. **1997**, *171* (98).

(17)   Rossenaar, B. D.; Kleverlaan, C. J.; Ven, M. C. E. van de; Stufkens, D. J.; Oskam, A.; Fraanje, J.; Goubitz, K. *J. Organomet. Chem.* **1995**, *493*, 153–162.

(18)   Rossenaar, B. D.; Stufkens, D. J.; Oskam, A.; Fraanje, J.; Goubitz, K. *Inorganica Chim. Acta* **1996**, *247*, 215–229.

(19)   Stufkens, D. J.; van der Graaf, T. Van; Stor, G. J.; Oskam, A. *Coord. Chem. Rev.* **1991**, 331–336.

(20)   Rossenaar, B. D.; Graaf, T. van der; Eldik, R. van; Langford, C. H.; Stufkens, D. J.; Vlcek, A. J. *Inorg. Chem.* **1994**, *33* (13), 2865–2873.

(21)   Rossenaar, B. D.; Hartl, F.; Stufkens, D. J.; Amatore, C.; Maisonhaute, E.; Verpeaux, J.-N. *Organometallics* **1997**, *16*, 4675–4685.

(22)   Breikss, I.; Abruna, D. *J. Electroanl. Chem.* **1986**, *201*, 347–358.

(23)   Sullivan, B. P.; Bolinger, C. M.; Conrad, D.; Vining, W. J.; Meyer, T. J. *J. Chem. Soc., Chem. Commun.* **1985**, No. 20, 1414–1416.

(24)   Johnson, F. P. A.; George, M. W.; Hartl, F.; Turner, J. J. *Organometallics* **1996**, *15* (15), 3374–3387.

(25)   Bourrez, M.; Molton, F.; Chardon-Noblat, S.; Deronzier, A. *Angew. Chem. Int. Ed. Engl.* **2011**, *50* (42), 9903–9906.

(26)   Staal, L. H.; Oskam, A.; Vrieze, K. *J. Organomet. Chem.* **1979**, *170* (2), 235–245.

(27)   Costentin, C.; Drouet, S.; Passard, G.; Robert, M.; Save, J. *J. Am. Chem. Soc.* **2013**, *135*, 9023–9031.

(28)   Costentin, C.; Drouet, S.; Robert, M.; Savéant, J.-M. *Science (80-.).* **2012**, *338*, 90–94.

(29)   Franco, F.; Cometto, C.; Ferrero Vallana, F.; Sordello, F.; Priola, E.; Minero, C.; Nervi, C.; Gobetto, R. *Chem. Commun. (Camb).* **2014**, *50* (93), 14670–14673.

(30)   Carter, E. a. *ACS Catal.* **2014**, *5*, 900–908.

(31)   Riplinger, C.; Sampson, M. D.; Ritzmann, A. M.; Kubiak, C. P.; Carter, E. A. *J. Am. Chem. Soc.* **2014**, *136*, 16285–16298.

(32)   Machan, C. W.; Sampson, M. D.; Chabolla, S. a; Dang, T.; Kubiak, P. *Organometallics* **2014**, *33*, 4550–4559.

(33)   Zeng, Q.; Tory, J.; Hartl, F. *Organometallics* **2014**, *33* (18), 5002–5008.

(34)   Vollmer, M. V; Machan, C. W.; Clark, M. L.; Antholine, W. E.; Agarwal, J.; Schaefer, H. F.; Kubiak, P.; Walensky, J. R. *Organometallics* **2014**, *34* (1), 3–12.

(35)   Rossenaar, B. D.; Stufkens, D. J.; Vlcek, A. J. *Inorg. Chem.* **1996**, *35*, 2902–2909.

(36)   Rossenaar, B. D.; Kleverlaan, C. J.; Ven, M. C. E. Van De; Stufkens, D. J.; Vlcek, A. J. *Chem.Eur. J* **1996**, *2* (2), 228–237.

(37)   Bond, M.; Grabaric, B. S.; Grabaric, Z. *Inorg. Chem.* **1978**, *17* (4), 1013–1018.

(38)   Doux, M.; Mezailles, N.; Ricard, L.; Floch, P. Le. *Inorg. Chem.* **2005**, *44*, 9213–9224.

(39)   Pereira, C.; Ferreira, H. G.; Schultz, M. S.; Milanez, J.; Izidoro, M.; Leme, P. C.; Santos, R. H. a.; Gambardella, M. T. P.; Castellano, E. E.; Lima-Neto, B. S.; Carlos, R. M. *Inorganica Chim. Acta* **2005**, *358* (13), 3735–3744.

(40)   Doux, M.; Mézailles, N.; Ricard, L.; Le Floch, P.; Vaz, P. D.; Calhorda, M. J.; Mahabiersing, T.; Hartl, F. *Inorg. Chem.* **2005**, *44* (25), 9213–9224.

(41)   Kleverlaan, C. J.; Hartl, F.; Stufkens, D. J. *J. Organomet. Chem.* **1998**, *561* (1–2), 57–65.

(42)   Atkin, A. J.; Lynam, J. M.; Moulton, B. E.; Sawle, P.; Motterlini, R.; Boyle, N. M.; Pryce, M. T.; Fairlamb, I. J. S. *Dalt. Trans.* **2011**, *40*, 5755–5761.

(43)   Ruggi, A.; Zobi, F. *Dalt. Trans.* **2015**, *44* (24), 10928–10931.

(44)   Strinitz, F.; Trautner, P.; Pfeiffer, H.; Schatzschneider, U.; Burzlaff, N. *Tetrahedron* **2015**, *71* (19), 2951–2954.

(45)   Hawecker, J.; Lehn, J.; Ziessel, R. *J. Chem. Soc., Chem. Commun.* **1983**, 536–538.

(46)   Carrington, S. J.; Chakraborty, I.; Mascharak, P. K. *Dalt. Trans.* **2015**.

(47)   Mclean, S.; Mann, B. E.; Poole, R. K. *Anal. Biochem.* **2012**, *427* (1), 36–40.

(48)   Wood, P. M. *Biochim. Biophys. Acta.* **1984**, *768* (768), 293–317.

(49)   Gonzalez, M. A.; Carrington, S. J.; Fry, N. L.; Martinez, J. L.; Mascharak, P. K. *Inorg. Chem.* **2012**, *51* (21), 11930–11940.

3. Investigating substituted rhenium tricarbonyl bis(mestiylimino)-acenaphthene complexes for CO_2 reduction.

3.1.1 Introduction

In recent decades awareness of the effects of climate change has been a cause for concern amongst both scientists and the general public.[1,2,3] This awareness has driven forward the development of technologies to reduce anthropogenic carbon dioxide emissions. As discussed in chapter 1 amongst the more well-known technologies aimed to reduce carbon dioxide emissions, such as wind turbines and battery electric vehicles, interest has arisen in solar fuels[4] as a means to combat the short comings of other technologies mentioned above, such as intermittent supply and ease of handling.[5] Excluding technologies such as algae biofuel discussion has centred around two key concepts; photochemical and photo-electrochemical reduction, and electrocatalytic reduction.[6] To this end rhenium tricarbonyl α-diimines have proven to be a popular class of compounds to investigate as CO_2 reducing complexes. due to many complexes being both photocatalytically[7] and electrocatalytically[8] active towards CO_2 reduction[9] combined with their inherent stability to light exposure. This stands in contrast to manganese tricarbonyl α-diimines which exhibit marked sensitivity to light (see chapter 2) which has prohibited their application as photocatalysts using conventional methods.[10]

Development of rhenium α-diimines for CO_2 reduction has mostly concentrated on bipyridine based systems[11,12,13] and although effective as photocatalysts such species have suffered due to the region of MLCT absorption being located mainly below 450 nm,[14] whereas the region of peak solar irradiation is located around 500 to 750 nm (Fig. 3.1).
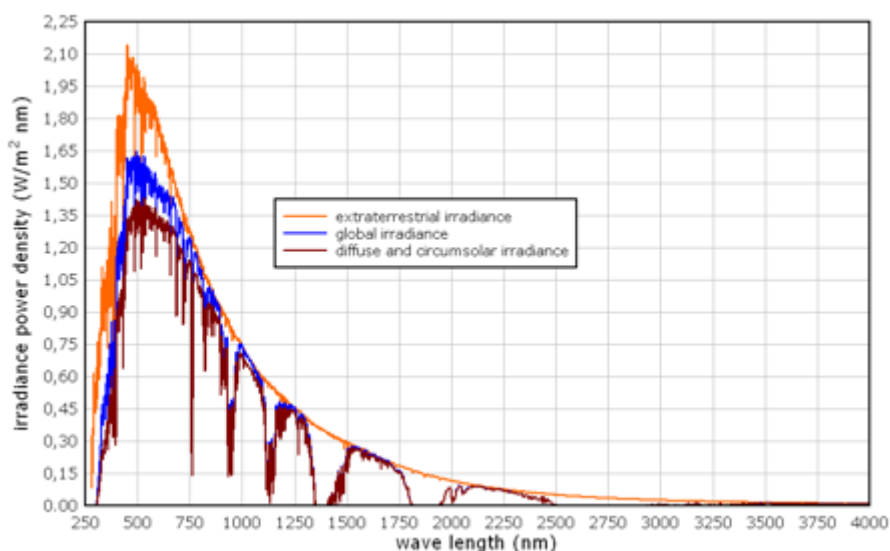
Figure 3.1. ASTM G173-03 Reference Solar Spectral Irradiance where orange is extraterrestrial irradiance, blue is global irradiance and red is diffuse and circumsolar irradiance. Credit: Renewable Resource Data Center (RReDC): Standard Solar Spectra.

In contrast complexes containing bis(mesitylimino)acenaphthene (mesBIAN) ligands exhibit broad absorption cross sections in this region[15] and have thus been applied previously to the generation of charge separated states. This has drawn our attention to their potential use as photocatalysts. The downside to the low lying absorption bands is that they lack energy and thus may be unable to facilitate photocatalytic CO_2 reduction. In addition what may also prove problematic is the energy gap law which states the rate of nonradiative decay in metal ligand complexes increases exponentially as the energy-gap decreases.[16] It has been observed in prior research on rhenium(I) bis(phenylimino)acenaphthene tricarbonyl complexes has shown that they are non-emissive[17,18] suggesting that the photo excited state may not be long lived enough to interact with the sacrificial electron donor. Importantly rhenium bis(imino)acenaphthene carbonyl complexes have already been shown to exhibit electrocatalytic CO_2 reduction.[19]

In the recent paper by Knör *et al.* a family of rhenium complexes with bis(imino)acenaphthene ligands were investigated for electrocatalytic CO_2 reduction.[19] The work described the change in electrocatalytic activity towards CO_2 reduction when the substitution of the phenyl rings was varied. It was found that more substituted aryl rings at the imine functionality resulted in increased activity towards CO_2 reduction with an unsubstituted aryl ring showing little activity.[18,19] These aromatic rings are orthogonal to the aromatic acenaphthene system so there is no overlap of the π-systems, this implies that the effect of changing the ring substituents is due to the steric hindrance around the tricarbonyl-chloro-rhenium unit. This seems a reasonable assumption as it is often concluded that the dissociation of the halide is important in the rate of CO_2 reduction and additional steric bulk is likely to affect the dissociation.[20] Independently of this publication we had become curious as to the effect of utilising substituted mesBIAN ligands for CO_2 reduction due to the experience in the group of utilising substituted mesBIAN ligands for investigating the chemistry of Pt donor accepter complexes.[21]

3.1.2 Aims

For the purpose of investigating CO_2 reduction three [ReCl(CO)$_3$(4-R-mesBIAN)] complexes utilising mesBIAN ligands in which the R substituent varies in electron withdrawing/donating ability were synthesised by Andrew Sadler (scheme 3.1). The aim was to investigate what effect placing an electron donating/withdrawing group has on the catalytic activity of the complexes as it will alter the electronics of the acenaphthene aromatic system.

In addition to electrochemical characterisation it was intended to determine if it was possible to utilise the mesBIAN ligand for photochemical CO_2 reduction.

The unmodified mesBIAN (where R = H) has been synthesised as described by the Knör paper and will serve as a standard to compare the other systems with.

R = H, N₃,COOEt
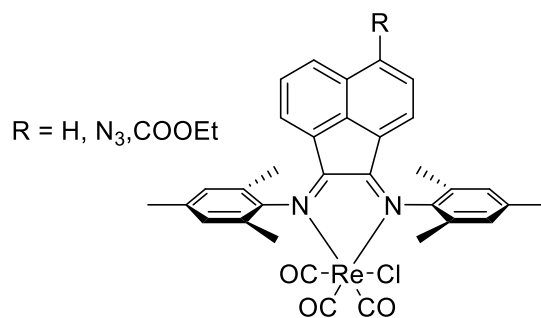
Scheme 3.1 Chemical structures of the rhenium tricarbonyl complexes investigated for CO_2 reduction synthesised by Andrew Sadler.

The three complexes investigated will be referred to as Re mesBIAN where R = H, Re mesBIAN-COOEt where R = COOEt and Re mesBIAN-N_3 where R = N_3.

3.2 Experimental

3.2.1 Materials and General Procedures

2,4,6-trimethylaniline (97 %), n-butyl lithium (2.5 M in hexane), 9,10-phenanthrene (95 %), titanium tetrachloride (99.9 %) and pentacarbonylchlororhenium(I) (98 %) were provided by Acros Organics. 5-bromoacenaphthene was provided by Manchester Organics. Ethyl chloroformate (97 %) was provided by Alfa Aesar. Acetic Anhydride was provided by Fisher Scientific. Chromium trioxide (>98 %) was provided by Sigma Aldrich. Acenaphthene was provided by Aldrich. Triethanolamine (>99 %) was provided by Sigma. Glacial acetic acid was provided by VWR. Tetrabutylammonium hexafluorophosphate (Sigma-Aldrich) was recrystallized from hot ethanol and dried overnight in a vacuum oven. All solvents (Fisher Scientific, Sigma-Aldrich, VWR) were of HPLC grade or higher and were used without further purification unless otherwise stated. Dry solvents were obtained from a Grubbs solvent drying system.

3.2.2 Instrumentation and Analysis

3.2.2.1 UV-Visible Absorption Spectroscopy

UV-Visible absorption spectra were recorded on either a Cary 50 Bio spectrophotometer or Cary 5000 UV-VIS-NIR spectrophotometer utilising 1 cm path length quartz curvettes.

3.2.2.2 Cyclic Voltammetry

Cyclic voltammetry was performed in a 0.002 M solution using acetonitrile with recrystallized [Bu₄N][PF₆] at 0.2 mol dm⁻³ concentration as a supporting electrolyte. The potential was controlled with a Princeton Applied Research VersaSTAT 3 potentiostat. A glassy carbon working electrode (0.07 cm²), platinum wire counter electrode and Ag/AgCl (0.1 M) reference

electrode were used. All potentials are quoted vs Fc/Fc$^+$ unless otherwise stated. Initial scans were measured using a scan rate of 100 mV s^{-1} and reversibility was assessed using scan rates of 20 – 200 mV s^{-1}.

The solutions were degassed by bubbling thoroughly with N_2 and a nitrogen atmosphere was maintained over the samples during the experiment. To test for current enhancement the samples were bubbled thoroughly with CO_2 and measurements taken. 0.3 ml of water was then added to each sample to test the effects of adding a Brönsted acid. During these later experiments a CO_2 atmosphere was maintained over the samples during the experiment.

Cyclic voltammograms recorded under N_2 in the presence of water were gathered, however, the voltammograms yielded poor results as it appeared that under N_2 in the presence of water side reactions occur causing the decay of the complex. As such no N_2 in the presence of water voltammograms are included and calculations of catalytic current enhancement are made against the N_2 voltammograms.

3.2.2.3 Photocatalysis

An experiment was designed to assess whether the rhenium complexes were photocatalytically active for the reduction of CO_2. The set up a bespoke photochemical solution cell with a glass headspace, sealed with a suba seal from which gas samples could be extracted. The sample complex (0.11 mM) was dissolved in acetonitrile (24 ml) and saturated with CO_2. Triethanolamine (TEOA) (4.5 ml) was added as a sacrificial electron donor. This solution was then irradiated with light from a xenon lamp and at regular time intervals (one hour) a sample of the gas in the gas collection compartment was withdrawn with a gas tight syringe and analysed by gas chromatography (GC) to detect any CO that may have been produced photocatalytically. This experiment was initially tested with known photocatalyst [ReCl(CO)$_3$(dmbpy)] and after one hour of irradiation there was a strong CO signal in the GC trace, confirming that the method was suitable.

3.2.2.4 Spectroelectrochemistry (SEC)

Infrared spectroelectrochemistry was performed using Princeton Applied Research VersaSTAT 3 potentiostat. 4 mmol dm^{-3} of the complex in presence of 0.17 g (0.3 mol dm^{-3}) of [Bu$_4$N][PF$_6$] in dry acetonitrile was analysed using an optically transparent thin-layer spectroelectrochemical cell (OTTLE cell) equipped with Pt minigrid working electrodes, a Ag microwire psudoreference electrode and CaF$_2$ windows. Samples were prepared in argon atmosphere and samples for catalytic measurements were prepared by bubbling the electrolyte with CO_2 for 15 minutes. IR spectral monitoring of the experiment was performed on a Perkin Elmer Spectrum 1 FT-IR spectrometer using an MCT detector at 4 cm^{-1} resolution. Thin layer cyclic voltammograms were recorded at the same time.

3.3 Results and discussion

3.3.1 Determination of photocatalytic activity

As can be seen all of the complexes show intense absorptions in the visible region. The UV-vis spectra show important differences in the absorption profiles of the three complexes. As predicted the unmodified mesBIAN complex exhibits behaviour in between the electron donor substituted (N_3-mesBIAN) and the electron withdrawing substituted (COOEt-mesBIAN). In particular the N_3-mesBIAN complex shows very intense redshifted absorption. This is very much in line with what has been reported for similar complexes[17,18,22] The greater red shifted absorption of the N_3-substitued mesBIAN complex can be explained by the decreased HOMO-LUMO energy gap that has been observed in electron donor substituted Re diimine complexes[23] and such it is unlikely that Re mesBIAN-N_3 will be able to photochemically reduce CO_2 (*vide supra*).

Absorption

λ_{max} / nm (ε / M^{-1} cm^{-1})

[ReCl(CO)$_3$(mesBIAN)]	294 (18870), 332 (8790), 374 (7740), 502 (9760)
[ReCl(CO)$_3$(4-COOEt-mesBIAN)]	300 (13290), 336 (8660), 396 (6510), 510 (6940)
[ReCl(CO)$_3$(4-N$_3$-mesBIAN)]	308 (14520), 407 (11350), 511 (9440)

Figure 3.3 Absorption spectra of the rhenium mesBIAN complexes recorded in DCM.

In order to test for photocatalytic CO_2 reduction samples of the compounds were prepared according to the procedure outlined in section 3.2.2.3. After several hours of irradiation with a Xe lamp no CO was detected from any of the complexes, nor was any colour change in the solution observed. We therefore conclude that these complexes are unsuitable as photocatalysts. In some ways this is surprising as Re mesBIAN has already shown itself to be electrocatalytically active and Takeda *et al.* have shown that it is possible to drive photocatalytic CO_2 reduction using a ruthenium based photosensitiser with MLCT bands that extend out to ca. 560 nm.[10] This raises the question of whether the lack of observed photocatalysis is due to the lower lying MLCT states in the mesBIAN complexes not having a sufficiently long lifetime thus becoming deactivated too quickly to be able to interact

with the sacrificial TEOA and become reduced. Or whether this is due to the excited MLCT state not being sufficiently oxidising in order to be able to oxidise the TEOA and generate the reduced Re mesBIAN complex.

In order to determine if the problem lies from the photoexcited state becoming deactivated too quickly to interact with the sacrificial electron donor time resolved infrared (TRIR) data was gathered at the Rutherford Appleton laboratories by Dr Edward Greenough and George Farrow on the Re mesBIAN complex. Figure 3.4 shows the fitting of the decay of a carbonyl transient and the lifetimes associated with it which was performed by Alexander J. Auty.
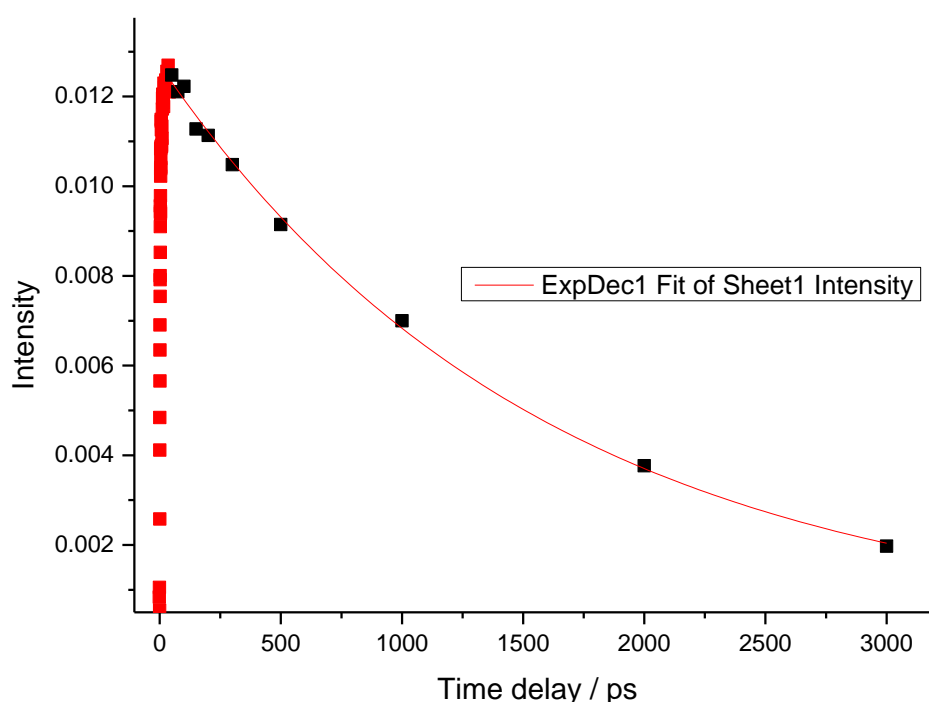
Complex	Life time / Nano Seconds
[ReCl(CO)$_3$(mesBIAN)]	1.6

Figure 3.4 Fitted decay trace of the carbonyl region of Re mesBIAN recorded in DCM

From the results shown in table 3.1 the lifetime of Re mesBIAN gives a rate of relaxation at 6.25×10^8 s^{-1}. Assuming[24] a diffusion limited rate constant of 2×10^{10} M^{-1} S^{-1} and given the concentration of TEOA of 1.1 mol dm^{-3} it appears that there is ample time for the excited state Re mesBIAN to interact with the sacrificial electron donor. This suggests that the problem lies with the lack of oxidising power in the excited state complex relative to the sacrificial electron donor.

Because these complexes are non-emissive in the visible range it is not possible to easily estimate the oxidation potential of the triplet MLCT state. However an estimate of the oxidation potential of a

vibrationally hot singlet MLCT state, based on the first oxidation potential observed in a cyclic voltammogram recorded at a scan rate of 0.1 Vs^{-1} in acetonitrile, gives an oxidation potential of +0.96 V vs SCE (SCE is used in order to allow comparison with literature data where no Fc/Fc$^+$ redox potential has been reported). This compares with the oxidation potential of TEOA of +0.8 V vs SCE and means a vibrationally hot singlet MLCT state would be sufficiently oxidising to be reduced by TEOA. However, due to intersystem crossing, vibrational cooling and solvent reorganisation the triplet MLCT state may not be sufficiently oxidising to be reductively quenched by the sacrificial electron donor.

Additionally in the experiments carried out at the University of Sheffield the lowest lying reduction potential lies at -0.69 V vs SCE (though a much stronger and more evident redox pair lies at E$_{1/2}$ - 0.825 V vs SCE). The evidence presented by Takeda *et al.*[25] has shown that rhenium complexes did not exhibit strong photocatalytic activity where the lowest lying reduction was less negative that -1.4 V vs Ag/AgNO$_3$ estimated to be -1.7 V vs SCE.

From this evidence it appears that there is sufficient time for the photo excited state to interact with the sacrificial electron donor, however, the estimates of the oxidation potential of the singlet MLCT state suggest that after intersystem crossing there will not be a sufficient oxidation potential to allow the sacrificial electron donor to reductively quench the photo excited Re mesBIAN. In addition the comparatively less negative first reduction potential of the Re mesBIAN compared to what was observed to be necessary for efficient photocatalysis by Takeda *et al.* strongly suggests these complexes are not photocatalytic due to the triplet MLCT states lack of oxidation potential as compared to the sacrificial electron donor.

3.3.2 Determination of electrocatalytic activity

3.3.2.1 Cyclic Voltammetry

Before discussing the electrocatalytic activity of the rhenium mesBIAN complexes it is worth discussing the cyclic voltammetry of Re mesBIAN as significant differences were observed compared with what was reported by Knör *et al.* in 2014.[10] It is important to note that while Knör *et al.* only explored the reduction window down to around -1.9 V vs Fc/Fc$^+$ the voltammograms shown here go down to -2.9 V vs Fc/Fc$^+$.
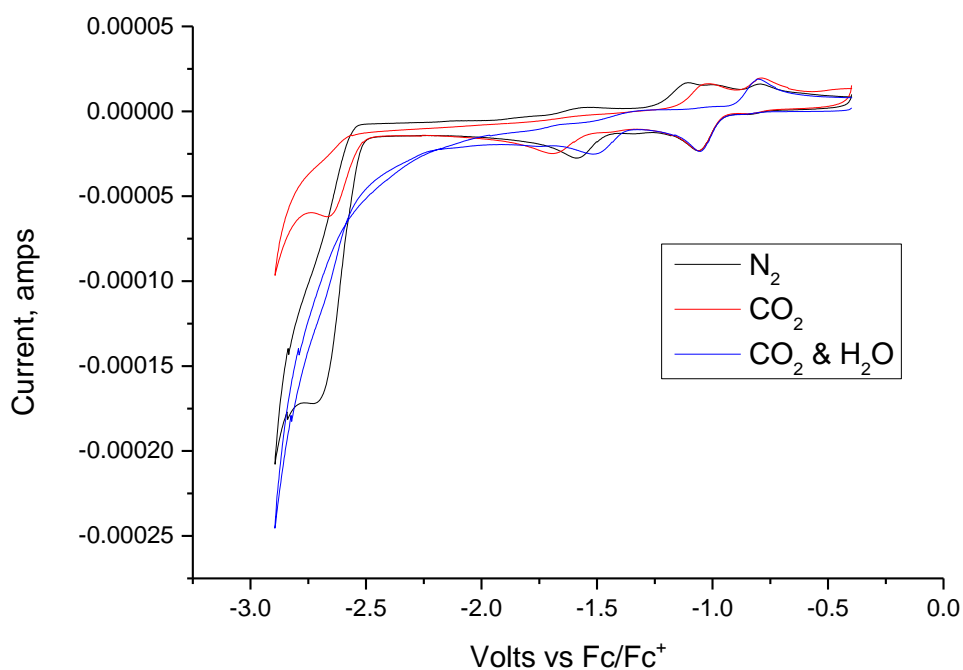
Figure 3.5 Cyclic voltammetry traces of Re mesBIAN under N_2, CO_2 and CO_2 with 0.3 ml of H_2O in 6 ml of Grubbs dried acetonitrile with 0.2 M [Bu$_4$N][PF$_6$].

Under N_2 the reduction peak at -0.84 V vs Fc/Fc$^+$ was substantially less intense than that reported in figure S1 by Knör *et al.* this may be due to their use of Pt electrodes in their experiments or the solution volume/electrode diameter used in their experiments (these parameters have not been reported). There also appears to be an oxidation peak at -1.1 V vs Fc/Fc$^+$ observable under N_2 which was not reported under N_2 by Knör *et al.* This suggests that a dissociative process is occurring in our experimental set up that was not occurring for Knör *et al.* followed by binding of some other species (most likely solvent molecules).
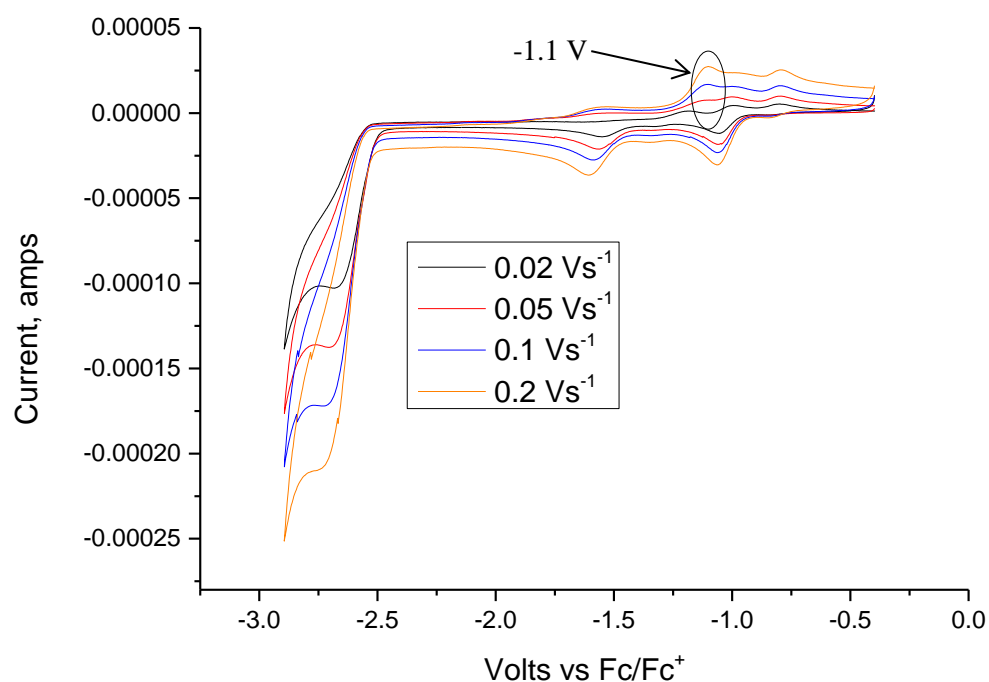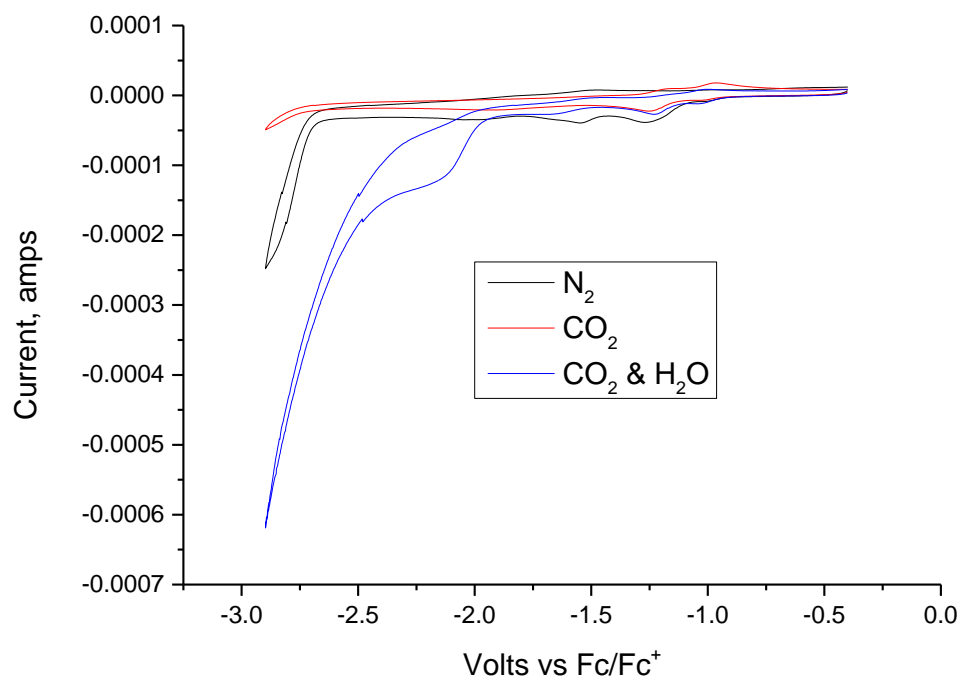
Figure 3.6 Cyclic voltammetry traces of Re mesBIAN under N$_2$ at different scan rates in 6 ml of Grubbs dried acetonitrile with 0.2 M [Bu$_4$N][PF$_6$].

Figure 3.6 shows the full reduction of Re mesBIAN at different scan rates. As can be seen there is a strong scan rate dependence on the oxidation peak at -1.1 V vs Fc/Fc$^+$ with a larger current observed at a scan rate of 0.2 Vs^{-1} as opposed to 0.02 Vs^{-1}. This is very strong evidence for an Electrochemical Chemical (EC) process (such as a dissociative process) occuring during the reduction. What is especially interesting is that cyclic voltammograms taken in the range -0.87 to -1.1 V vs Fc/Fc$^+$ (fig. 3.7 B) at the same scan rates show strong reversibility of the redox couple although it is not clear if this complete reversibility or pseudo reversibility. This suggests that the reaction resulting in the formation of the oxidised species observed at -1.1 V vs Fc/Fc$^+$ occurs as a result of electrochemical processes occurring at more negative reduction potentials.
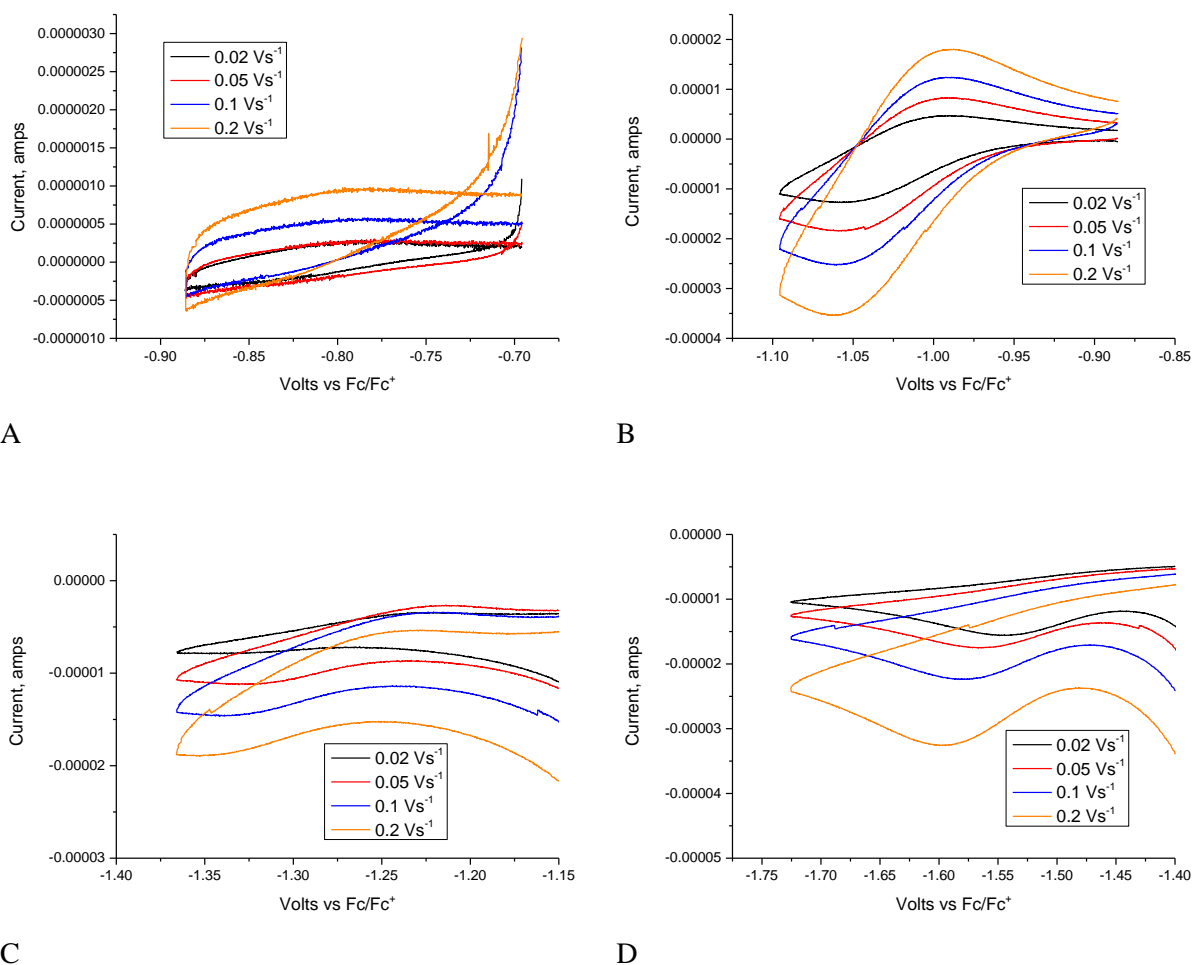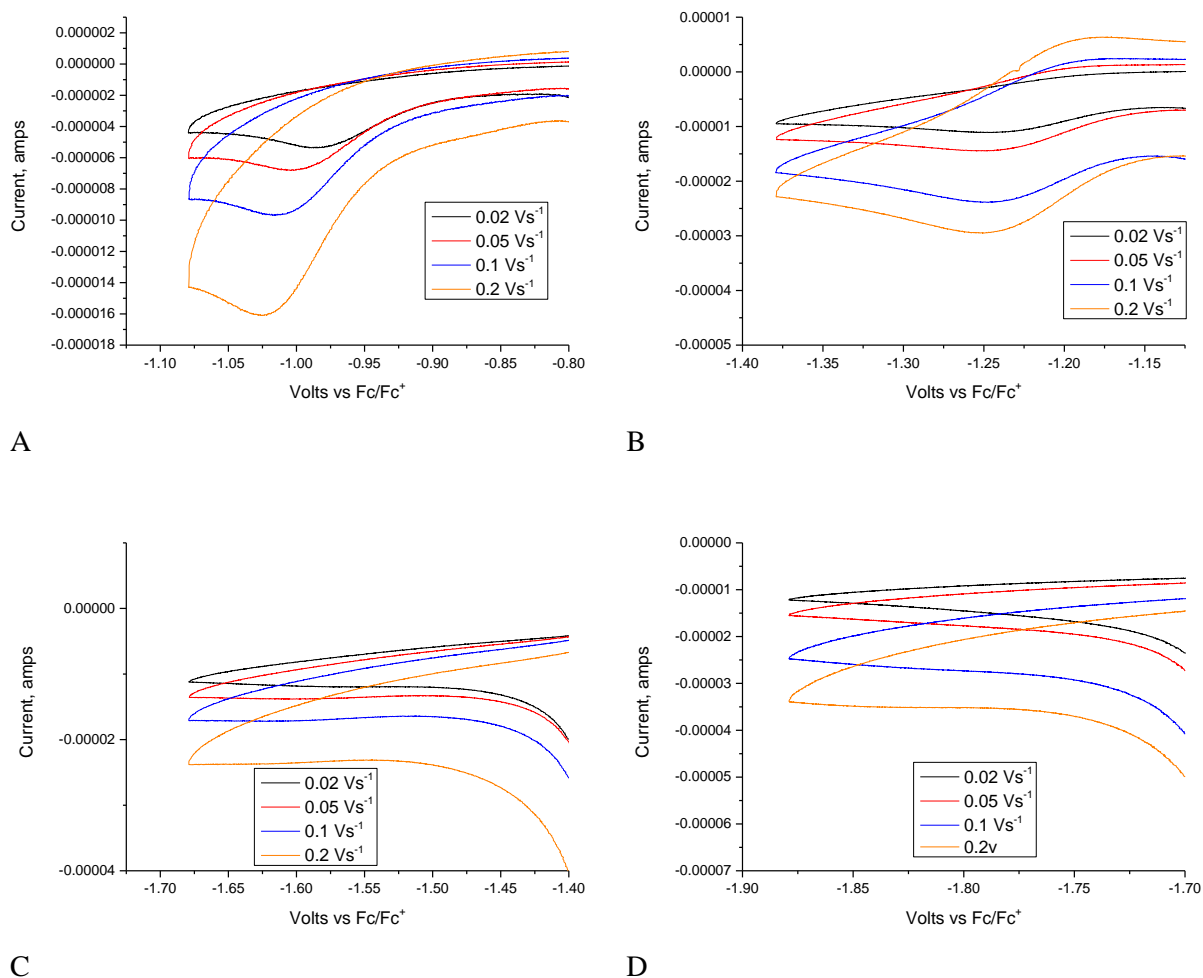
Figure 3.7 Cyclic voltammetry traces of redox processes in Re mesBIAN under N_2 at different scan rates in 6 ml of Grubbs dried acetonitrile with 0.2 M [Bu$_4$N][PF$_6$].

Knör *et al.* reported that the two least negative reduction potentials are reversible, the scans shown in figure 3.7 A and B are in largely in agreement with what has been reported, although the scans in 3.7 A are not especially clear (this is most probably due to differences in experimental set up). Knör *et al.* also reported that the following two reduction were semi-reversible and for the redox process shown in figure 3.7 C there does appear to be a very small degree off quasi reversibility, however, this is not observed for the redox process shown in figure 3.7 D.

The most striking difference between the results observed by Knör *et al.* and those observed at Sheffield on the Re mesBIAN complex is that no CO_2 reduction was observed in cyclic voltammograms recorded under CO_2 without water being added as a proton source. In contrast Knör *et al.* report observing CO_2 reduction at -1.9 V vs Fc/Fc$^+$ under CO_2, which was very contrary to what was observed in Sheffield with current enhancement at this voltage not being observed until a proton source was added. Indeed at even lower reduction potentials of around -2.7 V vs Fc/Fc$^+$ upon saturating with CO_2 the peak current observed in Re mesBIAN (as well as the other substituted mesBIAN complexes) actually decreased until water was added. This would suggest that Re

mesBIAN complexes form a very stable CO_2 associated species which cannot be reduced further in the absence of a proton source.
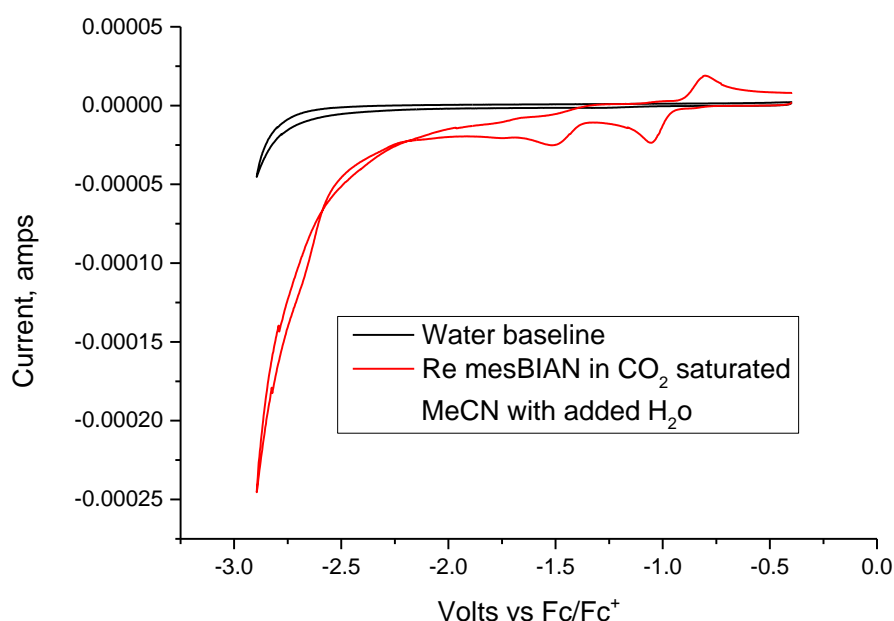
Figure 3.8 Cyclic voltammetry traces of Re mesBIAN under CO_2 rates in 6 ml of acetonitrile with 0.3 ml of water added in the presence of 0.2 M [Bu$_4$N][PF$_6$] overlaid with a baseline of 6 ml of acetonitrile with 0.3 ml of water under N$_2$ in the presence of 0.2 M [Bu$_4$N][PF$_6$] recorded at 0.1 Vs^{-1}.

Due to the issues experienced when trying to collect cyclic voltammograms of the mesBIAN complexes in a solution of acetonitrile and water under N_2 an alternative method was needed to support the assertion that current enhancement was due to CO_2 reduction. As such a baseline measurement was taken in a solution of 6 ml of acetonitrile and 0.3 ml of water in the presence of 0.2 M [Bu$_4$N][PF$_6$] which had been purged with N_2. As can be seen the current produced by the Re mesBIAN in the presence of CO_2 and water is far greater than that produced as a result of the reduction of water at the electrode surface. Combined with the inability to gather voltammograms when the Re mesBIAN complexes were present (most likely due to a destructive side reaction) we can be confident that the current enhancement is most probably due to the catalytic reduction of CO_2 by the Re mesBIAN complex.

The behaviour of the substituted complex Re mesBIAN-COOEt is quite similar to what was observed with unsubstituted Re mesBIAN with the first two redox pairs being reversible and the two more negative reduction potentials being irreversible . Under CO_2 some small current enhancement is observed but much larger current enhancement is seen with the addition of the water to act as a Brönsted acid.
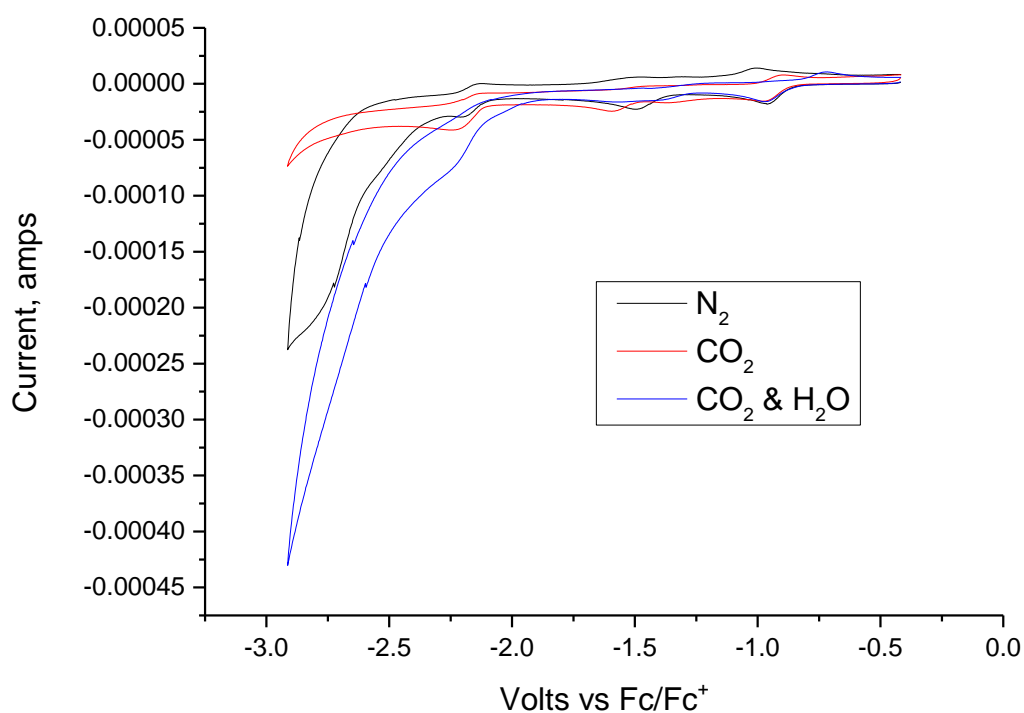
Figure 3.9 Cyclic voltammetry traces of Re mesBIAN-COOEt under N_2 at different scan rates in 6 ml of Grubbs dried acetonitrile with 0.2 M [Bu$_4$N][PF$_6$].

Re mesBIAN-N$_3$ shows even greater current enhancement under CO_2 with added water than either of the other two mesBIAN complexes. The sweeps of the redox areas show very little, the first reduction does not appear to be reversible at all whilst the second reduction appears to exhibit quasi reversibility only at higher scan rates. The two lowest reductions are irreversible.
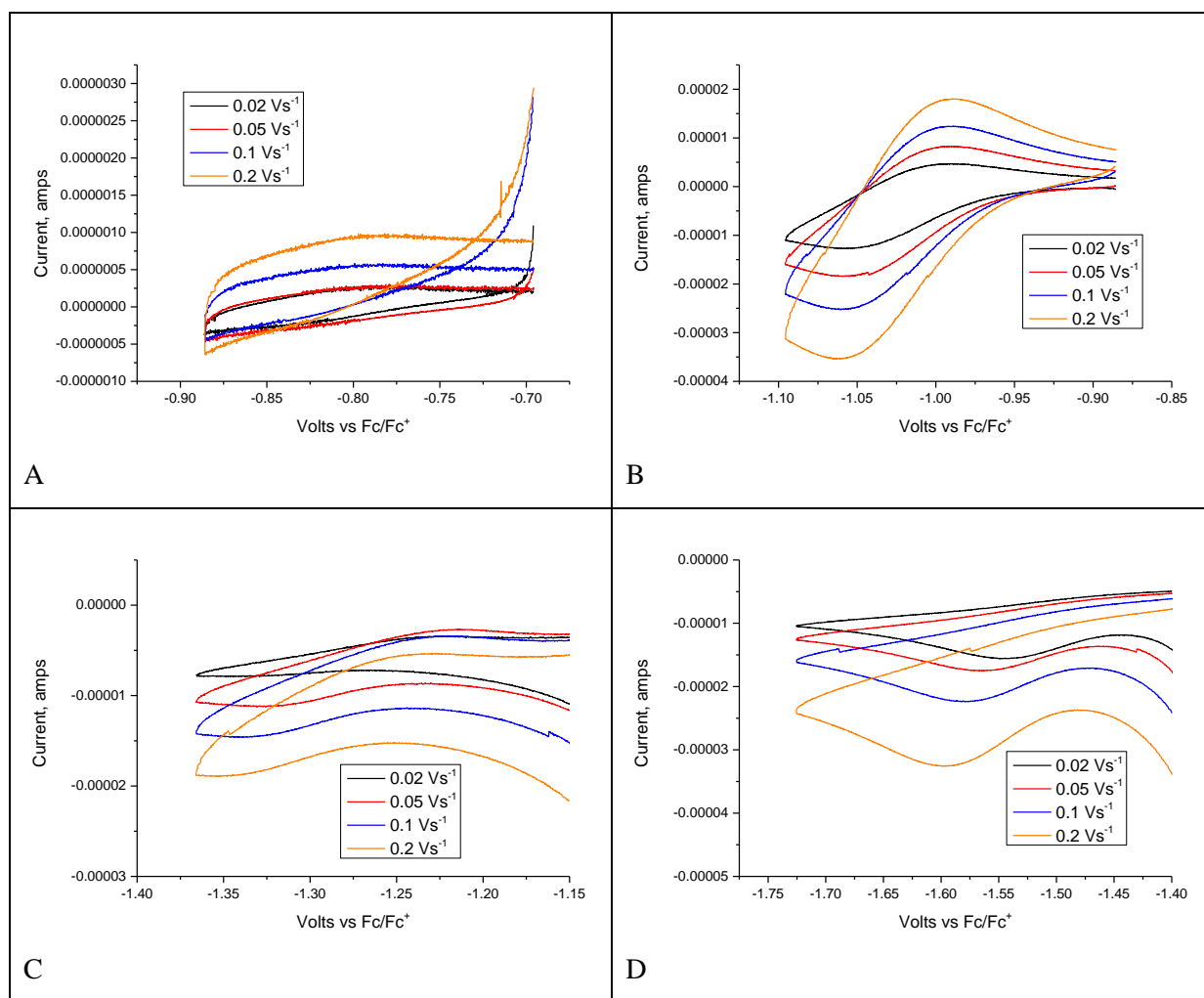
Figure 3.7 Cyclic voltammetry traces of redox processes in Re mesBIAN under N₂ at different scan rates in 6 ml of Grubbs dried acetonitrile with 0.2 M [Bu₄N][PF₆].

Figure 3.11 Cyclic voltammetry traces of Re mesBIAN-N$_3$ under N$_2$ at different scan rates in 6 ml of Grubbs dried acetonitrile with 0.2 M [Bu$_4$N][PF$_6$].

A

B

C

D

Figure 3.12 Cyclic voltammetry traces of redox processes in Re mesBIAN-N$_3$ under N$_2$ at different scan rates in 6 ml of Grubbs dried acetonitrile with 0.2 M [Bu$_4$N][PF$_6$].

3.3.2.2 Spectroelectrochemistry

IR-SEC of the complexes was performed under argon and CO$_2$ in order to observe the reductive chemistry and catalysis of the complexes. It was felt especially important to gather spectroelectrochemistry of the Re mesBIAN complex as this had not previously been reported.

Assignment of the species was performed via comparisons to literature sources[12,26,27,28,29]; unfortunately it was not possible to perform computational modelling of complexes due to time constraints. During the experiments a slight shift in peak position was observed under CO$_2$ as compared to samples run under argon, we believe this was due to either slight changes in the water concentration of the solvent after saturating with CO$_2$ or due to instrument drift.

Table 3.1 confirms that the complex [ReCl(CO)$_3$(4-COOEt-mesBIAN)], containing the electron withdrawing substituted COOEt-mesBIAN, has the strongest metal-carbonyl bonds; as would be expected. In turn the [ReCl(CO)$_3$(4-N$_3$-mesBIAN)] has the weakest metal-carbonyl bonds confirming that the azide moiety acts as an electron donating group.

Figure 3.13 (left) shows IR spectra taken during the thin layer reduction of Re mesBIAN under argon in an OTTLE cell. Upon first reduction the one electron reduced complex [ReCl(CO)$_3$(NN)]$^{\cdot-}$ is formed and a metastable population is observed. The one electron reduced complex is not stable however and gradually the chloride is eliminated forming the acetonitrile coordinated radical complex [Re(CO)$_3$(CH$_3$CN)(NN)]$^{\cdot}$. As the potential is lowered further more of the acetonitrile coordinated radical complex is observed as compared to the one electron reduced complex, in contrast to what has been reported for [ReCl(CO)$_3$(bipyridine)] no dimer is observed in the IR-SEC traces following formation of the radical complex, this is unsurprising due to the enormous steric bulk of the mesityl moieties. Following formation of the acetonitrile coordinated radical complex and upon further lowering of the potential the acetonitrile coordinated anion is formed which in turn forms the five-coordinate anion.
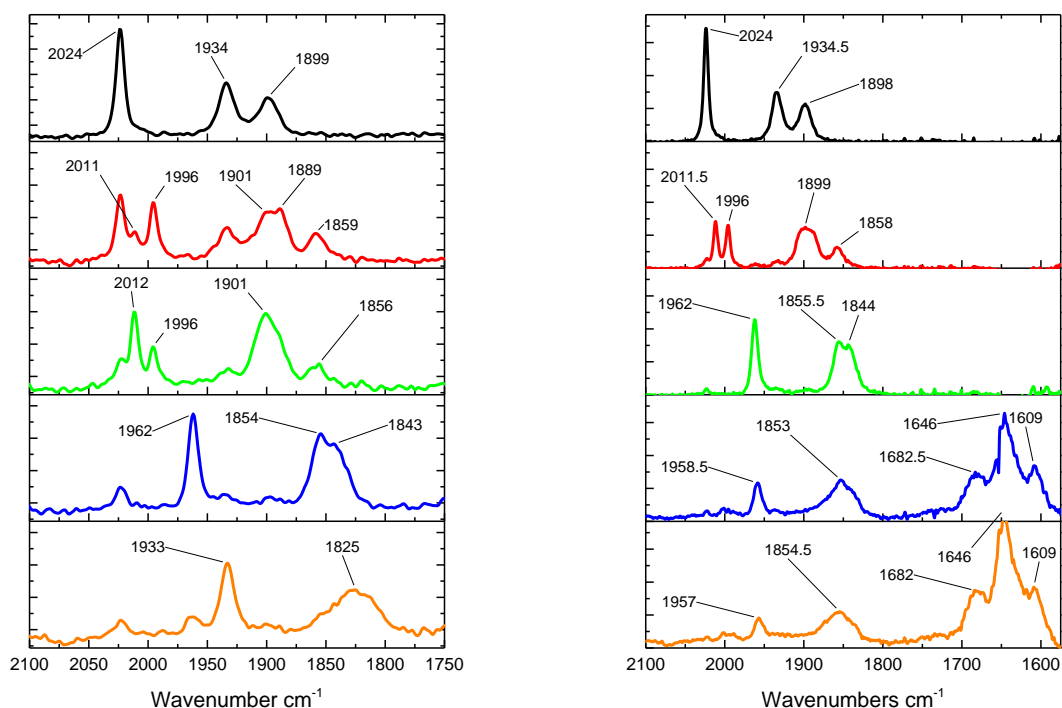
Figure 3.13 IR-SEC traces of Re mesBIAN under argon (left) and CO$_2$ (right) performed in Grubbs dried acetonitrile in the presence of 0.3 M [Bu$_4$N][PF$_6$].

Under CO$_2$ the complex behaves in an identical fashion during the early part of the reduction forming the one electron reduced complex, acetonitrile coordinated radical complex and the acetonitrile coordinated anion in the same manner as under argon, however, as soon as the acetonitrile dissociates from the anion it rapidly coordinates CO$_2$ forming a CO$_2$ associated species.

Parent complex

+ e⁻

One electron reduced complex

Acetonitrile coordinated radical complex

+ e⁻

Acetontrile coordinated anion

CO₂

CO₂ associated bicarbonate complex

Argon

Five-coordinate anion
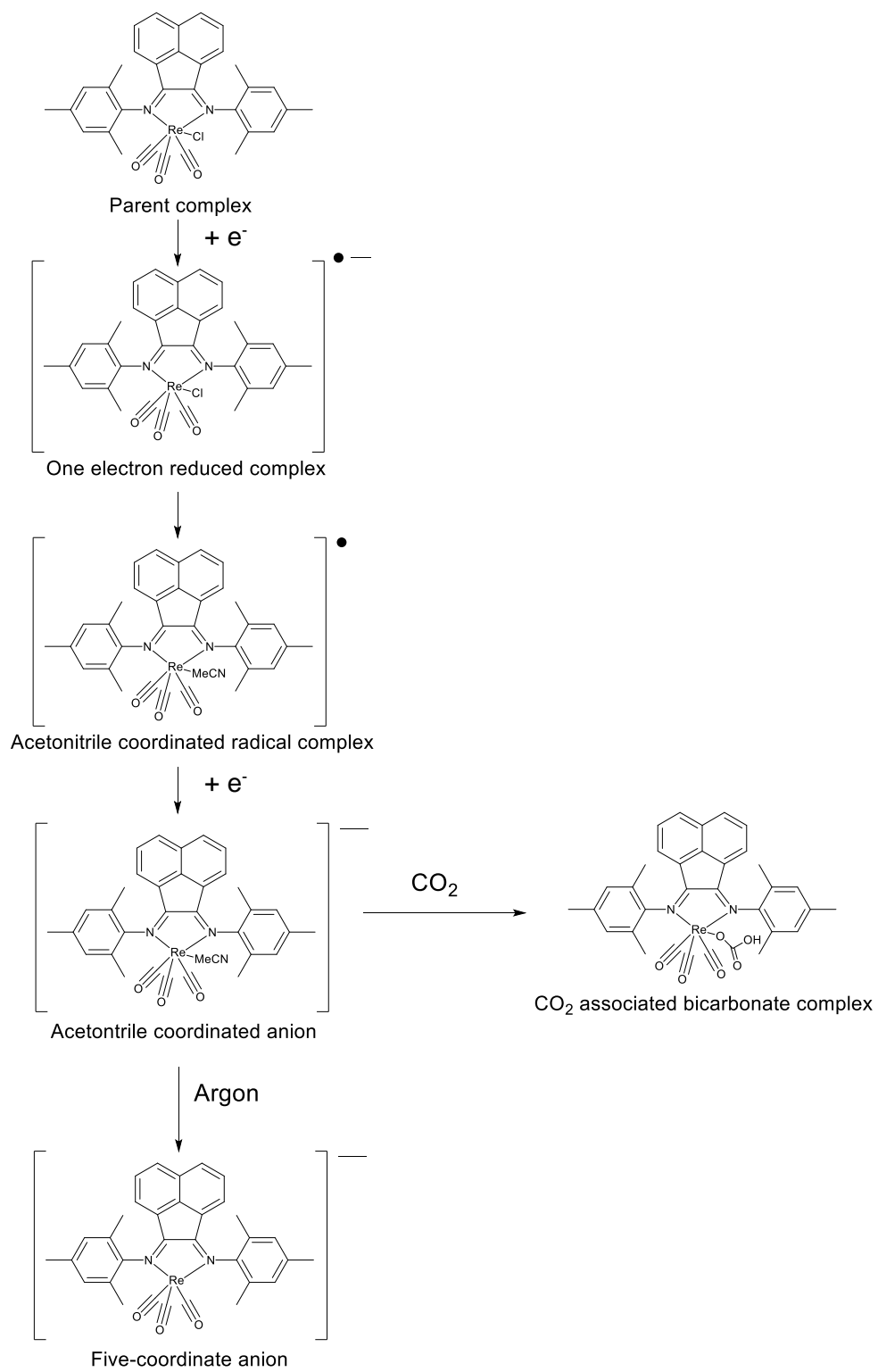
The reduction pathway for Re mesBIAN under argon and CO_2 are shown in scheme 3.2 and the results are very similar to what has been observed with [ReCl(CO)₃(bpy)] which also forms the acetonitrile coordinated radical complex and acetonitrile coordinated anion.[12] It is not surprising that the concentration of the acetonitrile coordinated anion is much higher with respect to the five-coordinate anion since acetonitrile is a relatively soft base and coordinates well to the rhenium centre.
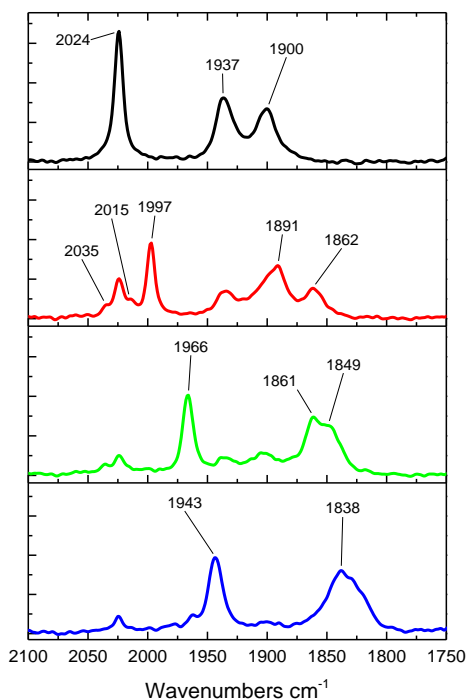
Re mesBIAN-COOEt
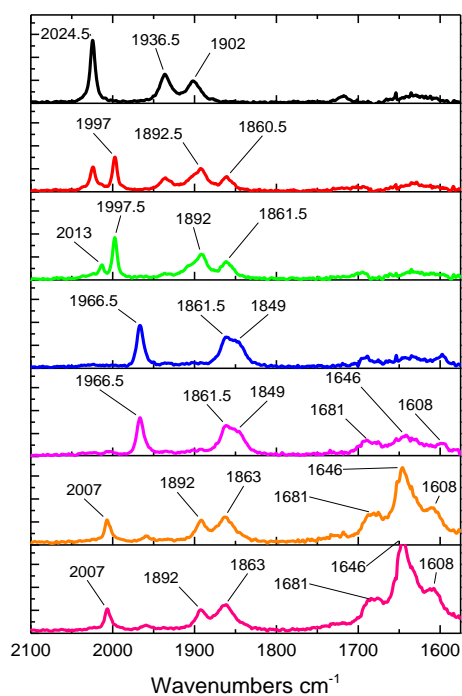
Re mesBIAN-COOEt
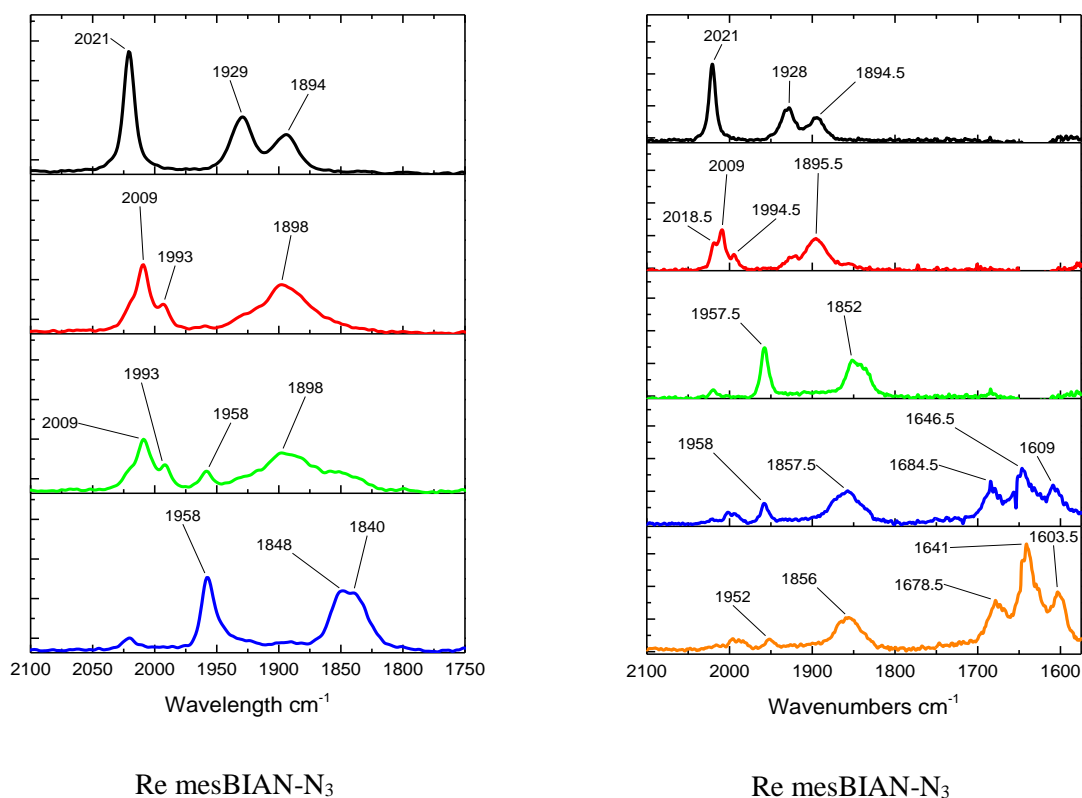
Figure 3.14 IR-SEC traces of Re mesBIAN-COOEt (top) and Re mesBIAN-N$_3$ (bottom) under argon (left) and CO$_2$ (right) performed in Grubbs dried acetonitrile in the presence of 0.3 M [Bu$_4$N][PF$_6$].

The spectra shown in figure 3.14 show that Re mesBIAN-COOEt and Re mesBIAN-N$_3$ follow the same reaction pathway as that outlined in scheme 3.2 and so it can be seen that functionalisation of the mesBIAN moiety does not result in changes in the electrochemical behaviour.

There are two peaks observed in the spectra that do not appear to be apparent in the spectra of Re mesBIAN, those being the peak under argon at 2035 cm^{-1} for Re mesBIAN-COOEt and at 2018.5 cm^{-1} for Re mesBIAN-N$_3$ under CO$_2$. It is possible that the peak observed at 2018.5 cm^{-1} is simply due to the parent complex with the maximum absorption shifted slightly due to the concomitant growth of the acetonitrile coordinated radical complex. The small peak at 2035 cm^{-1} might be due to a small amount of aqua complex being formed [Re(CO)$_3$(H$_2$O)(mesBIAN-COOEt)]$^+$ as a peak in a similar location was observed in manganese analogues of the Lehn catalyst.[30]

Table 3.1 Carbonyl stretching frequencies of species observed in the spectroelectrochemistry experiments.

[ReCl(CO)$_3$(mesBIAN)]	cm^{-1}	cm^{-1}	cm^{-1}
parent	2024	1934	1899
[ReCl(CO)$_3$(NN)]$^{\bullet-}$	1996	1889	1859
[Re(CO)$_3$(CH$_3$CN)(NN)]$^{\bullet}$	2011	1901	
[Re(CO)$_3$(CH$_3$CN)(NN)]$^-$	1962	1854	1843
[Re(CO)$_3$(NN)]$^-$	1933	1825	
under CO$_2$			
parent	2024	1934.5	1898
[ReCl(CO)$_3$(NN)]$^{\bullet-}$	1996	1858	
[Re(CO)$_3$(CH$_3$CN)(NN)]$^{\bullet}$	2011.5	1899	
[Re(CO)$_3$(CH$_3$CN)(NN)]$^-$	1962	1855.5	1844
CO$_2$ associated complex	1957	1854.5	
bicarbonate and formate	1682	1646	1609
[ReCl(CO)$_3$(mesBIAN-COOEt)]	**cm^{-1}**	**cm^{-1}**	**cm^{-1}**
parent	2024	1937	1900
[ReCl(CO)$_3$(NN)]$^{\bullet-}$	1997	1891	1862
[Re(CO)$_3$(CH$_3$CN)(NN)]$^{\bullet}$	2015?	2035?	
[Re(CO)$_3$(CH$_3$CN)(NN)]$^-$	1966	1861	1849
[Re(CO)$_3$(NN)]$^-$	1943	1838	
under CO$_2$			
parent	2024.5	1936.5	1902
[ReCl(CO)$_3$(NN)]$^{\bullet-}$	1997	1892.5	1860.5
[Re(CO)$_3$(CH$_3$CN)(NN)]$^{\bullet}$	2013		
[Re(CO)$_3$(CH$_3$CN)(NN)]$^-$	1966.5	1861.5	1849
CO$_2$ associated complex	2007	1892	1863
bicarbonate and formate	1681	1646	1608
[ReCl(CO)$_3$(mesBIAN-N$_3$)]	**cm^{-1}**	**cm^{-1}**	**cm^{-1}**
parent	2021	1929	1894
[ReCl(CO)$_3$(NN)]$^{\bullet-}$	1993	1898 (v br)	
[Re(CO)$_3$(CH$_3$CN)(NN)]$^{\bullet}$	2009	1897	
[Re(CO)$_3$(CH$_3$CN)(NN)]$^-$	1958		
[Re(CO)$_3$(NN)]$^-$	1958	1848	1840
under CO$_2$			
parent	2021	1928	1894.5
[ReCl(CO)$_3$(NN)]$^{\bullet-}$	1994.5	1895.5	
[Re(CO)$_3$(CH$_3$CN)(NN)]$^{\bullet}$	2009		
[Re(CO)$_3$(CH$_3$CN)(NN)]$^-$	1957.5	1852	
CO$_2$ associated complex	1958	1857.5	
bicarbonate and formate	1878.5	1641	1603.5

3.3.2.3 Evaluation of electrocatalytic performance

The accurate determination of the electrocatalytic performance of homogenous CO_2 reduction catalysts in extremely challenging and much time and effort was taken in an attempt to make accurate estimates with little success (see chapter 8). In order to provide estimates of the relative catalytic performance estimation of efficiency from CV data was done by relative i_{cat}/i_p values following the method described by Kubiak *et al.*[31,32] comparing the current values detected in the cathodic wave CV at -2.2 V (vs Fc/Fc$^+$) in acetonitrile saturated with N_2 and CO_2 with added water at 0.1 Vs^{-1}. Due to the reduced current observed under CO_2 as compared to N_2 the values compared were those under CO_2 with water/ CO_2. Also shown is the current enhancement at -2.67 V vs Fc/Fc$^+$ where the current enhancement is that taken between from the cathodic wave under CO_2 with water over the current collected under CO_2.

As expected the Re mesBIAN-N_3 out performs the other catalysts explored under identical conditions this is most likely due to the electron donating azide moiety proving a more nucleophilic rhenium centre.[33] What is especially unusual is that Re mesBIAN-COOEt also significantly out performs the unsubstituted Re mesBIAN which is contrary to what is expected based on the results obtained by Kubiak *et al.* with similar rhenium bipyridine complexes.[33]

Table 3.2 ratio of catalytic current to peak current over inert atmosphere

Complex	$\frac{i_{cat}}{i_p}$ at -2.2 V vs Fc/Fc$^+$	$\frac{i_{cat}}{i_p}$ at -2.67 V vs Fc/Fc$^+$
[ReCl(CO)$_3$(mesBIAN)]	1.53	2.56
[ReCl(CO)$_3$(mesBIAN-COOEt)]	2.16	5.30
[ReCl(CO)$_3$(mesBIAN-N_3)]	3.98	14.30

It was suggested by Kubiak *et al.* that this increased catalytic current is due to factors other than simply the nucleophilicity of the rhenium as this was also observed in the bipyridine complexes which they had reported in which the most nucleophilic complex [ReCl(CO)$_3$(2,2'-bipyridine-4,4'-OMe)] showed no catalytic activity.

It is my suggestion that the catalyst efficiency is not due simply to the degree of electron donating ability of the diimine ligand but rather due to the unwillingness of the 5-coordinate anion to undergo back donation into the carbonyls. This is because there is a very clear relationship between increased $\frac{i_{cat}}{i_p}$ ratio and the carbonyl stretching frequency of the 5-coordinate anion which is the species that actually acts as the catalyst for CO_2 reduction, this relationship is summarised in table 3.3.

Table 3.3 carbonyl stretching frequencies and $\frac{i_{cat}}{i_p}$ ratio of the 5-coordinate anion and parent complex.

Complex	Parent complex / cm^{-1}	5-coordinate anion / cm^{-1}	$\frac{i_{cat}}{i_p}$ at -2.2 V
[ReCl(CO)$_3$(mesBIAN)]	2024, 1934, 1899	1933, 1825	1.53
[ReCl(CO)$_3$(mesBIAN-COOEt)]	2024, 1937, 1900	1943, 1838	2.16
[ReCl(CO)$_3$(mesBIAN-N$_3$)]	2021, 1929, 1894	1958, 1848, 1840	3.98

In many ways this observation makes sense as less back donation means that there will be greater electron density available on the rhenium centre resulting in a more nucleophilic metal centre. However, why the ester substituted mesBIAN is able to outperform the unsubstituted mesBIAN still remains mysterious.

It is certainly reasonable to say that the three Re mesBIAN complexes do not provide proof of this concept and an iterative study investigating this concept was performed in chapter 6.

3.4 Conclusions

The Rhenium mesBIAN complexes have shown that they are not photocatalytic and this appears to be due the triplet MLCT state not being sufficiently oxidising to be reduced by the sacrificial electron donor. All three of the complexes are however electrocatalytically active with the azide substituted mesBIAN complex having the largest observed current enhancement. Surprisingly the current enhancement observed for the Re mesBIAN-COOEt was greater than that of the Re mesBIAN which is contrary to what has been observed before. A correlation between greater current enhancement and the stronger carbonyl bonds of the 5-coordinate anion (the active catalytic species in the reduction of CO_2) was observed and this has been rationalised as greater electron density being available on the rhenium centre resulting in a more nucleophilic species.

IR-SEC investigations confirmed that no dimer is formed during the reduction under argon or CO_2 and that the 5-coordinate anion is reached via an acetonitrile coordinated complex.

3.5 References

(1)   Taylor, A. L.; Dessai, S.; Bruine de Bruin, W. *Clim. Risk Manag.* **2014**, *4–5*, 1–16.

(2)   Ratter, B. M. W.; Philipp, K. H. I.; von Storch, H. *Environ. Sci. Policy* **2012**, *18*, 3–8.

(3)   van der Linden, S. *J. Environ. Psychol.* **2015**, *41*, 112–124.

(4)   Gray, H. B. *Nat. Chem.* **2009**, *1*, 7.

(5)   Armaroli, N.; Balzani, V. *Chem. - A Eur. J.* **2016**, *22*, 32–57.

(6)   Herron, J. A.; Kim, J.; Upadhye, A. A.; Huber, G. W.; Maravelias, C. T. *Energy Environ. Sci.* **2015**, *8* (1), 126–157.

(7)   Hawecker, J.; Lehn, J.; Ziessel, R. *J. Chem. Soc., Chem. Commun.* **1983**, 536–538.

(8)   Hawecker, J.; Lehn, J.-M.; Ziessel, R. *J. Chem. Soc, Chem. Commun.* **1984**, 328–330.

(9)   Portenkirchner, E.; Fh, D. I.; Di, K. O. **2013**, *2*, 134–147.

(10)   Takeda, H.; Koizumi, H.; Okamoto, K.; Ishitani, O. *Chem. Commun. (Camb).* **2014**, *50* (12), 1491–1493.

(11)   Hori, H.; Johnson, F. P. A.; Koike, K.; Ishitani, O.; Ibusuki, T. *J. Photochem. Photobiol. A Chem.* **1996**, *96*, 171–174.

(12)   Johnson, F. P. A.; George, M. W.; Hartl, F.; Turner, J. J. *Organometallics* **1996**, *15* (15), 3374–3387.

(13)   Kurz, P.; Probst, B.; Spingler, B.; Alberto, R. *Eur. J. Inorg. Chem.* **2006**, 2966–2974.

(14)   Rossenaar, B. D.; Lindsay, E.; Stufkens, D. J.; Vlcek, A. *Inorganica Chim. Acta* **1996**, *250*, 5–14.

(15)   Archer, S.; Weinstein, J. A. *Coord. Chem. Rev.* **2012**, *256* (21–22), 2530–2561.

(16)   Lakowicz. *Principles of Fluorescence Spectroscopy*, 2nd Editio.; Springer Science+Buisness Media: New York, 1999.

(17)   Knor, G.; Leirer, M.; Vogler, A. *J. Inf. Rec.* **1998**, *24* (1–2), 69–73.

(18)   Knör, G.; Leirer, M.; Keyes, T. E.; Vos, J. G.; Vogler, A. *Eur. J. Inorg. Chem.* **2000**, *2000* (4), 749–751.

(19)   Portenkirchner, E.; Kianfar, E.; Sariciftci, N. S.; Knör, G. *ChemSusChem* **2014**, *7* (5), 1347–1351.

(20)   Rossenaar, B. D.; Stufkens, D. J.; Vlcek, A. J. *Inorg. Chem.* **1996**, *35*, 2902–2909.

(21)   Archer, S. The Synthesis and Photophysical Properties of Light-Harvesting Platinum (II) Diimine Acetylides, 2015.

(22)   Wong, H. L.; Lam, L. S. M.; Cheng, K. W.; Man, K. Y. K.; Chan, W. K.; Kwong, C. Y.; Djurišić, A. B. *Appl. Phys. Lett.* **2004**, *84* (14), 2557–2559.

(23)   Smieja, J. M.; Kubiak, C. P. *Inorg. Chem.* **2010**, *49* (20), 9283–9289.

(24)   Micic, O.; Cercek, B. *J. Phys. Chem.* **1977**, *81* (9), 833–837.

(25)   Takeda, H.; Koike, K.; Morimoto, T.; Inumaru, H.; Ishitani, O. *Adv. Inorg. Chem.* **2011**, *63*, 137–186.

(26)   Christensen, P.; Hamnett, A.; Muir, A. V. G.; Timney, J. A. *J. Chem. Soc. Dalt. trans* **1992**, 1455–1463.

(27)   Rossenaar, B. D.; Graaf, T. van der; Eldik, R. van; Langford, C. H.; Stufkens, D. J.; Vlcek, A. J. *Inorg. Chem.* **1994**, *33* (13), 2865–2873.

(28)   Rossenaar, B. D.; Kleverlaan, C. J.; Van de, M. C. E. van de; Stufkens, D. J.; Oskam, A.; Fraanje, J.; Goubitz, K. *J. Organomet. Chem.* **1995**, *493*, 153–162.

(29)   Stor, G. J.; Hartl, F.; Outersterp, J. W. M. Van; Stufkens, D. J. *Organometallics* **1995**, *14* (3), 1115–1131.

(30)   Spall, S. J. P.; Keane, T.; Tory, J.; Cocker, D. C.; Adams, H.; Fowler, H.; Meijer, A. J. H. M.; Hartl, F.; Weinstein, J. A. *Inorg. Chem.* **2016**, *3*, acs.inorgchem.6b01477.

(31)   Smieja, J. M.; Benson, E. E.; Kumar, B.; Grice, K. A.; Seu, C. S.; Miller, A. J. M.; Mayer, J. M.; Kubiak, C. P. *Proc. Natl. Acad. Sci. USA* **2012**, *109* (39), 15646–15650.

(32)   Smieja, J. M.; Sampson, M. D.; Grice, K. A.; Benson, E. E.; Froehlich, J. D.; Kubiak, C. P. *Inorg. Chem.* **2013**, *52* (5), 2484–2491.

(33)   Smieja, J. M.; Kubiak, C. P. *Inorg. Chem.* **2010**, *49* (20), 9283–9289.

4. Probing sterically and electronically sensitive systems: a 'lab-mouse' approach.

4.1.1 Introduction

There are many chemical systems where it would be desirable to investigate the effect of changing steric or electronic properties of ligands[1] in order to study the resulting effects on the catalytic properties of the metal complexes. However, if we were to introduce a strongly inductive moiety such as tertiary butyl group to our hypothetical system, we would also be introducing a strongly sterically hindering group and as such it may be difficult to separate these two factors when analysing the results. It is therefore important to attempt to separate steric effects of the substituents from their electronic effects when choosing ligands for such investigations. As a model system the Lehn type catalyst[2,3] has been chosen to investigate whether steric and electronic factors can be separated when studying a catalytic system which is sensitive to both steric and electronic effects.[4] A family of asymmetric α-diimines (shown in figure 4.1) in which steric and electronic effects are decoupled was chosen for comparison to bipyridine based analogues with an aim to determine whether such ligands have potential as "lab mice" for investigating systems where it is desirable to separate steric and electronic effects.
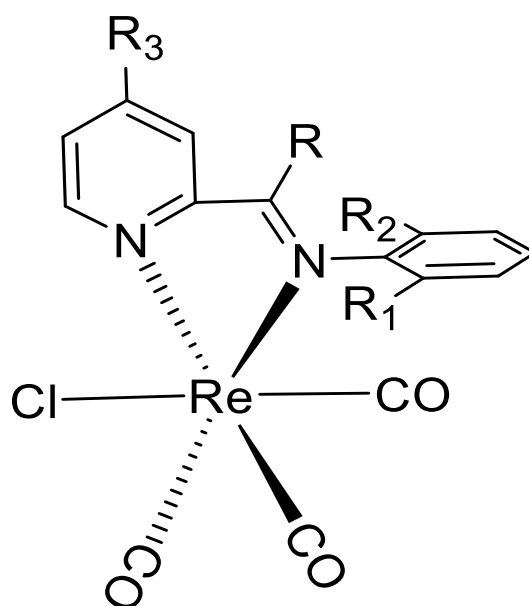
Figure 4.1 General structure of the rhenium complexes with asymmetric α-diimine ligand studied. Naming of the complexes shows the most pertinent aspects of the names of the ligands, for example 2-[(2,-tertiarybutylphenylimino)ethyl]pyridine is abbreviated to TBIEP with TB representing tertiary butyl, I for imino, E indicating ethyl and pyridyl being represented by P, therefore all of the ligands that have a methyl-substituted backbone have E as the penultimate letter in the abbreviation and those that have a hydrogen-substituted backbone have an M representing methyl.[5]

Rhenium tricarbonyl α-diimines are a well-known and studied species of electrochemical and photochemical CO_2 reduction catalyst[2,3] first reported by Hawecker *et al.* in 1983. The archetypal

catalyst ([ReCl(CO)$_3$(bpy)] is highly CO selective with no H$_2$ or formate generation[6] (in contrast to other catalysts[7,8,9]).

Electrochemical characterization of [ReCl(CO)$_3$(dmbpy)] concluded that the complex can undergo a reversible one-electron reduction to the radical anion as well as a further irreversible reduction to the dianion. In the absence of CO$_2$[10] the former can dimerize to give a metal-metal bonded dimer and the latter undergoes rapid loss of chloride and incorporation of acetonitrile.[11] In order to explain the catalysis observed Sullivan *et al.* in 1985[12] proposed two routes of CO$_2$ reduction; a slower one electron pathway and a faster two electron pathway going through a five coordinate radical and a five coordinate anion respectively[10]. In situations utilizing a coordinating solvent such as MeCN the two electron pathway is dominant as the solvent molecule is able to coordinate to the radical [Re(CO)$_3$(bpy)]$^•$ producing a solvated species [Re(CO)$_3$(bpy)(MeCN)]$^•$ which is then reduced forming the active five coordinate species. Schemes of both of these pathways are shown in chapter 1.

4.1.2 Aims

In this study the electrochemical behavior of two rhenium complexes incorporating either the TBIMP (where R, R$_2$, R$_3$ = H and R$_1$ = tert-butyl) or TBIEP ligands (where R = CH$_3$, R$_2$, R$_3$ = H and R$_1$ = tert-butyl) were compared with the Re-complex of bpy (which should be comparable with TBIMP) and of dmbpy (which should be comparable to TBIEP) complexes. We have chosen to use ligands incorporating a tert-butyl moiety as computational analysis has revealed that incorporating a sterically demanding moiety into the R$_1$ or R$_2$ position results in the inhibition of rotation about the N-C bond and thus, due to the break of the plane of symmetry, the orbital overlap between the diimine and phenyl moieties is reduced even more than would be observed in similar complexes where a proton occupied the R$_1$ or R$_2$ position (see figure 4.2).

The aim of this study is to determine if the asymmetric ligands are comparable to bipyridine in the application of their Re(1) complexes to CO$_2$ reduction. If the electrocatalytic behaviour of the two complexes is similar this would allow us to perform a detailed study of the metal complexes with asymmetric ligands, in order to draw meaningful conclusions about the effect of electron donating/withdrawing groups independent of steric factors, and of steric factors without interference from the electronic factors.

4.2 Experimental

4.2.1 Materials and General Procedures

Pentacarbonylchlororhenium(I) (98 %) was purchased from Acros Organics. Tetrabutylammonium hexafluorophosphate (Sigma-Aldrich) was recrystallized from hot ethanol and dried overnight in a vacuum oven. All solvents (Fisher Scientific, Sigma-Aldrich, VWR) were of HPLC grade or higher and were used without further purification unless otherwise stated. Dry solvents were obtained from a

Grubbs solvent drying system. TBIMP and TBIEP were synthesised by Dr Joseph Gaunt during the course of his PhD and were supplied by Dr Dean Cocker.

4.2.2 Instrumentation and Analysis

2.2.2.1 Nuclear Magnetic Resonance (NMR) Spectroscopy

^{1}H and ^{13}C NMR spectra were recorded using Bruker Avance 400 (DPX-400), Bruker Avance 400, Bruker Avance III HD 400, Bruker Avance III 400 and Bruker Avance III HD 500 spectrometers. Deuterated solvents of spectroscopic grade were purchased from Sigma-Aldrich

4.2.2.2 Mass Spectrometry

High resolution mass spectrometry data were collected using direct infusion Na^{+} ionisation and analysed using time of flight.

4.2.2.3 UV-Visible Absorption Spectroscopy

UV-Visible absorption spectra were recorded on either a Cary 50 Bio spectrophotometer or Cary 5000 UV-VIS-NIR spectrophotometer in solution, in 1 cm path length quartz curvettes.

4.2.2.4 Cyclic Voltammetry

Cyclic voltammetry was performed using a Princeton Applied research VersaSTAT 3 on 0.002 M solutions of each of the asymmetric complexes in 6 cm^{3} of acetonitrile with 0.2 M tetrabutyl ammonium hexafluorophosphate as supporting electrolyte. A glassy carbon working electrode and platinum wire counter electrode were used alongside a 0.1 M KCl Ag/AgCl reference electrode.

The solutions were degassed by bubbling thoroughly with N_2 and a nitrogen atmosphere was maintained over the samples during the experiment. To test for current enhancement the samples were bubbled thoroughly with CO_2 and measurements taken. 0.3 ml of water was then added to each sample to test the effects of adding a Brönsted acid. During these later experiments a CO_2 atmosphere was maintained over the samples during the experiment.

4.2.2.5 Bulk electrolysis

In order to confirm that the complexes were reducing CO_2, 0.05 g of each complex in 60 ml of 91.5 % acetonitrile to 8.5 % H_2O was subjected to controlled potential electrolysis (-1.8 V vs silver wire reference electrode) in a single compartment cell under stirring. Gas samples from the head space were taken at regular intervals using a gas tight syringe and analysed using gas chromatography (H_2 carrier gas) fitted with a thermal conductivity detector.

4.2.2.6 IR-SEC and UV-SEC

In a typical experiment infrared spectroelectrochemistry was performed using a Princeton applied research VersaSTAT 3 potetntiostat. 4 mmol dm^{-3} of the complex in the presence of 0.17 g (0.3 mol dm^{-3}) of $TBAPF_6$ in dry acetonitrile was analyzed using an optically transparent thin-layer spectroelectrochemical cell (OTTLE cell) equipped with Pt minigrid working electrodes, a Ag microwire psudoreference electrode and CaF_2 windows. Samples were prepared in argon atmosphere. IR spectroscopy was performed on a Perkin Elmer Spectrum 1 IR spectrometer. Assignments were made using a combination of literature sources[10,13] and comparison with computational data.

4.2.2.7 Computational Methods

Density functional theory (DFT) calculations were performed using the Gaussian 09 program package.[14] All calculations utilised the global hybrid exchange correlation functional B3LYP,[15,16] a 'mixed' basis set consisting of the SDD basis set as defined in Gaussian for Re and the 6-311G(d,p) basis set for all other atoms.[17,18,19,20] The solvent acetonitrile was included using the Polarizable Continuum Model (PCM) as implemented in Gaussian.[21,22] All species were modelled at the lowest multiplicity appropriate for the electron count and the restricted formalism was used for closed shell cases. An 'ultrafine' integral grid, as defined by Gaussian, was used and all geometries were confirmed as minima by the absence of imaginary frequencies in their vibrational spectra as calculated within the harmonic approximation. The values of vibrational frequencies have been scaled by 0.966 to match experimental υ(CO) of the parent neutral complexes.

4.2.3 Synthesis

4.2.3.1 Synthesis of ReTBIMP

0.84 mmol (0.3 g) $ReCl(CO)_5$ was combined with 0.84 mmol (0.2 g) of TBIMP (see chapter 4 section 4.2.1) and refluxed under aerobic conditions in 20 cm^3 of toluene overnight. Yield 98 %.

^{1}H NMR (400 MHz, $CDCl_3$) δ 9.25 – 9.07 (m, 1H), 8.92 – 8.80 (m, 1H), 8.15 (td, J = 7.8, 1.5 Hz, 1H), 8.01 (d, J = 7.5 Hz, 1H), 7.89 – 7.84 (m, 1H), 7.68 (ddd, J = 7.8, 5.4, 1.4 Hz, 1H), 7.62 – 7.57 (m, 1H), 7.36 – 7.30 (m, 2H), 1.46 (s, 9H). ^{13}C NMR (101 MHz, $CDCl_3$) δ 169.43, 153.49, 139.21, 128.98, 128.88, 128.07, 126.89, 124.64, 77.23, 33.64. Anal. Calcd for ReTBIMP: C, 43.05; H, 3.61; N, 5.02; Cl, 6.35. Found: C, 42.77; H, 3.72; N, 4.90; Cl, 6.57. MS (TOF, +ve): m/z 567 (MNa+)

4.2.3.2 Synthesis of ReTBIEP

0.8 mmol (0.29 g) of ReCl(CO)$_5$ was combined with 0.8 mmol (0.2 g) of TBIEP (see chapter 4 section 4.2.1) and refluxed under aerobic conditions in 20 cm^3 of toluene overnight. Crude yield 83 %. Elemental analysis revieled the recrystalisation in hot ethanol was carried out resulting in a 69 % yield.

^{1}H NMR (400 MHz, CDCl$_3$) δ 9.22 – 9.02 (m, 1H), 8.16 (td, J = 7.8, 1.1 Hz, 1H), 8.05 (d, J = 8.0 Hz, 1H), 7.70 – 7.65 (m, 1H), 7.61 (td, J = 7.1, 2.8 Hz, 1H), 7.37 – 7.30 (m, 1H), 2.42 (t, 1H), 1.56 (t, 1H), 1.41 (t, 3H). ^{13}C NMR (101 MHz, CDCl$_3$) δ 175.50, 156.24, 153.41, 147.35, 138.92, 129.76, 128.38, 127.54, 127.42, 123.58, 36.69, 32.63, 19.89. Anal. Calcd for ReTBIEP: C, 43.05; H, 3.61; N, 5.02; Cl, 6.35. Found: C, 42.77; H, 3.46; N, 4.85; Cl, 6.20. MS (TOF, +ve): m/z 581(MNa+)

4.2.3.3 Synthesis of [ReCl(CO)$_3$(bpy)] (Rebpy)

0.256 mmol (0.0926g) of ReCl(CO)$_5$ was combined with 0.257 mmol (0.04 g) 2,2'-bipyridine and refluxed under aerobic conditions in 15 cm^3 of toluene overnight. Quantitate yield. ^{1}H NMR (400 MHz, CDCl$_3$) δ 9.09 (ddd, J = 5.5, 1.5, 0.8 Hz, 2H), 8.21 (d, J = 8.1 Hz, 2H), 8.09 (td, J = 7.9, 1.6 Hz, 2H), 7.56 (ddd, J = 7.6, 5.5, 1.3 Hz, 2H). ^{13}C NMR (101 MHz, CDCl$_3$) δ 155.67, 153.31, 138.92, 127.18, 123.03.

4.2.3.4 Synthesis of [ReCl(CO)$_3$(dmbpy)] (Redmbpy)

0.217 mmol (0.078g) of ReCl(CO)$_5$ was combined with 0.217 mmol (0.04 g) 4,4'-dimethyl-2,2'-bipyridine and refluxed under aerobic conditions in 15 cm3 of toluene overnight. Quantative yield. 1H NMR (400 MHz, CDCl$_3$) δ 8.88 (d, J = 5.7 Hz, 1H), 7.97 (s, 1H), 7.32 (dt, J = 13.4, 6.7 Hz, 1H), 2.57 (s, 3H). ^{13}C NMR (101 MHz, CDCl$_3$) δ 155.44, 152.62, 151.19, 127.90, 123.73, 21.67.

4.3 Results and Discussion

4.3.1 Computational Investigations

Density Functional Theory calculations were provided by Dr Theo Keane, Department of Chemistry, University of Sheffield.

The aim of the calculations was to confirm that the asymmetric ligands would adopt a perpendicular geometry in solution and if so that such a geometry would result in minimised orbital overlap between the pyridine and phenyl moieties.

We hypothesised that in the asymmetric ligands the phenyl group should lie out of the plane of the diimine resulting in electronic decoupling between these two moieties. If the phenyl group is not participating in either the HOMO or the LUMO by altering the substituents on the

phenyl group it should be possible to incorporate steric bulk[23] into the molecular system without affecting the HOMO-LUMO energy gap.
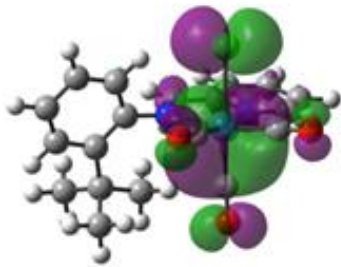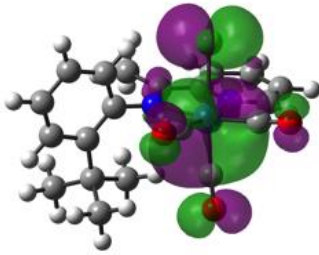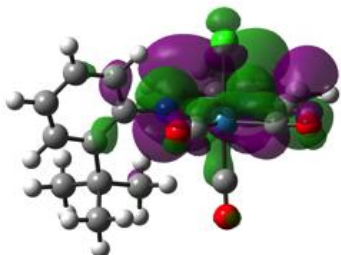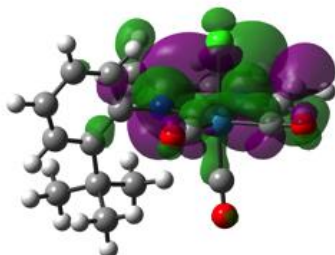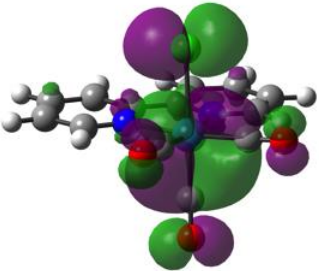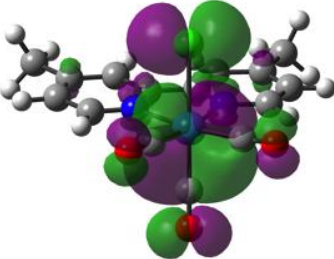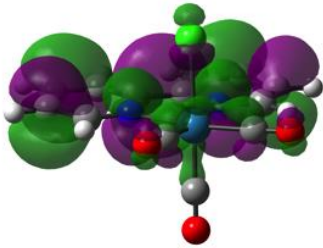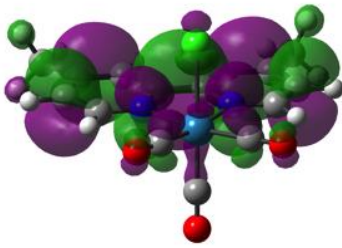
HOMO: ε = -6.35 eV	HOMO: ε = -6.30 eV
LUMO: ε = -3.05 eV	LUMO: ε = -2.87 eV
ReTBIMP HOMO (top) and LUMO (bottom)	ReTBIEP HOMO (top) and LUMO (bottom)
HOMO: ε = -6.26 eV	HOMO: ε = -6.21 eV
LUMO: ε = -2.72 eV	LUMO: ε = -2.62 eV
Rebpy HOMO (top) and LUMO (bottom)	Redmbpy HOMO (top) and LUMO (bottom)

Figure 4.2 DFT calculations of the HOMO (upper image) and LUMO (lower image) of ReTBIMP and ReTBIEP (Dr T Keane). See text for details.

Figure 4.2 shows DFT calculations of ReTBIMP, ReTBIEP and their complementary bipyridine complexes Rebpy and Redmbpy. As can be seen the HOMO of the asymmetric complexes lies extensively over the diimine, carbonyls and the metal centre with no contribution from the phenyl moiety. The LUMO is similar although there is some small contribution from the phenyl group on the 2 and 6 carbons; this is unfortunate as these are the positions most likely to be functionalised. The major contribution to the LUMO, however, lies on the alpha diimine, pyridyl and metal centre meaning that the contribution should be limited. This means the chosen ligands provide as near to total separation as is practically possible between the sterically demanding substituents on the R_1 and R_2 positions of the phenyl and the R & R_3 substituent which contributes directly to the HOMO and the LUMO. Thus changing the R or R_3 groups would affect the HOMO-LUMO gap without affecting the steric properties, whilst changing R_1 or R_2 groups should affect the electronic properties to a very minimal degree but will have considerable effects upon the steric properties of the molecule and accessibility of the metal centre to solvent molecules and dissolved CO_2. By contrast the LUMO of the bipyridine complexes lies extensively over both the pyridine ring.

Calculations revealed that the HOMO and HOMO-1 of the asymmetric complexes are relatively close in energy and therefore both a HOMO-1 to LUMO and a HOMO to LUMO transition may be possible. The HOMO, HOMO-1, LUMO and LUMO+1 are all located exclusively over the metal centre and α-diimine meaning transitions of this nature should also be decoupled from the steric controlling phenol moiety. The HOMO-2 is partially located over the phenyl moiety, however, the *ca.* 0.4 eV gap between the HOMO and HOMO-2 means that the HOMO-2 is unlikely to participate in the redox processes relevant to catalysis. A full set of orbitals and relative energy levels are shown as an appendix for this chapter for both the asymmetric complexes and bipyridine complexes. The results of the DFT calculations show that the electronic structure of the asymmetric complexes are very similar to those of their bpy analogues; the HOMO localises mostly over the metal, halogen and carbonyls whilst the LUMO lies mostly over the diimine. The trends in energy levels of the HOMO-LUMO between Rebpy and Redmbpy are also seen between ReTBIMP and ReTBIEP; both ReTBIEP and Redmbpy have MO's at lower energy than ReTBIMP and Rebpy and both ReTBIEP and Redmbpy have a greater HOMO-LUMO energy gap than ReTBIMP and Rebpy.

The computational results so far support the hypothesis that ReTBIMP and ReTBIEP are suitable as analogues for Rebpy and Redmbpy due to the similarities in their frontier orbital origin and energy gaps.

4.3.2 Comparison of the spectroscopic properties of ReTBIEP and ReTBIMP with Rebpy and Redmbpy

Figure 4.3 shows normalised absorption spectra of the four complexes. DCM has been used as the solvent of choice for spectroscopy due to the much greater solubility of the complexes in DCM as opposed to acetonitrile. The absorption at <350 nm is likely to correspond to an intraligand π-π* transition(s) and the band at >350 nm is likely an MLCT-XLCT transition(s). As can be seen there is a marked shift to lower energies in the MLCT absorption band of the asymmetric complexes relative to the bpy complexes and a blue shift for the IL bands. It is also clear that the introductionof a Me-group in Redmbpy and ReTBIEP leads to MLCT absorption shift to higher energies due to an the increase in the π* energy of the LUMO of the diimine ligands due to the electron donating methyl groups. Also of note is the small absorption at ca. 325 nm for the asymmetric complexes which we believe may be associated with the phenyl moiety.

Figure 4.3 Normailsed absorption spectra of ReTBIMP, ReTBIEP, Rebpy and Redmbpy in DCM.

In the carbonyl stretching region the IR spectra of the asymmetric complexes exhibit 3 peaks, a single sharp peak at ca. 2024 cm^{-1} and two slightly overlapping broader peaks in the region 1890 to 1930 cm^{-1} (see figures 4.6 and 4.7). Importantly both of the asymmetric rhenium complexes follow the same trend as seen in the bpy complexes with the carbonyl stretching modes being of ReTBIMP occurring at slightly higher energies than those of ReTBIEP. This

is in much the same fashion as the carbonyl stretching modes of Rebpy occur at larger wavenumbers than those of Redmbpy.

Table 4.1 Carbonyl stretching peaks of the complexes recorded in DCM.

Complex	CO $\tilde{v}$ cm^{-1}
Rebpy	2025, 1918, 1902
Redmbpy	2023, 1916, 1899
ReTBIMP	2028, 1926, 1901
ReTBIEP	2023, 1924, 1896

It is clear from computational data as well as the UV and IR spectra that the asymmetric complexes follow the trends of the bipyridine analogues.

4.3.3 Electrochemical behaviour

Cyclic voltammetry was performed in nitrogen saturated acetonitrile under a nitrogen atmosphere in order to compare how the complexes behave upon reduction. As can be seen both ReTBIMP and ReTBIEP are reduced at less negative potentials than their bipyridine analogues but their general reduction profile is quite similar: both show a reversible first reduction followed by an irreversible second reduction in line with what would be expected. The only significant difference is the second reoxidation wave observed in ReTBIMP at ca. -1.2 V vs Fc/Fc$^+$ (which is most likely a solvent coordinated complex that is formed via an ECC process following the first reduction). The shape of the return wave depends on the scan rate: at higher scan rates (see figure 4.5) the intensity of this additional peak diminishes relative to the main re-oxidation process at -1.45 V vs Fc/Fc$^+$, but is still very noticeable. Spectroelectrochemical data (*vide infra*) confirms that formation of acetonitrile coordinated complex is rapid and occurs concurrently with the formation of the one electron reduced radical supporting this hypothesis. It therefore appears that ReTBIMP differs from Rebpy in

that the one electron reduced species is more labile in ReTBIMP than Rebpy.
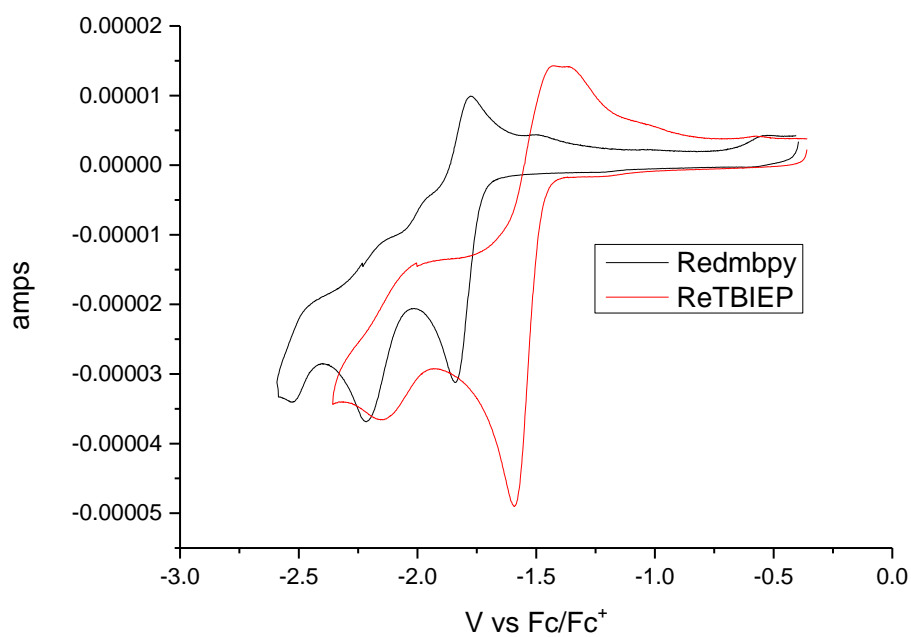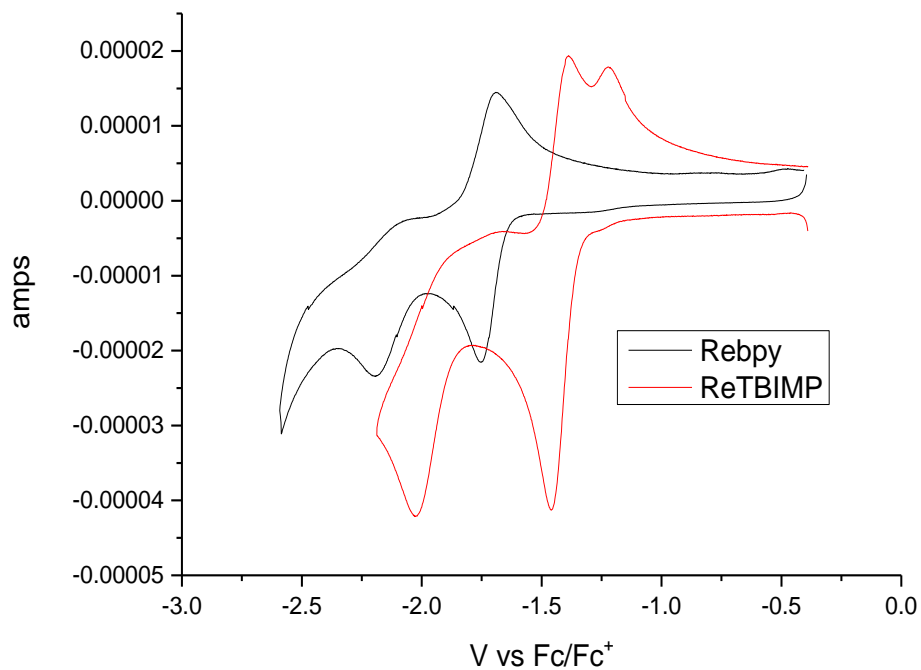
Figure 4.4 CV traces at 0.1 Vs^{-1} of ReTBIMP with Rebpy and ReTBIEP with Rebpy in acetonitrile with 0.2 M TBAPF$_6$ as supporting electrolyte under N$_2$.
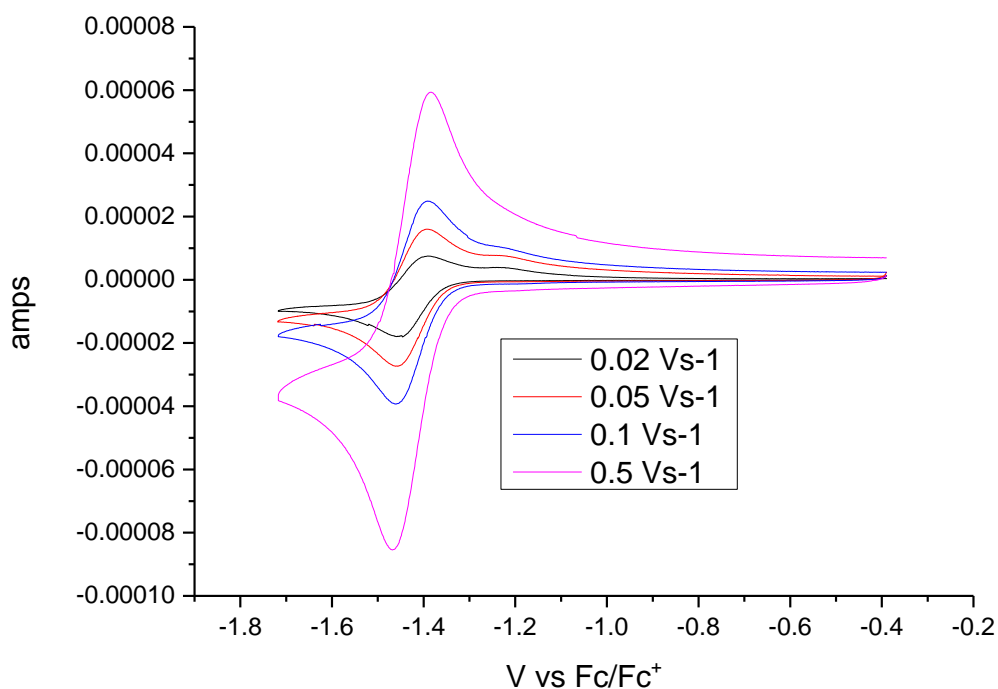
Figure 4.5 CV traces of ReTBIMP in acetonitrile with 0.2 M TBAPF$_6$ as supporting electrolyte, under N$_2$ in the region -0.395 V to -1.795 V vs Fc/Fc$^+$ recorded at 0.1 Vs^{-1}.

In order to investigate whether the asymmetric complexes behave in a similar manner to the bipyridine analogues when reduced, infrared-spectroelectrochemistry was used to observe the intermediates and reduction products that were observed in the cyclic voltammetry. The reduction behaviour of the two asymmetric complexes is almost identical to the bpy analogues with the first reduction involving formation of a radical anion, observed by the growth of the three peaks at slightly lower energy, followed by elimination of the chloride anion and rapid association of a solvent molecule to form a neutral radical complex, observed by the three peaks at intermediate energy between the parent and radical anion complexes.
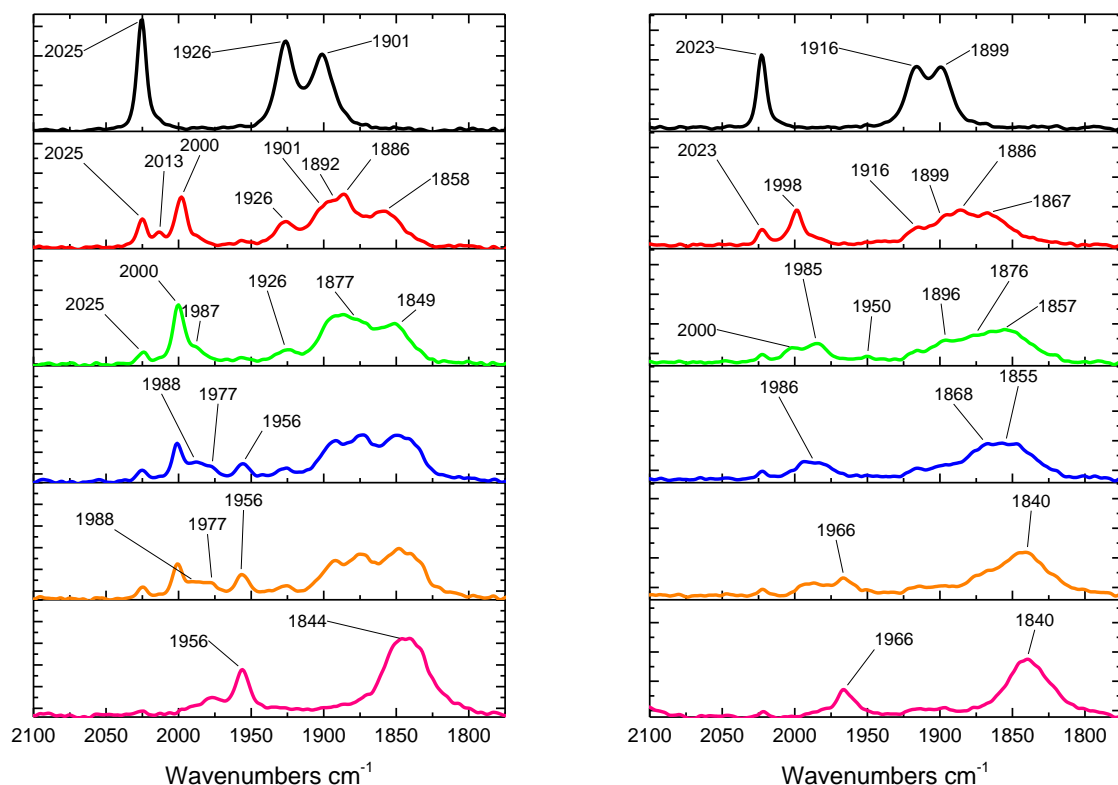
Figure 4.6 IR spectral changes following OTTLE cell reduction of ReTBIMP (left) and Rebpy (right) in acetonitrile solution with TBAPF$_6$ as supporting electrolyte.

Following the coordination of the acetonitrile molecule some of the [Re(CO)$_3$(CH$_3$CN)(TBIMP)]$^\bullet$ appears to dimerize, this can be seen most clearly by the growth of the peak at 1977 as many of the other peaks (determined by computational work) are either partially or wholly masked by bands assigned to other reduced species. This occurs concurrently with the formation of [Re(CO)$_3$(CH$_3$CN)(TBIMP)]$^-$ which leads to the formation of the 5-coordinate anion [Re(CO)$_3$(TBIMP)]$^-$. The 5-coordinate anion is the most recognisable complex with a single peak in the region ca. 1960 cm^{-1} and a very broad low energy peak at ca. 1840 cm^{-1}.

In this respect ReTBIMP's behaviour under reduction is identical to what we have observed for Rebpy. Like its asymmetric analogue it too forms both a dimer and a solvent coordinated anion which eliminates to form 5-coordinate anion. It should be noted here that this is slightly in contrast to what was found by Johnson *et al.*[10] (who performed a similar experiment on Rebpy also in acetonitrile) who observed dimer formation only in THF and not in acetonitrile. We are not sure as to why this may have been case.
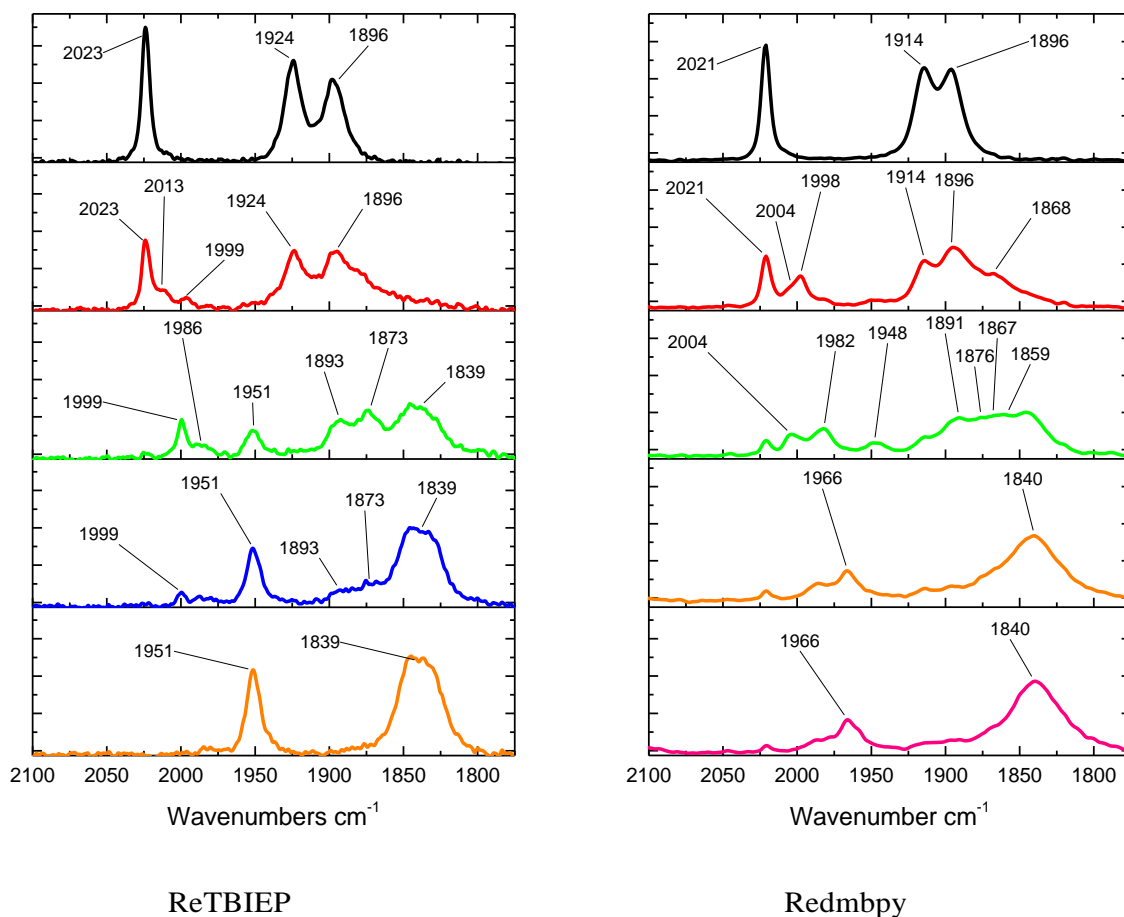
Figure 4.7 IR spectral changes following OTTLE cell reduction of ReTBIEP (left) and Redmbpy (right) in argon saturated acetonitrile solution with TBAPF$_6$ as supporting electrolyte.

Redmbpy behaves in an identical fashion to ReTBIMP and Rebpy matching what was reported by Christensen *et al.*[13], however, unlike ReTBIMP the ReTBIEP does not appear to dimerise upon reduction. This may be due to combination of the t-Bu moiety on the R$_1$ position and the CH$_3$ R moiety creating a more rigid complex which is unable to adopt geometry suitable for dimer formation.

Table 4.1 Vibrational frequencies of species observed in the reduction of the complexes under argon.

Species	Peak position / cm^{-1}
[ReCl(CO)$_3$(TBIMP)]	2025, 1926, 1901
[ReCl(CO)$_3$(TBIMP)]$^{•-}$	2000, 1886, 1858
[Re(CO)$_3$(TBIMP)]$_2$	1988, 1977, 1867, 1886, 1873
[Re(CO)$_3$(TBIMP)(CH$_3$CN)]$^{•}$	2013, 1892 (br), 1886 (br)
[Re(CO)$_3$(TBIMP)(CH$_3$CN)]$^{-}$	1987, 1873, 1849
[Re(CO)$_3$(TBIMP)]$^{-}$	1956, 1844 (br)
[ReCl(CO)$_3$(TBIEP)]	2023, 1924, 1896
[ReCl(CO)$_3$(TBIEP)]$^{•-}$	1999, 1893, 1873
[Re(CO)$_3$(TBIEP)(CH$_3$CN)]$^{•}$	2013*
[Re(CO)$_3$(TBIEP)(CH$_3$CN)]$^{-}$	1986*
[Re(CO)$_3$(TBIEP)]$^{-}$	1951, 1839 (br)
[ReCl(CO)$_3$(bpy)]	2023, 1916, 1899
[ReCl(CO)$_3$(bpy)]$^{•-}$	1998, 1886, 1867
[Re(CO)$_3$(bpy)]$_2$	1985, 1950, 1896, 1876, 1857
[Re(CO)$_3$(bpy)(CH$_3$CN)]$^{•}$	2000, 1895
[Re(CO)$_3$(bpy)(CH$_3$CN)]$^{-}$	1986, 1868, 1855
[Re(CO)$_3$(bpy)]$^{-}$	1966, 1840 (br)
[ReCl(CO)$_3$(dmbpy)]	2021, 1914, 1896
[ReCl(CO)$_3$(dmbpy)]$^{•-}$	1998, 1891, 1868
[Re(CO)$_3$(dmbpy)]$_2$	1978, 1948, 1876*
j[Re(CO)$_3$(dmbpy)(CH$_3$CN)]$^{•}$	2004*
[Re(CO)$_3$(dmbpy)(CH$_3$CN)]$^{-}$	1982, 1867, 1859
[Re(CO)$_3$(dmbpy)]$^{-}$	1966, 1840

*Other peaks are likely present but masked by more intense peaks, computed peaks are shown in appendix to this chapter.

Table 4.2 calculated vibrational frequencies of the asymmetric complexes. These values have been used to assist in the assignment of peaks in observed in spectroelectrochemistry.

Species	Peak position / cm^{-1}
[ReCl(CO)$_3$(TBIMP)]	1904, 1930, 2030
[ReCl(CO)$_3$(TBIMP)]$^{•-}$	1861, 1885, 2000
[Re(CO)$_3$(TBIMP)]$^{-}$	1826, 1836, 1947
[Re(CO)$_3$(TBIMP)(CH$_3$CN)]$^{•}$	1897, 1908, 2016

[Re(CO)$_3$(TBIMP)(CH$_3$CN)]$^-$	Did not converge
[Re(CO)$_3$(TBIMP)]$_2$	1874, 1878, 1884, 1888, 1962, 1985
[ReCl(CO)$_3$(TBIEP)]	1900, 1926, 2028
[ReCl(CO)$_3$(TBIEP)]$^{\cdot-}$	1859, 1882, 1998
[Re(CO)$_3$(TBIEP)]$^-$	1821, 1833, 1943
[Re(CO)$_3$(TBIEP)(CH$_3$CN)]$^{\cdot}$	1893, 1904, 2013
[Re(CO)$_3$(TBIEP)(CH$_3$CN)]$^-$	Did not converge
[Re(CO)$_3$(TBIEP)]$_2$	1863, 1868, 1879, 1881, 1954, 1979

Scaling factor: 0.978

4.3.4 CO$_2$ reduction

As can be seen (*vide supra*) the asymmetric complexes behave very similarly to the bpy analogues in terms of their electrochemical and spectroscopic behaviour and are very good candidates for 'lab mouse compounds' in this regard.

However, in order to prove that the 'lab mouse' approach is an apt method to use for probing sterically and electronically sensitive systems we must prove that the complexes perform the chemistry that is desired of them, in this case CO$_2$ reduction. Figure 4.8 shows CV traces of the two asymmetric complexes under N$_2$, CO$_2$ and CO$_2$ with 0.3 ml of H$_2$O. As can be seen when the solutions are bubbled with CO$_2$ current enhancement of the most negative reduction can be seen which is evidence of CO$_2$ reduction. This current enhancement was increased even further upon the addition of 0.3 ml of water, in particular for ReTBIMP. This behaviour is consistent with what has been reported for the bpy analogues.[4,3,12,24,25]
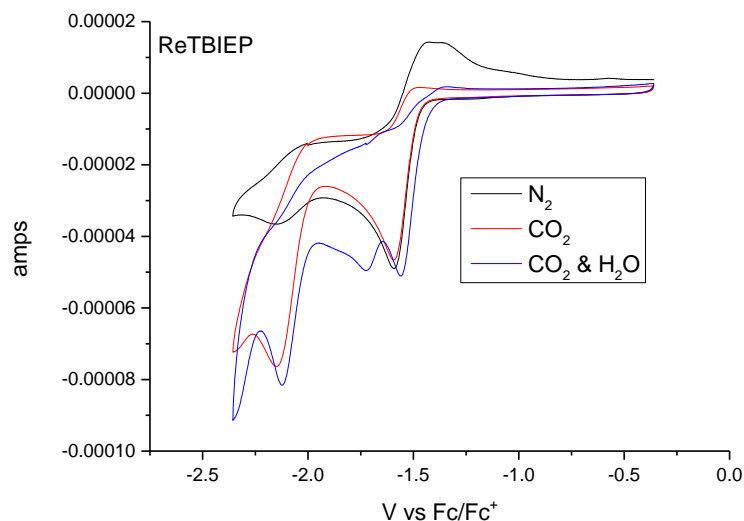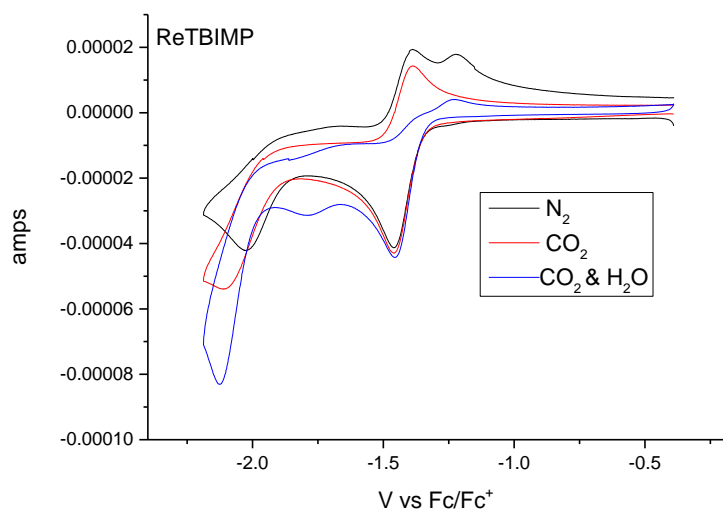
Figure 4.8 CV traces at 0.1 Vs^{-1} of ReTBIMP and ReTBIEP under N$_2$, CO$_2$ and CO$_2$ with 0.3 ml H$_2$O in acetonitrile with 0.2 M TBAPF$_6$ as supporting electrolyte.

In order to confirm that the current enhancement was the result of CO$_2$ reduction head space gas analysis by GC-TCD was performed on bulk electrolysis samples. The results demonstrated that CO was produced during the electrolysis with no other products observed in the head apace gas analysis, however, due the necessity of using H$_2$ as a carrier gas it was not possible to determine whether H$_2$ was produced during the electrolysis.
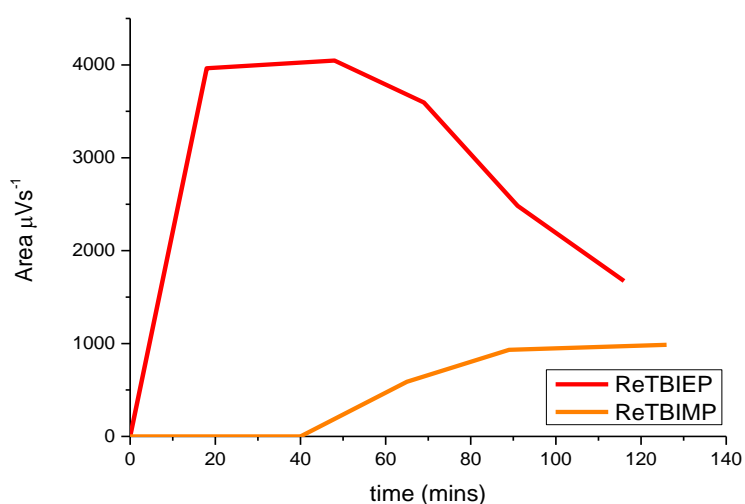
Figure 4.9 GC response of head space gas samples taken from controlled potential (-1.8 V vs Ag wire) electrolysis of 0.05 g of complex in a CO₂ saturated solution of 91.5 % acetonitrile to 8.5 % H₂O (60 ml).

It is worth stressing that the results obtained by GC-TCD cannot be used for quantitative analysis (see chapter 8).
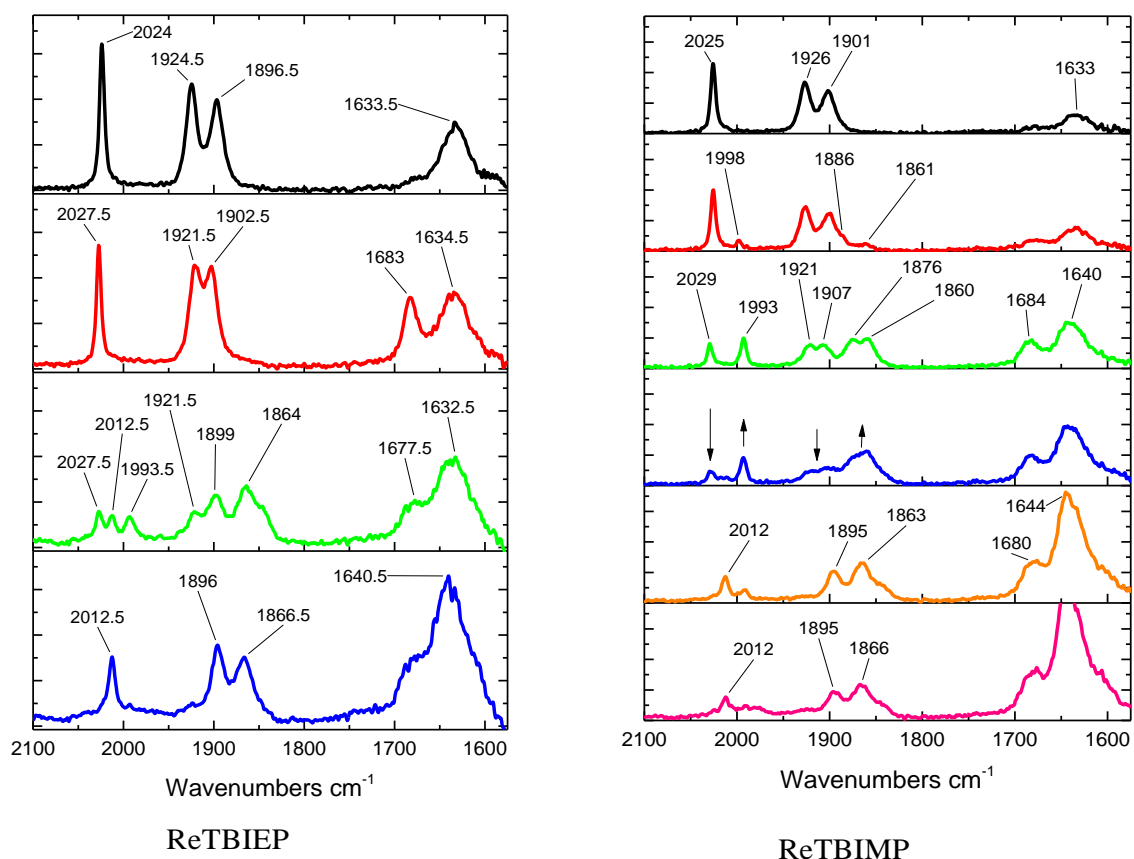
ReTBIEP

ReTBIMP

Figure 4.10 IR spectral changes following OTTLE cell reduction of ReTBIEP (left) and ReTBIMP (right) in CO₂ saturated acetonitrile solution with TBAPF₆ as supporting electrolyte.

Mechanistic insight into the reduction of CO_2 using the asymmetric rhenium catalysts were provided using infra-red spectroelectrochemistry. Despite the use of two drying columns of calcium carbonate, dried alumina, silica gel and magnesium sulphate the saturation of the acetonitrile with bottled CO_2 resulted in the introduction of water into the solution, this is observed as a peak at 1633 cm^{-1}.

The two complexes follow broadly the same reaction pathway, which is to be expected, with the one electron reduced [ReCl(CO)$_3$(TBIMP)]$^{\bullet-}$ being observed at 1998 and 1861 cm^{-1}. Upon reduction in CO_2, unlike under argon, the chloride ion quickly dissociates and is followed by rapid CO_2 coordination (see the growth of the peak at ca. 1680 cm^{-1}). Importantly no five coordinate anion or similar complexes were observed in the IR-SEC experiments under CO_2. This is where the two complexes begin to differ. For the ReTBIEP complex the only observable species upon CO_2 association is the CO_2 associated radical [Re(CO)$_3$(TBIEP)(COOH)]$^{\bullet}$ (2027.5, 1921.5, 1902.5, 1683 cm^{-1}) whereas the ReTBIMP complex forms a mixture of [Re(CO)$_3$(TBIMP)(COOH)]$^{\bullet-}$ (2029, 1921, 1907, 1684 cm^{-1}) and [Re(CO)$_3$(TBIMP)(COOH)]$^{\bullet}$. (1993, 1876, 1860 cm^{-1}). It is only when the potential is lowered further that ReTBIEP forms the CO_2 associated radical anion (1993.5, 1864 cm^{-1}). As can be seen over time the neutral radical complex is converted to the radical anion which in turn is converted to a new complex identified by the peaks at ca. 2012, 1895 and 1866 cm^{-1} for both complexes. This complex was not reported by Johnson *et al.* in their studies of [ReX(CO)$_3$(bpy)] complexes[10] and were are unable to characterise it, however, it is believed to be a stable CO_2 coordinated species that acts as an intermediate in the reduction of CO_2 to CO as its appearance is correlated with the rapid growth of the free bicarbonate peak (characteristic of CO_2 reduction).

4.4 Conclusions

The two new rhenium complexes were synthesised using ligands which result in the decoupling of sterically important and electronically important moieties. We have used these as a proof of concept for the suitability of this ligand family for the 'lab mouse' method of exploring rhenium catalysts i.e. using molecules that may not be as effective catalysts as those we intend to use (although both of these catalysts compare favourably in terms of over potential with Re(CO)$_3$Cl(bpy) and Re(CO)$_3$Cl(dmbpy)) but which allow us to explore the optimised conditions for these catalysts.

Density functional theory was used to confirm that there was no overlap in HOMO or LUMO between the electronically dominant diimine portion of the ligand and the sterically dominant phenyl portion of the molecule.

The behaviour of these molecules was for the most part very similar to their bipyridine analogues exhibiting similar trends in spectroscopy such as position of absorption bands between the methylated and non-methylated ligands and similar electrochemistry.

Compared to the bipyridine complexes the asymmetric ligands appear to have a more labile chloride ligand and the ReTBIEP does not appear to dimerise upon reduction in argon.

Like the bipyridine complexes the asymmetric complexes do reduce CO_2 to CO although spectroelectrochemistry showed that they appear to have a slightly different reduction pathway as compared with the bipyridine complexes.

Overall it appears that complexes offer some potential for examine steric and electronic factors in isolation to each other although their use must be made with some caution if the intention is to use them as a 'lab mouse' complex for investigating bipyridines.

4.5 References

(1)   Bullock, J. P.; Carter, E.; Johnson, R.; Kennedy, A. T.; Key, S. E.; Kraft, B. J.; Saxon, D.; Underwood, P. *Inorg. Chem.* **2008**, *47* (17), 7880–7887.

(2)   Hawecker, J.; Lehn, J.; Ziessel, R. *J. Chem. Soc., Chem. Commun.* **1983**, 536–538.

(3)   Hawecker, J.; Lehn, J.-M.; Ziessel, R. *J. Chem. Soc, Chem. Commun.* **1984**, 328–330.

(4)   Smieja, J. M.; Kubiak, C. P. *Inorg. Chem.* **2010**, *49* (20), 9283–9289.

(5)   Gaunt, J. A. Ligand Effects on Oxidative Addition and Migratory Insertion Reactions of Rhodium Complexes, University of Sheffield, 2003.

(6)   Shinozaki, K.; Hayashi, Y.; Brunschwig, B. S.; Fujita, E. *Res. Chem. Intermed.* **2007**, *33* (1–2), 27–36.

(7)   Takeda, H.; Ishitani, O. *Coord. Chem. Rev.* **2010**, *254*, 346–354.

(8)   Froehlich, J. D.; Kubiak, C. P. *Inorg. Chem.* **2012**, *51* (7), 3932–3934.

(9)   Qiao, J.; Liu, Y.; Hong, F.; Zhang, J. *A review of catalysts for the electroreduction of carbon dioxide to produce low-carbon fuels.*; 2013.

(10)   Johnson, F. P. A.; George, M. W.; Hartl, F.; Turner, J. J. *Organometallics* **1996**, *15* (15), 3374–3387.

(11)   Breikss, I.; Abruna, D. *J. Electroanl. Chem.* **1986**, *201*, 347–358.

(12)   Sullivan, B. P.; Bolinger, C. M.; Conrad, D.; Vining, W. J.; Meyer, T. J. *J. Chem. Soc., Chem. Commun.* **1985**, No. 20, 1414–1416.

(13)   Christensen, P.; Hamnett, A.; Muir, A. V. G.; Timney, J. A. *J. Chem. Soc. Dalt. trans* **1992**, 1455–1463.

(14)   Frisch, M. J.; Trucks, G. W.; Schlegel, H. B.; Scuseria, G. E.; Robb, M. A.; Cheeseman, J. R.; Scalmani, G.; Barone, V.; Mennucci, B.; Petersson, G. A.; Nakatsuji, H.; Caricato, M.; Li, X.; Hratchian, H. P.; Izmaylov, A. F.; Bloino, J.; Zheng, G.; Sonnenberg, J. L.; Hada, M.; Ehara, M.; Toyota, K.; Fukuda, R.; Hasegawa, J.; Ishida, M.; Nakajima, T.; Honda, Y.; Kitao, O.;

Nakai, H.; Vreven, T.; Montgomery Jr., J. A.; Peralta, J. E.; Ogliaro, F.; Bearpark, M.; Heyd, J. J.; Brothers, E.; Kudin, K. N.; Staroverov, V. N.; Kobayashi, R.; Normand, J.; Raghavachari, K.; Rendell, A.; Burant, J. C.; Iyengar, S. S.; Tomasi, J.; Cossi, M.; Rega, N.; Millam, J. M.; Klene, M.; Knox, J. E.; Cross, J. B.; Bakken, V.; Adamo, C.; Jaramillo, J.; Gomperts, R.; Stratmann, R. E.; Yazyev, O.; Austin, A. J.; Cammi, R.; Pomelli, C.; Ochterski, J. W.; Martin, R. L.; Morokuma, K.; Zakrzewski, V. G.; Voth, G. A.; Salvador, P.; Dannenberg, J. J.; Dapprich, S.; Daniels, A. D.; Farkas, Ö.; Foresman, J. B.; Ortiz, J. V.; Cioslowski, J.; Fox, D. J. *Gaussian 09, Revision D.01, Gaussian, Inc., Wallingford CT*. 2013.

(15)   Becke, A. D. *J. Chem. Phys.* **1993**, *98* (7), 5648–5652.

(16)   Lee, C.; Yang, W.; Parr, R. G. *Phys. Rev. B* **1988**, *37* (2), 785–789.

(17)   Nicklass, A.; Dolg, M.; Stoll, H.; Preuss, H. *J. Chem. Phys.* **1995**, *102* (22), 8942–8952.

(18)   Dunning Jr., T. H.; Hay, P. J. Schaefer, H. F., Ed.; Plenum: New York, 1976.

(19)   Krishnan, R.; Binkley, J. S.; Seeger, R.; Pople, J. A. *J. Chem. Phys.* **1980**, *72* (1), 650–654.

(20)   McLean, A. D.; Chandler, G. S. *J. Chem. Phys.* **1980**, *72* (10), 5639–5648.

(21)   Mennucci, B.; Tomasi, J. *J. Chem. Phys.* **1997**, *106* (12), 5151–5158.

(22)   Cossi, M.; Barone, V.; Mennucci, B.; Tomasi, J. *Chem. Phys. Lett.* **1998**, *286* (3–4), 253–260.

(23)   Sampson, M. D.; Kubiak, C. P. *J. Am. Chem. Soc.* **2016**, *138* (4), 1386–1393.

(24)   Hawecker, J.; Lehn, J.; Ziessel, R. *Helv. Chim. Acta* **1986**, *69* (9), 1990–2012.

(25)   Keith, J. A.; Grice, K. A.; Kubiak, P.; Carter, E. A. *J. Am. Chem. Soc.* **2013**, *135*, 15823–15829.

5. Manganese tricarbonyl complexes with asymmetric α-diimine 2-imino-pyridine ligands: towards decoupling steric and electronic factors in electrocatalytic CO_2 reduction.

5.1.1 Introduction

Interest in solar fuels produced using photocatalytic and electrocatalytic methods, in the latter case utilising sustainable electricity, for CO_2 reduction[1] has been increasing markedly in the new millennium due to the threat of global warming and demands for energy security. The recent demonstration of the electrocatalytic activity of manganese[2] analogues of the archetypal Re(I) catalysts[3,4,5] for CO_2 reduction has given a new impetus to research into noble-metal-free catalytic systems and [MnBr(CO)$_3$(α-diimine)] complexes have been shown to outperform rhenium-based analogues with regard to CO_2 reduction under certain conditions.[6] The manganese analogues show some differences compared with the rhenium based Lehn catalysts most notably, the presence of a Brönsted acid[6,7,8] seems to be a prerequisite for catalysis with a range of tricarbonyl Mn α-diimine complexes.[9]

Mechanistic studies[10] of the active 2,2′-bipyridine-based (R-bpy) manganese catalysts[11] have shown that one-electron reduction of the parent complex [MnBr(CO)$_3$(R-bpy)] precursor results in the formation of the Mn–Mn dimer [Mn(CO)$_3$(R-bpy)]$_2$[8,9] and notably, neither the primary reduction product [MnBr(CO)$_3$(R-bpy$^{•-}$)] nor the five-coordinate radical intermediates [Mn(CO)$_3$(R-bpy)]$^{•}$ have been detected by either UV-vis or IR spectroscopy[2,6]. Nanosecond time-resolved infrared (TRIR) studies reveal that unlike most rhenium complexes (see chapter 3 and 4) no detectable solvent adduct is formed before the dimerisation on the timescale of the experiment; instead, the five-coordinate species is observed, which rapidly dimerises[10] by reacting with unreduced parent complex.[9,11] For some of the Re analogues, a one-electron reduced complex, [ReCl(CO)$_3$(R-bpy$^{•-}$)] was observed by IR spectroscopy and identified by the ca. 15-20 cm^{-1} decrease in the ν(CO) energy,[12,13] as was the five-coordinate radical [Re(CO)$_3$(tBu-bpy)]$^{•}$ by an additional 15-20 cm^{-1} shift.

Two mechanisms have been proposed[10,14,15,16,17,18] for the ultimate reduction of [Mn(CO)$_3$(α-diimine)]$_2$ in the presence of CO_2, which can be referred to as the anionic, and the oxidative addition pathways. The anionic pathway involves reduction of the dimer [Mn(CO)$_3$(α-diimine)]$_2$ at a more negative potential than the parent complex generating the five-coordinate anion [Mn(CO)$_3$(α-diimine)]$^-$ to which CO_2 coordinates and is catalytically reduced in the presence of a Brönsted acid (the source of H$^+$).[19] The anionic pathway is broadly similar to the two-electron pathway observed for Re complexes.[18,20] In contrast, the uncommon second pathway identified using pulsed EPR studies[21] involves coordination of CO_2 to the dimer [Mn(CO)$_3$(2,2′-bpy)]$_2$ in the presence of a Brönsted acid in a concerted oxidative addition step. This process generates a low-spin Mn^{II}-COOH complex, from which CO is subsequently released following the two electron reduction of the Mn^{II}-COOH intermediate.

Since the catalytic CO_2 reduction with the use of [MnX $(CO)_3$(α-diimine)] (α-diimine = R-bpy; X = halide or pseudo halide)[15] has been shown to proceed in many cases[22] via a dimerisation step, sterically hindering groups on the bpy moiety can have a profound effect on the catalytic activity.[23] Indeed, it has recently been shown that the use of bipyridines incorporating bulky groups in the 6,6′-positions[24] inhibits dimerisation in the catalytic cycle[25,26] resulting in the formation of the stable 5-coordinate anion via the two-electron transfer (ECE) at the first cathodic wave. However, coordination of CO_2 to the 5-coordinate anion produces a stable species which must be reduced at considerably more negative potentials[27] in order for catalysis to be observed. It has recently been shown that in the presence of a Lewis acid, Mg^{2+},[7,28] the catalytic overpotential[29] is decreased by approximately 400 mV.

A similar behaviour was observed for [MnBr$(CO)_3$(R-DAB)] complexes featuring non-aromatic 1,4-diazabuta-1,3-diene (R-DAB)[8,30] ligands. The reduction potentials of the dimers [Mn$(CO)_3$(R-DAB)]$_2$ are almost identical to those of the parent complexes, implying that the five-coordinate anion is produced directly upon reduction and reacts readily with CO_2 in solution to form a stable CO_2 associated complex and, as has been observed with the sterically-hindered 2,2'-bipyridine ligands,[25] a much more negative potential (below 2 V vs. Fc/Fc+) must be applied to trigger catalytic CO_2 reduction. Functionalization of the α-diimine with a sterically bulky group such as ^{t}Bu should also modify[31] the electronic properties of the ligand. In particular, this change should affect the energy of the LUMO, the reduction potential, and catalytic activity.[12,32]

As such introducing steric bulk to prevent unwanted reactions of the catalytic species, including dimerisation as either Mn–Mn, or C(imino)–C(imino) bound species,[20] whilst at the same time reducing the risk of increased overpotential is a challenging task and molecular designs that allow for steric and electronic effects to be decoupled are required.

In order to investigate the effect of steric hindrance in the manganese based Lehn catalysts a family of tricarbonyl manganese complexes featuring substituted asymmetric α-diimine ligands, imino-pyridines (IP). They combine an accessible –C=N– imino bond of the diazabuta-1,3-diene deriva-tives DAB, with the aromatic pyridine part, thereby being a "hybrid" of 2,2′-bipyridine ligands and non-aromatic R-DAB ligands. Each of the parts is important: for instance, a Mn(I) complex with Ph-DAB demonstrates formation of 5-coordinate anions, with the steric bulk of the ligand preventing dimerisation, but does not act as a catalyst for CO_2 reduction due to insufficiently negative reduction potential.[8,26,33] Introduction of the pyridine moiety allows one to reach the required reduction potentials, whilst the Ph group attached to the C=N fragment can be decorated by sterically demanding substituents, ensuring steric bulk whilst only slightly affecting the electronic properties. As the phenyl moiety lies out-of-plane with the conjugated α-diimine (because of steric effects), the π-electrons of the phenyl substituent are decoupled from the metallacycle formed by the metal centre and the α-diimine. Therefore, functionalisation of the phenyl ring in the R_1 and R_2 positions with large sterically hindering groups that also have a +I effect will have only very minimal effects on the

electronics of the active site of the molecule (*vide infra*). These ligands offer an opportunity to a certain extent separate steric and electronic effects in a chelating α-diimine ligand. Thus, the possibility arises of a systematic variation of the steric hindrance by changing R_1 and R_2 groups, whilst the R-group strongly influences the electronics (but could also hinder the C=N bond).

These ligands are readily accessible via simple synthetic routes, which are suitable for the purpose of comparatively independent alteration of steric and electronic effects (Scheme 5.1). [23,34,35,36,37] The potential of such ligands has been convincingly illustrated by the recent work on a Re tricarbonyl complex with 2-(2-cyclohexyl-1-methyl)-methylimino-pyridine (both the one-electron reduced parent complex and the neutral 5-coordinate Re(0) species were detected) and Mo pyridine-monoimides [37]

Ligand	R	R_1	R_2
IMP (1)	H	H	H
IPIMP (2)	H	^{i}Pr	H
DIPIMP (3)	H	^{i}Pr	^{i}Pr
TBIMP (4)	H	^{t}Bu	H
TBIEP (5)	CH$_3$	^{t}Bu	H
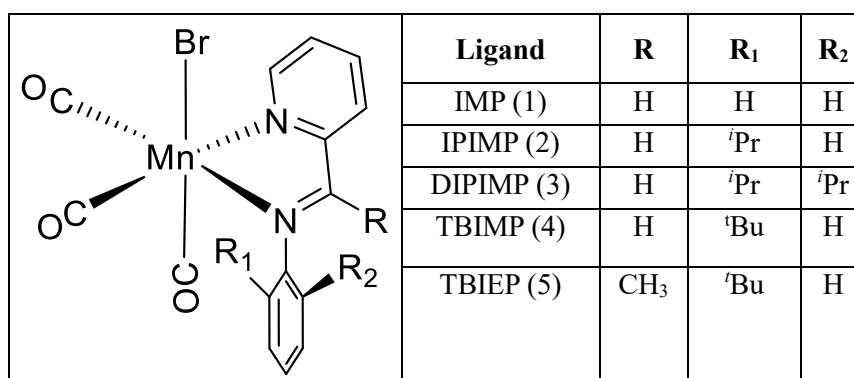
Scheme 5.1 General Structure of the Complexes with the asymmetric α-diimine ligands (2-R_1-6-R_2-phenyl)(R-imino) pyridine. Numbers given in parentheses correspond to the Mn complexes. When R = H, the ligands will be derivatives of [(phenylimino)-methyl]pyridine: IMP (R1,2 = H), IPIMP (R1 = iPr, R2 = H), and DIPIMP (R1,2 = iPr), TBIMP (R1 = tBu, R2 = H). R = CH3 gives TBIEP, [((tert-butylphenyl)imino)ethyl]pyridine.

5.1.2 Aims

The aims of this project were to build on the preliminary results obtained in chapter 4 and determine if a series of asymmetric complexes functionalised with increasingly sterically demanding groups exhibit the decoupling behaviour that was desired.

Three asymmetric complexes with R = H were synthesised incorporating increasing numbers of the sterically demanding iso-propyl group (zero to two) alongside two complexes with R_1 = tertiary butyl where R was varied from H to CH$_3$. These later two complexes were synthesised in order to determine if the R functionalisation had any effect of chemical or spectroscopic behaviour.

5.2 Experimental

5.2.1 Materials and General Procedures

All solvents were supplied by VWR and used as received. The compounds were purchased from either Sigma-Aldrich or STREM Chemicals and, unless stated, used as received. Tetrabutylammonium hexafluorophosphate, [Bu$_4$N][PF$_6$], was recrystallized from hot ethanol and dried overnight in a vacuum oven before use in the electrochemical studies. TBIEP (2-[2-tert-

butylphenyl-imino)-ethyl] pyridine) and TBIMP were synthesized as previously described,[35] the analytical data matched that reported previously. Dried solvents for spectroelectrochemistry were acquired by distillation over magnesium sulphate in an argon atmosphere, other dried solvents were obtained from a Grubbs solvent drying system.

5.2.2 Instrumentation and Analysis

5.2.2.1 Nuclear Magnetic Resonance (NMR) Spectroscopy

^{1}H NMR spectra were recorded using Bruker Avance 400 (DPX-400), Bruker Avance 400, Bruker Avance III HD 400, Bruker Avance III 400 and Bruker Avance III HD 500 spectrometers. Deuterated solvents were purchased from Sigma-Aldrich and were of spectroscopic grade.

5.2.2.2 Mass Spectrometry

High resolution mass spectrometry samples were collected using direct infusion Na^+ ionisation and analysed using time of flight.

5.2.2.3 UV-Visible Absorption Spectroscopy

Unless otherwise stated, UV-Visible absorption spectra were recorded on either a Cary 50 Bio spectrophotometer or Cary 5000 UV-VIS-NIR spectrophotometer utilising 1 cm path length quartz curvettes.

5.2.2.4 Cyclic Voltammetry

Cyclic voltammetry was performed using a Princeton Applied research VersaSTAT 3 on 0.002 M solutions of each of the asymmetric complexes in 6 cm^3 of acetonitrile with 0.2 M tetrabutyl ammonium hexafluorophosphate as supporting electrolyte. A glassy carbon working electrode and platinum wire counter electrode were used alongside a 0.1 M KCl Ag/AgCl reference electrode.

The solutions were degassed by bubbling thoroughly with N_2 and a nitrogen atmosphere was maintained over the samples during the experiment. To test for current enhancement the samples were bubbled thoroughly with CO_2 and measurements taken. 0.3 ml of water was then added to each sample to test the effects of adding a Brönsted acid. During these later experiments a CO_2 atmosphere was maintained over the samples during the experiment.

5.2.2.5 Bulk electrolysis

Bulk electrolysis was performed on a 0.17 mM solution of each of the complexes in a 60 mL solution of acetonitrile/water (9/1 v/v). The cell setup consisted of a Pt-mesh working electrode, a Pt-rod counter electrode contained in in a semiporous compartment and an Ag-wire pseudoreference electrode in a 0.1 M KCl solution. The potential of the Fc/Fc$^+$ recorded in this setup using a glassy-

carbon 3 mm diameter electrode was +0.350 V vs Ag wire pseudoreference. Hence, in order to reach the necessary potential for the CO_2 reduction as estimated from the CV data, the potential was held at −1.9 V vs Ag wire for all samples (−2.25 V vs Fc/Fc$^+$). The same potential was used for all complexes because of the potential dependent nature of CO_2 reduction.[38,39,40,41] Gas samples (100 μL) were withdrawn from the head space at regular intervals and analysed by a gas chromatograph fitted with a thermal conductivity detector (Perkin ElmerArnel autosystem XL) running an isothermal method. H_2 was used as the carrier gas.

5.2.2.6 Spectroelectrochemistry

Infrared spectroelectrochemistry was performed using an EmStat3 or EmStat3+ potentiostat (PalmSense, The Netherlands). A solution of 0.004 M complex in the presence of 0.3 M [Bu$_4$N][PF$_6$] in dry acetonitrile was analysed using an optically transparent thin-layer electrochemical (OTTLE) cell equipped with Pt minigrid working and auxiliary electrodes, an Ag microwire pseudoreference electrode and CaF$_2$ windows. Samples were prepared under an argon atmosphere; for electrocatalytic measurements, the solutions were bubbled with CO_2 on a frit for several minutes to saturation under normal pressure. Parallel IR and UV-vis spectral monitoring during the spectroelectrochemical experiment was performed on a Bruker Vertex 70v FT-IR spectrometer or Perkin Elmer Spectrum 1, and a Scinco S-3100 spectrophotometer, respectively. Thin-layer CVs were recorded alongside in the course of the experiment.

5.2.2.7 X-ray Crystallography

Crystals were grown using anti-solvent crystallization method, with the solvent dichloromethane and hexane as the anti-solvent. Single-crystal X-ray diffraction data were collected on a Bruker SMART APEX-II CCD diffractometer operating a Mo-Kα sealed-tube X-ray source or a Bruker D8 Venture diffractometer equipped with a PHOTON 100 dual-CMOS chip detector and operating a Cu-Kα IμS microfocus X-ray source. The data were processed using Bruker APEX3 software and corrected for absorption using empirical methods (SADABS) based upon symmetry-equivalent reflections combined with measurements at different azimuthal angles.[42] The crystal structures were solved and refined using the Bruker SHELXTL software package.

5.2.2.8 Computational Methods

Density functional theory (DFT) calculations were performed using the Gaussian 09 program package.[43] All calculations utilised the global hybrid exchange correlation functional B3LYP,[44,45] a 'mixed' basis set consisting of the SDD basis set as defined in Gaussian for Mn and the 6-311G(d,p) basis set for all other atoms.[46,47,48,49] The solvent acetonitrile was included using the Polarizable Continuum Model (PCM) as implemented in Gaussian.[50,51] All species were modelled at the lowest

multiplicity appropriate for the electron count and the restricted formalism was used for closed shell cases. An 'ultrafine' integral grid, as defined by Gaussian, was used and all geometries were confirmed as minima by the absence of imaginary frequencies in their vibrational spectra as calculated within the harmonic approximation. The values of vibrational frequencies have been scaled by 0.966 to match experimental υ(CO) of the parent neutral complexes.

5.2.3 Syntheses

5.2.3.1 IMP (2-[(phenylimino)methyl]pyridine)

Aniline (11.3 mmol, 1.05 g, 1.02 ml) was added to 2-pyridine carboxaldehyde (11.3 mmol, 1.2 g, 1.1 ml) in flame-dried glassware and stirred for 1 h. Hexane (10 ml) was added and the solution dried over sodium sulphate. The solution was filtered, concentrated under vacuum, and placed in a freezer overnight. Large yellow needle-like crystals formed were filtered and washed with hexane. Yield: 73 %. ^{1}H NMR (400 MHz, CDCl$_3$) δ 8.72 (d, J = 4.7 Hz, 1H), 8.61 (s, 1H), 8.21 (d, J = 7.9 Hz, 1H), 7.83 (td, J = 7.7, 1.6 Hz, 1H), 7.47 – 7.35 (m, 3H), 7.29 (d, J = 7.7 Hz, 3H), 1.58 (s, 4H).

5.2.3.2 IPIMP (2-[2-isopropylphenylimino)methyl]pyridine)

2-isopropylaniline (12.4 mmol, 1.7 g, 1.8 ml) was mixed with 2-pyridine carboxaldehyde (12.4 mmol, 1.3 g, 1.2 ml) in flame-dried glassware and stirred for 1 h. Hexane (20 ml) was added and the solution dried over sodium sulphate. The solution was filtered and solvent removed under vacuum, yielding the product as a brown oil. Previous reports indicated that this compound could not be crystalized therefore, the oil was used in the next reaction step without further purification (purity by NMR: > 97 %). ^{1}H NMR (400 MHz, CDCl$_3$) δ 8.72 (ddd, J = 4.8, 1.6, 0.9 Hz, 1H), 8.54 (s, 1H), 8.26 (dd, J = 7.9, 0.9 Hz, 1H), 7.82 (ddd, J = 7.9, 1.7, 0.8 Hz, 1H), 7.45 – 7.32 (m, 2H), 7.31 – 7.22 (m, 2H), 7.08 – 6.96 (m, 1H), 3.56 (dp, J = 13.8, 6.8 Hz, 1H), 1.26 (dd, J = 6.8, 4.1 Hz, 7H).

5.2.3.3 DIPIMP (2-[(2,6-diisoPr-phenylimino)-Me]-pyridine)

2,6-diisopropylaniline (11.3 mmol, 2 g, 2.1 ml) was mixed with 2-pyridine carboxaldehyde (11.3 mmol, 1.2 g, 1.1 ml) in flame-dried glassware and stirred for 2 h. Hexane (10 ml) was added and the solution dried over sodium sulphate. The solution was filtered and concentrated before having been placed in a freezer overnight. Light brown to yellow crystals were formed, which were filtered off and washed with hexane. Yield: 67 %. ^{1}H NMR (400 MHz, CDCl$_3$) δ 8.73 (ddd, J = 4.8, 1.7, 0.9 Hz, 1H), 8.31 (s, 1H), 8.27 (dt, J = 7.9, 1.0 Hz, 1H), 7.90 – 7.82 (m, 1H), 7.42 (ddd, J = 7.5, 4.9, 1.2 Hz, 1H), 7.22 – 7.07 (m, 3H), 2.97 (hept, J = 6.9 Hz, 2H), 1.62 (s, 1H), 1.18 (d, J = 6.9 Hz, 13H).

5.2.3 Synthesis

Complexes **1-6** were prepared from [MnBr(CO)$_5$] and the corresponding ligand, using diethyl ether as a solvent. The products were collected by centrifuge, and washed with diethyl ether to afford analytically pure **1-6**.

5.2.3.4 [MnBr(CO)$_3$(IMP)] (MnIMP - 1)

[MnBr(CO)$_5$] (1.1 mmol, 0.3 g) was combined with (IMP 1.1 mmol, 0.2 g) in diethyl ether (20 ml) and refluxed under aerobic conditions for 4 h.[52,53] Product was formed in quantitative yield. ^{1}H NMR (500 MHz, CDCl$_3$) δ 9.26 (d, J = 5.0 Hz, 1H), 8.45 (s, J = 27.9 Hz, 1H), 8.14 – 7.79 (m, 3H), 7.68 – 7.36 (m, 5H). HRMS (TOF-ES, + ve): *m/z* (M+Na$^+$) Calcd for C$_{15}$H$_{10}$N$_2$O$_3$NaBrMn: 422.9153; found 422.9149.

5.2.3.5 [MnBr(CO)$_3$(IPIMP)] (MnIPIMP - 2)

[MnBr(CO)$_5$] (0.89 mmol, 0.24 g) was combined with IPIMP (0.89 mmol, 0.2 g) in diethyl ether (20 ml) and refluxed under aerobic conditions for 4 h.[52,53] The product was formed in quantitative yield. ^{1}H NMR (500 MHz, CDCl$_3$) δ 9.27 (s, 1H), 8.39 (s, 1H), 8.04 (s, 1H), 7.94 (d, J = 4.1 Hz, 1H), 7.78 (d, J = 7.0 Hz, 1H), 7.61 (s, 1H), 7.48 (d, J = 15.3 Hz, 1H), 7.43 (d, J = 6.7 Hz, 1H), 7.37 (t, 1H), 7.30 (d, J = 6.9 Hz, 1H), 3.58 (s, 1H), 3.03 (d, J = 35.6 Hz, 1H), 1.47 – 1.11 (m, 1H). HRMS (TOF-ES, + ve): *m/z* (M+Na$^+$) Calcd for C$_{18}$H$_{16}$N$_2$O$_3$NaBrMn: 464.9622; Found 464.9644.

5.2.3.6 [MnBr(CO)$_3$(DIPIMP)] (MnDIPIMP - 3)

[MnBr(CO)$_5$] (0.75 mmol, 0.2 g) was combined with DIPIMP (0.75 mmol, 0.2 g) in diethyl ether (20 ml) and refluxed under aerobic conditions for 4 h.[52,53] The product was formed in 97 % yield. ^{1}H NMR (500 MHz, CDCl$_3$) δ 9.30 (s, 1H), 8.41 (s, 1H), 7.99 (d, J = 50.7 Hz, 2H), 7.63 (s, 1H), 7.34 (s, 2H), 4.04 (s, 1H), 2.91 (s, 1H), 1.34 (d, J = 3.1 Hz, 6H), 1.05 (dd, J = 80.6, 35.1 Hz, 6H). HRMS (TOF-ES, + ve): *m/z* (M+Na$^+$) Calcd for C$_{21}$H$_{22}$N$_2$O$_3$NaBrMn 507.0092; Found 507.0107.

5.2.3.7 [MnBr(CO)$_3$(TBIMP)] (MnTBIMP - 4)

[MnBr(CO)$_5$] (0.84 mmol, 0.23 g) was combined with DIPIMP (0.84 mmol, 0.2 g) in diethyl ether (20 ml) and refluxed under aerobic conditions for 4 h.[52,53] The product was formed in quantitative yield. ^{1}H NMR (400 MHz, CDCl$_3$) δ 9.27 (d, J = 4.4 Hz, 1H), 8.50 (s, 1H), 8.12 (d, J = 6.9 Hz, 1H), 8.03 (t, J = 7.2 Hz, 1H), 7.91 (d, J = 7.1 Hz, 1H), 7.61 (t, J = 6.2 Hz, 1H), 7.57 (d, J = 7.4 Hz, 1H), 7.30 (t, 1H), 1.43 (s, 1H). HRMS (TOF-ESI, + ve): *m/z* (M+Na$^+$) Calcd for C$_{19}$H$_{18}$N$_2$O$_3$NaBrMn 478.9774; Found 478.9789.

5.2.3.8 MnBr(CO)₃(TBIEP)] (MnTBIEP - 5)

[MnBr(CO)$_5$] (0.8 mmol ,0.22 g) was combined with TBIEP (0.8 mmol, 0.2 g) and refluxed under aerobic conditions in diethyl ether (20 ml) for 4 h.[52,53] The product was formed in quantitative yield. ^{1}H NMR (400 MHz, CDCl$_3$) δ 9.28 (d, J = 5.0 Hz, 1H), 8.04 (td, J = 7.8, 1.3 Hz, 1H), 7.95 (d, J = 7.7 Hz, 1H), 7.88 (dd, J = 6.1, 3.4 Hz, 1H), 7.65 – 7.54 (m, 2H), 7.34 – 7.27 (m, 2H), 2.39 (s, 3H), 1.39 (s, 8H). HRMS (TOF-ES, + ve): m/z (M+Na+) Calcd for C$_{20}$H$_{20}$N$_2$O$_3$NaBrMn 492.9935; Found 492.9934.

5.2.3.9 [MnBr(CO)₃(bpy)] (Mnbpy - 6)

This complex was prepared following literature procedure outlined by Bourrez *et al.*;[2] analytical data is in agreement with the literature data. [MnBr(CO)$_5$] (1.28 mmol, 0.35 g) was combined with 2,2'-bipyridine (1.28 mmol, 0.2 g) in diethyl ether (20 ml) and refluxed under aerobic conditions for 4 h. The product was formed in 80 % yield. ^{1}H NMR (500 MHz, CDCl$_3$) δ 9.27 (d, J = 4.3 Hz, 1H), 8.12 (d, J = 6.5 Hz, 1H), 7.99 (t, 1H), 7.53 (t, 1H). HRMS (TOF-ESI, + ve): *m/z* (M+Na$^+$) Calcd for C$_{13}$H$_8$N$_2$O$_3$NaBrMn 396.8991; Found 369.8988.

5.3 Results and Discussion

5.3.1 X-ray Crystallography

The crystal structures of the complexes [MnBr(CO)$_3$(α-diimine)] (α-diimine = TBIEP, IMP, IPIMP, DIPIMP) are shown in Figure 5.1 and selected bond distances and angles are listed in appendix 3. Similar bond lengths are observed for the four complexes, and these are in good agreement with related [MnBr(CO)$_3$(α-diimine)] species reported in the literature. The X-ray data is in good agreement with the results obtained through DFT calculations. As predicted by DFT, the pyridine and phenyl rings lie approximately orthogonally to one another (dihedral angles between the corresponding planes are: MnTBIEP, 84.55°, MnIPIMP, 83.64°, MnDIPIMP, 78°), resulting in little orbital overlap between these two moieties, with the exception of MnIMP where the two ring systems were significantly less orthogonal (56.54°).
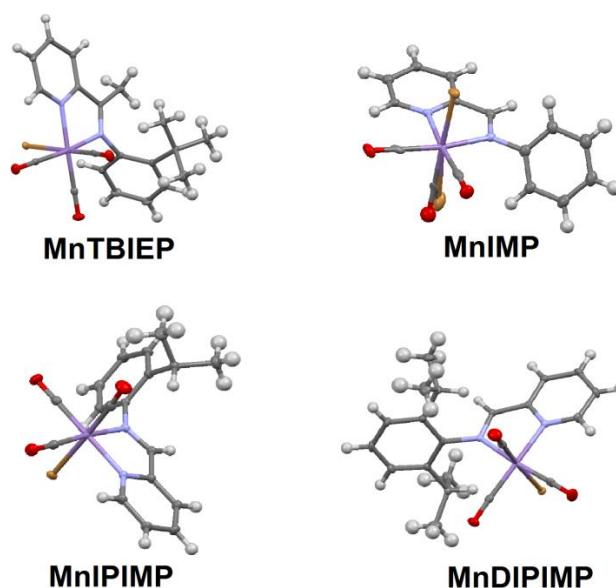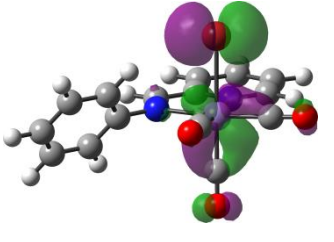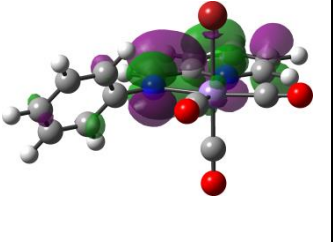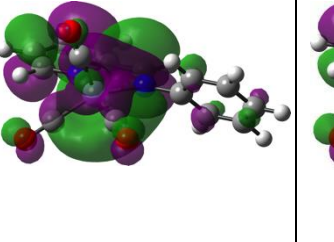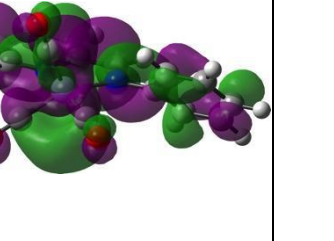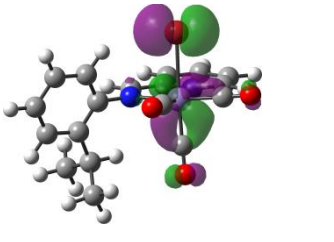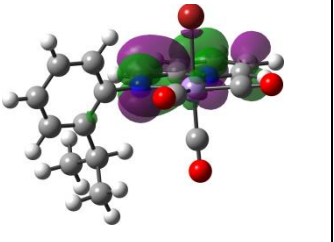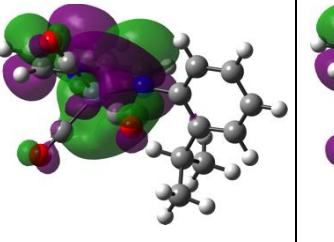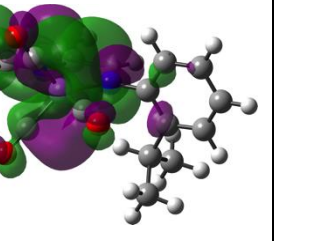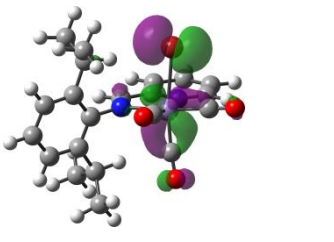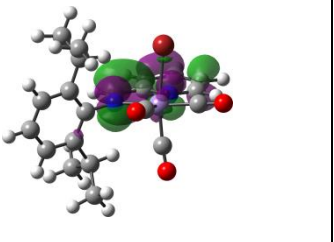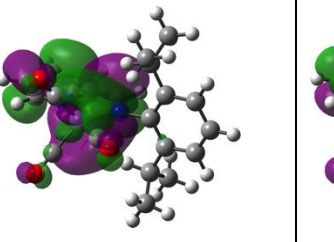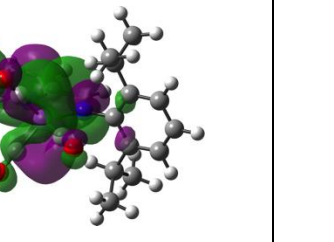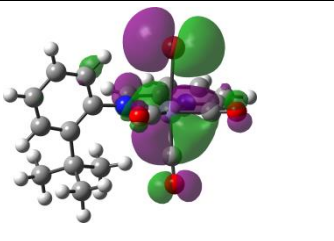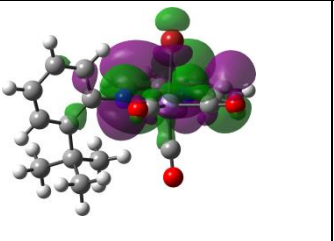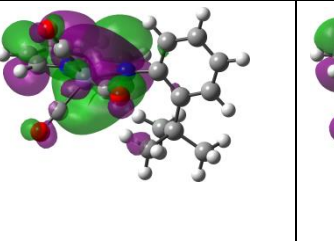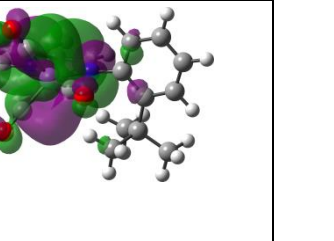
Figure 5.1 X-ray crystal structures of the studied complexes shown with thermal ellipsoids at the 50 % probability level. CCDC 1457930, MnTBIEP, 1457931, MnDIPIMP, 1457932, MnIPIMP, 1457933, MnIMP.

The crystal structures have revealed significant steric hindrance between the substituents R = Me and the R_1 = ^tBu in MnTBIEP, which inhibits rotation of the phenyl ring and confers conformational rigidity. Rotation of the phenyl ring in MnDIPIMP is also inhibited by the two ^iPr groups and hence also has the conformational rigidity. In contrast, MnIMP and MnIPIMP exhibit much smaller steric hindrance, permitting the rotation of the phenyl ring.
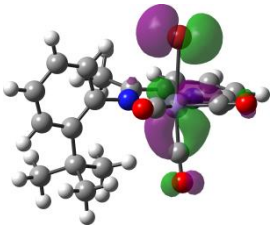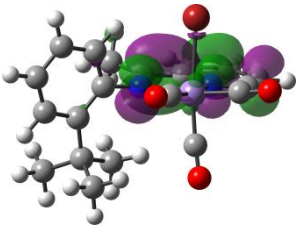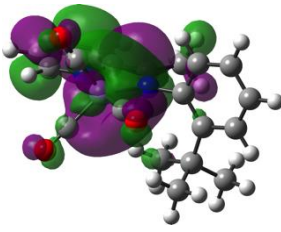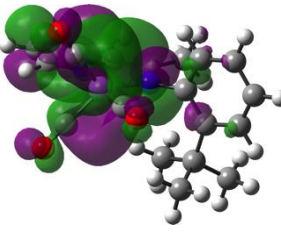
5.3.2 Computational Investigations of Molecular Structures and Frontier Orbitals by DFT

The optimized geometries of the studied complexes with frontier orbitals overlaid as calculated by DFT are displayed in Table 5.1. As anticipated, the phenyl group lies out of plane of the chelating diimine. The HOMO is localized predominantly over the axial Br–Mn–C(O) bonds with almost no contribution from the phenyl moiety. The LUMO resides largely on the imine, pyridyl and metal centre, with minimal contribution from the C1–C2 and C1–C6 σ bonds of the phenyl groups. In the case of MnIMP, due to the lack of substitution at R_1 and R_2, the phenyl moiety is less sterically hindered and thus is positioned closer to the plane of the imino–pyridine fragment, resulting in a small degree of involvement of the phenyl π system in the low energy unoccupied orbitals. This trend continues in the other low-energy unoccupied orbitals (see appendix 2).

Table 5.1 Frontier orbitals of the complexes 1-5 and the corresponding 5-coordinate anions calculated at the B3LYP/SDD+6-311G(d,p)/IEFPCM level. Isovalue of 0.04 $\sqrt{e^- \, bohr^{-3}}$.

HOMO	LUMO	HOMO	LUMO
Parent	complex	Five-coordinate	anion
MnIMP		MnIMP	
ε = -6.31 eV	ε = -2.84 eV	ε = -3.67 eV	ε = -1.18 eV
MnIPIMP		MnIPIMP	
ε = -6.33 eV	ε = -2.81 eV	ε = -3.70 eV	ε = -1.01 eV
MnDIPIMP		MnDIPIMP	
ε = -6.31 eV	ε = -2.83 eV	ε = -3.67 eV	ε = -0.99 eV
MnTBIMP		MnTBIMP	
HOMO: ε = -6.36 eV	LUMO: ε = -2.80 eV	HOMO: ε = -3.64 eV	LUMO: ε = -1.02 eV
MnTBIEP		MnTBIEP	

| ε = -6.33 eV | ε = -2.62 eV | ε = -3.55 eV | ε = -0.99 eV |

Table 5.2 Experimentally obtained and calculated frequencies of carbonyl stretching vibrations of: the neutral Mn complexes (1-5), transient one-electron reduced form, 5-coordinate anion, a cationic aqua complex, and the Mn–Mn bound dimer, in acetonitrile at 293 K.

Species	$\upsilon(CO)$ / cm^{-1} Calculated	$\upsilon(CO)$ / cm^{-1} Experimental
[MnBr(CO)$_3$(IMP)] **(1)**	2020, 1943, 1931	2029, 1941, 1926
[MnBr(CO)$_3$(IMP)]$^-$	1992, 1906, 1897	Not observed
[Mn(CO)$_3$(H$_2$O)(IMP)]$^+$	2046, 1966, 1957	2051, 1964[b], 1958[b]
[Mn(CO)$_3$(IMP)]$^-$	1906, 1830, 1813	1930, 1826
[Mn(CO)$_3$(IMP)]$_2$	1964, 1918, 1891, 1882, 1872, 1868	1994, 1949, 1902, 1875
[MnBr(CO)$_3$(IPIMP)] **(2)**	2020, 1945, 1929	2029, 1943, 1923
[MnBr(CO)$_3$(IPIMP)]$^-$	1988, 1905, 1891	Not observed
[Mn(CO)$_3$(H$_2$O)(IPIMP)]$^+$	2044, 1963, 1956	2049, 1959(br)
[Mn(CO)$_3$(IPIMP)]$^-$	1905, 1826, 1808	1929, 1824
[Mn(CO)$_3$(IPIMP)]$_2$	1964, 1917, 1890, 1881, 1866, 1860	1981, 1949, 1901, 1882, 1862
[MnBr(CO)$_3$(DIPIMP)] **(3)**	2019, 1945, 1929	2028, 1944, 1922
[MnBr(CO)$_3$(DIPIMP)]$^-$	1985, 1906, 1890	Not observed
[Mn(CO)$_3$(H$_2$O)(DIPIMP)]$^+$	2045, 1964, 1957	2050, 1960(br)[b]
[Mn(CO)$_3$(DIPIMP)]$^-$	1903, 1824, 1806	1929, 1829/22
[Mn(CO)$_3$(DIPIMP)]$_2$	1965, 1918, 1890, 1880, 1860, 1850	Not observed
[MnBr(CO)$_3$(TBIMP)] **(4)**	2020, 1947, 1925	2029, 1945, 1923
[MnBr(CO)$_3$(TBIMP)]$^-$	1988, 1907, 1890	Not observed
[Mn(CO)$_3$(H$_2$O)(TBIMP)]$^+$	2045, 1965, 1956	Not observed
[Mn(CO)$_3$(TBIMP)]$^-$	1906, 1827, 1807	1928, 1823
[Mn(CO)$_3$(TBIMP)]$_2$	1964, 1916, 1889, 1879, 1862, 1854	Not observed

[MnBr(CO)$_3$(TBIEP)] **(5)**	2018, 1944, 1921	2028, 1943, 1917
[MnBr(CO)$_3$(TBIEP)]$^-$	1980. 1904, 1883	Not observed
[Mn(CO)$_3$(H$_2$O)(TBIEP)]$^+$	2042, 1962, 1950	2048, 1960, 1954
[Mn(CO)$_3$(TBIEP)]$^-$	1897, 1819, 1798	1922, 1814(br)
[Mn(CO)$_3$(TBIEP)]$_2$	1958, 1909, 1880, 1870, 1850, 1841	Not observed

[a] In acetonitrile at 293 K. [b] Positions are approximate as the parent CO stretching vibrations obscure those of the cationic aqua complex.

The energies of the HOMO in all complexes are within 0.02 eV of each other and all the IMP subset of complexes have a LUMO that lie within 0.03 eV of the other complexes. In contrast MnTBIEP shows a difference in LUMO energy of +0.19 eV compared with IPIMP. This larger difference in LUMO energy comes as result of methylation at the R position. In contrast, adding two isopropyl groups at the R_1 and R_2 positions resulted in an energy difference of just 0.02 eV between MnIMP and MnDIPIMP. The results of the calculations on the trends in the energies of HOMO/LUMO are in full agreement with the experimentally determined redox potentials (see below). These results imply that an almost complete separation between the steric and the electronic effects in the context of few-electron reductions can indeed be achieved in this series of complexes. Changing the R group will strongly affect the energy of the LUMO while having also some impact on the steric properties at the carbon of imino C=N bond, whilst changing the R_1 or R_2 groups should have considerable effects upon the steric hindrance of the molecule (protecting the Mn and imino N centers), but hardly affecting its electronic properties.

The experimental and calculated carbonyl vibrational frequencies of the studied complexes are shown in Table 1. The calculated frequencies are in good agreement with the experimental values. Some systematic discrepancies are apparent: the high energy A′(1) mode tends to be underestimated by ~10 cm^{-1}, the A″ mode tends to have a lower deviation of only ~2 cm^{-1}, and the low energy A′(2) mode tends to be overestimated by ~10 cm^{-1}. It is clear that attachment of the methyl group as R increases the electron density on the metal centre and thus also the Mn-to-CO π-back bonding, as evidenced by the smaller values of υ(CO) for MnTBIEP compared to the IMP sub-series (complexes 1-4). However, substitution at R1 and R2 has only little effect on the frequencies. It should be noted that the magnitude of these effects is small (<10 cm-1) and that it is beyond the scope of this computational work to unravel the various factors effecting changes in CO stretching frequencies.[54]

The results of DFT calculations (Table 5.2) of IR spectra for the parent Br-complexes, [MnBr(CO)$_3$(α-diimine)] **1-5**, and the corresponding cationic aqua complexes ([Mn(CO)$_3$(H$_2$O)(α-diimine)]$^+$) match well the experimental data. We therefore use the calculated ν(CO) wavenumbers for

the hydrolysed aqua and reduced (dimer and anion) species to aid the analysis of the IR spectra and product assignment in the course of the corresponding cathodic IR-SEC experiments (*vide infra*).

Adding electron-donating groups (iPr and tBu) to the phenyl ring of the IMP sub-series does not have a large effect on the ν(CO) frequency, the band positions being virtually unchanged between complexes **1-4**. The two higher-frequency bands are at 2028-2029 cm^{-1} and 1943-1944 cm^{-1} for all 5 complexes, whilst the lowest ν(CO) band is seen at 1923-1922 cm^{-1} for the "IMP" series but shifted to lower energy, 1917 cm^{-1} in [MnBr(CO)$_3$(TBIEP)] where the increased π-back-donation is caused by R = Me. This invariability of ν (CO) frequencies, whilst the dihedral angle between the planes of the pyridine and phenyl moieties of the IP ligands is clearly changing drastically, from ~56 to ~84°, confirm the opportunity of the somewhat independent tuning of electronic and steric factors.

Calculations performed on the five-coordinate anions of the studied compounds, [Mn(CO)$_3$(diimine)]$^-$, show very similar trends to what has been observed in the parent complexes. Both the HOMO and LUMO are predominantly delocalized over the tricarbonyl-Mn and α-diimine metalacycle, with little participation from the phenyl ring, with the exception of MnIMP, the LUMO of which having a significant contribution from the phenyl moiety.
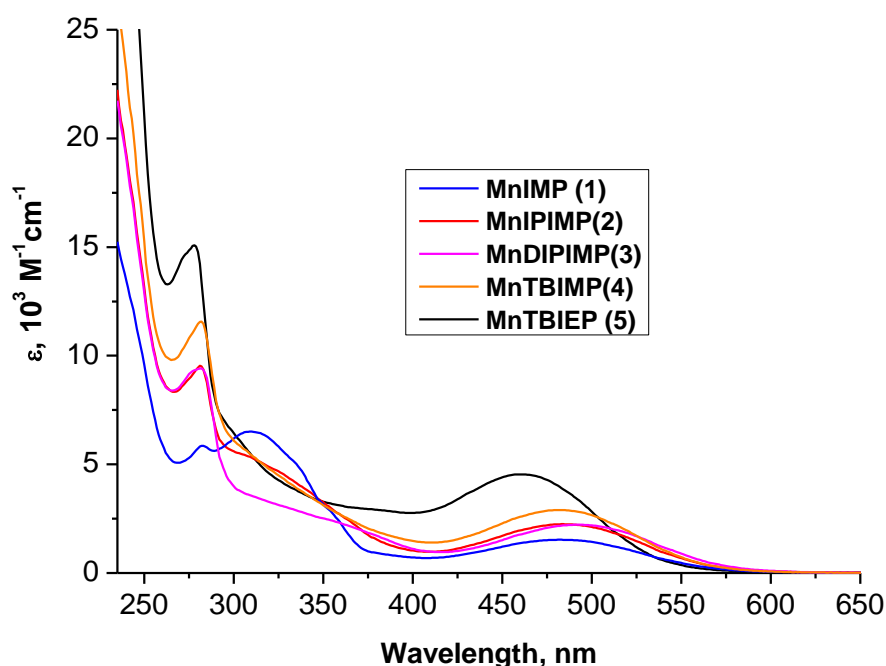
Figure 5.2 Electronic absorption spectra of the manganese complexes 1-5 studied in this work, in DCM at 293 K.

The UV-vis absorption spectra (Figure 5.2) are consistent with the nature of the frontier orbitals obtained from the calculated data. The lowest energy absorption band for the complexes of the IMP sub-series **1-4**, occurs at approximately the same, ca. 500-nm position. In contrast MnTBIEP (**5**) exhibits an absorption band with maximum at a shorter wavelength, 460 nm, due to electron donation from the Me group which destabilizes the LUMO.

5.3.3 Cyclic Voltammetry

Electrochemical studies showed significant differences between the cathodic path of MnTBIEP (**5**) and those of the IMP sub-series (**1-4**).

Under an N_2 atmosphere, [MnBr(CO)$_3$(TBIEP)] (see figure 5.3) shows a single reduction wave at $E_{p,c}$ = -1.53 V and an intense anodic wave at $E_{p,a}$ = -1.3 V observed on the reverse anodic scan. This behaviour is similar to that of [MnBr(CO)$_3$(iPr-DAB)] (iPr-DAB = 1,4-diisopropyl-1,4-diazabuta-1,3-diene),[8] which is reduced by an ECE mechanism. The initial one-electron reduction results in dissociation of the bromide to form a five-coordinate radical, [Mn(CO)$_3$(TBIEP]$^•$, which is concomitantly reduced to the five-coordinate anion [Mn(CO)$_3$(TBIEP)]$^-$ (reoxidised at -1.3 V) at the potential required for the reduction of [MnBr(CO)$_3$(TBIEP)]. A small anodic wave at -0.6 V is characteristic of oxidation of [Mn(CO)$_3$(TBIEP)]$_2$ formed in the course of the anodic path of the five-coordinate anion, and indicates that dimerisation can still occur with the R = Me. The dimer could also be produced in a reaction of [Mn(CO)$_3$(TBIEP)]$^-$ with neutral [MnBr(CO)$_3$(TBIEP)] on the cathodic scan; but the absence of a cathodic wave for reduction of [Mn(CO)$_3$(TBIEP)]$_2$ indicates that its reduction potential is too close to that of [MnBr(CO)$_3$(TBIEP)] for a separate reduction wave to be observed.
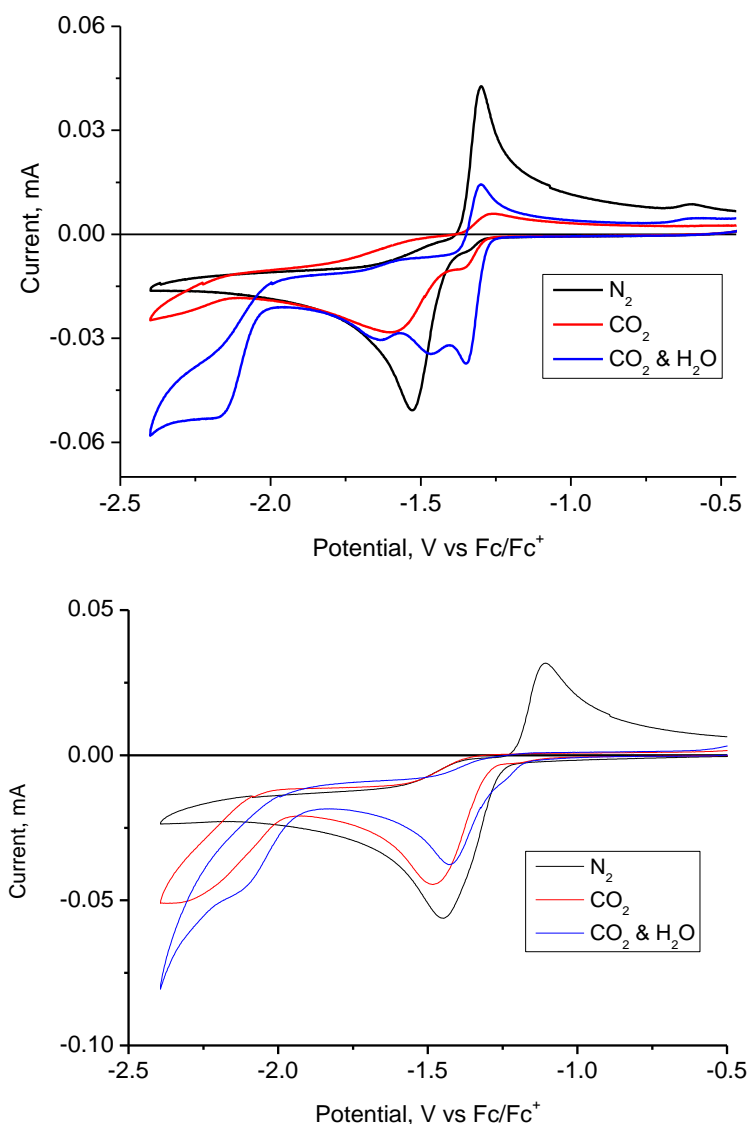
Figure 5.3 Cyclic voltammograms of 1 mM MnTBIEP (top panel) and MnTBIMP (bottom panel) in acetonitrile, 0.2 M [Bu₄N][PF₆] as supporting electrolyte, under N₂ atmosphere (black), CO₂ atmosphere (red) and CO₂ with 4.7% added water (blue) at scan rate 0.1 Vs⁻¹.

The CV traces of MnIMP (see figure 5.4) obtained under N_2 atmosphere show three cathodic reduction peaks, at $E_{p,c}$ = -1.28, -1.41 and -1.54 V and a strong anodic peak at $E_{p,a}$ = -1.24 V. The first reduction at -1.28 V can be assigned to the cation $[Mn(CO)_3(H_2O)(IMP]^+$; it is likely that the peak at -1.41 V is due to remaining non-hydrolysed $[MnBr(CO)_3(IMP)]$, or a solvent adduct,[11] whilst the -1.54 V wave corresponds to the reduction of the dimeric species (see also the IR spectroelectrochemical section below). The 5-coordinate anion $[Mn(CO)_3(IMP)]^-$ is probably the reduction product at all three different cathodic waves (the parent complex $[MnBr(CO)_3(IMP)]$, aqua-complex, and the IMPMn–MnIMP dimer), as evidenced by its anodic wave at $E_{p,a}$ = -1.24 V on the reverse anodic scan (accompanied by the dimer oxidation above -0.5 V). Over time a smaller cathodic wave emerges at $E_{p,c}$ = -1.35 V, due to the aqua-coordinated cationic complex forming via hydrolysis of the parent Br-

119

complex (see section 5.3.4). Under an atmosphere of CO_2 the anodic wave of $[Mn(CO)_3(TBIEP)]^-$ at -1.3 V disappears, and the profile of the CV also changes, (Figure 5.3), with a broad cathodic wave of $[MnBr(CO)_3(TBIEP)]$ shifted slightly negatively, indicating an interaction with CO_2. However, similar to Mn–bpy complexes,[2] catalytic reduction of CO_2 in the absence of a Brönsted acid was not observed (the small peak beginning around -2.18 V is due to a small amount of water entering the CV cell when it is being saturated with CO_2). Addition of 0.3 ml of water leads to significant current enhancement at -2.18 V in line with what has been observed with $[MnBr(CO)_3(iPr-DAB)]$.[8]
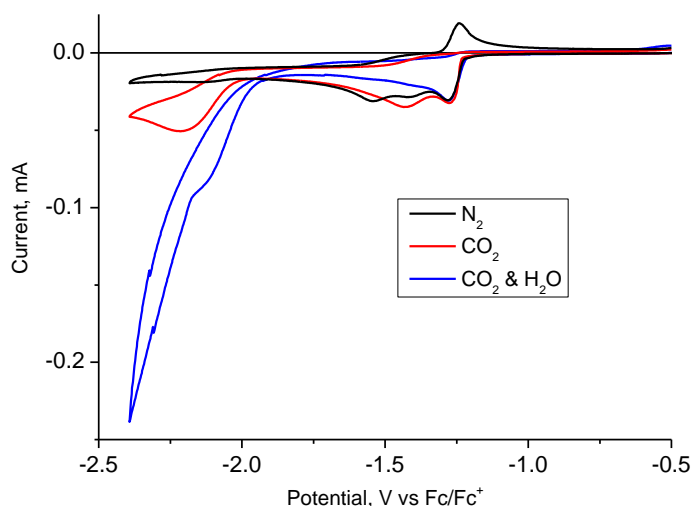
Figure 5.4 Cyclic voltammograms of 1 mM MnIMP in acetonitrile, 0.2 M [Bu$_4$N][PF$_6$], scan rate 0.1 Vs^{-1}. Under atmosphere of N$_2$ (black), CO$_2$ (red), and CO$_2$ with 4.7% H2O (blue).

Under a CO_2 atmosphere, the increased cathodic current is seen at approximately -2.2 V for all complexes. We believe this is due to some amount of the bicarbonate complex (for a discussion of the formation of the bicarbonate complex see the discussion of the spectroelectrochemistry in chapter 2 section 2.3.1) being formed, likely due to traces of water in the CO_2 used.[33] When 10% water is added to the CO_2 saturated solution, a strong current enhancement is observed at -2.21 V. Importantly, CVs recorded under N_2 atmosphere in acetonitrile in presence of water do not show catalytic current enhancement (see appendix 2, figure A2.15); thus, both CO_2 and water are required for the current enhancement to be observed. Under a CO_2 atmosphere, no anodic wave corresponding to re-oxidation of the five-coordinate anion is observed for the least sterically hindered $[Mn(CO)_3(IMP)]^-$, see figure 5.4), and for the monosubstituted complexes **2** and **4**; a behaviour indicative of a rapid reaction of the anion with CO_2. A diminished but clear anodic wave of $[Mn(CO)_3(TBIEP)]^-$ can be observed under CO_2 vs. N_2 atmosphere (figure 5.3), suggesting that $[Mn(CO)_3(TBIEP)]^-$ associates with CO_2 less efficiently. Whilst, similarly to MnIPIMP (see figure 5.5), no anodic wave corresponding to $[Mn(CO)_3(TBIMP)]^-$ re-oxidation under CO_2 atmosphere could be observed indicating that CO_2 association is rapid, the overall current enhancement for this complex is comparatively low indicating

lower efficiency at reducing CO_2, perhaps due to the bicarbonate intermediate somewhat preventing the recovery of the 5-coordinate catalytic species.
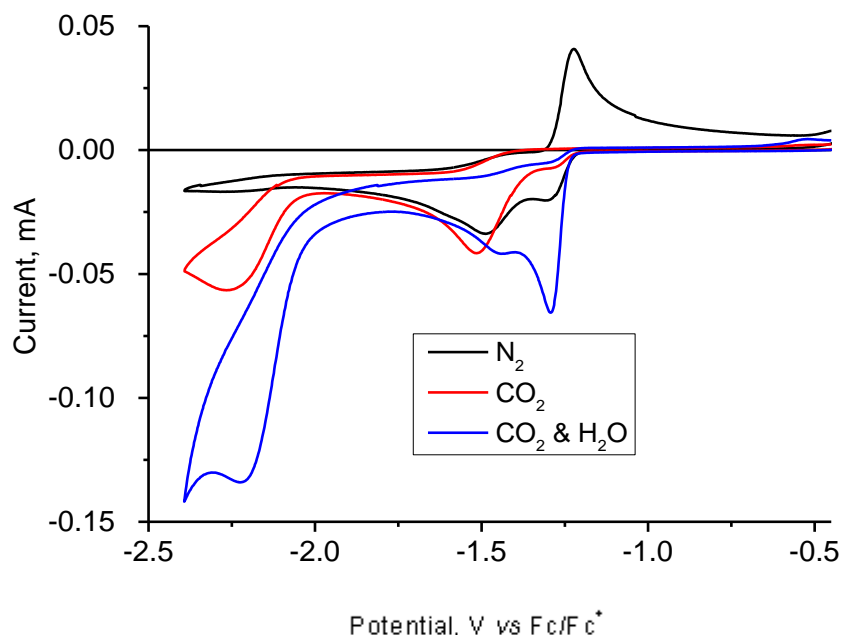
Figure 5.5 Cyclic voltammograms of 1 mM MnIPIMP in acetonitrile, 0.2M [Bu$_4$N][PF$_6$], scan rate 0.1 Vs^{-1}. Under atmosphere of N$_2$ (black), CO$_2$ (red), and CO$_2$ with 4.7% H$_2$O (blue).
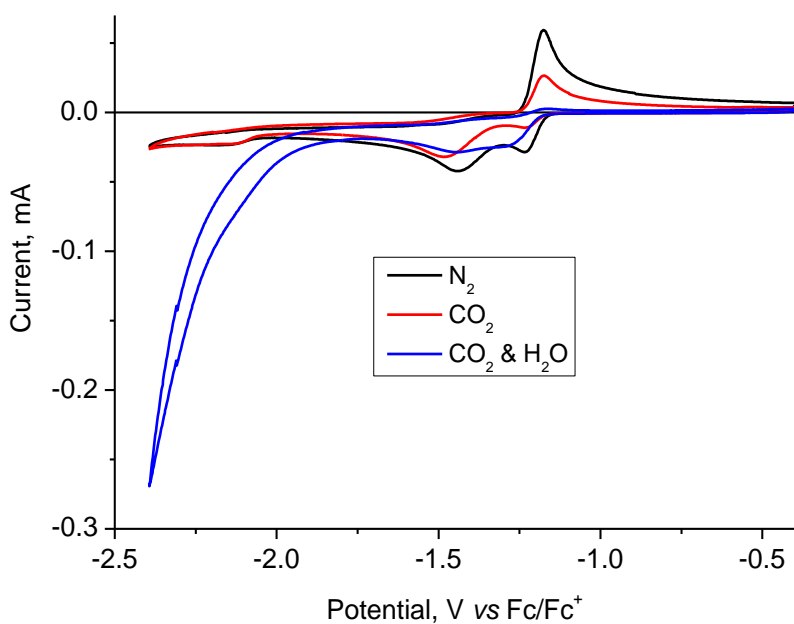
Figure 5.6 Cyclic voltammograms of 1 mM MnDIPIMP in acetonitrile, 0.2M [Bu$_4$N][PF$_6$], scan rate 0.1 Vs^{-1}. Under atmosphere of N$_2$ (black), CO$_2$ (red), and CO$_2$ with 4.7% H$_2$O (blue).

Under N_2, reduction of [MnBr(CO)$_3$(IPIMP)] is seen at $E_{p,c}$ = -1.49 V, accompanied by a wave at $E_{p,c}$ = -1.29 V, assigned to the cationic aqua complex [Mn(CO)$_3$(H$_2$O)(IPIMP)]$^+$. As discussed above,

upon addition of CO_2 the oxidation wave of the anion $[Mn(CO)_3(IPIMP)]^-$ is not observed, indicating a rapid reaction between the 5-coordinate anion and CO_2. Some current enhancement at -2.26 V is observed upon saturation with CO_2 which is enhanced greatly upon the addition of 0.3 ml of water (the current enhancement corresponds to the cathodic wave of the bicarbonate complex, identified in the IR spectra (*vide infra*): some catalysis occurs due to hydrolysis caused for example by residual water in the electrolyte, or in the CO_2).

CV of MnTBIMP (Figure 5.3, bottom panel) is similar to that of MnIPIMP and MnTBIEP with a strong cathodic wave at -1.45 V. At ca. -2.28 V current enhancements ascribed to CO_2 reduction can be observed under CO_2 and CO_2 with added H_2O, though the i_{cat}/i_p values (*vide infra*) are somewhat lower compared to the other complexes studied here. Importantly, the anodic wave of the five-coordinate anion re-oxidation is not detected for MnIPIMP and MnTBIMP, but is clearly seen for slower reacting MnTBIEP and MnDIPIMP anions.

MnDIPIMP (figure 5.6) shows significant differences in the CV traces to the other complexes of the IMP sub-series. Similarly to the IMP and IPIMP complexes, a formation of an aqua-cation complex ($[Mn(CO)_3(H_2O)(DIPIMP)]^+$) is observed in solution. However, upon saturation with CO_2 no additional processes (intermediate bicarbonate complex reduction) or current enhancement below -2 V are observed and the anodic peak due to oxidation of $[Mn(CO)_3(DIPIMP)]^-$ does not fully disappear. This suggests that the reduced complex is less prone to interact with CO_2, as would be expected due to the increased steric hindrance and structural rigidity of the complex arising from the two iPr- substituents at the N-phenyl rings.

Table 5.3 Cathodic potentials (V, vs. Fc/Fc$^+$) of the parent complexes $[MnBr(CO)_3(IP)]$ (1 mM, acetonitrile, 0.2 M $[Bu_4N][PF_6]$) and corresponding cationic Mn–aqua derivatives formed *in situ* by partial hydrolysis

Complex	$E_{p,c}$	Catalytic potential[b]
$[MnBr(CO)_3(IMP)]$ (**1**) $[Mn(CO)_3(H_2O)(IMP)]^+$	-1.41, -1.54[a] -1.28	-2.21
$[MnBr(CO)_3(IPIMP)]$ (**2**)	-1.49	-2.26
$[Mn(CO)_3(H_2O)(IPIMP)]^+$	-1.29	
$[MnBr(CO)_3(DIPIMP)]$ (**3**)	-1.44	-2.16
$[Mn(CO)_3(H_2O)(DIPIMP)]^+$	-1.23	
$[MnBr(CO)_3(TBIMP)]$ (**4**)	-1.45	~ -2.28
$[MnBr(CO)_3(TBIEP)]$ (**5**)	-1.53	-2.18
$[Mn(CO)_3(H_2O)(TBIEP)]^+$	-1.35	

This process probably corresponds to a reduction of the dimer; [b]Corresponding to the peak cathodic potential under CO_2. These are largely coinciding with the reduction of a bicarbonate complex (see the spectroelectrochemical section).

5.3.4 IR and UV-Vis Spectroelectrochemistry under Inert Atmosphere

IR spectroscopy[20] is an ideal tool to monitor the cathodic processes in the studied complexes, due to presence of the carbonyl ligands as strong IR reporters. Table 5.2 lists the key experimental and calculated vibrational frequencies for the starting complexes and several relevant intermediate and dimer species. IR spectroelectrochemistry (IR-SEC) was used to probe the intermediates produced upon reduction and to monitor their presence during CO_2 reduction.

IR spectra of MnTBIEP (Figure 5.7) show, upon the first reduction, depletion of the parent $\nu(CO)$ bands, with new bands growing in at 1922 cm^{-1}, 1898 cm^{-1} and a broad feature at 1814 cm^{-1}. The bands at 1922 cm^{-1} and 1814 cm^{-1} can be assigned to the five-coordinate anion [Mn(CO)$_3$(TBIEP)]$^-$, an assignment supported by DFT calculations. The band at 1898 cm^{-1}, which grows in after the five-coordinate anion begins to form, could tentatively be attributed to a decomposition product. UV/Vis spectroelectrochemistry (see appendix 2) supports this notion as only a band at ca. 570 nm has been detected, which corresponds to the five-coordinate anion. Differently from the MnIMP and MnIPIMP complexes (see below), there is no indication of a dimer ([Mn(CO)$_3$(TBIEP)]$_2$) formation during the reduction of MnTBIEP on the timescale of the experiments performed.
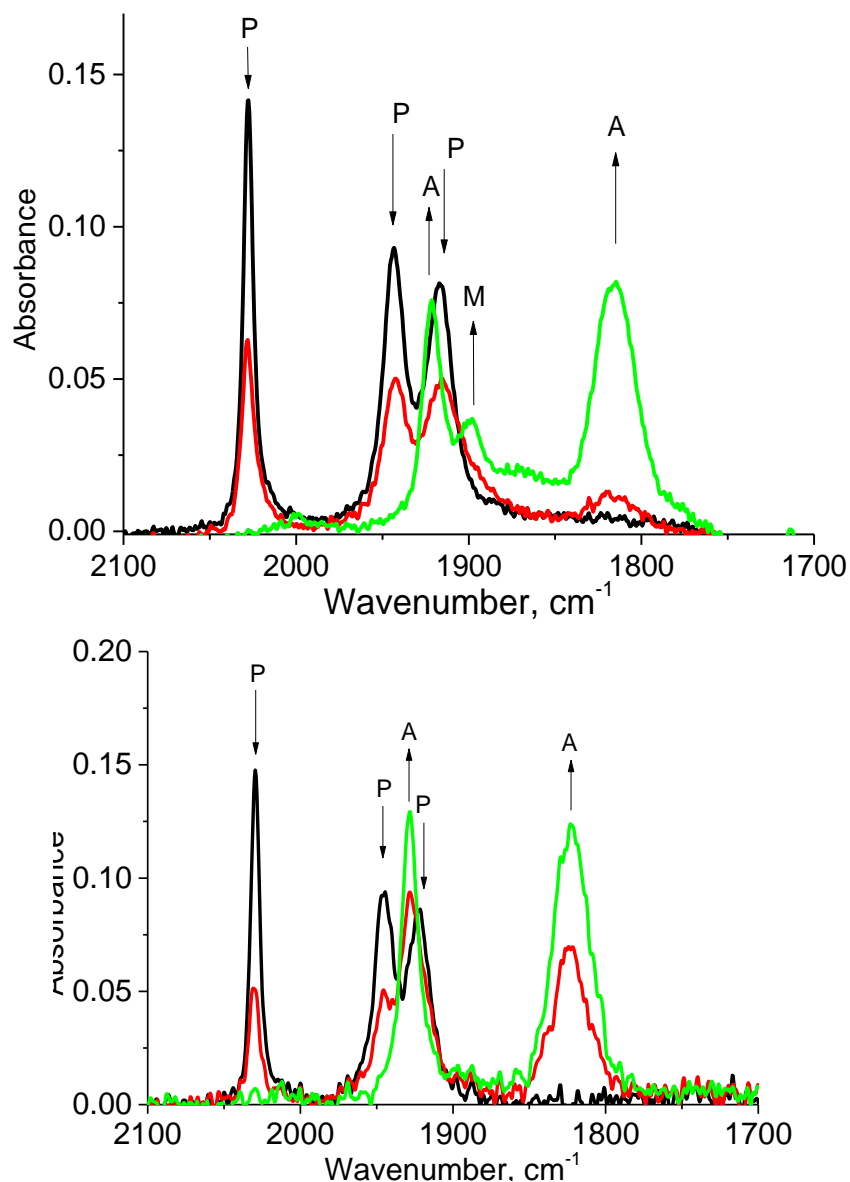
Figure 5.7 IR spectral changes accompanying *in situ* **reduction of complexes in Ar-saturated acetonitrile/0.2 M [Bu₄N][PF₆] within an OTTLE cell.** *Top panel:* **For MnTBIEP, A direct reduction of the parent complex (black line) to 5-coordinate anion (green line) is observed. (P) [MnBr(CO)₃(TBIEP)]; (A) [Mn(CO)₃(TBIEP)]⁻; (M) an unassigned side product.** *Bottom panel:* **For MnTBIMP, A direct reduction of the parent complex (black line) to 5-coordinate anion (green line) is observed. (P) [MnBr(CO)₃(TBIMP)]; (A) [Mn(CO)₃(TBIMP)]⁻.**

MnTBIMP mirrors the behaviour of MnTBIEP with the bands at 2029, 1945 and 1923 cm⁻¹ corresponding to the parent complex being replaced concertedly with bands at 1928 and 1823 cm⁻¹ corresponding to the five-coordinate anion, with no intermediate species being observed. This would suggest that the direct formation of the five-coordinate anion is due to the steric demands of the ᵗBu group, since the mono-ⁱPr derivative **2** does exhibit dimer formation (Table 5.2).

The results of the IR-SEC study of MnIMP are shown in Fig. 5.8. The first reduction of MnIMP in CH₃CN under an Ar atmosphere is accompanied by depletion of the parent IR bands at 2029, 1941

and 1926 cm^{-1}. Simultaneously, it shows the growth of new bands at 1994, 1949, 1902 and 1875 cm^{-1}, which are characteristic of the Mn–Mn dimer[8,9,13,30] [Mn(CO)$_3$(IMP)]$_2$. Additionally, a peak at 2051 cm^{-1} grows in initially, which is assigned to the intermediate aqua-cation [Mn(CO)$_3$(H$_2$O)(IMP)]$^+$ observed also by cyclic voltammetry. Further reduction of the dimer leads to formation of broad absorption bands at 1826 cm^{-1} and 1930 cm^{-1}, once the formation of the dimer species is complete. These features are characteristic of the formation of the five-coordinate anion,[8,9,13] [Mn(CO)$_3$(IMP)]$^-$. UV-Vis spectroelectrochemistry performed in parallel with the IR-SEC experiment confirms the presence of both of these species (see appendix 2) via the broad absorption band at ca. 800 nm (assigned to the dimer) and the intense absorption at ca. 675 nm (assigned to the five-coordinate anion).[8] All compounds in the IMP sub-series exhibited a small transient peak at ca. 2050 cm^{-1} upon reduction. This is assigned to the aqua-complex [Mn(CO)$_3$(H$_2$O)(IMP)]$^+$.
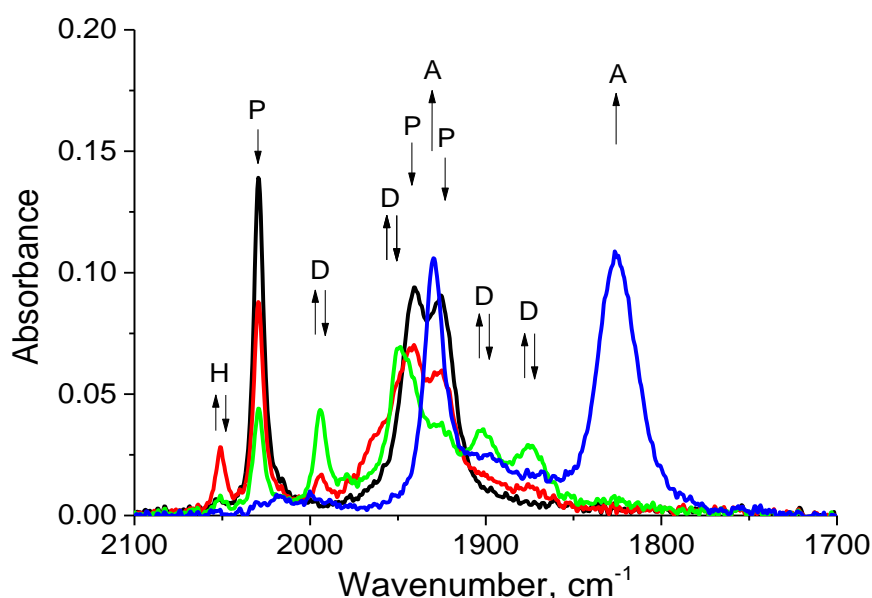
Figure 5.8 IR spectral changes accompanying *in-situ* reduction of MnIMP in Ar-saturated acetonitrile / 0.2 M [Bu$_4$N][PF$_6$] within an OTTLE cell. The parent complex [MnBr(CO)$_3$(IMP)] (P, black line), and aqua-cation [Mn(CO)$_3$(H$_2$O)(IMP)]$^+$ (H, additional features in the red spectrum) are reduced to a dimer [MnBr(CO)$_3$(IMP)]$_2$ (D, green line) followed by reduction of the dimer to 5-coordinate anion [Mn(CO)$_3$(IMP)]$^-$ (A, blue line). The intermediate spectrum (red line) recorded between those of the parent complex and the dimer also shows the features of the aqua-complex.

Differently to MnIMP, MnIPIMP showed concurrent formation of the dimer and the five-coordinate anion upon reduction of the parent complex (Figure 5.9, top). The introduction of the isopropyl substituent at the phenyl ring leads to the observation of a small amount of five-coordinate anion [Mn(CO)$_3$(IPIMP)]$^-$ (absorbing at 1929 cm^{-1} and 1824 cm^{-1}), which grows in alongside peaks indicative of dimer formation (1981, 1949, 1901, 1882 and 1862 cm^{-1}).

Importantly, the IR absorption bands, corresponding to both the dimer and the five-coordinate anion, grew in simultaneously. UV-Vis spectroelectrochemistry confirmed the presence of both dimer and five-coordinate species in this case.

In contrast, only the five-coordinate anion detected already from the onset of the reduction of MnDIPIMP under the experimental conditions used. In this case, there is no evidence for the dimer formation during the reduction of parent complex. As shown in Figure 5.9 (bottom), an intense peak at 1823 cm^{-1}, assigned to the five-coordinate anion, grew in, followed closely by smaller peaks at 2007 cm^{-1}, and 1899 cm^{-1}. The second peak assigned to the five-coordinate anion at 1929 cm^{-1} was masked by the absorption of the parent complex at the beginning of the reduction process. We tentatively assign the peaks at 2007 cm^{-1} / 1899 cm^{-1} to a solvent coordinated radical species [Mn(CO)$_3$(MeCN)(DIPIMP)]$^{\bullet}$, on the analogy with [Re(CO)$_3$(PrCN)(iPr-PyCa)][17] (where iPr-PyCa = iso-propyl-imino-pyridine; PrCN = butyronitrile) which shows ν(CO) at 2005 cm^{-1} and 1885(br) cm^{-1}. Further, since the anodic wave of the dimer oxidation is not observed in the CV of MnDIPIMP, but a 1electron reduced radical species are observed in IR-SEC, it is evident that the DIPIMP ligand prevents dimerisation.

MnTBIMP shows an intermediate behaviour to MnTBIEP and MnIPIMP: similarly to MnTBIEP, the ^{t}Bu substituent prevent dimer formation upon reduction; however, differently to MnTBIEP, and similar to MnIPIMP, a rapid reaction with CO$_2$ takes place, which in case of MnTBIEP is considerably slowed down by the R = Me group. It is important to note that if Mn–Mn dimer is reduced at the same, or even less negative potentials, than the parent complex, it will not be detected in the studies.[9] Thus the comments above regarding the absence of dimer formation only relate to the Br-complexes studied here. Substituting Br^{-} with a different group, which would lead to the parent complex being reduced at less negative potentials, it may become possible to detect these species.
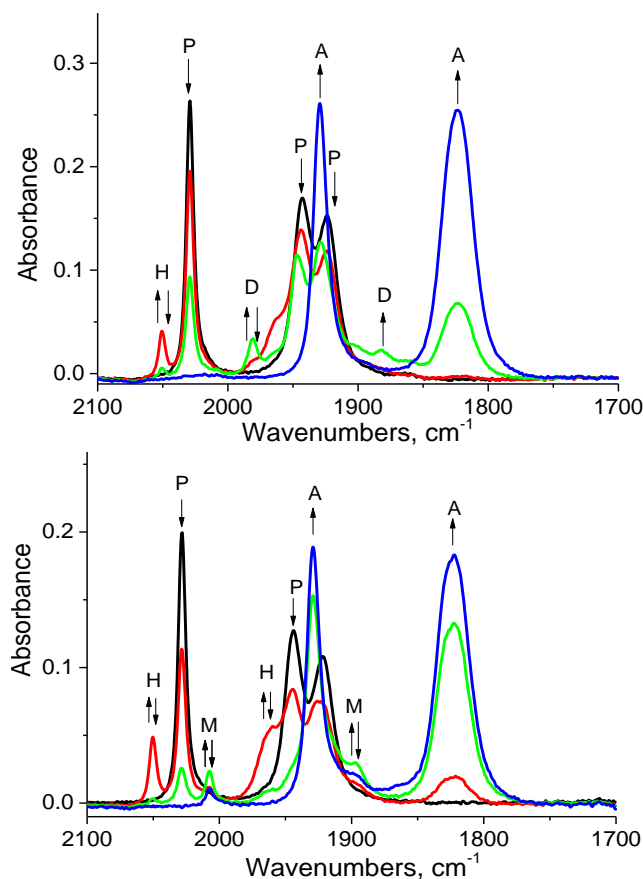
Figure 5.9 IR spectral changes accompanying *in situ* reduction of the complexes in Ar-saturated acetonitrile/0.2M [Bu$_4$N][PF$_6$] within an OTTLE cell.

Top panel: **MnIPIMP, concurrent formation of a dimer and a 5-coordinate anion on reduction of the parent complex is observed. (P) [MnBr(CO)$_3$(IPIMP)]; (D) [Mn(CO)$_3$(IPIMP)]$_2$; (A) [Mn(CO)$_3$(IPIMP)]$^-$; (H) [Mn(CO)$_3$(H$_2$O)(IPIMP)]$^+$.** *Bottom panel:* **MnDIPIMP, reduction of parent complex to 5-coordinate anion is observed. (P) [MnBr(CO)$_3$(DIPIMP)]; (A) [Mn(CO)$_3$(DIPIMP)]$^-$; (H) [Mn(CO)$_3$(H$_2$O)(DIPIMP)]$^+$; (M) [Mn(CO)$_3$(MeCN)(DIPIMP)]$^\bullet$.**

Five-coordinate complex formation appears to correlate with a less negative first reduction potential (see Table 5.3). A comparable correlation was found for Mn–R-DAB complexes and sterically hindered 2,2′-bipyridines already reported in the literature. These complexes also exhibit less negative 1st reduction potentials in comparison to their less sterically hindered counterparts, and form five-coordinate anions directly upon reduction.[8,25]

5.3.5 IR and UV-vis Spectroelectrochemistry under CO$_2$ Atmosphere

Electrochemical behaviour under a CO$_2$ atmosphere is vastly different to that under N$_2$ or Ar atmosphere. The electrocatalytic reduction of CO$_2$ with the four Mn complexes can be described in terms of three different types of behaviour, largely controlled by the steric hindrance of the active imino C=N bond. The MnIMP and MnIPIMP are relatively unhindered and the catalytic behaviour is almost identical. The initial reduction of parent and/or the cationic aqua complex results in the

formation of the 2-electron reduced five-coordinate anion that reacts efficiently with CO_2, no dimer is observed during the reduction of MnIMP (Figure 5.10) or MnIPIMP (Figure 5.11).
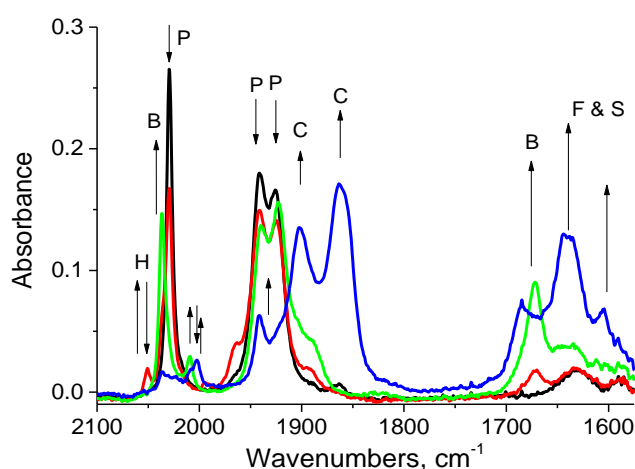
Figure 5.10 IR spectral changes accompanying in situ reduction of MnIMP ([MnBr(CO)$_3$(IMP)]) in CO$_2$-saturated acetonitrile/0.2M [Bu$_4$N][PF$_6$] within an OTTLE cell. (P) [MnBr(CO)$_3$(IMP)]; (B) [Mn(CO)$_3$(IMP)(η^1-OCO$_2$H)]; (C) [Mn(CO)$_5$]$^-$; (H) [Mn(CO)$_3$(H$_2$O)(IMP)]$^+$; (F & S) free bicarbonate (OCO$_2$H$^-$) and subordinate formate (OCHO$^-$) accompanying the catalytic reduction of CO$_2$ to CO.

The catalytic process at the initial cathodic wave is however inhibited by the rapid formation of a stable bicarbonate complex, absorbing at 2036, 1940, 1924 and 1671 cm^{-1} for the IPIMP, in line with the reports for sterically hindered Mn–mesityl-bipyridine[25] complexes and Mn–R-DAB complexes[8]. Further negative potential shift of ca. 0.7 V is needed to reduce the bicarbonate complex, resulting in the recovery of the five-coordinate anion that triggers the catalytic conversion of CO_2.
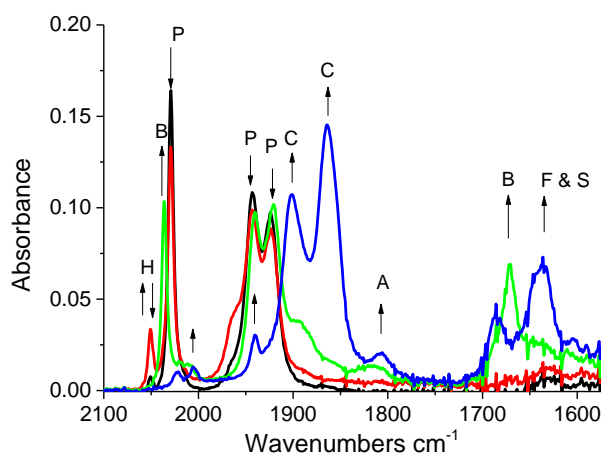
Figure 5.11 IR spectral changes accompanying in situ reduction of MnIPIMP ([MnBr(CO)$_3$(IPIMP)]) in CO$_2$-saturated acetonitrile / 0.2M [Bu$_4$N][PF$_6$] in an OTTLE cell. (P) [MnBr(CO)$_3$(IPIMP)]; (A) [Mn(CO)$_3$(IPIMP)]$^-$; (B) [Mn(CO)$_3$(IPIMP)(η^1-OCO$_2$H)]; (C) [Mn(CO)$_5$]$^-$; (H) [Mn(CO)$_3$(H$_2$O)(IPIMP)]$^+$; (F & S) free bicarbonate (OCO$_2$H$^-$), subordinate formate (OCHO$^-$) accompanying the catalytic reduction of CO$_2$ to CO.

For the non-hindered IMP and IPIMP ligands the five-coordinate anion reacts rapidly and is not observed in the IR spectra on this timescale (for IMP) and only at a low concentration (for IPIMP). The production of CO in the thin-solution layer results in the displacement of the α-diimine ligand in the five-coordinate anion, forming the pentacarbonyl species $[Mn(CO)_5]^-$ clearly seen in the IR spectra via the growth of bands at 1897 and 1865 cm^{-1} (species "C" in Figs 5.10-5.13). Remarkably, in these two cases only comparatively small amount of free bicarbonate or free formate (1685, 1638 and 1604 cm^{-1} for the IPIMP species) relative to $[Mn(CO)_5]^-$ is observed, marking the high catalytic efficiency towards CO production.
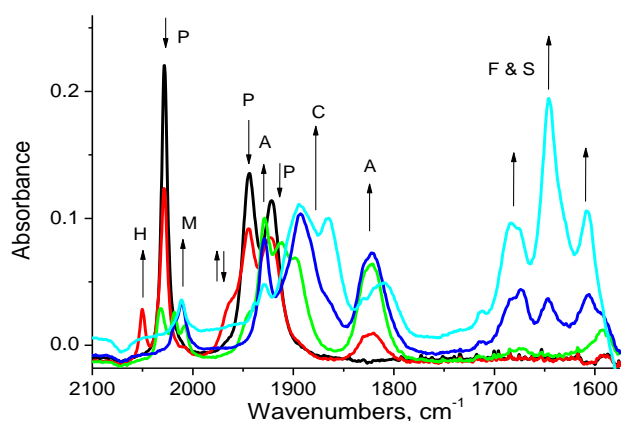
Figure 5.12 IR spectral changes accompanying in situ reduction of MnDIPIMP in CO$_2$-saturated acetonitrile / 0.2M [Bu$_4$N][PF$_6$] within an OTTLE cell. (P) [MnBr(CO)$_3$(DIPIMP)]; (A) [Mn(CO)$_3$(DIPIMP)]$^-$; (B) [Mn(CO)$_3$(DIPIMP)(η^1-OCO$_2$H)]; (H) aqua-complex [Mn(CO)$_3$(H$_2$O)(DIPIMP)]$^+$; (C) [Mn(CO)$_5$]$^-$; (M) [Mn(CO)$_3$(MeCN)(DIPIMP)]$^•$; (F & S) free bicarbonate (OCO$_2$H$^-$) and subordinate formate (OCHO$^-$).

Upon reduction of the more C=N-hindered DIPIMP complex, the five-coordinate anion formed does not react with CO$_2$ efficiently and a metastable population of the anionic five-coordinate MnDIPIMP species, $[Mn(CO)_3(DIPIMP)]^-$, is detected even under high excess of CO$_2$. Interestingly, and differently from the other complexes in the Mn-IP series, the formation of a bicarbonate complex is only detected at the potential corresponding to the reduction of CO$_2$-associated species at around -2 V vs Fc/Fc$^+$, whilst prior coordination of CO$_2$ to the five-coordinate anion at the parent MnDIPIMP cathodic wave no bicarbonate ligand signature not detected. At the catalytic potential where the bicarbonate complex is reduced the conversion of CO$_2$ to CO is also inefficient. High concentration of the five-coordinate anion is still seen, converting slowly to $[Mn(CO)_5]^-$ when the concentration of CO increases; at the same time the production of free bicarbonate (and free formate) is much higher compared to the MnIMP and MnIPIMP cases, marking the low catalytic efficiency toward CO production. Notably, the lower CO-stretching band of $[Mn(CO)_3(DIPIMP)]^-$ becomes shifted from its standard position (1829/2 cm^{-1}) to lower energy (ca. 1810 cm^{-1}) at the advanced stage of the catalytic conversion. This shift may indicate the presence of an observable adduct of the five-coordinate anion, most likely with CO$_2$ or formate (over the Mn–N=C bond). In this context it is interesting to note that

the related Re-IP complex[37] forms the carbonate complex in two 1e-reduction steps, via a direct coordination to the Re centre, without C=N being directly involved.

In the case of MnTBIEP the imino C=N bond is hindered both at the carbon atom via the methyl group and by the t-butyl group on the phenyl moiety. There are similarities but also differences with the hindered DIPIMP complex, which does not have a hindering group at the C-atom of the imino C=N moiety. Upon reduction of the parent complex in CO_2 saturated acetonitrile the five-coordinate anion $[Mn(CO)_3(TBIEP)]^-$ coordinates CO_2 forming the bicarbonate complex readily (similar to IMP and IPIMP) with the characteristic IR absorption band at 1673 cm^{-1}.[8,30]

A small amount of the five-coordinate anion $[Mn(CO)_3(TBIEP)]^-$ is observed in the initial step. Lowering the potential to around -1.5 V vs Fc/Fc$^+$ results in catalytic conversion of the bicarbonate complex, however, similar to MnDIPIMP this conversion is not efficient compared with MnIMP and MnIPIMP. This is shown via the slower growth of $[Mn(CO)_5]^-$ compared to IPIMP and the greater quantities of free bicarbonate produced. As with MnDIPIMP the five-coordinate anion 'adduct' form is observed with the lower energy CO-stretching band shifted to a lower wavenumber (from 1814 to 1803 cm^{-1}). Thus, hindering the imine C atom does not affect adduct formation between CO_2 and $[Mn(CO)_3(TBIEP)]^-$.
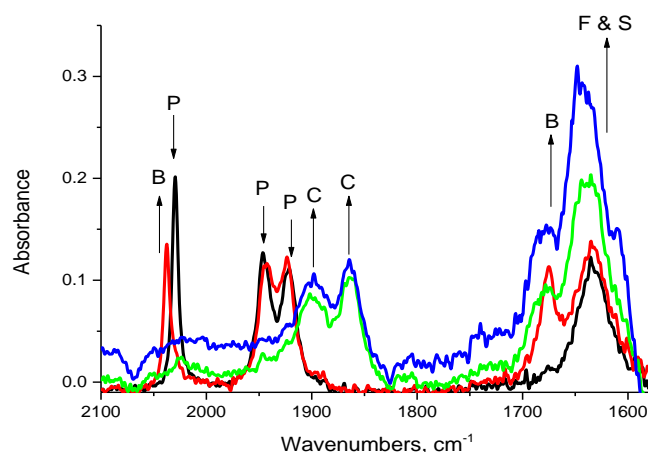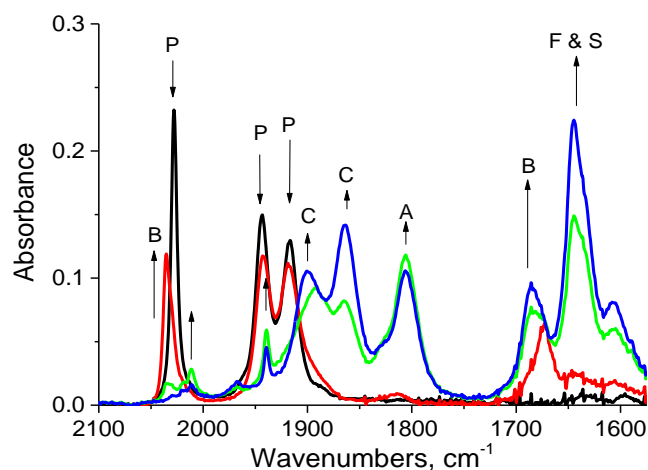
Figure 5.13 IR spectral changes accompanying in situ reduction of complexes in CO_2-saturated acetonitrile/0.2 M [Bu₄N][PF₆] within an OTTLE cell. Top panel: For MnTBIEP, (P) [MnBr(CO)₃(TBIEP)]; (A) [Mn(CO)₃(TBIEP)]⁻; (B) [Mn(CO)₃(TBIEP)(η¹-OCO₂H)]; (C) [Mn(CO)₅]⁻; (F & S) free bicarbonate (OCO₂H⁻) and formate (OCHO⁻) accompanying the catalytic reduction of CO_2 to CO. Bottom panel: For MnTBIMP, (P) [MnBr(CO)₃(TBIMP)]; (B) [Mn(CO)₃(TBIMP)(η¹-OCO₂H)]; (C) [Mn(CO)₅]⁻; (F & S) free bicarbonate (OCO₂H⁻) and formate (OCHO⁻) accompanying the catalytic reduction of CO_2 to CO.

However, at the negative potentials where the bicarbonate complex is reduced (recovering the catalytic five-coordinate anion) the hindrance provided by the methyl and ᵗBu groups also negatively affects the catalytic formation of CO_2 to CO (as evidenced by large amounts of free bicarbonate and slow formation of [Mn(CO)₅]⁻ at lower CO concentration. It is not very clear whether this greater hindrance is due directly to the presence of the methyl group on the C position or whether this is due to the ᵗBu group inhibiting rotation of the phenyl moiety and preventing the five-coordinate anion from adopting a more suitable (pyramidal) geometry for CO_2 association.

Again MnTBIMP behaves in a similar fashion to MnTBIEP. Upon reduction the parent complex rapidly associates CO_2 forming the bicarbonate complex, as the reduction potential is lowered further the bicarbonate complex is reduced forming CO which is able to displace the TBIMP and forming [Mn(CO)₅]⁻. One important difference is that significantly less (if any) five-coordinate anion is observed in the presence of CO_2 than was the case with both MnTBIEP and MnDIPIMP. This

131

suggests that ^tBu is not as sterically demanding as two ^iPr groups in these systems as CO_2 is still able to coordinate.

5.3.6 Estimation of Electrocatalytic Activity towards CO Production

Despite the inherent difficulty of generating data that can be used to meaningfully compare different catalysts we were recommended by peers to attempt to compare the performance of these catalysts (this issue is discussed further in chapter 8). Due to our concerns about how comparable and robust the quantitative techniques commonly used are two different methods were used to evaluate performance of the catalysts: gas chromatography and comparison of current enhancement.

5.3.6.1 Comparison of performance Using Gas Chromatography

In order to try and increase the number of data points before catalyst breakdown occurred gas samples were run using an isothermal method developed in chapter 8 in order to try and provide higher quality data than the ramping method used in other chapters. The detector response for each run is shown in figure 5.14 and shows that MnIMP appears to consistently outperform the other catalysts and that Mnbpy is only about as effective as the more sterically hindered complexes. This data has been included so as to provide the raw results as the TCD response cannot be misinterpreted, however, in order to attempt to quantify the relative performance of the catalysts an estimation of the amount of CO in the headspace is required. To translate the TCD detector response into a quantitative output is not trivial and calibration techniques such as calibration curves problems in using them are discussed in chapter 8. The method ultimately settled upon was to convert the TCD response to % CO using the response of the atmospheric oxygen and nitrogen.

The background to this was a technique employed by a prior PhD student in the group which involved comparing the TCD response of gas mixtures of 2 % CO with 2 % methane and 0 % CO with 2 % methane. Using the methane as an internal standard it would therefore be possible to calculate experimentally the % of CO in the headspace.[55] The problem with using this method to determine the CO concentration in our experimental set up was that we did not have access to solutions of 2 % CO and we doubted how effective a one point calibration curve would be. In order to get around this problem it was decided to use other gases in order to calibrate the TCD, atmospheric oxygen and nitrogen.

During the preparation of the experimental set up the solution is purged with CO_2 in order to saturate the solvent. This results in the concentration of CO_2 in the headspace increasing at the expense of N_2 and O_2. It is assumed that due to the similar polarity and size of these gases that during the purging of the solution the concentration of N_2 and O_2 in the headspace changes at the same rate and that their relative distribution in the headspace is the same as that for atmospheric N_2 and O_2. Because N_2 and O_2 are by far the largest components of the atmosphere it has been assumed that together they make up 100 % of the atmosphere with relative percentages of 80.23 % and 19.77 % respectively. In order

to determine the TCD response of atmospheric N_2 and O_2 three readings of atmospheric gas were taken and the average response calculated as shown in table 5.4. From this the response of the O_2 and N_2 peaks in the GC run could be used to estimate the concentration of these gases in the headspace at the start of the experiment using equation 5.1

$$\frac{\text{Headspace gas } \mu Vs^{-1}}{\text{Atmospheric gas } \mu Vs^{-1}} \times \textbf{Atmospheric gas } \% = \textbf{Headspace gas } \% \quad \textbf{Equation 5.1}$$

Table 5.4 TCD response to Atmospheric composition, N₂ and O₂

	Run 1 μVs^{-1}	Run 2 μVs^{-1}	Run 3 μVs^{-1}	Average μVs^{-1}	Atmosphere %
N_2	117233.96	116745.46	116193.66	116724.36	80.23
O_2	28881.55	28790.1	28621.8	28764.48333	19.77

Using the combined values of TCD response and the estimated percentages of the gases we can estimate what response in μVs^{-1} 1 % of CO would yield, this gave a reasonably consistent result of 1 % = 1454.88 μVs^{-1} in each experiment. From this value the percentage of CO in the headspace could be estimated.

Table 5.5 calculation of % CO in the head space for Mnbpy (run number 2)

Time S	O_2 μVs^{-1}	N_2 μVs^{-1}	CO μVs^{-1}	CO %	Combined μVs^{-1}	1 % μVs^{-1}
0	1769.85	7069.96	0	0	8839.81	1454.88764
60			0	0		
300			62.61	0.04303		
567			81.13	0.05576		
826			111.91	0.07692		
1071			123.53	0.08491		
1321			146.97	0.10102		
1569			149.64	0.10285		
1800			112.89	0.07759		
	% = 1.21643	% = 4.85951			% = 6.07594	
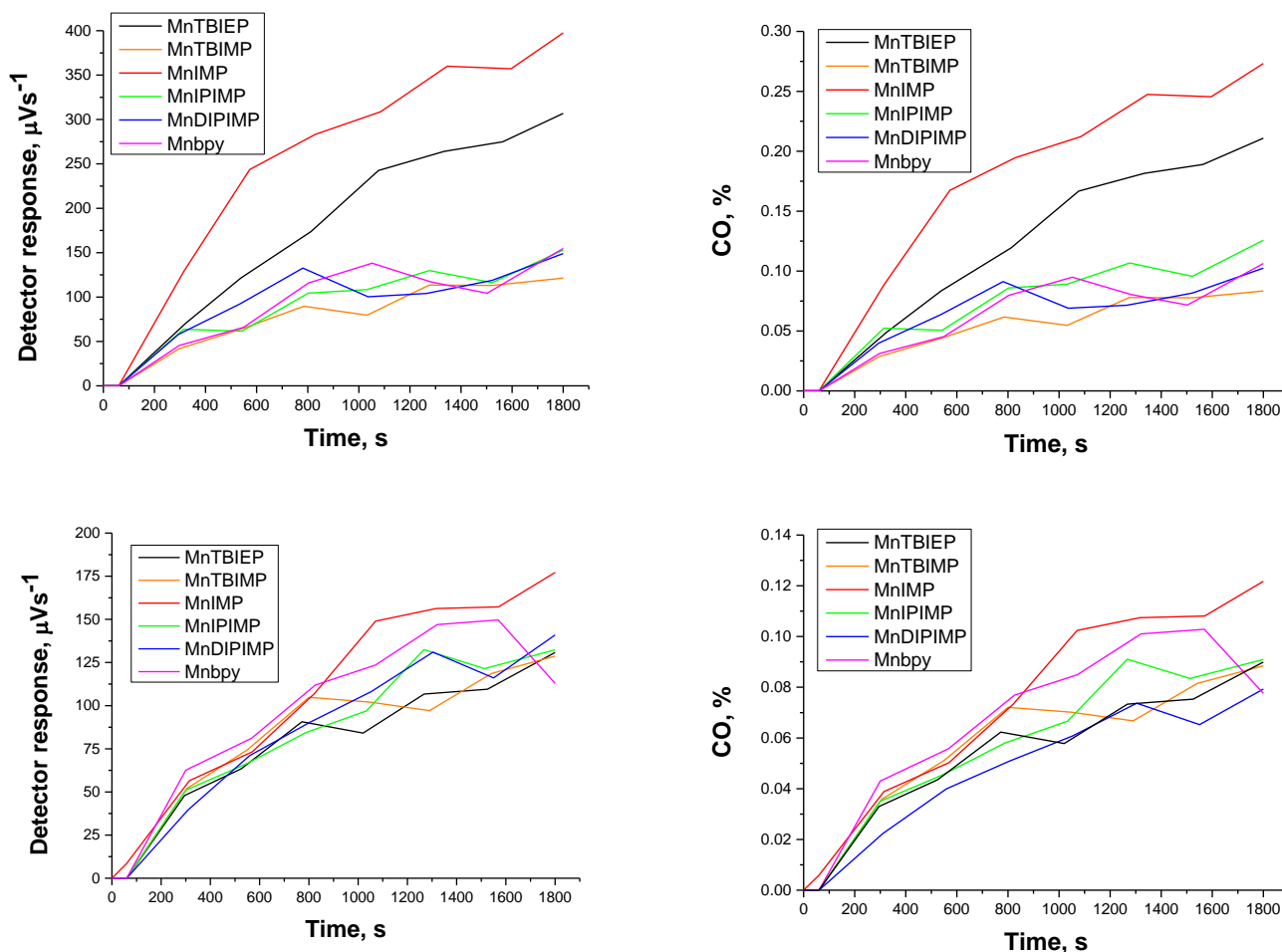
Figure 5.14 Headspace CO values from run 1 (top) and run 2 (bottom); TCD response (left) and estimated CO concentration (right).

As can be seen in figure 5.14 the CO of the head-space in the electrolysis cell shows a gradual build-up of CO in the course of the electrolysis. By comparing the catalysts with the performance of [MnBr(CO)$_3$(bpy)] under identical conditions the efficiency of CO production for the catalysts (**1-5**) is comparable to that of [MnBr(CO)$_3$(bpy)], with the least sterically hindered, MnIMP complex appearing to be somewhat more efficient although these results should certainly be viewed with caution due to the many factors that may influence the result.

Due to the large volumes used in the experiment, considerable secondary processes occur during bulk electrolysis, manifested in the loss of the initial intense yellow/red colour of the solution as the reaction progressed, which was concomitant with an increase in current towards the end of the electrolysis. These deviations from an ideal behaviour suggests that as CO$_2$ is depleted in solution, competing catalyst degradation pathways begin to occur, precluding reliable estimates of efficiencies. This behaviour was consistently observed in all bulk electrolysis experiments carried out in this and other chapters.

5.3.6.2 Comparison of performance using cyclic voltammetry

In order to provide a more usable estimation of catalyst performance CV data was used to calculate the relative i_{cat}/i_p values (The CV traces used to calculate these values of which are shown in appendix 2). The method used was the same as that used by Smeija *et al.* described in reference 4 and Lau *et al.* in reference 6. Comparing the current values detected in cyclic voltammograms recorded under identical conditions at -2.24 V vs. Fc/Fc$^+$ under CO_2 and N_2 atmosphere in an acetonitrile/water shows that the catalytic current enhancement of **1-5** is comparable to one another, and is comparable to that of [MnBr(CO)$_3$(bpy)] with approximately 30-60% of the observed current enhancement. Because the performance of electrocatalysts is directly related to the applied over potential it was important to record values at the same voltage for each catalyst. It is important to note that most sterically protected, MnDIPIMP and MnTBIEP, seem to perform better as far as i_{cat}/i_p values are concerned, but that the least sterically hindered MnIMP is the most efficient in the series. These observations are different to the observation of the MnTBIMP producing more CO than [MnBr(bpy)(CO)$_3$] in the bulk electrolysis/GC experiments. Whilst these data can only be considered in relative terms, they do show the potential of these complexes to act as a test-bed for optimizing steric vs. electronic effects in CO_2 reduction, whereby the thermodynamic factors, the rate of CO_2 coordination, and the rate of decomposition of catalyst precursor species, need to be balanced.

Table 5.6 i_{cat}/i_p values estimated from the CV's recorded under CO_2 in CH_3CN/H_2O and the corresponding CVs recorded under 2 in CH_3CN/H_2O using a glassy carbon working electrode with a 3 mm diameter. All values were calculated at -2.24 V vs Fc/Fc$^+$.

Complex	$\dfrac{i_{cat}}{i_p}$	Relative activity to [MnBr(CO)$_3$(bpy)]
MnIMP	2.4	0.47
MnIPIMP	1.8	0.35
MnDIPIMP	2.4	0.5
MnTBIMP	1.6	0.3
MnTBIEP	2.1	0.4
Mnbpy	5.2	1

5.3.7 Hydrolysis investigation

The results of the IR-SEC studies suggested that MnTBIEP was more resistant to hydrolysis that the IMP subseries due to the clear observation of the aqua cation [Mn(CO)$_3$(diimine)(H$_2$O)]$^+$ for all of the

Imp subseries. In order to determine if that was the case IR spectra were taken over the course of an hour of solution of MnTBIEP and MnIPIMP (chosen due to similar steric properties of the ligands) at rest potential in a 91.5/8.5 % acetonitrile/water mixture. The results showed that MnTBIEP is much more prone to spontaneous hydrolysis than MnIPIMP (figure 5.15) at rest potential. The solutions of MnTBIEP and MnIPIMP (which had been kept in darkness) showed nearly complete hydrolysis after 4 days, with no sign of other degradation products (see IR spectra in Figure5.16) suggesting that when no current is applied the aqua complexes are stable. Since the aqua complex is also a catalyst precursor and not a deactivation pathway for catalysis this is an attractive quality.
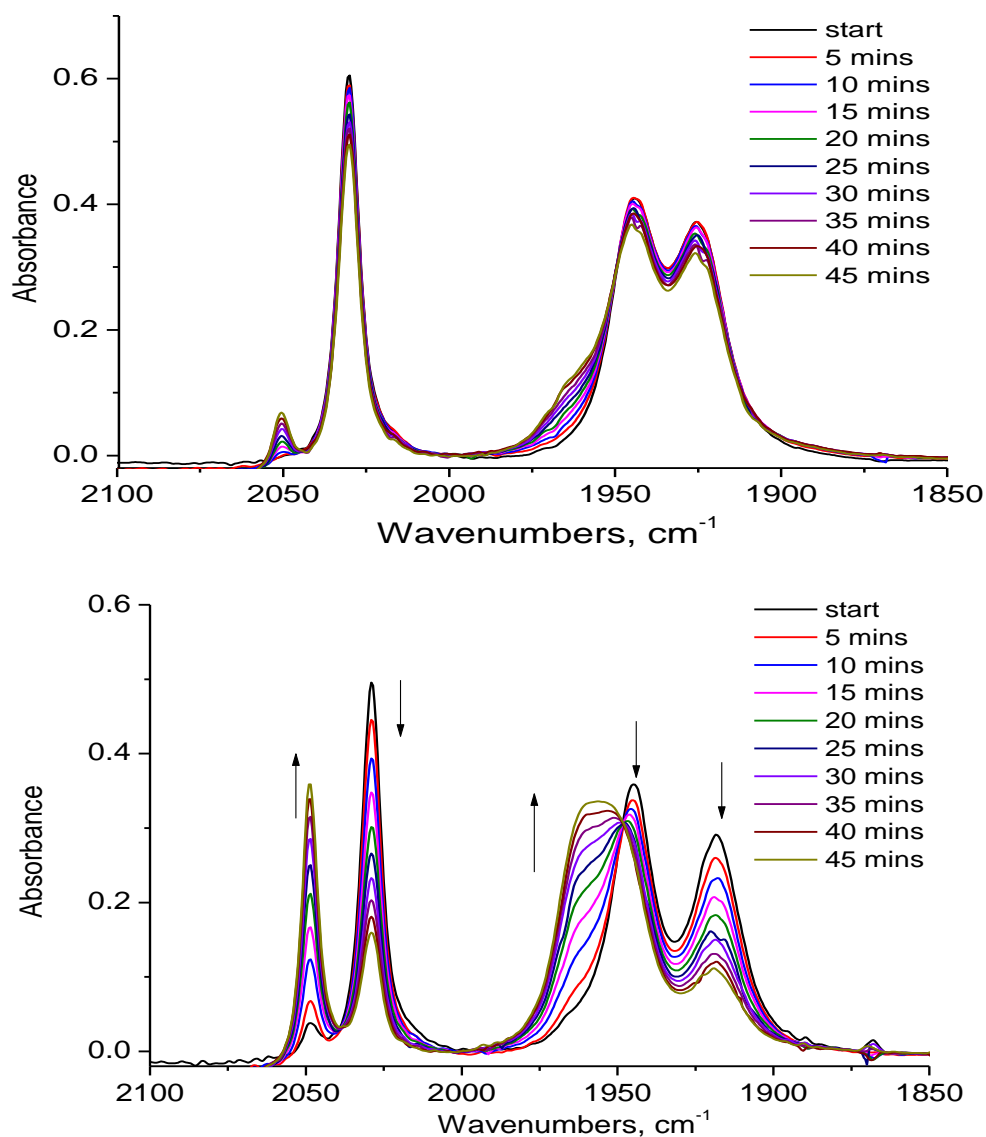
Figure 5.15 IR spectra of MnIPIMP (top), and MnTBIEP (bottom) in 91.5/8.5% acetonitrile/water at rest potential show growth of the IR absorption bands attributed to the aqua-cations [Mn(CO)$_3$(diimine)(H$_2$O)]$^+$.
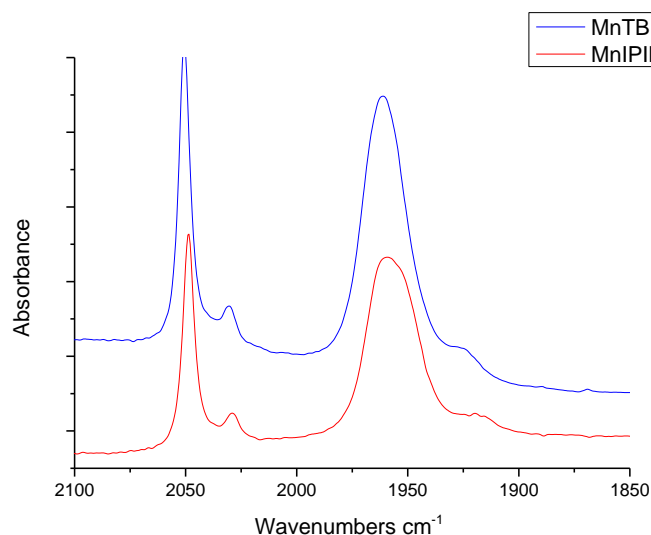
Figure 5.16 IR spectra of MnTBIEP and MnIPIMP in 91.5 % acetonitrile & 8.5 % water at rest potential after 4 days being kept in the dark.

5.4 Conclusions

A series of Mn(I) tricarbonyl electrocatalysts for CO_2 reduction, which employ, for the first time, asymmetric α-diimine ligands, imino-pyridines, has been developed, and their catalytic activity confirmed and evaluated in detail.

We have demonstrated through conventional and thin-layer cyclic voltammetry, UV-vis and IR spectroscopy and DFT computational analysis the π-decoupling of the phenyl from the Mn(pyridine-CCN) metallacycle. The practical effect of this feature is the ability to disentangle steric and electronic effects of the α-diimine ligand on the catalytic properties. Until now, introduction of sterically bulky groups, which are also typically electron donating, was coming at a price of the increased overpotential required for CO_2 reduction. The use of asymmetric α-diimine has allowed us to probe the effect of adding ever greater sterically demanding groups without much change in the catalytic potential. We have demonstrated that systematic increase in the steric hindrance of the R_1 & R_2 in the IMP sub-series results in the switch of the nature of the first reduction product detected on the timescale of the experiment under an inert gas atmosphere, from a dimer to a five-coordinate anion, at the very similar reduction potential. In the absence of sterically hindering groups on the phenyl ring, MnIMP, a dimer is formed, whilst increasing the steric hindrance by adding ^{i}Pr groups to the R_1 and R_2 positions (MnDIPIMP) resulted in direct formation of the five-coordinate anion in line with prior observations from similar sterically hindered ligands.[23,26] MnIPIMP (in which case the dimer may be reduced at the parent cathodic wave due to slightly negatively shifted reduction potential vs. that for MnIMP) exhibited intermediate behaviour to MnIMP and MnDIPIMP with both the dimer, and the five-coordinate anion observed forming concurrently. MnTBIMP and MnTBIEP both formed the five-coordinate anion directly upon reduction of the parent complex.

Under CO_2 atmosphere, all of the complexes reduce CO_2 to CO. The build-up of CO in the thin-layer spectro-electrochemical cell resulted in the displacement of the α-diimine ligand forming $[Mn(CO)_5]^-$. The complex containing the most sterically demanding ligand DIPIMP is, as anticipated, least susceptible to α-diimine displacement with CO, forming exclusively the five-coordinate anion upon the first reduction; it also has least propensity to coordinating CO_2, resulting in a considerable build-up of the concentration of the five-coordinate anion. An intermediate formation of the bicarbonate is also likely as the band at 1686 cm^{-1} is present at intermediate times. Of particular interest is that least sterically hindered MnIMP seemed to form a CO_2 associated complex directly upon the first reduction, with no significant formation of the dimer being observed on the timescale of the experiment. This behaviour is similar to that reported for the symmetric non-aromatic Mn–R-DAB (R = alkyl) compounds.[8,30] The formation of a stable bicarbonate complex, either through the coordination to the metal centre or via the imino C=N bond[23,37] leads to the need of increased overpotential. From that point of view, the steric hindering (protection) of the metal centre/the imino C=N bond in the Mn(IP) complexes is advantageous as it disfavours the Mn–Mn dimerisation (when comparing MnIMP with MnDIPIMP) and the formation of the bicarbonate complex. However, such steric crowding also slows down the catalytic conversion of CO_2 to CO at the negative over potentials, as can be seen in the GC data and from the i_{cat}/i_p values. A difference in the reactivity of MnTBIMP and MnTBIEP, where no dimer formation has been detected for either of the complexes in the IR-SEC experiments, but where MnTBIEP exhibits slower CO_2 due to R=CH_3 altering the HOMO-LUMO gap in comparison to the "IMP" series, as well as introducing additional steric bulk, further supports the notion that it is possible to separate steric and electronic factors to a large extent. Balancing these factors by a careful ligand design may lead to the optimal solution.

The new family of CO_2 reduction catalysts presents an exciting platform for versatile and relatively independent tuning of steric and electronic properties, offering a far greater tuneability than catalysts with aromatic bpy-based or non-aromatic R-DAB-based ligands, and abundant options to refine and optimize Mn tricarbonyl CO2 reduction catalysts

5.4 References

(1)   Morris, A. J.; Meyer, G. J.; Fujita, E. *Acc. Chem. Res.* **2009**, *42* (12), 1983–1994.

(2)   Bourrez, M.; Molton, F.; Chardon-Noblat, S.; Deronzier, A. *Angew. Chem. Int. Ed. Engl.* **2011**, *50* (42), 9903–9906.

(3)   Hawecker, J.; Lehn, J.-M.; Ziessel, R. *J. Chem. Soc, Chem. Commun.* **1984**, 328–330.

(4)   Smieja, J. M.; Benson, E. E.; Kumar, B.; Grice, K. A.; Seu, C. S.; Miller, A. J. M.; Mayer, J. M.; Kubiak, C. P. *Proc. Natl. Acad. Sci. U. S. A.* **2012**, *109* (39), 15646–15650.

(5)   Grice, K. A.; Kubiak, C. P. In *Advances in Inorganic Chemistry*; 2014; Vol. 66, pp 163–188.

(6)   Wong, K.; Chung, W.; Lau, C. *Jounal Electroanal. Chem.* **1998**, *453*, 161–170.

(7)   Smieja, J. M.; Sampson, M. D.; Grice, K. A.; Benson, E. E.; Froehlich, J. D.; Kubiak, C. P. *Inorg. Chem.* **2013**, *52* (5), 2484–2491.

(8)   Zeng, Q.; Tory, J.; Hartl, F. *Organometallics* **2014**, *33* (18), 5002–5008.

(9)   Rossenaar, B. D.; Hartl, F.; Stufkens, D. J.; Amatore, C.; Maisonhaute, E.; Verpeaux, J.-N. *Organometallics* **1997**, *16*, 4675–4685.

(10)   Grills, D. C.; Farrington, J. A.; Layne, B. H.; Lymar, S. V.; Mello, B. A.; Preses, J. M.; Wishart, J. F. *J. Am. Chem. Soc.* **2014**, *136* (15), 5563–5566.

(11)   Johnson, F. P. A.; George, M. W.; Hartl, F.; Turner, J. J. *Organometallics* **1996**, *15* (15), 3374–3387.

(12)   Smieja, J. M.; Kubiak, C. P. *Inorg. Chem.* **2010**, *49* (20), 9283–9289.

(13)   Machan, C. W.; Sampson, M. D.; Chabolla, S. a; Dang, T.; Kubiak, P. *Organometallics* **2014**, *33*, 4550–4559.

(14)   Cabeza, J. A.; García-Álvarez, P.; Gobetto, R.; González-Álvarez, L.; Nervi, C.; Pérez-Carreño, E.; Polo, D. *Organometallics* **2016**, *35* (11), 1761–1770.

(15)   Machan, C. W.; Stanton, C. J.; Vandezande, J. E.; Majetich, G. F.; Schaefer, H. F.; Kubiak, C. P.; Agarwal, J. *Inorg. Chem.* **2015**, *54* (17), 8849–8856.

(16)   Sieh, D.; Kubiak, C. P. *Chem. - A Eur. J.* **2016**, *22*, 10638–10650.

(17)   Riplinger, C.; Sampson, M. D.; Ritzmann, A. M.; Kubiak, C. P.; Carter, E. A. *J. Am. Chem. Soc.* **2014**, *136*, 16285–16298.

(18)   Franco, F.; Cometto, C.; Ferrero Vallana, F.; Sordello, F.; Priola, E.; Minero, C.; Nervi, C.; Gobetto, R. *Chem. Commun. (Camb).* **2014**, *50* (93), 14670–14673.

(19)   Bourrez, M.; Orio, M.; Molton, F.; Vezin, H.; Duboc, C.; Deronzier, A.; Chardon-Noblat, S. *Angew. Chem. Int. Ed. Engl.* **2014**, *53* (1), 240–243.

(20)   Sullivan, B. P.; Bolinger, C. M.; Conrad, D.; Vining, W. J.; Meyer, T. J. *J. Chem. Soc., Chem. Commun.* **1985**, No. 20, 1414–1416.

(21)   Stor, G. J.; Hartl, F.; Outersterp, J. W. M. Van; Stufkens, D. J. *Organometallics* **1995**, *14* (3), 1115–1131.

(22)   Walsh, J. J.; Smith, C. L.; Neri, G.; Whitehead, G. F. S.; Robertson, C. M.; Cowan, A. J. *Faraday Discuss.* **2015**, *183*, 147–160.

(23)   Stor, G. J.; Morrison, S. L.; Stuf, D. J.; Oskamt, A. *Organometallics* **1994**, *13* (7), 2641–2650.

(24)   Sampson, M. D.; Kubiak, C. P. *Inorg. Chem.* **2015**, *54* (14), 6674–6676.

(25)   Sampson, M. D.; Nguyen, A. D.; Grice, K. A.; Moore, C. E.; Rheingold, A. L.; Kubiak, C. P. *J. Am. Chem. Soc.* **2014**, *136* (14), 5460–5471.

(26)   Agarwal, J.; Shaw, T. W.; Stanton III, C. J.; Majetich, G. F.; Bocarsly, A. B.; Schaefer III, H. F. *Angew. Chemie* **2014**, *126*, 5252–5255.

(27)   Costentin, C.; Robert, M.; Savéant, J.-M. *Chem. Soc. Rev.* **2013**, *42* (6), 2423–2436.

(28)   Sampson, M. D.; Kubiak, C. P. *J. Am. Chem. Soc.* **2016**, *138* (4), 1386–1393.

(29)   Lam, Y. C.; Nielsen, R. J.; Gray, H. B.; Goddard, W. A. *ACS Catal.* **2015**, *5* (4), 2521–2528.

(30)   Vollmer, M. V.; Machan, C. W.; Clark, M. L.; Antholine, W. E.; Agarwal, J.; Schaefer, H. F.; Kubiak, C. P.; Walensky, J. R. *Organometallics* **2015**, *34* (1), 3–12.

(31)   Agarwal, J.; Shaw, T. W.; Schaefer III, H. F.; Bocarsly, A. B. *Inorg. Chem.* **2015**, *54* (11), 5285–5294.

(32)   Stufkens, D. J.; van Outersterp, J. W. M.; Oskam, a.; Rossenaar, B. D.; Stor, G. J. *Coord. Chem. Rev.* **1994**, *132*, 147–154.

(33)   Rossenaar, B. D.; Kleverlaan, C. J.; Ven, M. C. E. van de; Stufkens, D. J.; Oskam, A.; Fraanje, J.; Goubitz, K. *J. Organomet. Chem.* **1995**, *493*, 153–162.

(34)   Sieh, D.; Lacy, D. C.; Peters, J. C.; Kubiak, C. P. *Chem. - A Eur. J.* **2015**, *21*, 8497–8503.

(35)   Gonsalvi, L.; Gaunt, J. A.; Adams, H.; Castro, A.; Sunley, G. J.; Haynes, A. *Organometallics* **2003**, *22*, 1047–1054.

(36)   Machan, C. W.; Chabolla, S. A.; Kubiak, C. P. *Organometallics* **2015**, *34* (19), 4678–4683.

(37)   Alvarez, C. M.; García-Rodríguez, R.; Miguel, D. *J. Organomet. Chem.* **2007**, *692* (26), 5717–5726.

(38)   Rountree, E. S.; McCarthy, B. D.; Eisenhart, T. T.; Dempsey, J. L. *Inorg. Chem.* **2014**, *53* (19), 9983–10002.

(39)   Costentin, C.; Drouet, S.; Robert, M.; Savéant, J.-M. *Science (80-.).* **2012**, *338*, 90–94.

(40) Costentin, C.; Drouet, S.; Robert, M.; Save, J. *J. Am. Chem. Soc.* **2012**, *134*, 11235–11242.

(41) Costentin, C.; Drouet, S.; Passard, G.; Robert, M.; Save, J. *J. Am. Chem. Soc.* **2013**, *135*, 9023–9031.

(42) Krause, L.; Herbst-Irmer, R.; Sheldrick, G. M.; Stalke, D. *J. Appl. Crystallogr.* **2015**, *48* (1), 3–10.

(43) Frisch, M. J.; Trucks, G. W.; Schlegel, H. B.; Scuseria, G. E.; Robb, M. A.; Cheeseman, J. R.; Scalmani, G.; Barone, V.; Mennucci, B.; Petersson, G. A.; Nakatsuji, H.; Caricato, M.; Li, X.; Hratchian, H. P.; Izmaylov, A. F.; Bloino, J.; Zheng, G.; Sonnenberg, J. L.; Hada, M.; Ehara, M.; Toyota, K.; Fukuda, R.; Hasegawa, J.; Ishida, M.; Nakajima, T.; Honda, Y.; Kitao, O.; Nakai, H.; Vreven, T.; Montgomery Jr., J. A.; Peralta, J. E.; Ogliaro, F.; Bearpark, M.; Heyd, J. J.; Brothers, E.; Kudin, K. N.; Staroverov, V. N.; Kobayashi, R.; Normand, J.; Raghavachari, K.; Rendell, A.; Burant, J. C.; Iyengar, S. S.; Tomasi, J.; Cossi, M.; Rega, N.; Millam, J. M.; Klene, M.; Knox, J. E.; Cross, J. B.; Bakken, V.; Adamo, C.; Jaramillo, J.; Gomperts, R.; Stratmann, R. E.; Yazyev, O.; Austin, A. J.; Cammi, R.; Pomelli, C.; Ochterski, J. W.; Martin, R. L.; Morokuma, K.; Zakrzewski, V. G.; Voth, G. A.; Salvador, P.; Dannenberg, J. J.; Dapprich, S.; Daniels, A. D.; Farkas, Ö.; Foresman, J. B.; Ortiz, J. V.; Cioslowski, J.; Fox, D. J. *Gaussian 09, Revision D.01, Gaussian, Inc., Wallingford CT*. 2013.

(44) Becke, A. D. *J. Chem. Phys.* **1993**, *98* (7), 5648–5652.

(45) Lee, C.; Yang, W.; Parr, R. G. *Phys. Rev. B* **1988**, *37* (2), 785–789.

(46) Nicklass, A.; Dolg, M.; Stoll, H.; Preuss, H. *J. Chem. Phys.* **1995**, *102* (22), 8942–8952.

(47) Dunning Jr., T. H.; Hay, P. J. Schaefer, H. F., Ed.; Plenum: New York, 1976.

(48) Krishnan, R.; Binkley, J. S.; Seeger, R.; Pople, J. A. *J. Chem. Phys.* **1980**, *72* (1), 650–654.

(49) McLean, A. D.; Chandler, G. S. *J. Chem. Phys.* **1980**, *72* (10), 5639–5648.

(50) Mennucci, B.; Tomasi, J. *J. Chem. Phys.* **1997**, *106* (12), 5151–5158.

(51) Cossi, M.; Barone, V.; Mennucci, B.; Tomasi, J. *Chem. Phys. Lett.* **1998**, *286* (3–4), 253–260.

(52) Alvarez, C. M.; García-Rodríguez, R.; Miguel, D. *Dalton Trans.* **2007**, *3* (32), 3546–3554.

(53) Bond, M.; Grabaric, B. S.; Grabaric, Z. *Inorg. Chem.* **1978**, *17* (4), 1013–1018.

(54) Bistoni, G.; Rampino, S.; Scafuri, N.; Ciancaleoni, G.; Zuccaccia, D.; Belpassi, L.; Tarantelli, F. *Chem. Sci.* **2015**, *7*, 1174–1184.

(55)   Parker, S. Anchored photo-electro-catalysts for CO2 reduction based on transition metal

          complexes, 2014.

.

6. Using asymmetric imino pyridine ligands on manganese based Lehn catalysts to investigate the effect of five-coordinate anion carbonyl stretching frequencies on catalytic current enhancement.

6.1.1 Introduction

As was discussed in chapter 2, a correlation between the carbonyl stretching frequency of the 5-coordinate anion and the current enhancement (specifically the ratio of current recorded under CO_2 over current under N_2 upon reduction at identical applied potential) was observed for the three rheniuum mesBIAN tricarbonyl comblexes investigated. In order to investigate whether this trend could be extrapolated to other Lehn-type catalysts a new series of complexes is required, which would incorporate functional groups that would affect the electronic properties (and hence the reduction potentials) of the molecule. The complexes bearing asymmetric ligands described in chapter 5[1] have shown their potential as 'lab mice' for investigating changes to steric properties complexes without effecting the electronic properties of those same complexes. Similar ligands investigated in chapter 4 have also shown the ability of effectively alter the electronics of complexes by altering the moiety on the R position with these results suggesting that asymmetric imino pyridine ligands would be ideal for such an investigation. However, functionalising in the R position (as with the TBIMP and TBIEP ligands investigated in chapter 4) presents several problems. The first problem is that synthesis of such ligands would be very challenging as the synthesis of asymmetric ligands with function groups in the R position requires pyridyl ketones as starting material, which are far less reactive than the pyridyl aldehydes used in the sythesis of the ligands investigated in chapter 5[2,3,4] to make the IMP subseries of ligands. Therefore, introducing functional groups such as esters or halogens into the R position may be more complicated than one would anticipate, especially if using strongly electron withdrawing or donating moieties. The second area of concern with such an approach is that suitable starting materials are not readily available limiting the choice of ligands to investigate. As such three new asymmetric complexes would be synthesised and studied alongside the MnIMP complex discussed in chapter 5, these complexes would be functionalised on the 4 position of the pyridine moiety of the diimine (hence referred to as the R_3 position. It was decided that manganese complexes would be investigated in this study rather than the rhenium complexes studied in chapters 3 and 4. This was because it was felt that this particular investigation would be a useful counterpart to the work studied in chapter 5 and provide more meaningful insights with the data which has already been gathered, however, investigation of the ligands used in this study on rhenium centres would certainly be an interesting area of future exploration.

These new complexes would also provide the final piece of evidence of the suitability of the asymmetric 2-(phenylimino)pyridine) ligands for separating steric and electronic effects and alongside the asymmetric manganese complexes four manganese complexes with similarly functionalised bipyridine ligands would be synthesised in order to serve as a point of comparison as

well as to provide an additional data set with which to investigate the relationship between current enhancement and the carbonyl stretching frequency of the 5-coordinate anion.
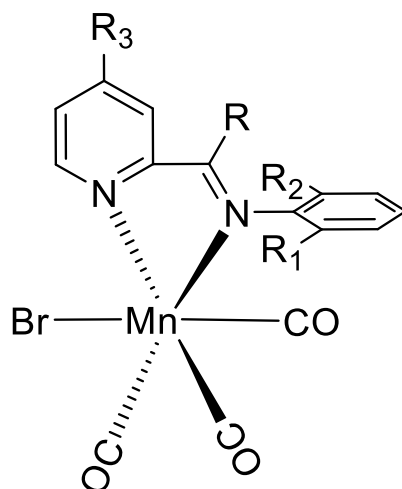
Figure 6.1 Complexes of the asymmetric α-diimine ligands investigated in this chapter where R, R₁ and R₂ are H, and R₃ is varied to affect the energy levels of the frontier orbitals in this type of complexes.

6.1.2 Aims

The aims of this chapter were to synthesise two families of manganese based Lehn type catalyst. One of the ligand families would be based on the asymmetric IMP type ligand incorporating functional groups in the R_3 position of differing electron donating/withdrawing properties. The other family of the ligands would be based on 4,4'-R_3-2,2'-bpy incorporating functional groups identical to the R_3 moieties used in the 4- and 4'-positions. The electrocatalytic properties of both families of complexes will be investigated, in order to ascertain if increased catalytic current enhancement can be correlated with the lower energy carbonyl stretching frequencies of the 5-coordinate anions. If a positive correlation exists this would suggest that reduced back donation into the π^* antibonding orbitals of the carbonyls (of the 5-coordinate anion) results in greater catalytic current enhancement and further investigation would be required.

Comparison of the asymmetric and bpy based catalysts would also be used to provide more evidence for the separation of steric and electronic factors in the asymmetric ligands of the type depicted in Fig. 6.1.

6.2 Experimental Methods

6.2.1 Materials and General Procedures

Commercially available starting materials and reagents were obtained from Sigma-Aldrich, Apollo Scientific and STREM and used as received, with the exception of tetrabutylammonium hexafluorophosphate (TBAPF₆, Sigma-Aldrich) which was recrystallized from hot ethanol and dried overnight in a vacuum oven. All solvents (Fisher Scientific, Sigma-

Aldrich, VWR) were of HPLC grade or higher, and were used without further purification unless otherwise stated. Dry solvents were obtained from a Grubbs solvent drying system.

6.2.2 Instruments and Analysis

6.2.2.1 Nuclear Magnetic Resonance (NMR) Spectroscopy

^{1}H and ^{13}C NMR spectra were recorded using Bruker Avance 400 (DPX-400), Bruker Avance 400, Bruker Avance III HD 400, Bruker Avance III 400 and Bruker Avance III HD 500 spectrometers. Deuterated solvents were purchased from Sigma-Aldrich and were of spectroscopic grade.

6.2.2.2 Mass Spectrometry

High resolution mass spectrometry samples were collected using direct infusion Na^+ ionisation and analysed using time of flight method.

6.2.2.3 UV-Visible Absorption Spectroscopy

UV-Visible absorption spectra were recorded on a Cary 50 Bio spectrophotometer utilising 1 cm path length quartz curvettes.

6.2.2.4 Cyclic Voltammetry

Cyclic voltammetry was performed using either an EmStat3+ (PalmSense, The Netherlands), or Princeton Applied research VersaSTAT 3 potentiostat.

Before experiments, the solutions were purged with bottled N_2 (British Oxygen Company) and an atmosphere of N_2 saturated with acetonitrile was maintained over the sample. The cell set up comprised a glassy-carbon working electrode, a platinum wire counter electrode, and a Ag/AgCl (0.1 M KCl solution) reference electrode in 6 cm^3 of Grubbs dried acetonitrile with [NBu$_4$][PF$_6$] (0.2 mol dm^{-3}) as supporting electrolyte. Ferrocene was added as an internal reference.

6.2.2.5 Spectroelectrochemistry (SEC)

In a typical experiment, infrared spectroelectrochemical study was performed using an EmStat3+ potentiostat (PalmSense, The Netherlands). A 4 mmol dm^{-3} solution of each complex in presence of 0.3 mol dm^{-3} of [NBu$_4$][PF$_6$] was prepared in dry acetonitrile and analysed in an optically transparent thin-layer spectroelectrochmeical cell (OTTLE cell) equipped with Pt minigrid working electrodes, a Ag microwire psudoreference electrode and CaF$_2$ windows. Samples were prepared under argon atmosphere and samples for catalytic measurements were prepared by bubbling the electrolyte with CO_2 for 15 minutes. IR

spectroscopy was performed on Bruker Vertex 70v FT-IR spectrometer and thin-layer voltammograms were recorded in the course of the experiment.

6.2.3 Synthesis

MnIMP was prepared according to the procedure outlined in chapter 5 (5.2.3.4).

6.2.3.1 IMP-Me (N-[(4-methylpyridin-2-yl)methylidene]aniline)

Aniline (2.15 mmol, 0.2 g, 0.19 ml) was added to 2-methyl-4-piconaldehyde (2.14 mmol, 0.259 g, 0.24 ml) in flame-dried glassware and stirred for 2 h. 10 ml of Grubbs dried THF was added in order to allow for effective stirring. Hexane (20 ml) was added and the solution dried over sodium sulphate. The solution was filtered, concentrated under vacuum, and placed in a freezer overnight. Unlike IMP no crystals were formed from this or any of the other functionalised IMP derivatives, an oily layer was observed in the hexane which was extracted. NMR and TLC results showed that the oil contained unreacted starting material but was used without further purification as prior synthesis of MnIPIMP had shown that chelation of the ligand to manganese allowed the complex to be easily isolated in a purified form. Product mass: 0.5878 g.^{1}H NMR (400 MHz, CDCl$_3$) δ 8.59 (s, 1H), 8.56 (d, J = 5.0 Hz, 1H), 8.07 – 7.99 (m, 1H), 7.45 – 7.38 (m, 1H), 7.26 (ddd, J = 8.5, 2.2, 1.2 Hz, 1H), 7.17 (ddd, J = 8.4, 4.7, 3.7 Hz, 1H), 2.42 (s, 1H).

6.2.3.2 IMP-OMe (Benzamine, N-[(4-methoxy-2-pyridinyl)methylene])

Aniline (2.15 mmol, 0.2 g, 0.19 ml) was added to 4-methoxypiconaldehyde (2.14 mmol, 0.27 g) in flame-dried glassware and stirred for 2 h. 10 ml of Grubbs dried THF was added in order to allow for effective stirring. Hexane (20 ml) was added then added to the reaction mixture, and the resulting solution dried over sodium sulphate. The solution was filtered, concentrated under vacuum, and placed in a freezer overnight. An oily layer was observed in the hexane which was collected. NMR and TLC results showed that the oil contained unreacted starting material, nonetheless, the oil was used in the next step without further purification as prior synthesis of MnIPIMP had shown that chelation of the ligand to manganese allowed the complex to be easily isolated in a pure form. Product mass: 0.5311 g. ^{1}H NMR (400 MHz, CDCl$_3$) δ 8.57 (s, 1H), 8.50 (d, J = 5.7 Hz, 1H), 7.74 (d, J = 2.6 Hz, 1H), 7.41 (tt, J = 3.9, 1.8 Hz, 2H), 7.26 (dd, J = 5.1, 3.5 Hz, 2H), 7.14 (t, 1H), 3.92 (s, 3H).

6.2.3.3 IMP-Br (N-[(4-bromopyrid-2-yl)methylidene]aniline)

Aniline (2.15 mmol, 0.2 g, 0.19 ml) was added to 4-methoxypiconaldehyde (2.14 mmol, 0.400 g) in flame-dried glassware and stirred for 2 h. 10 ml of Grubbs dried THF was added in order to allow for effective stirring. Hexane (20 ml) was added to the reaction mixture, and the resulting solution dried over sodium sulphate. The solution was filtered, concentrated under vacuum, and placed in a freezer overnight. An oily layer was observed in the hexane which was collected. NMR and TLC results

showed that the oil contained unreacted starting material but was used without further purification as prior synthesis of MnIPIMP had shown that chelation of the ligand to manganese allowed the complex to be easily isolated in a purified form. Product mass: 0.5896 g. ^{1}H NMR (400 MHz, CDCl$_3$) δ 8.59 (s, 1H), 8.52 (d, J = 5.2 Hz, 1H), 8.43 (s, 1H), 7.53 (d, J = 5.2 Hz, 1H), 7.45 (t, J = 7.5 Hz, 2H), 7.30 (d, J = 8.3 Hz, 1H).

6.2.3 Synthesis

Complexes **1-8** were prepared from [MnBr(CO)$_5$] and the corresponding ligand, using diethyl ether as a solvent. The reaction yielded a very fine precipitate in each case, which was collected by centrifugation, and washed with diethyl ether to afford analytically pure target complexes. NMR of the asymmetric complexes was recorded in both CDCl$_3$ and CD$_3$CN. The use of CD$_3$CN was necessary because the slight acidity of chloroform caused partial decomposition of the complexes, particularly with the MnIMP-Br complex and because the ^{1}H signal of the CHCl$_3$ was overlapping with some of the ^{1}H NMR signals from the compounds. The 1H NMR spectra recorded in CD$_3$CN often showed convolved signals from different protons on the phenyl rings, and as a consequence it is not possible to assign NMR signal of individual protons in some cases. [MnBr(CO)$_3$(2-[(phenylimino)methyl]pyridine)] (Referred to in this chapter as MnIMP), [MnBr(CO)$_3$(2,2'-bipyridine)] (referred to in this chapter as Mnbpy) and [MnBr(CO)$_3$(4,4'-methyl-2,2'-bipyridine)] (referred to in this chapter as Mndmbpy) were prepared as described in chapters 5 and 2, respectively.

6.2.3.4 [MnBr(CO)$_3$(IMP-Me)] (MnIMP-Me)

[MnBr(CO)$_5$] (1.02 mmol, 0.281 g) was combined with (IMP-Me 1.05 mmol, 0.205 g) in diethyl ether (20 ml) and refluxed under aerobic conditions for 4 h. Product was formed in quantitative yield. ^{1}H NMR (400 MHz, CD$_3$CN) δ 7.55 (s, 1H), 7.53 (s, 1H), 7.51 (d, J = 4.6 Hz, 1H), 7.46 (dt, J = 5.6, 4.0 Hz, 1H), 2.53 (s, 1H). ^{1}H NMR (400 MHz, CDCl$_3$) δ 9.07 (s, 1H), 8.39 (s, 1H), 7.74 (s, 1H), 7.52 (s, 1H), 7.42 (d, J = 11.1 Hz, 1H), 2.56 (s, 1H).MS (TOF-ES + ve): m/z (M+Na$^+$) 437, 438.9, 438, 440. HRMS (TOF-ES, + ve): m/z (M+Na$^+$) Calcd for C$_{16}$H$_{12}$N$_2$O$_3$NaMnBr 436.9309, found 436.9290.

6.2.3.5 [MnBr(CO)$_3$(IMP-OMe)] (MnIMP-OMe)

[MnBr(CO)$_5$] (0.944 mmol, 0.259 g) was combined with (IMP-OMe 0.955 mmol, 0.203 g) in diethyl ether (20 ml) and refluxed under aerobic conditions for 4 h, which resulted in a formation of an off-white precipitate, collected by centrifugation. Product was formed in quantitative yield. ^{1}H NMR (400 MHz, CD$_3$CN) δ 8.98 (d, J = 6.3 Hz, 1H), 8.52 (s, 1H), 7.68 (d, J = 2.7 Hz, 1H), 7.58 (d, 1H), 7.57 (s, 1H), 7.51 (dd, J = 9.4, 4.5 Hz, 1H), 7.24 (dd, J = 6.3, 2.7 Hz, 1H), 7.14 – 7.06 (m, 1H), 6.66 (d, J = 6.5 Hz, 1H). ^{1}H NMR (400 MHz, CDCl$_3$) δ 8.91 (s, 1H), 8.29 (s, 1H), 7.45 (s, 3H), 7.36 (s, 2H), 7.00 (s, 1H), 3.92 (s, 3H). MS (TOF-ES + ve): m/z (M+Na$^+$) 453, 455, 454, 456. HRMS (TOF-ES, + ve): m/z (M+Na$^+$) Calcd for C$_{16}$H$_{12}$N$_2$O$_4$NaMnBr 452.9259, found 452.9256.

6.2.3.6 [MnBr(CO)$_3$(IMP-Br)] (MnIMP-Br)

[MnBr(CO)$_5$] (0.769 mmol, 0.211 g) was combined with (IMP-Br 0.766 mmol, 0.200 g) in diethyl ether (20 ml) and refluxed under aerobic conditions for 4 h, resulting in formation of a fine, orange, precipitate. The latter was collected by centrifugation. ^{1}H NMR data confirmed formation of the analytically pure desired product in quantitative yield. ^{1}H NMR (400 MHz, CD$_3$CN) δ 9.06 (d, J = 5.9 Hz, 1H), 8.58 (s, 1H), 8.30 (d, J = 2.0 Hz, 1H), 7.89 (dd, J = 5.9, 2.1 Hz, 1H), 7.62 – 7.49 (m, 5H). ^{1}H NMR (400 MHz, CDCl$_3$) δ 9.06 (s, 1H), 8.45 (s, 1H), 8.10 (s, 1H), 7.76 (s, 1H), 7.29 (s, 1H). MS (TOF-ES + ve): m/z (M+Na$^+$) 502.9, 500.9, 504.9, 503.9, 501.9, 505.9 HRMS (TOF-ES, + ve): m/z (M+Na$^+$) Calcd for C$_{15}$H$_9$N$_2$O$_3$NaMnBr$_2$ 500.8258, found 500.8257.

6.2.3.7 [MnBr(CO)$_3$(bpy-OMe)] (Mnbpy-OMe)

[MnBr(CO)$_5$] (0.77 mmol, 0.211 g) was combined with (4,4'-dimethoxy-2,2'-bipyridine 0.77 mmol, 0.166 g) in diethyl ether (20 ml) and refluxed under aerobic conditions for 4 h, resulting in formation of a fine, orange, precipitate. The latter was collected by centrifugation. ^{1}H NMR data confirmed formation of the analytically pure desired product in quantitative yield. Yield 92 %. ^{1}H NMR (400 MHz, CDCl$_3$) δ 9.00 (d, J = 6.2 Hz, 1H), 7.51 (s, 1H), 7.00 (d, J = 6.3 Hz, 1H), 3.98 (s, 1H). HRMS (TOF-ES, + ve): m/z (M+Na$^+$) Calcd for C$_{15}$H$_{12}$N$_2$O$_5$NaMnBr 456.9208, found 456.9202.

6.2.3.6 [MnBr(CO)$_3$(bpy-Br)] (Mnbpy-Br)

[MnBr(CO)$_5$] (0.64 mmol, 0.1751 g) was combined with (4,4'-dimethoxy-2,2'-bipyridine 0.64 mmol, 0.2 g) in diethyl ether (20 ml) and refluxed under aerobic conditions for 4 h, resulting in formation of a fine, orange, precipitate. The latter was collected by centrifugation. ^{1}H NMR data confirmed formation of the analytically pure desired product in quantitative yield. Yield 97 %. ^{1}H NMR (400 MHz, CDCl$_3$) δ 9.06 (d, 1H), 8.23 (s, 1H), 7.71 (d, 1H). HRMS (TOF-ES, + ve): m/z (M+Na$^+$) Calcd for C$_{13}$H$_6$N$_2$O$_3$NaMnBr$_2$ 552.7207, found 552.7219.

6.3 Results and Discussion

6.3.1 Cyclic Voltammetry

Figure 6.2 shows a comparison of the negative sweep voltammograms recorded under N$_2$ functionalised IMP complexes and the functionalised bpy complexes (from 0 to -2.3 V vs. Fc/Fc+). All of the bpy complexes have very similar electrochemical behaviour as can be seen in the voltammograms. In all cases two irreversible reduction processes are observed on the cathodic wave

for the bpy complexes with two oxidation processes being observed in the anodic return wave, the only variation between the complexes being in the peak position.
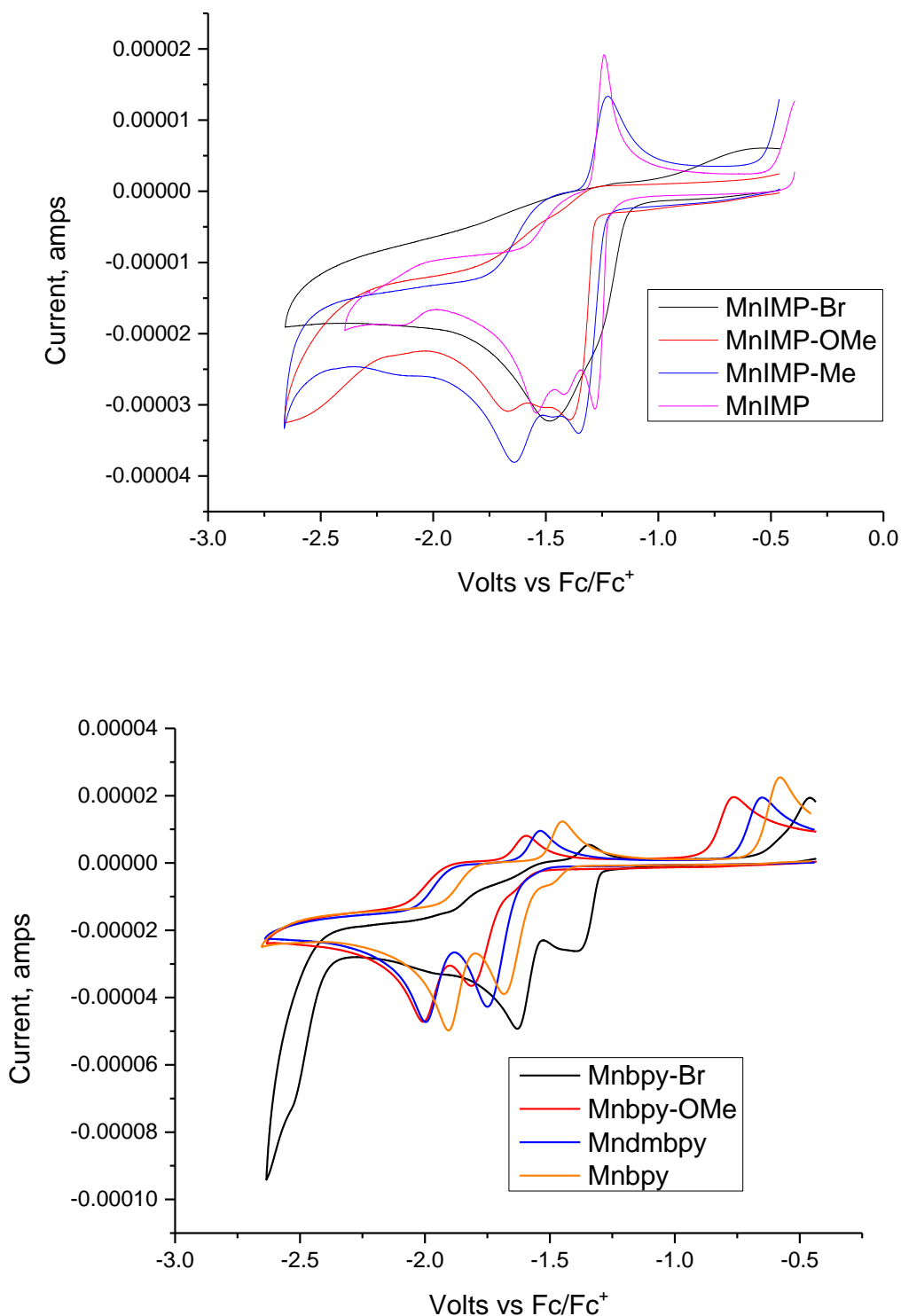
Figure 6.2 Cyclic Voltammograms of the IMP complexes (top) and the bipyrinde complexes (bottom) under N$_2$ in 6 cm^3 of Grubbs dried acetonitrile with 0.2 M [Bu$_4$N][PF$_6$].

What is immediately obvious is that unlike the bpy analogues the MnIMP-OMe and MnIMP-Br complexes do not show the anodic peaks at ca. -1.25 V corresponding to the oxidation of the five coordinate anion (*vide infra*)[1], although what may be a reoxidation peak at ca. -0.6 V is observed for MnIMP-Br. For the majority of the IMP complexes, three peaks are observed in the cathodic wave of the voltammograms. For these complexes the cathodic peak at least negative voltage most likely corresponds to the formation of the aqua cationic complex $[Mn(CO)_3(diimine)(H_2O)]^+$ the formation of which was only observed for the IMP complexes but not for the bpy complexes.

Although the asymmetric complexes are more prone to hydrolysis as compare with the bpy complexes the overall trends shown in both families of complexes is clear. The most electron withdrawing diimines (in both cases the bromine substituted complexes) undergo electrochemical reduction at the least negative potentials while the most electron donating complexes (in both cases the ether substituted complexes) undergo electrochemical reduction at the most negative potentials. Although this is to be expected[5] the important factor is that both complexes exhibit the same trends in the electrochemical behaviour upon reduction, this supports the hypothesis asserted in chapters 4 & 5 that the IMP complexes are suitable as lab mice for investigating catalytic systems which are sensitive to changes in the steric and electronic properties and crucially in this case the Lehn type catalyst.

Table 6.1 3 Cathodic peak potentials (V, vs. Fc/Fc$^+$) of the complexes (1 mM, acetonitrile, 0.2 M [Bu$_4$N][PF$_6$]).

Complex	1st reduction potential* V vs Fc/Fc$^+$	2nd reduction potential* V vs Fc/Fc$^+$	3rd reduction potential* V vs Fc/Fc$^+$
MnIMP	-1.28	-1.42	-1.54
MnIMP-Me	-1.36	-1.47	-1.64
MnIMP-OMe	-1.39	-1.54	-1.67
MnIMP-Br	-1.27$^\$$	-1.48$^\$$	-
Mnbpy	-1.68	-1.91	-
Mndmbpy	-1.75	-2	-
Mnbpy-OMe	-1.81	-2	-
Mnbpy-Br	-1.39	-1.63	-

Under N$_2$, $^\$$for MnIMP-Br both peaks are seen as one large overlapping reduction therefore the first cathodic peak is approximate.

MnIMP

MnIMP-Me

MnIMP-OMe

MnIMP-Br
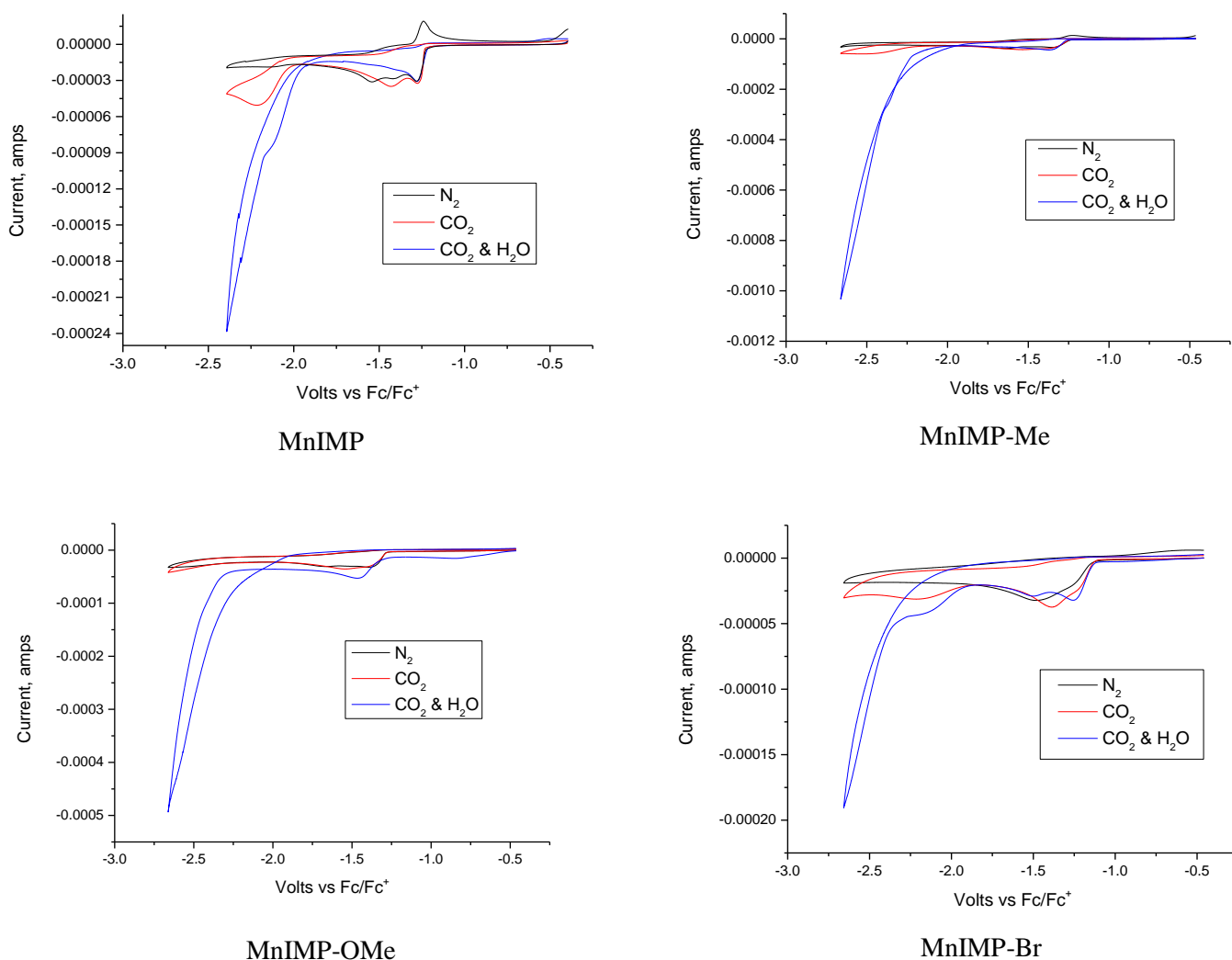
Figure 6.3 Cyclic Voltammograms of the IMP complexes under N_2 (black), CO_2 (red) and CO_2 & H_2O (blue), 0.002 M in 6 cm^3 of Grubbs dried acetonitrile with 0.2 M [Bu$_4$N][PF$_6$].

Figures 6.2 and 6.3 show the cyclic voltammograms for all of the complexes under N_2, CO_2 and CO_2 & H_2O. Figure 6.3 shows that under CO_2 a slight current enhancement is observed for MnIMP and MnIMP-Br a behaviour which is not observed for the bpy complexes which only exhibited current enhancement in the presence of water to act as a Brönsted acid.[6,7,8,9] It has been reported by Zeng *et al.* that manganese complexes with diazabutadiene ligands also show current enhancement in CO_2 saturated solution without the presence of a Brönsted acid[10] and indeed it may be that these ligands are able to provide either a thermodynamically favourable pathway to CO_2 reduction in the absence of a Brönsted acid[6,7,11] or have some moiety which is able to act as a local proton source.[12,13] It is important to note that in repeated experiments with MnIMP this behaviour was observed consistently and was also observed with the sterically inhibited cousin complexes discussed in chapter 5.[1]

Mnbpy

Mndmbpy

Mnbpy-OMe

Mnbpy-Br
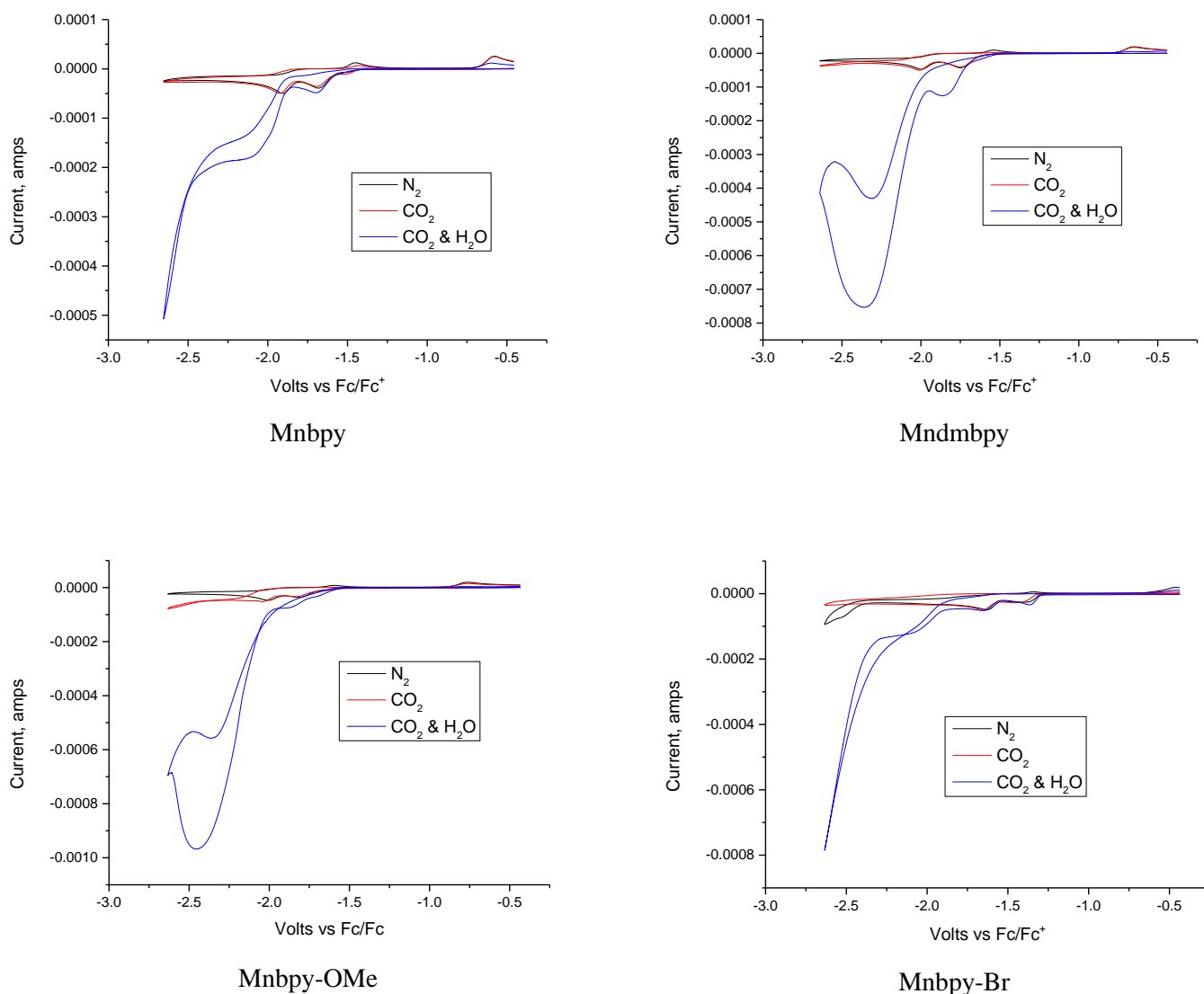
Figure 6.4 Cyclic Voltammograms of the bpy complexes under N$_2$ (black), CO$_2$ (red) and CO$_2$ & H$_2$O (blue), 0.002 M in 6 cm^3 of Grubbs dried acetonitrile with 0.2 M [Bu$_4$N][PF$_6$].

This may be significant as the sterically inhibited cousin complexes have an almost identical orbital structure and photophysical properties, while the other asymmetric complex to show current enhancement (MnIMP-Br) has lower reduction potentials that MnIMP, suggesting it may be a thermodynamic aspect that results in the observed current enhancement rather than a local proton source. As can be seen in figure 6.4 line crossing is observed in the scans under CO$_2$ with water for the Mnbpy-OMe and Mnbpy-Br complexes, this is usually due to mass transport being slower than the potential scan rate.

6.3.2 IR-Spectroelectrochemistry under Inert Atmosphere

IR-SEC experiments were carried out in order to understand the mechanism of electrochemical reduction by detecting intermediates formed. The second goal of these

experiments was to detect specifically (where possible) the 5-coordinate anionic species, and correlate the frequency of the carbonyl stretching vibrations with the electronic and steric properties of the ligand. It is important to note that only the intermediates which are sufficiently stable (minutes at least) can be recorded in these experiments. The experiments were performed by scanning the potential at 0.002 Vs^{-1} with a step potential of 0.0002 V. IR spectra were recorded alongside the reduction.

6.3.2.a. Reduction of the "MnIMP" complexes

The results of the IR SEC studies are summarised in figure 6.5, which show selected IR spectra recorded as the reduction process was progressing for the 4 IMP complexes. The vibrations attributed to the parent complex, the aqua-complex, the dimer, and the 5-coordinate anion are labelled on the panels A, B, C and D, respectively, for each complex.[1,10]

The results indicate that all asymmetric IMP complexes follow the same reduction pathway, initially forming a small quantity of aqua cationic complex $[Mn(CO)_3(IMP-X)(H_2O)]^+$ (identified by the characteristic peak at ca. 2050 cm^{-1} and the broad shoulder at ca. 1960 cm^{-1}) followed by consumption of both the parent and aqua complexes to form the dimer $[Mn(CO)_3(IMP-X)]_2$ (identified by the 4 new IR absorbancies observed upon reduction). The dimer, in turn is converted into the 5-coordinate anion complex $[Mn(CO)_3(IMP-X)]^-$ identified by the two peaks at ca. 1930 and ca. 1830 cm^{-1}.

The only complex to show any deviation from this mechanism is the MnIMP-OMe complex. For MnIMP-OMe only the aqua cation and 5-coordinate anion complexes can be clearly identified and it is not clear that what the peaks at 2018, 2002 and 1990 cm^{-1} correspond to but given the trends observed in the CV data and the IR spectra recorded for the other complexes it is reasonable to assume that these are probably associated with the dimer. We also note that the IR-spectra associated with MnIMP-Br complex and its reduction products show significant overlap of multiple peaks at any point in the reduction process, and it is not possible to record the spectra of individual species. This is probably caused by the very close reduction potentials for all species involved (see figure 6.2, CV).

6.3.2.b. Reduction pathway of the MnBpy complexes

The IR-SEC results for Mnbpy series are summarised in Fig. 6.6. All Mnbpy complexes follow the same, clearly identifiable, reduction pathway: all complexes form the dimer directly upon reduction of the parent complex which is in turn converted into 5-coordinate anion.

The data for $\nu(CO)$ are summarised in Table 6.2.
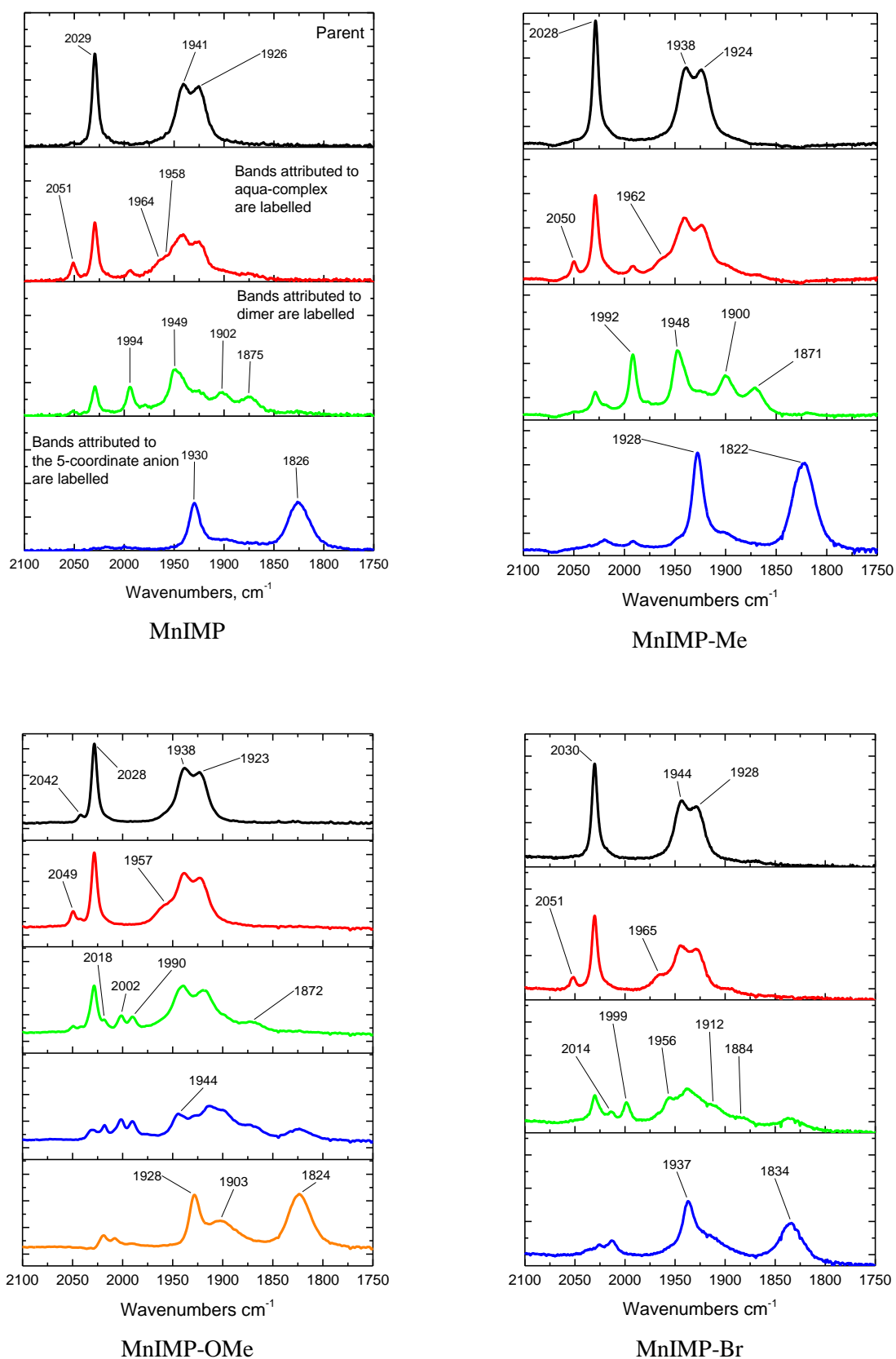
Figure 6.5 IR spectral changes accompanying *in situ* reduction of the asymmetric IMP complexes in Ar-saturated acetonitrile/0.2M [Bu₄N][PF₆] within an OTTLE cell.
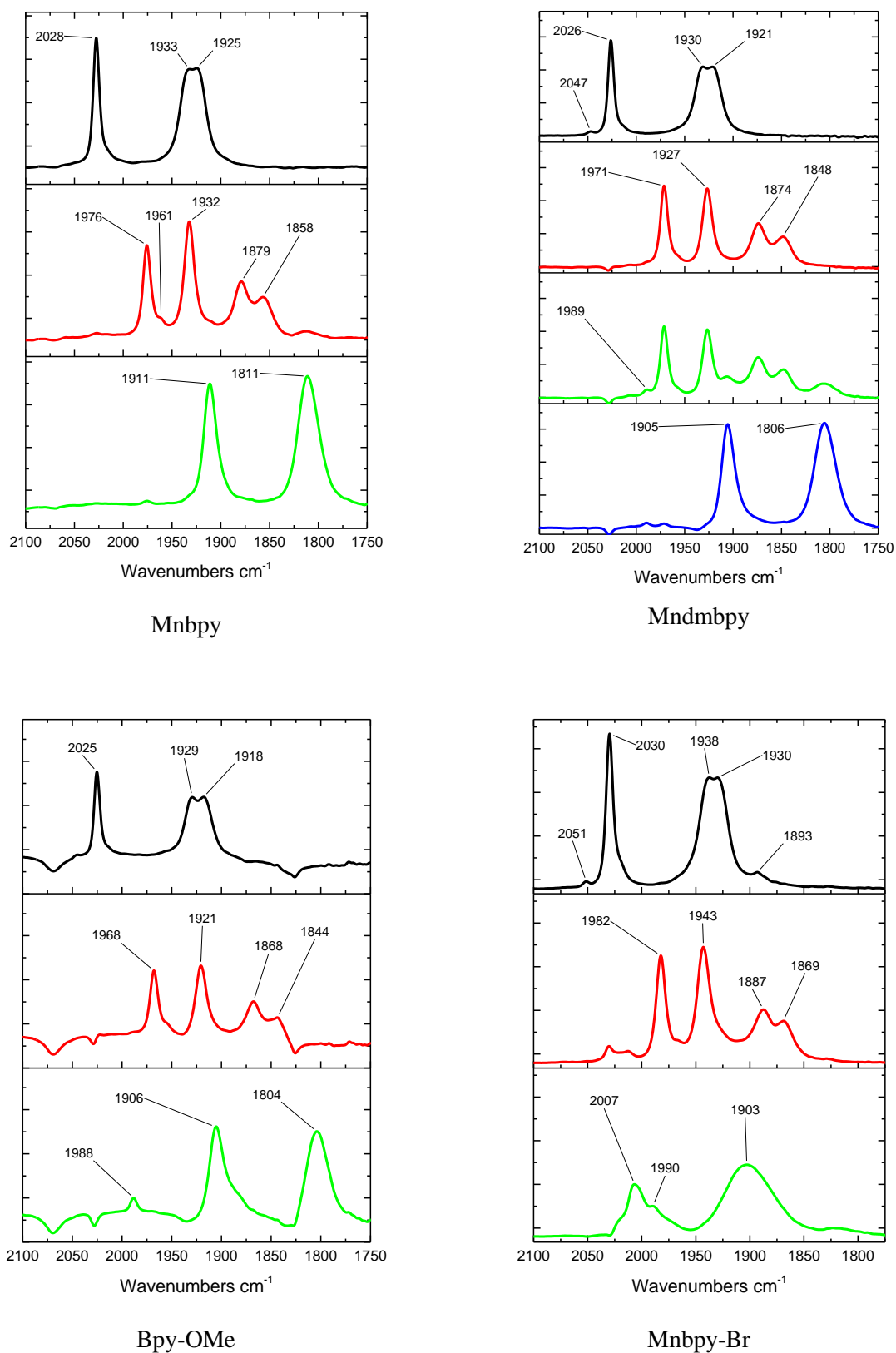
Figure 6.6 IR spectral changes accompanying *in situ* reduction of the symmetric bpy complexes in Ar-saturated acetonitrile/0.2M [Bu₄N][PF₆] within an OTTLE cell.

Table 6.2. Experimentally obtained frequencies of carbonyl stretching vibrations of: the neutral Mn complexes, 5-coordinate anion, a cationic aqua complex, and the Mn–Mn bound dimer, in acetonitrile at 293 K (Fig 6.5 and 6.6.).

Species	υ (CO) / cm^{-1}
[MnBr(CO)$_3$(IMP)]	2029, 1941, 1926
[Mn(CO)$_3$(H$_2$O)(IMP)]$^+$	2051, 1964, 1958
[Mn(CO)$_3$(IMP)]$^-$	1930, 1826
[Mn(CO)$_3$(IMP)]$_2$	1994, 1949, 1902, 1875
[MnBr(CO)$_3$(IMP-Me)]	2028, 1938, 1924
[Mn(CO)$_3$(H$_2$O)(IMP-Me)]$^+$	2050, 1962
[Mn(CO)$_3$(IMP-Me)]$^-$	1928, 1822
[Mn(CO)$_3$(IMP-Me)]$_2$	1992, 1948, 1900, 1871
[MnBr(CO)$_3$(IMP-OMe)]	2028, 1938, 1923
[Mn(CO)$_3$(H$_2$O)(IMP-OMe)]$^+$	2049, 1957
[Mn(CO)$_3$(IMP-OMe)]$^-$	1928, 1903, 1824
[Mn(CO)$_3$(IMP-OMe)]$_2$	2018, 2002, 1990, 1872
[MnBr(CO)$_3$(IMP-Br)]	2030, 1944, 1928
[Mn(CO)$_3$(H$_2$O)(IMP-Br)]$^+$	2051, 1965
[Mn(CO)$_3$(IMP-Br)]$^-$	1937, 1834
[Mn(CO)$_3$(IMP-Br)]$_2$	2014, 1999, 1956, 1912, 1884
[MnBr(CO)$_3$(bpy)]	2028, 1933, 1925
[Mn(CO)$_3$(H$_2$O)(bpy)]$^+$	2049, 1959
[Mn(CO)$_3$(bpy)]$^-$	1911, 1811
[Mn(CO)$_3$(bpy)]$_2$	1976, 1961, 1932, 1879, 1858
[MnBr(CO)$_3$(dmbpy)]	2026, 1930, 1921
[Mn(CO)$_3$(H$_2$O)(dmbpy)]$^+$	2047
[Mn(CO)$_3$(dmbpy)]$^-$	1905, 1806
[Mn(CO)$_3$(dmbpy)]$_2$	1971, 1927, 1874, 1848
[MnBr(CO)$_3$(bpy-OMe)]	2025, 1929, 1918
[Mn(CO)$_3$(H$_2$O)(bpy-OMe)]$^+$	2042, 1960
[Mn(CO)$_3$(bpy-OMe)]$^-$	1906, 1804
[Mn(CO)$_3$(bpy-OMe)]$_2$	1968, 1921, 1868, 1844
[MnBr(CO)$_3$(bpy-Br)]	2030, 1938, 1930
[Mn(CO)$_3$(H$_2$O)(bpy-Br)]$^+$	2051
[Mn(CO)$_3$(bpy-Br)]$^-$	2007, 1903
[Mn(CO)$_3$(bpy-Br)]$_2$	1982, 1943, 1887, 1869

It is certainly noteworthy that both the MnIMP-Br and Mnbpy-Br complexes show the strongest metal carbonyl bonds, which is antithetical to what would be expected.

6.3.3 Comparison of the electrocatalytic activity (as expressed by Current Enhancement under CO₂) with electronic structure of the catalysts (as expressed by the Carbonyl Stretching frequencies of the 5-coordinate anion species)

The primary aim of the project was to determine if the trend observed in the RemesBIAN complexes (chapter 3), namely, that there was a correlation between the increase in the $\frac{i_{cat}}{i_p}$ ratio and an increase in the frequency of the $\upsilon(CO)$ vibrations associated with the 5-coordinate anion. The data gathered in sections 6.3.1 for i_{cat}/i_p (voltammograms used in the calculation are displayed in appendix 2) and the IR SEC data in section 6.3.2, are summarised in Table 6.3, and plotted in figure 6.7. These data indicate that the complexes functionalised with electron donating moieties have lower $\upsilon(CO)$ frequencies, i.e., somewhat weaker carbonyl bonds due to the back donation from the ligand to the manganese centre, and in turn into the π^* antibonding orbital of the carbonyl ligands, as would be expected. However the relationship between carbonyl stretching frequency and $\frac{i_{cat}}{i_p}$ is the opposite to that reported for the Re mesBIAN complexes. Importantly this behaviour is consistent between both families of Mn complexes.

Table 6.3. $\upsilon(CO)$ carbonyl stretching frequencies attributed to the 5-coordinate anions, [Mn(diimine)(CO)₃]⁻, generated in IR SEC experiments in Ar-saturated acetonitrile/0.2M [Bu₄N][PF₆] and $\frac{i_{cat}}{i_p}$ current enhancement values recorded at -2.24 V vs Fc/Fc⁺ for the two families of manganese complexes studied.

Complex	$\upsilon(CO)$ of 5-coordinate ion, cm⁻¹	$\frac{i_{cat}}{i_p}$ (at -2.24 V vs Fc/Fc⁺)
MnIMP (**1**)	1930, 1826	2.4
MnIMP-Me (**2**)	1928, 1822	2.7
MnIMP-OMe (**3**)	1928, 1824, 1903	2.7
MnIMP-Br (**4**)	1937, 1834	2.2
Mnbpy (**5**)	1911, 1811	5.6
Mndmbpy (**6**)	1905, 1806	6.6
Mnbpy-OMe (**7**)	1906, 1804, 1988	6.2
Mnbpy-Br (**8**)	2007, 1903	1.7

Figure 6.7 shows the relationship between the carbonyl stretching frequencies of the complexes and the ratio of the $\frac{i_{cat}}{i_p}$. In both families of catalyst those with stronger carbonyl bonds show the least

current enhancement, Overall the bipyridine complexes exhibited greater current enhancement than the IMP derivatives. However, the variations in the υ(CO) frequencies between different complexes are very small, and no conclusive statements can be made.

These observations are consistent with what has been reported[14] as despite the fact that back donation[15] into the metal carbonyl bonds should result in a decrease in electron density on the metal centre this effect appears to be negligible relative to the increased electron donation arising from the inductive effects in the IMP-Me and dmbpy ligands or mesomeric electron donation in the IMP-OMe and bpy-OMe.
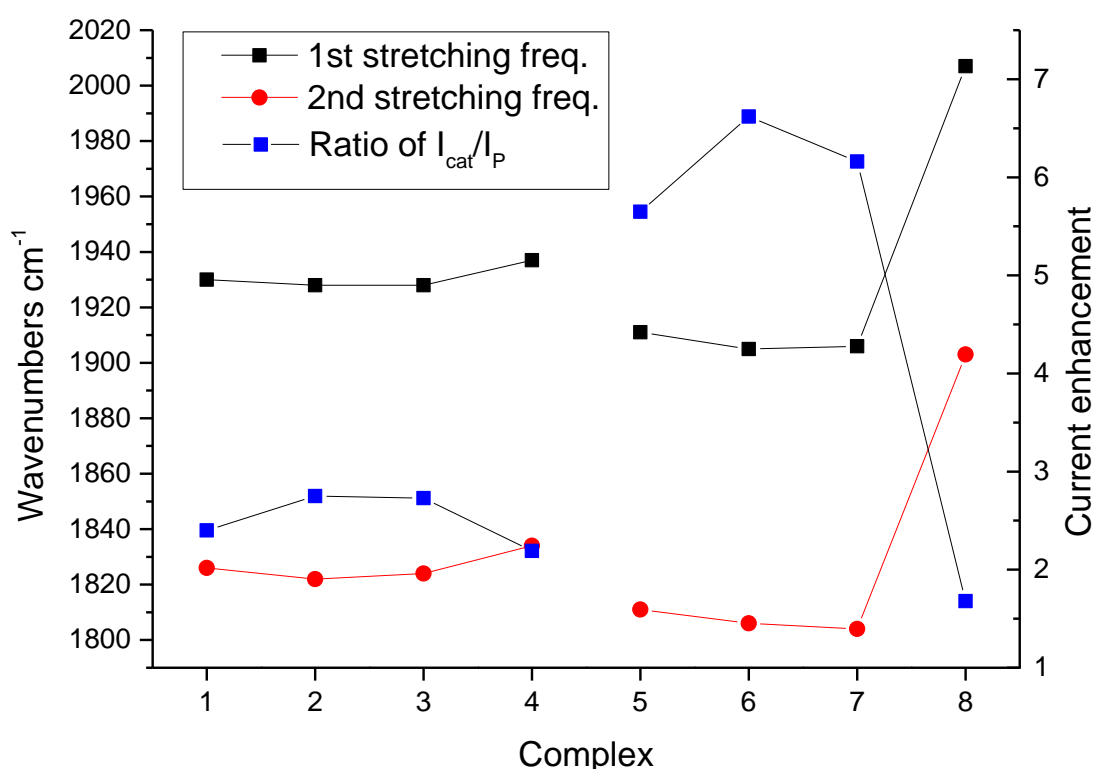
Figure 6.7 Graph of carbonyl stretching frequencies of the 5-coordinate anion complexes recorded in Ar-saturated acetonitrile/0.2M [Bu₄N][PF₆] and $\frac{i_{cat}}{i_p}$ values calculated at -2.24 V vs Fc/Fc⁺ showing the trends between the two families of manganese complexes.

6.3.4 IR-Spectroelectrochemistry under CO₂ atmosphere

In order to investigate (and confirm) that the Mn complexes studied were electocatalytially reducing CO_2 to CO, and to try and understand the mechanism of their action, IR-SEC experiments were performed upon reduction of the complexes under CO2 atmosphere. Figure 6.8 shows the IR-SEC data. The IR absorption band of free CO_2 was monitored during the course of the reduction and was observed to decrease in intensity for all complexes. As MnIMP, Mnbpy and Mndmbpy have been

previously reported, their interaction with CO_2 upon reduction will not be discussed in detail in this chapter.[1,16,17,18]

MnIMP

Mnbpy
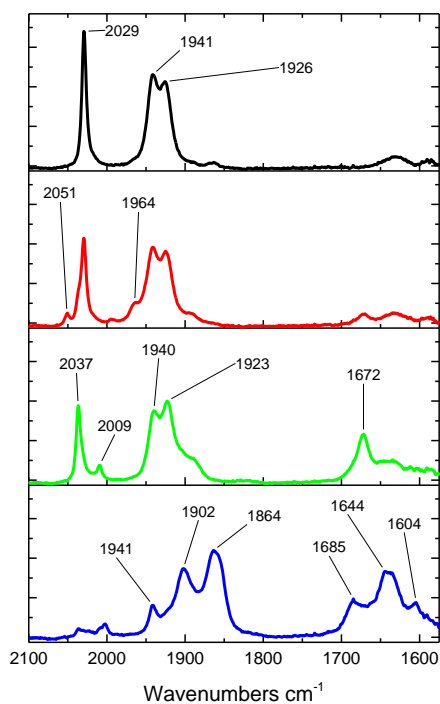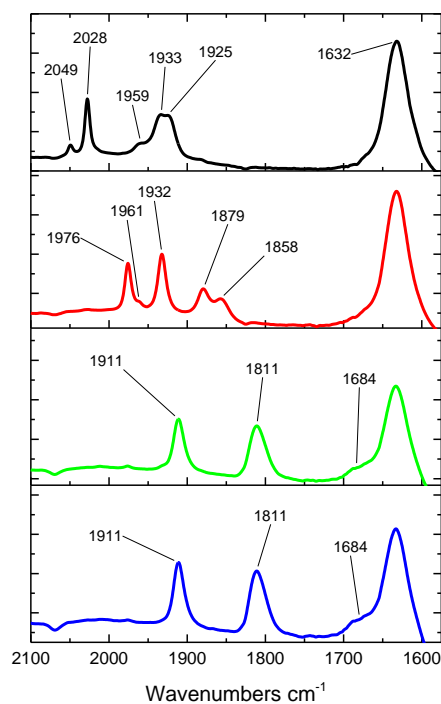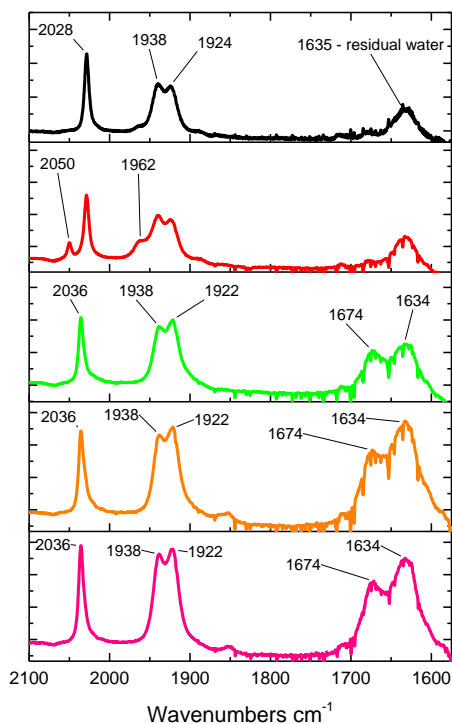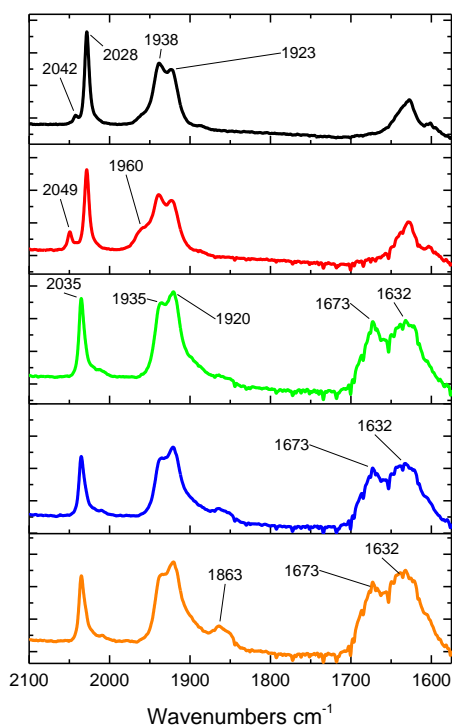
MnIMP-Me

Mndmbpy

MnIMP-OMe
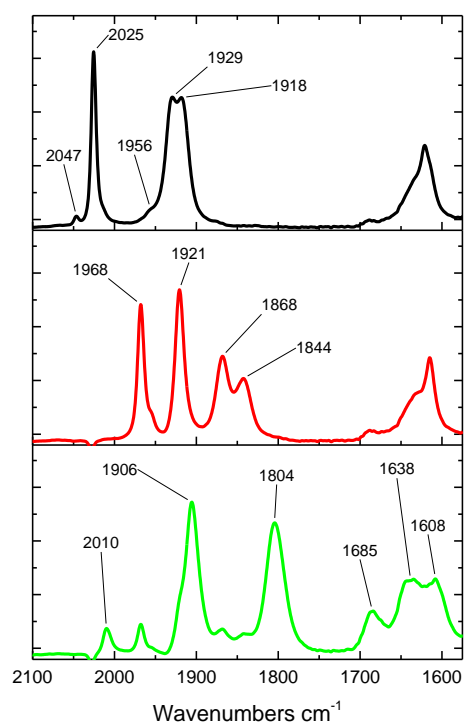
Mnbpy-OMe

MnIMP-Br

Mnbpy-Br
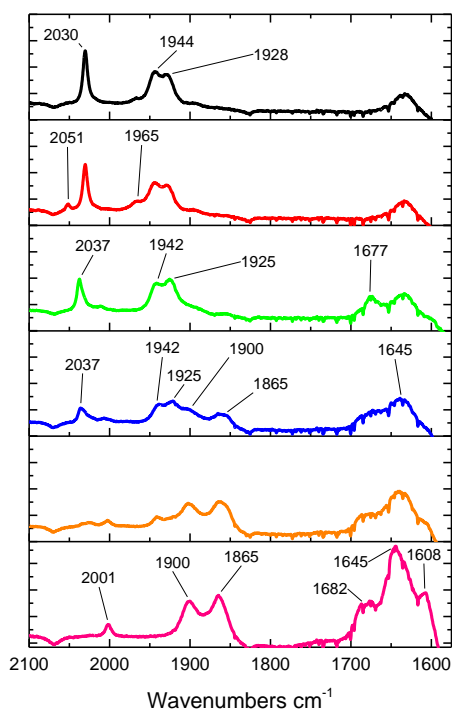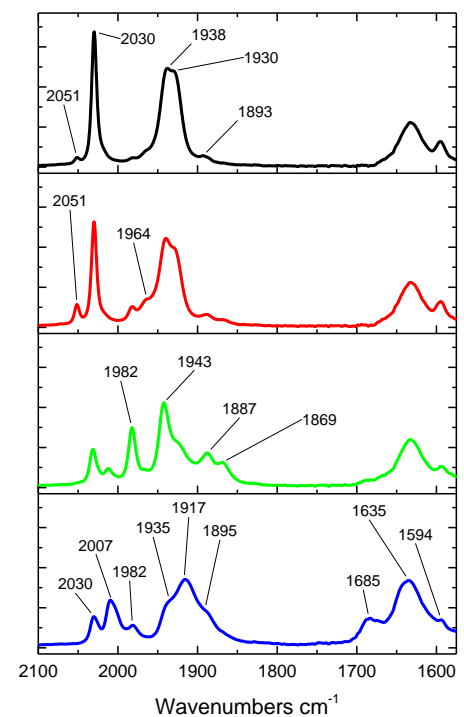
Figure 6.8 I IR spectral changes accompanying in situ reduction of all studied complexes in CO₂-saturated acetonitrile/0.2M [Bu₄N][PF₆] within an OTTLE cell.

Under the conditions in the CO_2 saturated OTTLE cell the IMP subs series appeared to show a greater propensity to the formation of the free bicarbonate and subordinate bands IR bands than the bpy analogues. What is especially noteworthy is that neither of these bands characteristic of CO_2 reduction was observed to be formed by the Mnbpy complex during the experiments, although, what we have assigned to be the bicarbonate complex $[Mn(CO)_3(bpy)(\eta^1-OCO_2H)]$ is observed at 1684 cm^{-1} and the free CO_2 in solution was observed to become depleted (not shown). Because Mnbpy is well studied complex the catalytic ability of which is at present reasonably well understood and investigated [6, 9,16,17,18] no further efforts were made to monitor catalysis of this complex. It is also worth noting that all of the diimine complexes showed the formation of the aqua cationic complex $[Mn(CO)_3(diimine)(H_2O)]^+$ during the course of the IR-SEC experiments. This is most likely due to the higher concentration of water in the solvent following saturation with CO_2. This occurred due to water being present in the bottled CO_2 although attempts were made to remove the water from the CO_2 gas being used by first passing the CO_2 over two drying columns composed of magnesium sulphate, calcium carbonate, silica gel and aluminium sulphate.

Upon reduction no dimer formation was observed for any of the IMP subseries complexes matching what was seen in the case of the reported MnIMP complex (see chapter 5). Instead immediately upon reduction of the parent complex it appears that the CO_2 coordinates with the reduced bromine dissociated molecule (which most likely corresponds to the two electron reduced five coordinate anion $[Mn(CO)_3(IMP-X)]^-$) forming the bicarbonate complex. This in turn is further reduced resulting the formation of free bicarbonate and subordinate formate indicating CO_2 reduction and CO formation (as seen by the bands in the region ca. 1675 and 1605 cm^{-1}). As the concentration of CO increased in the OTTLE cell due to the formation of free CO it became possible in some cases for the diimine to become displaced resulting in the formation of manganese penta carbonyl $[Mn(CO)_5]^-$. This can be seen clearly in this case of the MnIMP and MnIMP-Br complexes (with new peaks in the region ca. 1900 and 1865 cm^{-1} observed). In addition a small amount of penta carbonyl complex can be seen being formed with MnIMP-Me and MnIMP-OMe. At present we do not believe that this provides any evidence for increased stability of the manganese based IMP-Me and IMP-OMe complexes but may be due to differences in the concentration of CO_2 between samples runs.

The bpy complexes show some significant differences to the IMP complexes when subject reduction under identical conditions in the presence of CO_2. The first and most noticeable difference is that the bpy complexes all formed a dimer upon first reduction rather than forming a CO_2 associated complex. It can therefore be summarised that in the case of the bpy complexes dimer formation is significantly more thermodynamically favourable as compared with the IMP complexes. For the IMP series it appears that the 5-coordinate anion is formed directly upon reduction at the electrode, this then reacts with the unreduced parent complex forming the dimer (see chapter 5)[1,10] it may be that the bpy complexes also are reduced via such a mechanism or it may be that the two electron reduction (forming the 5-coordinate anion) does not occur and as has been observed with the rhenium

analogues[19] of the Lehn catalyst one electron reduction forming initially a $[MnBr(CO)_3(bpy-X)]^{\bullet-}$ complex. Since the reduced bromine coordinated complex has not been observed (for any manganese based Lehn type catalysts) it is not possible to say whether this is the case. Although it is our suspicion that the bpy derivatives are reduced via the one electron pathway, we believe this to be the case due to the very similar reduction behaviour of the Mnbpy and Rebpy complexes.

The final significant difference between the two families of complexes is that a metastable population of 5-coordinate anion was formed upon reduction of the bpy complexes. In contrast no such metastable population of 5-coordinate anion was observed upon reduction in CO_2 saturated acetonitrile for any of the IMP complexes discussed in this chapter. Although a metastable 5-coordinate anion population was observed for some of the IMP complexes discussed in chapter 5 this was only the case for the most sterically hindered IMP complexes such as MnDIPIMP.

6.3.5 Separating sterics and electronics

In order to compare the position of the absorption bands in the IMP complexes UV-Vis spectra were recorded in Grubbs dried DCM. This was data was collected in order to provide more evidence to support the theory that the asymmetric complexes are able to effectively separate the steric and electronic properties of the diimines which is the overarching theory behind the projects discussed in chapters 4 to 6. In chapter 4 it was shown that substitution in the R position would result in a shift of the MLCT band indicating that substitution at this positon had an effect on the HOMO-LUMO energy gap and hence the electronic properties of the complexes. In chapter 5 it was shown that substitution at the R_1 and R_2 position had no effect on the position of the MLCT band but did result in the inhibition of dimer formation when large sterically hindering moieties were substituted in these postions. The spectra shown in figure 6.9 show that substitution in the R_3 position has the same effect as substitution in the R position, the shifting in the position of the MLCT band. Figure 6.9 shows that both the bpy and IMP families of complexes exhibit the same trend with the most electron withdrawing bromine substituted complexes having MLCT bands at lower energy than the electron donating methylated and ester substituted complexes. All spectra were recorded in DCM due the hydroscopic nature of DCM which it was used to prevent or minimise spontaneous hydrolysis of the complexes.

Most importantly these results and those recorded during the IR-SEC, in combination with the results of chapters 4 and 5, provide conclusive evidence that the break in symmetry between the two rings results in effective separation of the steric and electronic properties of the molecule. As is discussed above changing the R_3 substituent for the IMP subseries resulted in a change in the position of the MLCT band. This is in contrast to the IMP subseries studied in chapter 5 which showed significant variation in their behaviour upon reduction with some forming dimer, only 5-coorindate anion or a mixture of both species but did not show any change in the position of the MLCT band when only the R_1 or R_2 substituent was altered.

Despite the significant differences between manganese based Lehn type catalysts incorporating the asymmetric ligands and those using bipyridines when reduced under CO_2 the use of the asymmetric ligands as 'lab-mice' to optimise steric and electronic factors appears to be a reasonable prospect when handled with care.
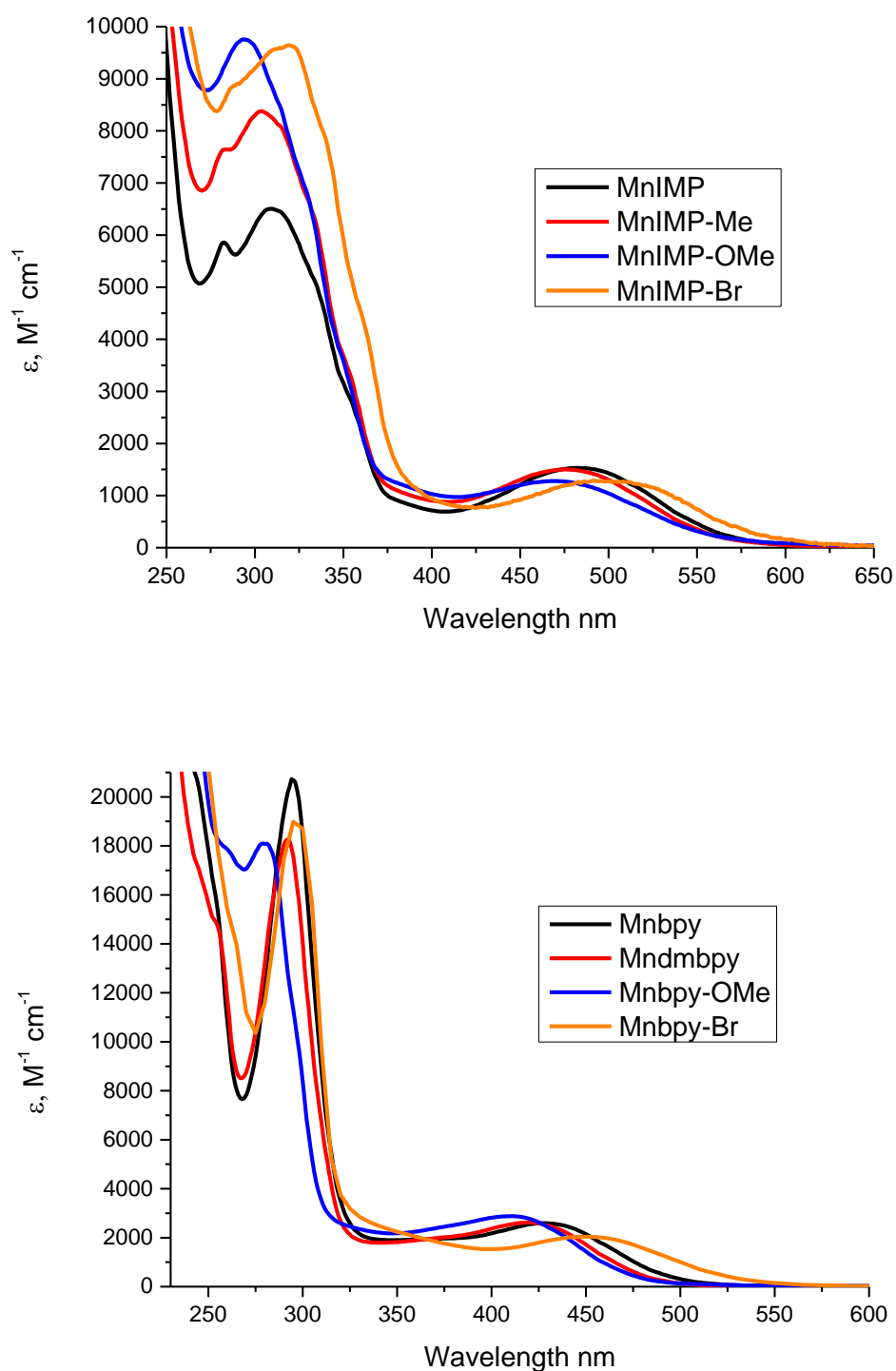
Figure 6.9 Electronic absorption spectra of the two families of manganese complexes studied in this chapter, in DCM.

6.4 Conclusions

The results show clearly that while there does appear to be a correlation between the carbonyl stretching frequencies recorded for the 5-coordinate anions (of the asymmetric and bpy based complexes) and catalytic current enhancement this trend is opposite to that observed in chapter 3. As such 5-coordinante anion complexes with carbonyl stretching bands at higher energy wavelengths exhibit greater catalytic current enhancement. This result is not surprising in many ways as it correlates with what has been published by Kubiak *et al.*[5] that Lehn catalysts with more strongly electron donating (up to a point) groups exhibit increased current enhancement. Never the less we believe it was important to further investigate the trend observed in chapter 3. These results show that the chemistry involved in the electrocatalytic reduction of the Re mesBIAN-N_3 complex is more complex than first assumed and would be interesting to explore further, as well as the mesBIAN ligands in general. Unfortunatly comparisons between the rhenium and manganese mesBIAN complexes is made difficult due to the extreme photosensitivity of the manganese mesBIAN complexes.[20]

The IMP ligands investigated in this chapter provide the final pieces of evidence relating to the use of asymmetric IP ligands to separate sterics and electronics. The complexes incorporating the IMP ligand series showed similar behaviour to both each other and the bpy complexes upon reduction in the OTTLE cell, forming cationic aqua complex followed by dimer which in turn was reduced to for the 5-coordinate anion. None of the IMP series formed the 5-coordinate anion directly upon reduction of the parent or aqua complexes on the time scales studied as was the case when steric bulk was added to the R_1 or R_2 positions of the IMP complexes investigated in chapter 5. As such any variation would appear to be the result of the changes in the electronic structure of the molecule which was observed to change depending on the R_3 substituent based upon the electronic absorption spectra.

It would be interesting to investigate a similar series of IMP and bpy catalysts using rhenium as the central metal as part of a larger study into the thermodynamic differences between IMP and bpy catalysts.[6,7] Such a study would benefit from the inclusion of ultra fast time resolved spectroscopy in order to determine if the first reduction of the parent complex results in the formation of the 5-coordinate anion and if so if the 5-coordinate anion reacts with parent complex to form the dimer in solution.

6.5 References

(1)   Spall, S. J. P.; Keane, T.; Tory, J.; Cocker, D. C.; Adams, H.; Fowler, H.; Meijer, A. J. H. M.; Hartl, F.; Weinstein, J. A. *Inorg. Chem.* **2016**, *55* (24), 12568–12582.

(2)   Gaunt, J. A. Ligand Effects on Oxidative Addition and Migratory Insertion Reactions of Rhodium Complexes, University of Sheffield, 2003.

(3)   Gonsalvi, L.; Gaunt, J. A.; Adams, H.; Castro, A.; Sunley, G. J.; Haynes, A. *Organometallics* **2003**, *22*, 1047–1054.

(4)   Sieh, D.; Kubiak, C. P. *Chem. - A Eur. J.* **2016**, *22*, 10638–10650.

(5)   Smieja, J. M.; Kubiak, C. P. *Inorg. Chem.* **2010**, *49* (20), 9283–9289.

(6)   Riplinger, C.; Sampson, M. D.; Ritzmann, A. M.; Kubiak, C. P.; Carter, E. A. *J. Am. Chem. Soc.* **2014**, *136*, 16285–16298.

(7)   Carter, E. a. *ACS Catal.* **2014**, *5*, 900–908.

(8)   Franco, F.; Cometto, C.; Ferrero Vallana, F.; Sordello, F.; Priola, E.; Minero, C.; Nervi, C.; Gobetto, R. *Chem. Commun. (Camb).* **2014**, *50* (93), 14670–14673.

(9)   Smieja, J. M.; Sampson, M. D.; Grice, K. A.; Benson, E. E.; Froehlich, J. D.; Kubiak, C. P. *Inorg. Chem.* **2013**, *52* (5), 2484–2491.

(10)   Zeng, Q.; Tory, J.; Hartl, F. *Organometallics* **2014**, *33* (18), 5002–5008.

(11)   Riplinger, C.; Carter, E. A. *ACS Catal.* **2015**, *5*, 900–908.

(12)   Franco, F.; Cometto, C.; Ferrero Vallana, F.; Sordello, F.; Priola, E.; Minero, C.; Nervi, C.; Gobetto, R. *Chem. Commun. (Camb).* **2014**, *50* (93), 14670–14673.

(13)   Manbeck, G. F.; Muckerman, J. T.; Szalda, D. J.; Himeda, Y.; Fujita, E. *J. Phys. Chem. B* **2015**, *119* (24), 7457–7466.

(14)   Smieja, J. M.; Kubiak, C. P. *Inorg. Chem.* **2010**, *49* (20), 9283–9289.

(15)   Orr, M. C.; Griswold, T.; Pitts, J. P.; Parker, F. D. *Curr. Biol.* **2016**, *26* (17), R792–R793.

(16)   Bourrez, M.; Molton, F.; Chardon-Noblat, S.; Deronzier, A. *Angew. Chem. Int. Ed. Engl.* **2011**, *50* (42), 9903–9906.

(17)   Bourrez, M.; Orio, M.; Molton, F.; Vezin, H.; Duboc, C.; Deronzier, A.; Chardon-Noblat, S. *Angew. Chem. Int. Ed. Engl.* **2014**, *53* (1), 240–243.

(18)   Grills, D. C.; Farrington, J. A.; Layne, B. H.; Lymar, S. V.; Mello, B. A.; Preses, J. M.; Wishart, J. F. *J. Am. Chem. Soc.* **2014**, *136* (15), 5563–5566.

(19)   Johnson, F. P. A.; George, M. W.; Hartl, F.; Turner, J. J. *Organometallics* **1996**, *15* (15), 3374–3387.

(20)   Carrington, S. J.; Chakraborty, I.; Mascharak, P. K. *Dalt. Trans.* **2015**.

7. Exploration of novel diimine ligands and the insights they offer to Lehn catalysts for CO₂ reduction.

7.1 Introduction to investigating N-ethyl-6-{6-[ethyl(4-hexylphenyl)carbamoyl] pyridin-2-yl}-N-(4-hexylphenyl)pyridine-2-carboxamide.

During the initial investigation of the catalytic properties of manganese phosphonate complex, [MnBr(CO)₃(4,4'-methylphosphonate-diethylester-2,2'-bipyridine] discussed in chapter 2 the photosensitivity of the complex became apparent. Our initial theory was that the photosensitivity may be addressed by incorporating electron donating moieties onto the bipyridine ring. These moieties would increase the electron density of the bipyridine ring resulting in stronger binding to the manganese which it was hoped would address photostability of the manganese complexes. Unfortunately the synthesis of these ligands proved to be challenging and further literature investigation had revealed that more electron donating diimine ligands would result in polarisation of the Mn-Br bond[1,2,3,4,5] as well as weaker metal carbonyl bonds which would most likely result in more facile dissociation and increased degradation.

Our collaborators at Lomonosov Moscow State University[6] offered to test a new ligand for this purpose, which has the electron withdrawing amide group. Previous research has shown that introduction of electron-withdrawing groups into diimine ligands led to decreased catalytic activity on rhenium based Lehn catalysts[7] ,most likely due to energy of the LUMO of the catalyst becoming insufficient for CO₂ reduction. Since the reduction mechanism may be different for Mn-complexes, we were curious to investigate if the new ligand would strike the balance between sufficient steric protection and sufficient driving force for the CO₂ reduction if it is used as a diimine ligand in [MnBr(CO)₃(diimine)].
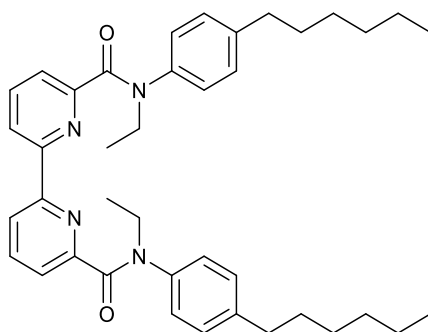
Scheme 7.1 Structure of the ligand provided by collaborators at Lomonosov Moscow State University - N-ethyl-6-{6-[ethyl(4-hexylphenyl)carbamoyl]pyridin-2-yl}-N-(4-hexylphenyl)pyridine-2-carboxamide (HPIB).

The ligand offered to us by our collaborators at Lomonosov Moscow State University (here after referred to as Hexyl-Phenyl-Imino-Bipyridine or HPIB) incorporates a very sterically demanding group which strongly appealed to us due to the results shown by Sampson *et al.* that steric hindrance has a major impact on the reactions of manganese complexes.[8] In particular we were curious to see whether the complex would be catalytically active at all or if this group would inhibit the association

of CO_2. The complex is also very interesting because this sterically demanding hexyl-phenyl moiety is directly attached to an electron withdrawing imide[7] offering not the sterically and electronically decoupled "chemistry" we had been investigating but rather sterically and electronically coupled chemistry.

7.1.3 Aims

The aims of this part of research are to investigate whether complexes incorporating such large, sterically demanding and electron accepting ligands are able to electrochemically reduce CO_2 and to investigate if there are any notable differences in the behaviour of rhenium based and manganese based derivatives. To use any information gathered from these novel complexes in order to advance our understanding of the chemistry of Lehn type catalysts for CO_2 reduction and use this as inspiration for further novel derivatives.

7.2 Experimental

7.2.1 Materials and General Procedures

Commercially available starting materials and reagents were obtained from Sigma-Aldrich, Apollo Scientific and STREM and used as received with the exception of tetrabutylammonium hexafluorophosphate (Sigma-Aldrich) which was recrystallized from hot ethanol and dried overnight in a vacuum oven. All solvents (Fisher Scientific, Sigma-Aldrich, VWR) were of HPLC grade or higher and were used without further purification unless otherwise stated. Dry solvents were obtained from a Grubbs solvent drying system.

7.2.2 Instrumentation and Analysis

7.2.2.1 Nuclear Magnetic Resonance (NMR) Spectroscopy

^1H and ^{13}C spectra were recorded using Bruker Avance 400 (DPX-400), Bruker Avance 400, Bruker Avance III HD 400, Bruker Avance III 400 and Bruker Advance III HD 500 spectrometers. Deuterated solvents were purchased from Sigma-Aldrich and were of spectroscopic grade.

7.2.2.2 Mass Spectrometry

High resolution mass spectra were obtained using direct infusion Na^+ ionisation and analysed using time of flight.

7.2.2.3 UV-Visible Absorption Spectroscopy

UV-Visible absorption spectra were recorded on a Cary 50 Bio spectrophotometer utilising 1 cm path length quartz curvettes.

7.2.2.4 Cyclic Voltammetry

Cyclic voltammetry on the complexes incorporating the HPIB ligand was performed in solution using acetonitrile with recrystallized [Bu$_4$N][PF$_6$] (TBAPF$_6$) at 0.2 mol dm^{-3} concentration as a supporting electrolyte. The potential was controlled using either a Princeton Applied Research VersaSTAT 3 potentiostat or an EmStat 3+ potentiostat. A glassy carbon working electrode (0.07 cm^2), platinum wire counter electrode and Ag/AgCl (0.1 M) reference electrode were used. All potentials are quoted vs Fc/Fc$^+$ unless otherwise stated. Initial scans were measured using a scan rate of 100 mV s^{-1} and reversibility was assessed using scan rates of 20 – 200 mV s^{-1}.

The solutions were degassed by bubbling thoroughly with N$_2$ and a nitrogen atmosphere was maintained over the samples during the experiment. To test for current enhancement the samples were bubbled thoroughly with CO$_2$ and measurements taken. 0.3 ml of water was then added to each sample to test the effects of adding a Brönsted acid. During these later experiments a CO$_2$ atmosphere was maintained over the samples during the experiment.

7.2.2.5 Spectroelectrochemistry (SEC) of the HPIB complexes

Infrared spectroelectrochemistry was performed using Princeton Applied Research VersaSTAT 3 potentiostat or EmStat 3+. 4 mmol dm^{-3} of the complex in presence of 0.17 g (0.3 mol dm^{-3}) of TBAPF$_6$ in dry acetonitrile was analysed using an optically transparent thin-layer spectroelectrochemical cell (OTTLE cell) equipped with Pt minigrid working electrodes, a Ag microwire pseudo-reference electrode and CaF$_2$ windows. Samples were prepared in argon atmosphere and samples for catalytic measurements were prepared by bubbling the electrolyte with CO$_2$ for 15 minutes. IR spectral monitoring of the experiment was performed on a Perkin Elmer Spectrum 1 FT-IR spectrometer using an MCT detector at 4 cm^{-1} resolution. Thin layer cyclic voltammograms were recorded at the same time.

7.2.2.6 Bulk electrolysis and Gas Chromatography of HPIB complexes

In order to confirm that the complex was reducing CO$_2$ 0.05 g of ReHPIB in 60 ml of 94.4 % acetonitrile to 5.6 % H$_2$O was subjected to controlled potential electrolysis (-2 V vs silver wire reference electrode) under stirring using a single compartment bulk electrolysis cell and an EG & G Instruments model 362 potentiostat. Gas samples from the head space were taken at regular intervals using a gas tight syringe and analysed using gas chromatography (H$_2$ carrier gas) fitted with a thermal conductivity detector in a ramping program.

The cell setup consisted of a Pt-mesh working electrode, a Pt-rod counter electrode contained in in a semiporous compartment and an Ag-wire pseudo-reference electrode in a 0.1 M KCl solution. The potential of the Fc/Fc$^+$ recorded in this setup using a glassy-carbon 3 mm diameter electrode was +0.350 V vs Ag wire pseudo-reference.

7.2.2.7 X-Ray crystallography

Crystals were grown using slow vapour diffusion antisolvent recrystalisation with DCM as the solvent and diethyl ether as an antisolvent. The resulting crystals were then analysed using X-ray crystallography. Figure 7.1 shows the X-ray structure of ReHPIB which agrees with the fac geometry of similar complexes reported in the literature.
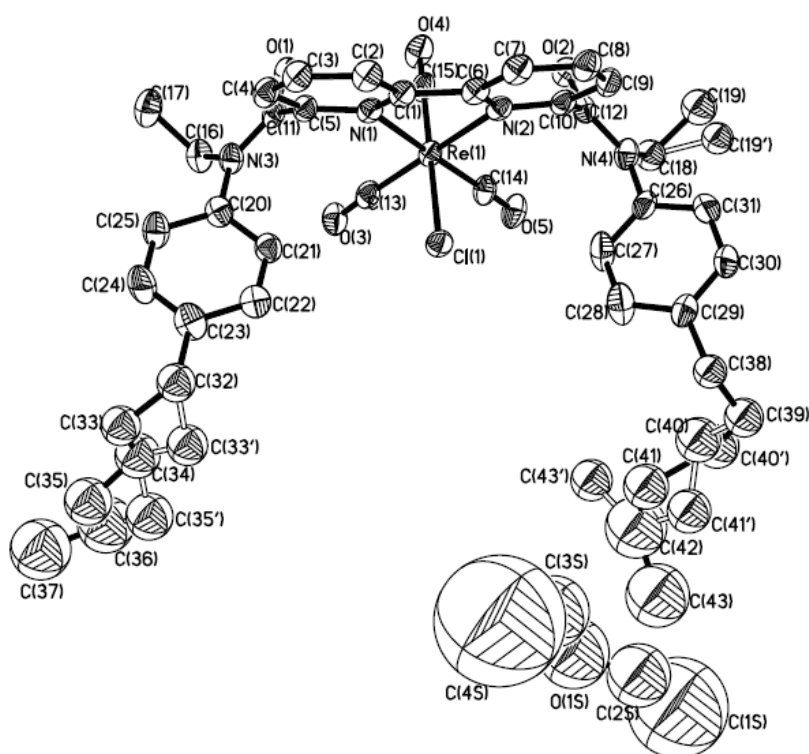
Figure 7.1 X-ray crystal structure of ReHPIB showing the alkane moieties and phenyl rings lying almost parallel to one another. The molecule in the foreground is diethyl ether anti-solvent which has been incorporated into the crystal

X-Ray crystallography showed that the phenyl rings lie almost parallel to one another with an angle between the planes of the phenyl rings of 157.51^O and the alkane chains point in the same direction. Importantly the phenyl rings and alkane chains are on the same side of the molecule as the chloride ligand, if a similar structure is maintained in solution then these moieties should have a large impact on the approach of CO_2 to the vacant coordination site. Most significantly the crystal structure confirms that binding to the metal centre is through the bipyridine moiety and not through the amide which was recognised as a possible binding mode.

7.2.3 Synthesis

7.2.3.1 Attempted synthesis of 6-aminoBOC-2,2'-bipyridine

In order to inhibit photodegradation it was hoped to develop a ligand that incorporated a strongly electron donating group on the 6 position of the bipyridine. This would hopefully donate enough electron density into the ring to allow stronger binding to the manganese (as at the time we suspected the bipyridine to be dissociating from the manganese) preventing photodegradation whilst leaving the 4 position free to incorporate a binding group (*vide supra*). The result was the attempted synthesis of 6-aminoBOC-2,2'-bipyridine.

7.2.3.1.1 Attempted BOC protection of 2-Bromo-6-amino-pyridine
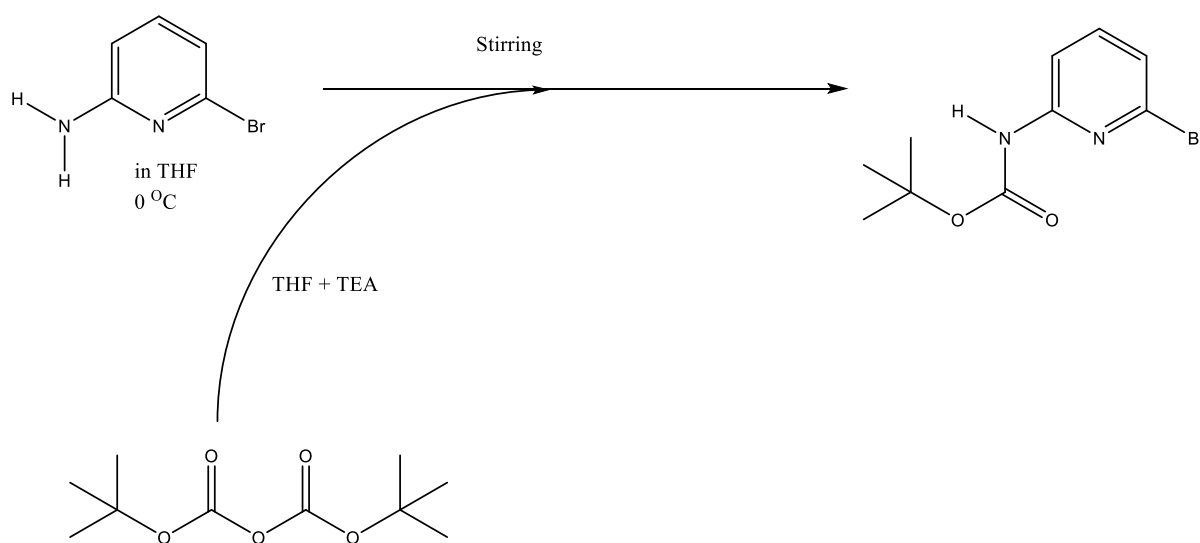
Scheme 7.2 Reaction scheme for the BOC protection of 2-Bromo-6-amino-pyridine.

2.619 g (1.2 molar equivalents) of di-tert-butyl-dicarbonate, dissolved in 10 ml of THF and 2.9 ml (2.1 molar equivalents) of TEA) was slowly added to 1.73 g (1 molar equivalent) of 2-bromo-6-amino-pyridine which dissolved in 10 ml of THF kept at 0 °C in an ice water bath. The solution was stirred for 4 hours at ambient temperature before being reduced to half volume and crashed out with hexane yielding pink crystals. Unfortunately NMR evidence revealed that the protection was unsuccessful.

7.2.3.1.2 Attempted cross coupling of 2-bromo-6-BOCamino-pyridine and 2-bromo-pyridine
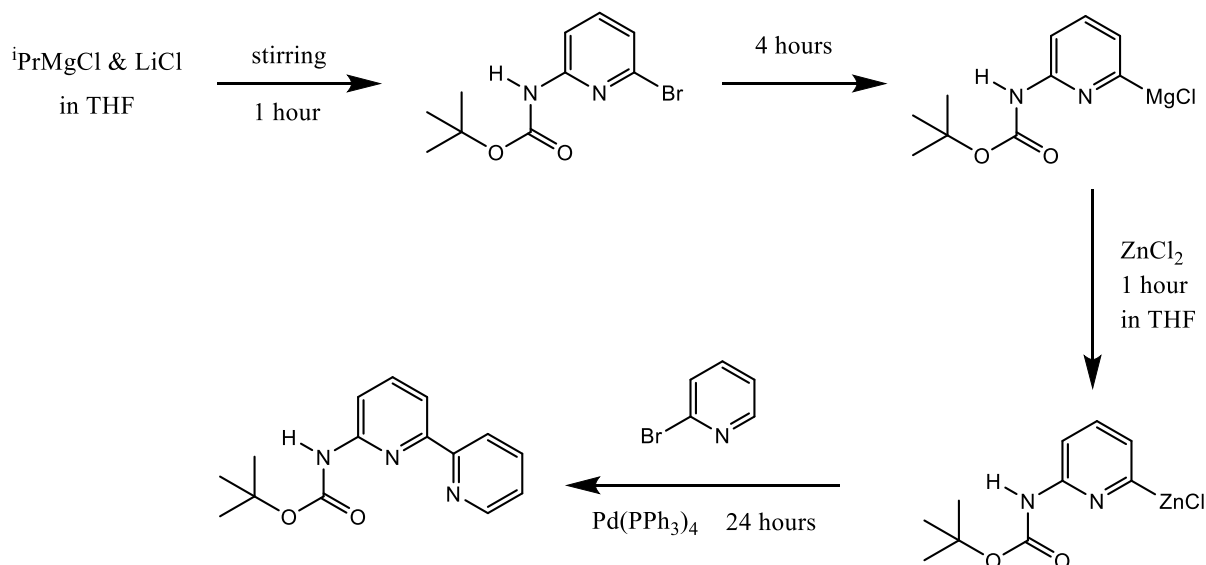
Scheme 7.3 Reaction scheme of cross coupling reaction to form 6-BOCamino-2,2'-bipyridine

In a dry Schlenk flask, under argon atmospehere, 4.2 mmol (2.1 cm^3) of 2.0 M ^{i}PrMgCl in THF was combined with 4.2 mmol (8.4 cm^3) of 0.5 M LiCl in THF and stirred for 1 hour. After an hour 2.4 mmol (0.6516 g) of what was believed to be the BOC protected 2-bromo-6-BOCamino-bipyridine and stirred for 4 hours, 1.6 molar equivalents (3.5 mmol) of dry ZnCl (0.5 M in THF) were injected into the reaction vessel and stirred for an hour. 2.4 mmol (0.23 ml) of 2-bromo-pyridine was added with 0.0611 g (0.053 mmol) of Pd(PPh$_3$)$_4$ and left to stir for 24 hours.

The reaction was quenched in 400 ml of Na$_2$CO$_3$ and EDTA (0.015 mol) and the layers separated. The organic layer was reduced to minimum volume and subjected to column chromatography on silica, first using petroleum ether as the eluent, which was gradualy changed to 1:1 petroleum ether:ethyl acetate system. Fractions 77-97 were combined and subjected to column chromatography on silica using 99:1 DCM:Methanol eluent. NMR and MS showed that this was starting material and the synthesis was not successful.

7.2.3.2 Synthesis of [ReCl(CO)₃(HPIB)]

The rhenium complex incorporating HPIB here after referred to as **ReHPIB** was synthesised in a manner similar to previously reported rhenium tricarbonyl α-diimines 0.323 mmols (0.200 g) of HPIB were added to 0.328 mmols (0.119 g) of Re(CO)₅Cl and refluxed aerobically in 20 cm^3 of toluene overnight. The reaction vessel was then left to cool to room temperature yielding very fine yellow/orange powder. 100 cm^3 of diethyl ether was added to the solution in an ice salt bath to crash out the remaining product. The crude product was filtered from solution using a glass sinter funnel

and the produced precipitate rinsed through with dichloromethane. Dichloromethane solution was evaporated to dryness, and the obtained yellow solid purified via column chromatography on silica using a 1:1 DCM: ethyl acetate mobile phase. This was sufficient to separate free ligand which was absorbed on the column whilst the complex has been eluted. The complex was then recrystalised by dissolving in 5 cm^3 of DCM, diethyl ether was then added until crystals formed. After purification fine bright yellow crystals were obtained in 43 % yield.

We felt it necessary to go to great lengths to purify the complex due the presence of smaller peaks in the NMR spectra (which do not correspond to free ligand), however, neither column chromatography nor recrystalisation proved able to remove these peaks in the NMR spectra (which had a relative integration of 0.03:1) and further investigation was conducted with trace amounts of unidentified material in. It is likely that this material is a different conformer of the complex as the RF values are identical and separation appears practically impossible, nor can any evidence for other complexes be seen in ^{13}C NMR or IR spectra. Additionally a second synthesis was carried out in an identical manner to the synthesis described above except that the product was isolated via centrifuging instead of filtering, no purification was applied (quantitative yield) and the resulting NMR spectra were identical to that of the purified complex, suggesting that several conformers are possible.

The complex shows carbonyl stretching bands at 1653 cm^{-1}, 1914 cm^{-1} and 2026 cm^{-1} with the latter two being based directly on the metal. Compared to the free ligand the carbonyl peak of the ligand shifts from 1640 cm^{-1} to 1653 cm^{-1} this is probably due to increased rigidity upon complexation.
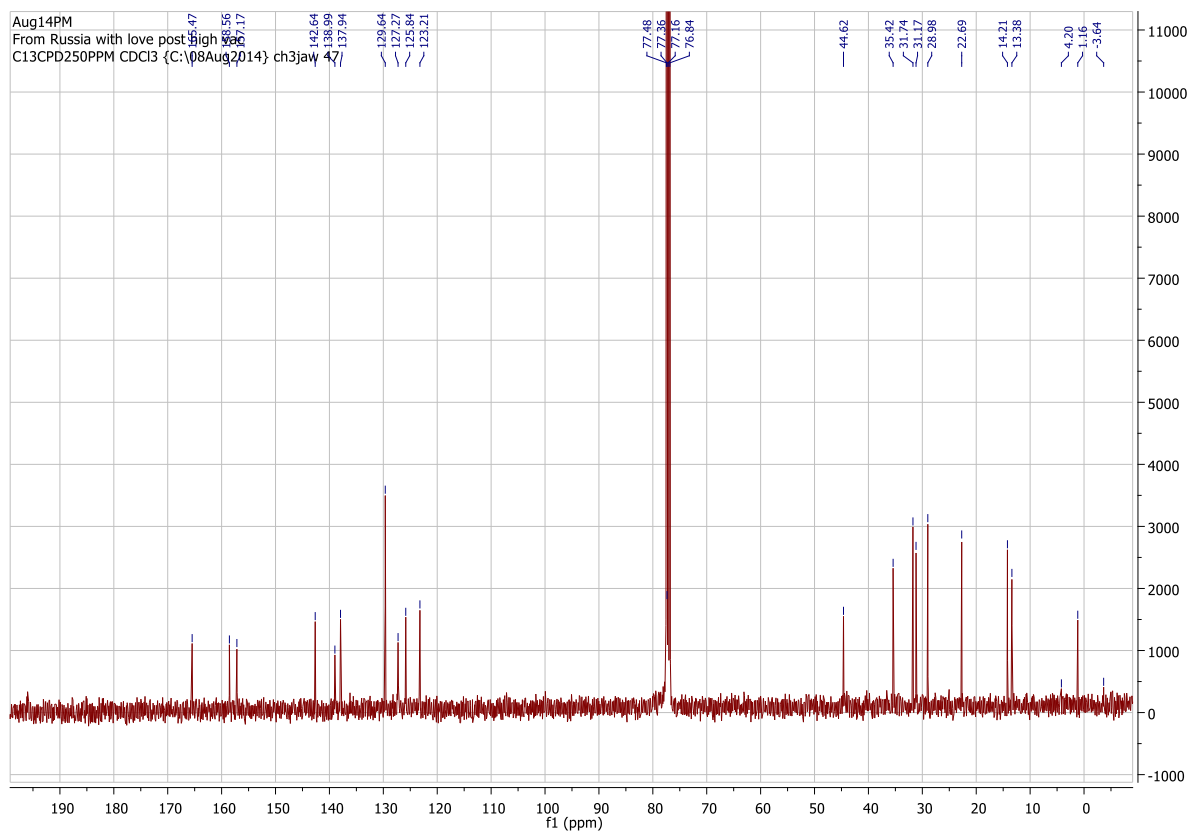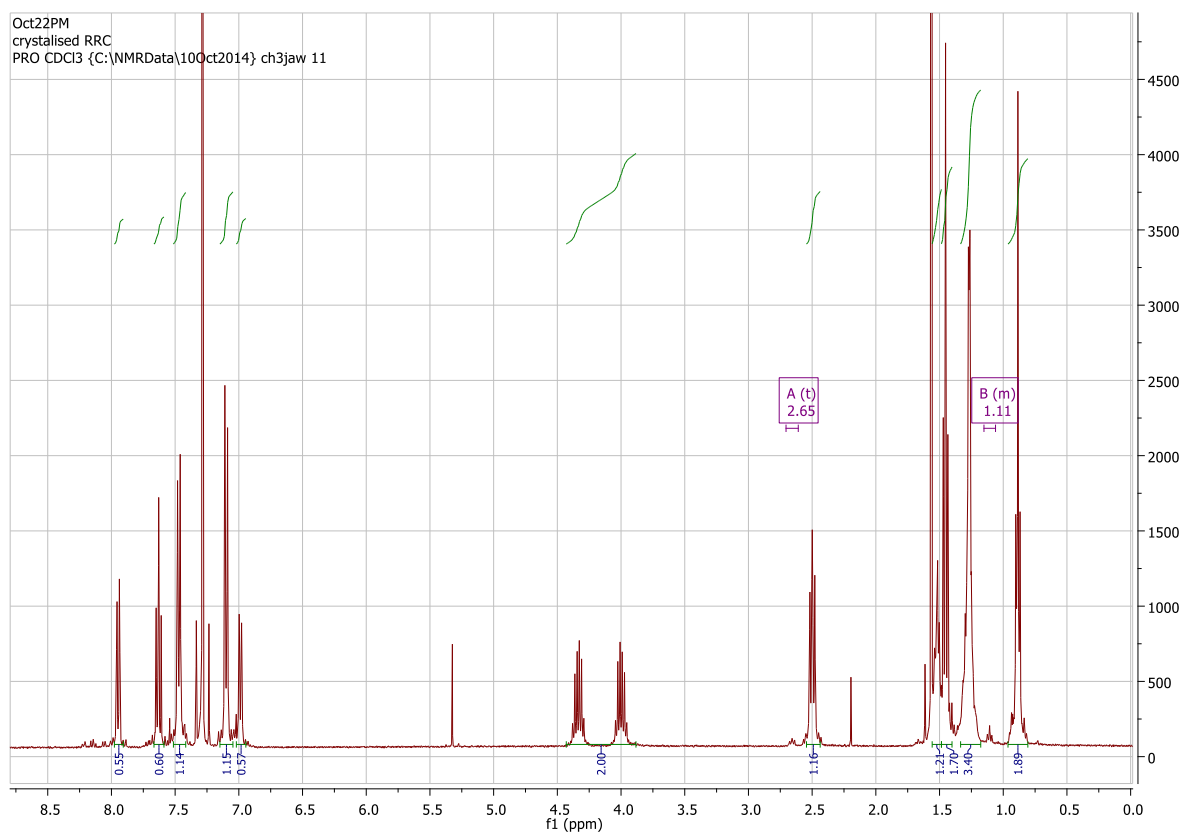
Figure 7.2 ^{1}H (top) & ^{13}C (bottom) NMR spectra recorded in CDCl$_3$ of Re HPIB.

Major peaks in ^{1}H NMR spectra (400 MHz, CDCl$_3$): δ 7.97 – 7.92 (m, 1H), 7.63 (t, J = 8.0 Hz, 1H), 7.47 (d, J = 8.3 Hz, 2H), 7.10 (d, J = 8.5 Hz, 2H), 6.99 (d, J = 7.7 Hz, 1H), 4.42 – 3.90 (m, 4H), 2.54 – 2.46 (m, 2H), 1.51 (dd, J = 13.5, 8.5 Hz, 2H), 1.48 – 1.41 (m, 3H), 1.36 – 1.20 (m, 7H), 0.88 (t, J = 6.8 Hz, 3H). ^{13}C NMR (101 MHz, CDCl$_3$) δ 195.99, 165.47, 158.64, 157.26, 142.62, 139.02, 137.90, 129.64, 127.29, 125.94, 123.13, 44.63, 35.43, 31.75, 31.17, 28.98, 22.70, 14.21, 13.38. MS (TOF, AP+): m/z 924.5. Elemental analysis calculated for C$_{43}$H$_{50}$ClN$_4$O$_5$Re: Carbon 55.86 %, Hydrogen 5.45 %, Nitrogen, 6.06 %, Chlorine 3.86 %. Found: Carbon 55.60 %, Hydrogen 5.39 %, Nitrogen 6.04 %, Chlorine, 3.69 %.
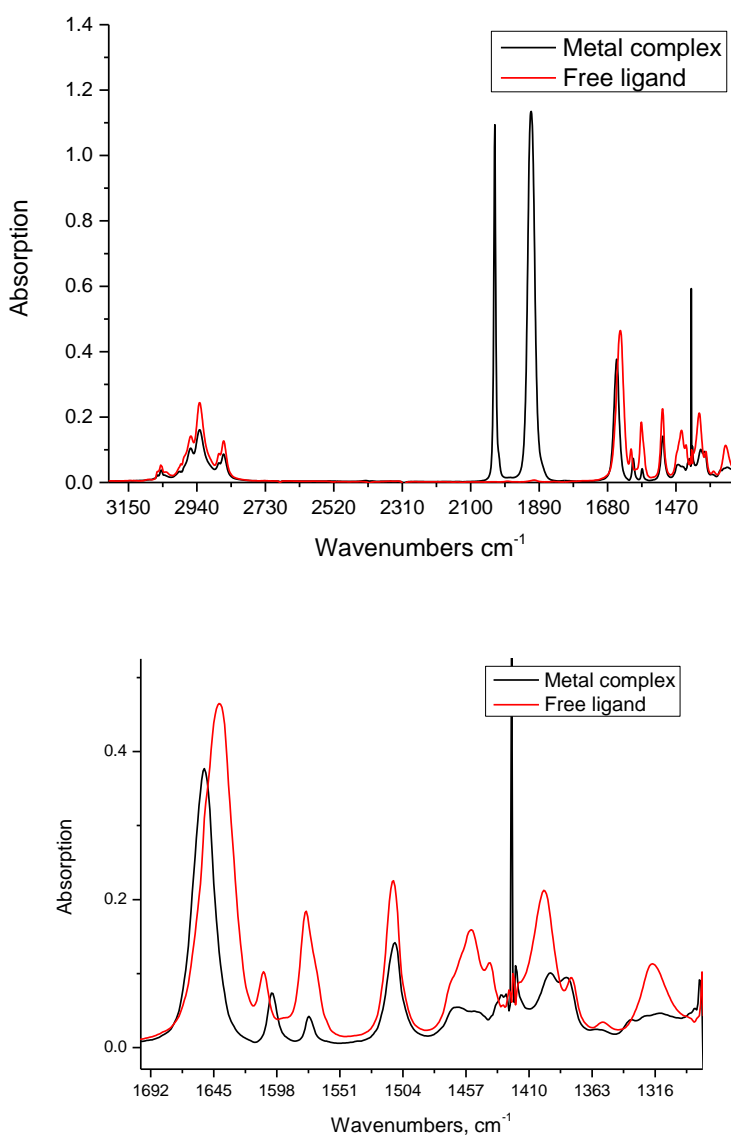
Figure 7.3 IR absorption spectra of the HPIB ligand and ReHPIB in CH$_2$Cl$_2$; the bottom panel shows an expansion of the fingerprint region.

7.2.3.3 Synthesis of [MnBr(CO)₃(HPIB)]

A discrete mixture the HPIB ligand (0.148g, 0.22 mmol) and [MnBr(CO)₅] (0.066g, 0.24 mmol) was refluxed at 40°C for 3 hours in diethyl ether (20ml). The reaction vessel was then left to cool and placed in the freezer overnight yielding fine orange powder. The powder was collected by centrifugation, and washed with diethyl ether to afford analytically pure MnHPIB. Yield 91 %. ^{1}H NMR (400 MHz, CDCl₃) δ 7.86 (s, 1H), 7.54 (d, J = 8.1 Hz, 3H), 7.09 (d, J = 8.3 Hz, 2H), 6.94 (d, J = 7.5 Hz, 1H), 4.17 (ddd, J = 21.3, 13.8, 6.9 Hz, 3H), 2.49 (t, J = 7.6 Hz, 2H), 1.50 (s, 3H), 1.40 (t, J = 7.1 Hz, 4H), 1.25 (s, 7H), 0.86 (t, J = 6.5 Hz, 4H). HRMS (TOF-ES, +ve): m/z (M+Na$^+$) Calcd for C₄₃H₅₀N₄O₅NaMnBr 859.2243; Found 859.2267.

7.3 Results and discussion

7.3.1 Photophysical properties of the rhenium and manganese HPIB complexes

The UV spectra shown in figure 7.4 reveal that both the rhenium and the manganese HPIB complexes have a strong absorption band at 325 nm which can be assigned to an intra ligand charge transfer due to its unshifted position between the two complexes. What is interesting is that the metal to ligand charge transfer band of the rhenium complex is at a shorter wavelength (ca. 400 nm) than the manganese analogue (ca. 450 nm). This is of course expected due to the lower energy HOMO of manganese compared to rhenium (first ionisation energy for manganese = 717.3 kJ mol^{-1}, second ionisation energy for manganese = 1509.0 kJ mol^{-1}, first ionisation energy for rhenium =760 kJ mol^{-1}, second ionisation energy for rhenium = 1260 kJ mol^{-1}).
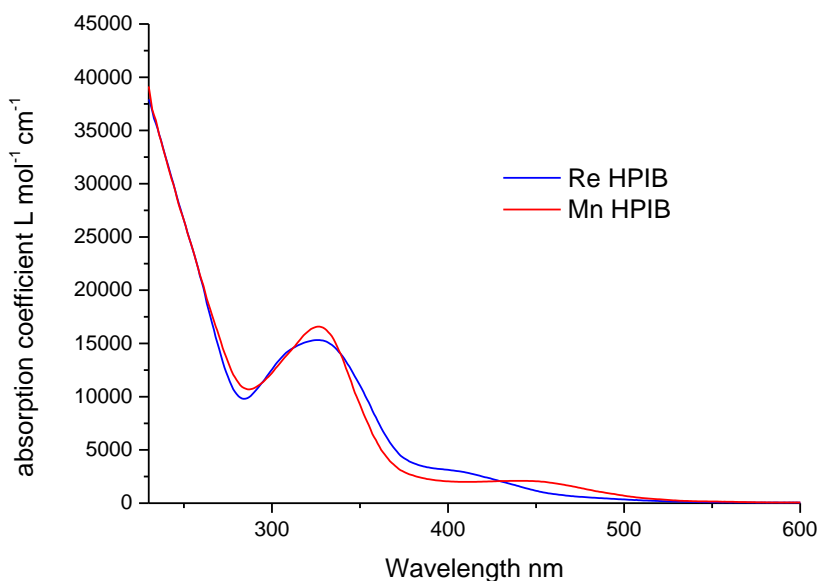
Figure 7.4 UV/vis absorption spectra of the rhenium and manganese complexes of the HPIB ligand, [ReCl(CO)₃(HIPB)] and [ReBr(CO)₃(HIPB)], in CH₂Cl₂ at r.t..

In line with reports from similar complexes[9,10,11,12,13] emission was observed for the ReHPIB complex whereas no emission was observed for the MnHPIB complex.
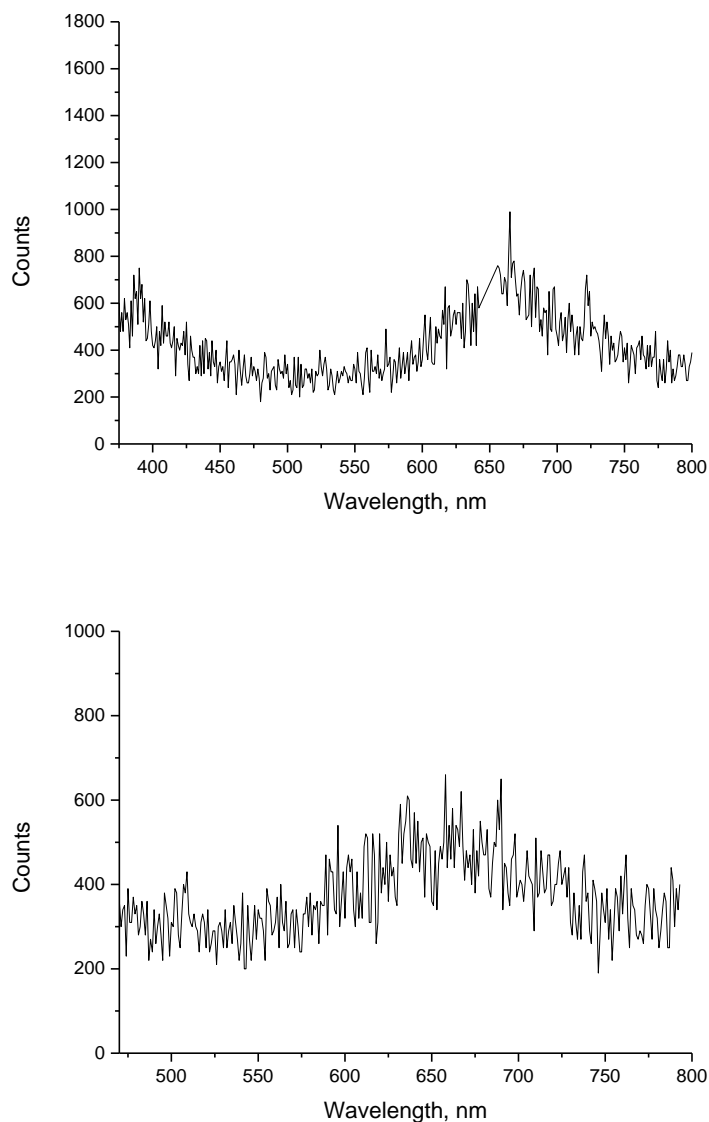
Figure 7.5 Emission spectra of ReHPIB recorded in DCM with excitation wavelengths of 325 nm (top) and 420 nm (bottom). Weak emission is observed at ca. 660 nm.

7.3.2 Electrochemistry of the rhenium and manganese HPIB complexes

Cyclic voltammetry experiments were carried out to evaluate the electrocatalytic properties and investigate the reduction behaviour of ReHPIB and MnHPIB.

Under nitrogen ReHPIB behaved very similarly to [ReCl(CO)$_3$(bpy)] with a reversible redox couple located at -1.72 V vs Fc/Fc$^+$ and an irreversible reduction peak at -2.19 V vs Fc/Fc in line with the reduction profile that is observed with [ReCl(CO)$_3$(bpy)]. Additionally however a smaller reduction peak is observed at -2.49 V vs Fc/Fc$^+$ we believe this smaller peak may be a

ligand centred reduction as it is observed for both ReHPIB and MnHPIB differing by only 20 mV and does not appear to be involved in catalysis. What is especially curious to note is the oxidation peak at -0.497 V vs Fc/Fc$^+$ observable at faster scan rates which is characteristic of dimer oxidation. No dimer was observed in the spectroelectrochemistry of ReHPIB which seems consistent with no dimer oxidation being observed at slower scan rates. Why this is the case is not clear and importantly no dimer oxidation is observed for MnHPIB.
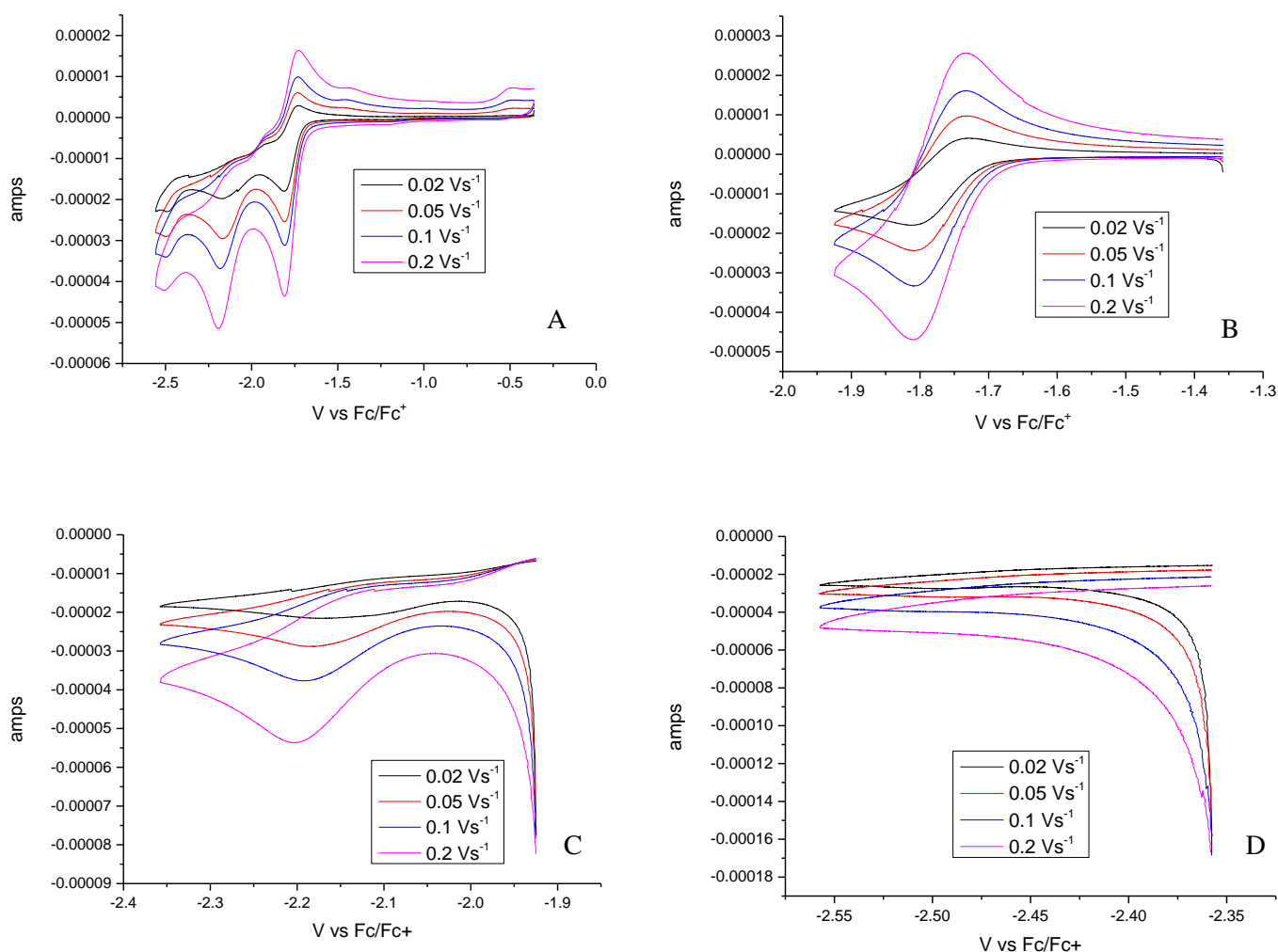
Figure 7.6 Cyclic voltammetry traces of redox processes in ReHPIB under N$_2$ at different scan rates in 6 ml of Grubbs dried acetonitrile with 0.2 M TBAPF$_6$.

For MnHPIB, the first and second reduction processes lie at -1.51 and -1.7 V vs Fc/Fc$^+$ giving only 0.19 V separation between theses electrochemical processes compared with 0.47 V for ReHPIB. As a result, in contrast to ReHPIB, under nitrogen MnHPIB shows behaviour which may be described as more constant with that observed in complexes incorporating asymmetric ligands, such as those discussed in chapter 5[14] or diazabutadiene ligands,[15] than with manganese complexes incorporating bipyridine ligands that are not decorated with highly sterically demanding groups.[16] The result of this

is that the five-coordinate anion should be generated at a much lower potential than bipyridine complexes. Interestingly the complex appears to behave more like these complexes than with manganese complexes that incorporate highly sterically demanding ligand 6,6'-dimesityl-2,2'-bipyridine[8] which show only a single well defined reduction under N_2. The voltammograms shown in figure 7.7 (B & C) show that the reduction and oxidation observed does not arise from a reversible redox pair (in which case the peak maxima would not vary with scan rate and the ratio between the reductive and oxidative peaks potentials would be defined by equation 7.1 where n is the number of electrons transfered) but rather the reduction and oxidation are two separate irreversible process arising from an electrochemical-chemical process (most likely bromide) loss producing the five-coordinate anion.

$$E_{pa} - E_{pc} = 56.5 \text{ mV/n} \qquad\qquad 7.1$$
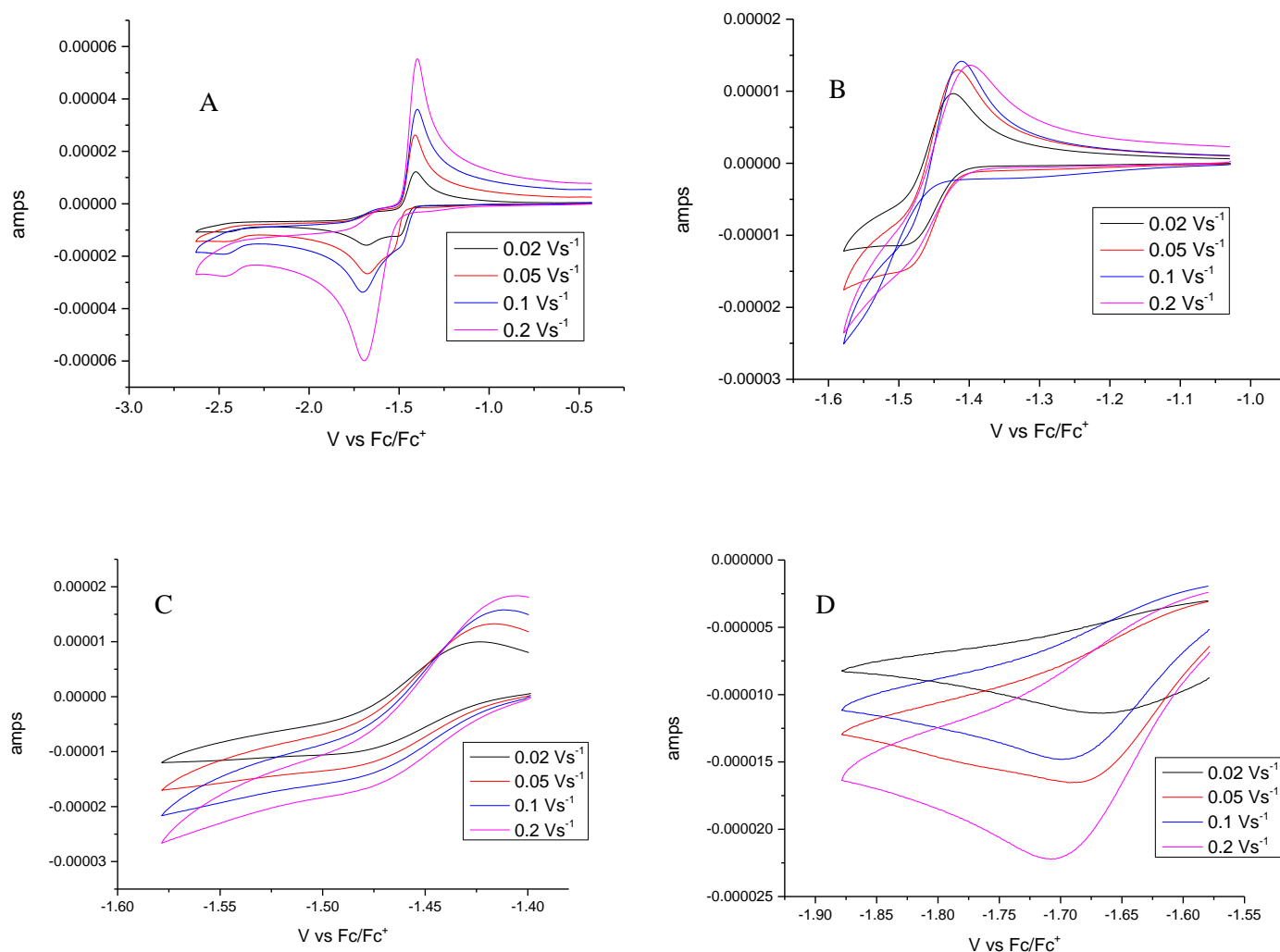
Figure 7.7 Cyclic voltammetry traces of redox processes in MnHPIB under N_2 at different scan rates in 6 ml of Grubbs dried acetonitrile with 0.2 M TBAPF$_6$.
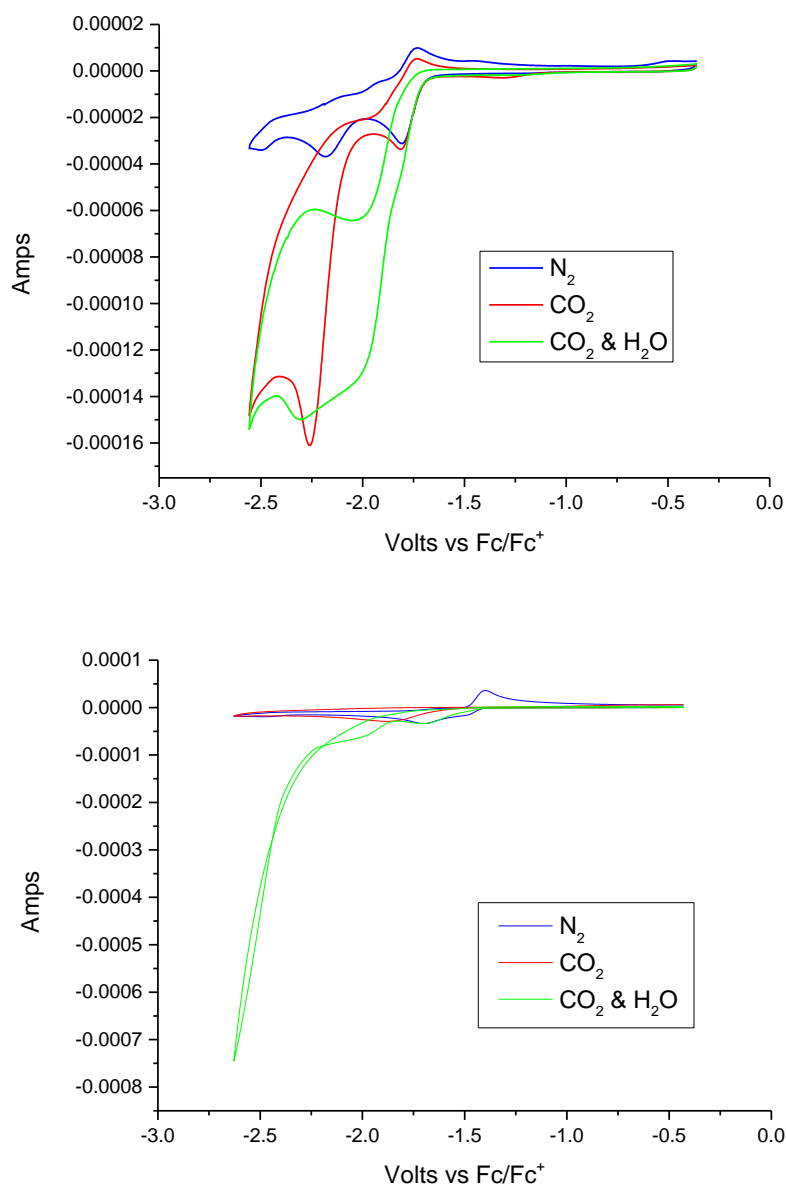
Figure 7.8 CV traces of ReHPIB (top) and MnHPIB (bottom) under N_2, CO_2 and CO_2 in the presence of 0.3 ml of water. Solvent MeCN with 0.2 M TBAPF$_6$ as supporting electrolyte.

For ReHPIB under CO_2 current enhancement can be seen on the second reduction peak (-2.19 V) and some reversibility of the redox pair at -1.72 V is observed at faster scan rates (figure 7.9). The presence of water results in increased catalytic activity and all reversibility of the first reduction is lost in line with what has been observed for other rhenium tricarbonyl α-diimine electrocatalysts. Importantly current enhancement can be observed under both CO_2 and CO_2 in the presence of a Brönsted acid (water)[17,18] with little change in the peak current or voltage of peak current enhancement. The presence of water seems to have shifted the onset potential from -2.19 V to -1.72 V, it may be that this is due to the presence of water facilitating the elimination of the chloride anion allowing for association of the CO_2 at lower potentials.
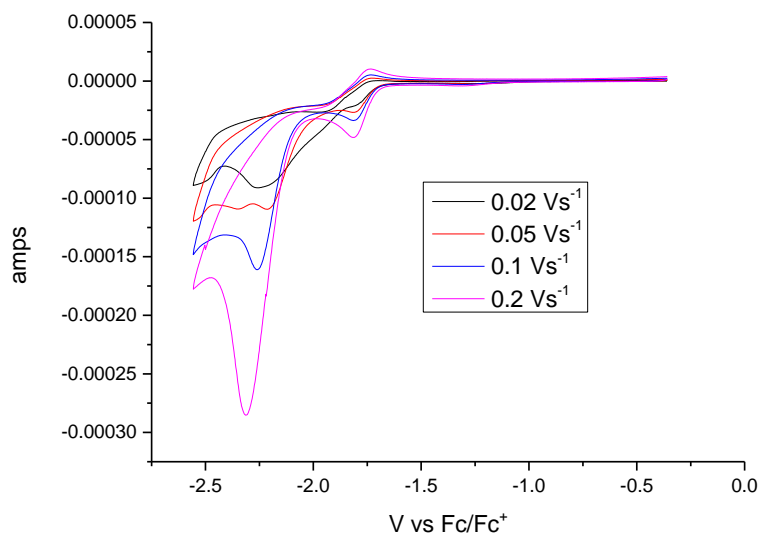
Figure 7.9 Cyclic voltammetry traces of redox processes in MnHPIB under CO_2 at different scan rates in 6 ml of Grubbs dried acetonitrile with 0.2 M TBAPF$_6$.

Under CO_2 MnHPIB exhibits only a single reduction peak at -1.88 V vs Fc/Fc$^+$ with no corresponding oxidation peak at lower scan rates and a small oxidation peak visible at higher scan rates. Unlike ReHPIB no current enhancement is observed under CO_2,[19] however in the presence of water some current enhancement can be observed at potentials between -1.88 V and -2.17 V vs Fc/Fc$^+$, although not to the same degree as ReHPIB, however, after -2.17 V vs Fc/Fc$^+$ the degree of current enhancement increases sharply and at lower potentials MnHPIB appears to outperform the rhenium analogue. It is important to remember that comparing performance at different overpotentials is not straightforward and must be done so with some caution.[20,21,22,23,24,25,26]

Table 7.1 Reduction potentials observed between 0 and -2.5 V vs Fc/Fc$^+$ in N$_2$ saturated MeCN solvent in the presence of 0.2 M TBAPF$_6$.

ReHPIB V vs Fc/Fc$^+$	MnHPIB V vs Fc/Fc$^+$
-1.72	-1.51
-2.19	-1.7
-2.49	-2.47

Table 7.2 Ratio of catalytic current to peak current under inert atmosphere.

	$\frac{i_{cat}}{i_p}$ -2 V vs Fc/Fc$^+$	$\frac{i_{cat}}{i_p}$ -2.5 V vs Fc/Fc$^+$
ReHPIB	6.24	4.21
MnHPIB	3.44	22.67

7.3.3 IR-SEC of the HPIB complexes

In order to understand how the complexes behave upon reduction IR-SEC analysis was performed under argon and CO_2.

The assignment of the ReHPIB spectra was complicated as there were many overlapping IR absorption bands of low intensity. In order to try and produce more clear spectra the experiment was performed on two different IR-Spectrometers using different potentiostats, as can be seen the results are similar in both cases. Assignment is based primarily on the reported spectra by Johnson *et al.*[27] The parent complex exhibits carbonyl stretching bands at 2025 and 1912 cm^{-1} and upon reduction forms the one electron reduced complex $[ReCl(CO)_3(HPIB)]^{\bullet-}$ with absorption bands shifted to 2004 and 1882 cm^{-1}, the 23 cm^{-1} decrease in frequency being identical to what is observed for $[ReCl(CO)_3(bpy)]$. Upon further reduction, two peaks are observed at 1992 and 1975 cm^{-1} as well as a very broad peak centred at 1868 cm^{-1}. This later peak appears to be composed of several absorption bands, which could be due to the growth of both the radical and the anionic acetonitrile coordinated species.
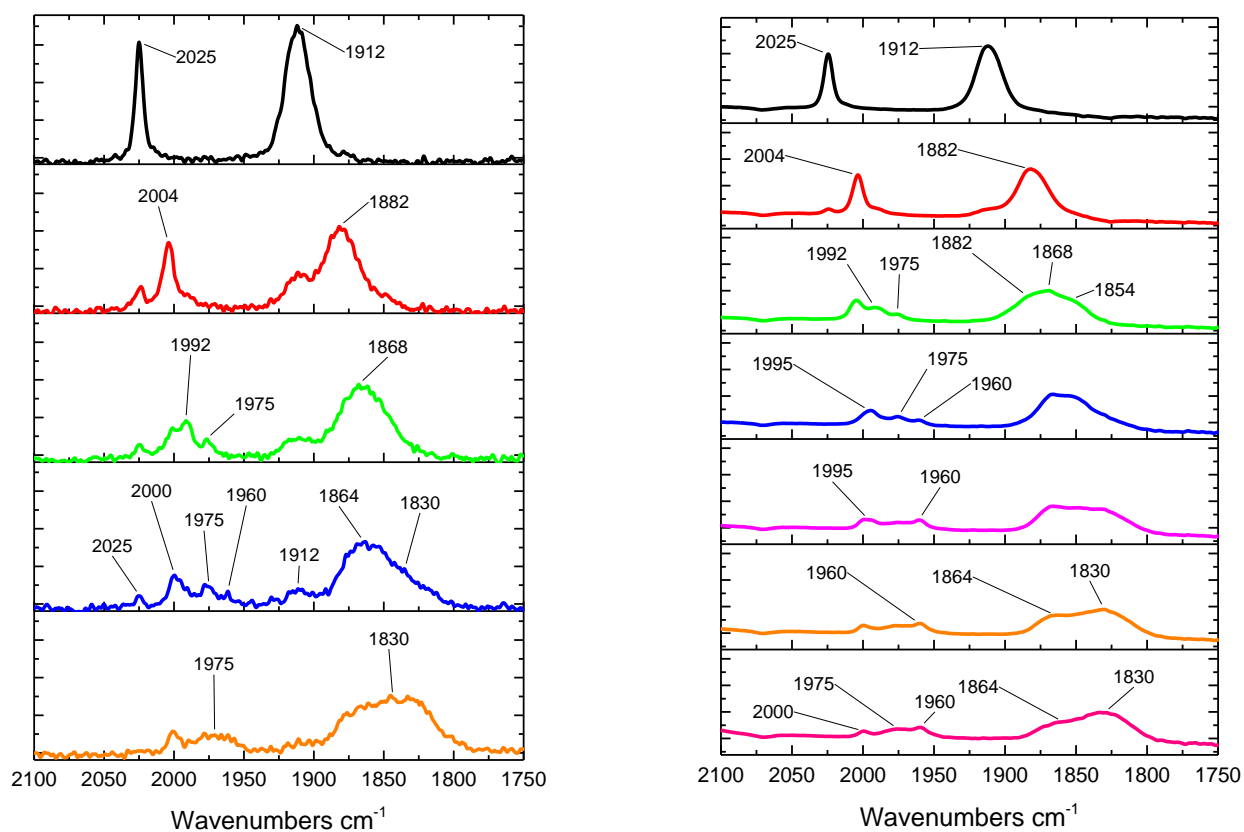
Figure 7.10 IR-SEC spectra of ReHPIB under argon performed in Grubbs dried acetonitrile in the presence of 0.3 M TBAPF$_6$. Reduction performed on a VersaSTAT 3 potentiostat and monitored on a Perkin Elmer Spectrum 1 IR spectrometer (left) and the spectra recorded using an EmSTAT 3+ potentiostat and Thermofisher IS10 spectrometer.

Upon further reduction the 5-coordinate anion was observed in the OTTLE cell (this was observed directly as the complex over the platinum mesh working electrode becomes an intense purple colour upon formation of the 5-coordinate anion, this has been observed for all complexes discussed in this thesis) based on peaks at 1960 and 1930 cm^{-1}, however, not all of the $[Re(CO)_3(HPIB)(MeCN)]^-$ was converted into the 5-coordinate anion.
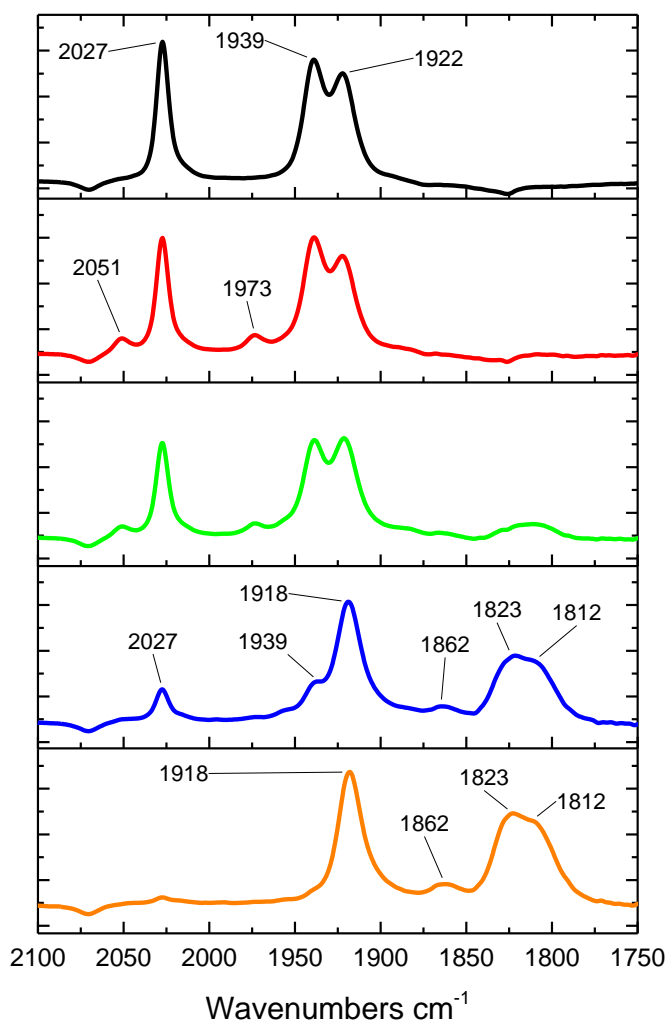
Figure 7.11 IR-SEC spectra of MnHPIB under argon performed in Grubbs dried acetonitrile in the presence of 0.3 M TBAPF$_6$.

The manganese analogue exhibits a much less ambivalent IR absorption spectrum and behaves as would be anticipated based upon the cyclic voltammograms. As the potential is made more negative a small population of aqua complex $[Mn(CO)_3(HPIB)(H_2O)]^+$ forms based on the peaks at 2051 and 1973 cm^{-1} which are very similar to what has been observed in other manganese complexes. [14,15] No dimer appears to form upon further reduction instead the 5-coordinate anion forms directly and is

identified by the peaks at 1918, 1823 and 1812 cm^{-1}. We believe the peak at 1862 cm^{-1} is also associated with the 5-coordinate anion.[14]

Table 7.3 Assigned carbonyl stretching frequencies of HPIB species[27]

Species	Peak position / cm^{-1}
[ReCl(CO)$_3$(HPIB)]	2025, 1912
[ReCl(CO)$_3$(HPIB)]$^{\bullet-}$	2004, 1882 (br)
[Re(CO)$_3$(CH$_3$CN)(HPIB)]$^{\bullet}$	1992, 1868 (br)
[Re(CO)$_3$(CH$_3$CN)(HPIB)]$^-$	1975, 1868 (br)
[Re(CO)$_3$(HPIB)]$^-$	1962, 1830 (br)
[MnBr(CO)$_3$(HPIB)]	2027, 1939, 1922
[Mn(CO)$_3$(HPIB)(H$_2$O)]$^+$	2051, 1973
[Mn(CO)$_3$(HPIB)]$^-$	1918, 1862, 1823, 1812

Upon reduction in CO$_2$ saturated MnHPIB initially forms a small quantity of the aqua cation, this along with the parent complex are then reduced directly to the 5-coordinate anion, which builds up a significant meta stable population. A small amount of CO$_2$ associate bicarbonate complex is observed at 1684 cm^{-1} alongside the free bicarbonate and subordinate formate band centred at 1645 cm^{-1} confirming the reduction of CO$_2$ (these assignments are speculative but are based previous work and literature sources[14,15,27]). A simultaneous depletion of the CO$_2$ absorption bands was observed (not shown).
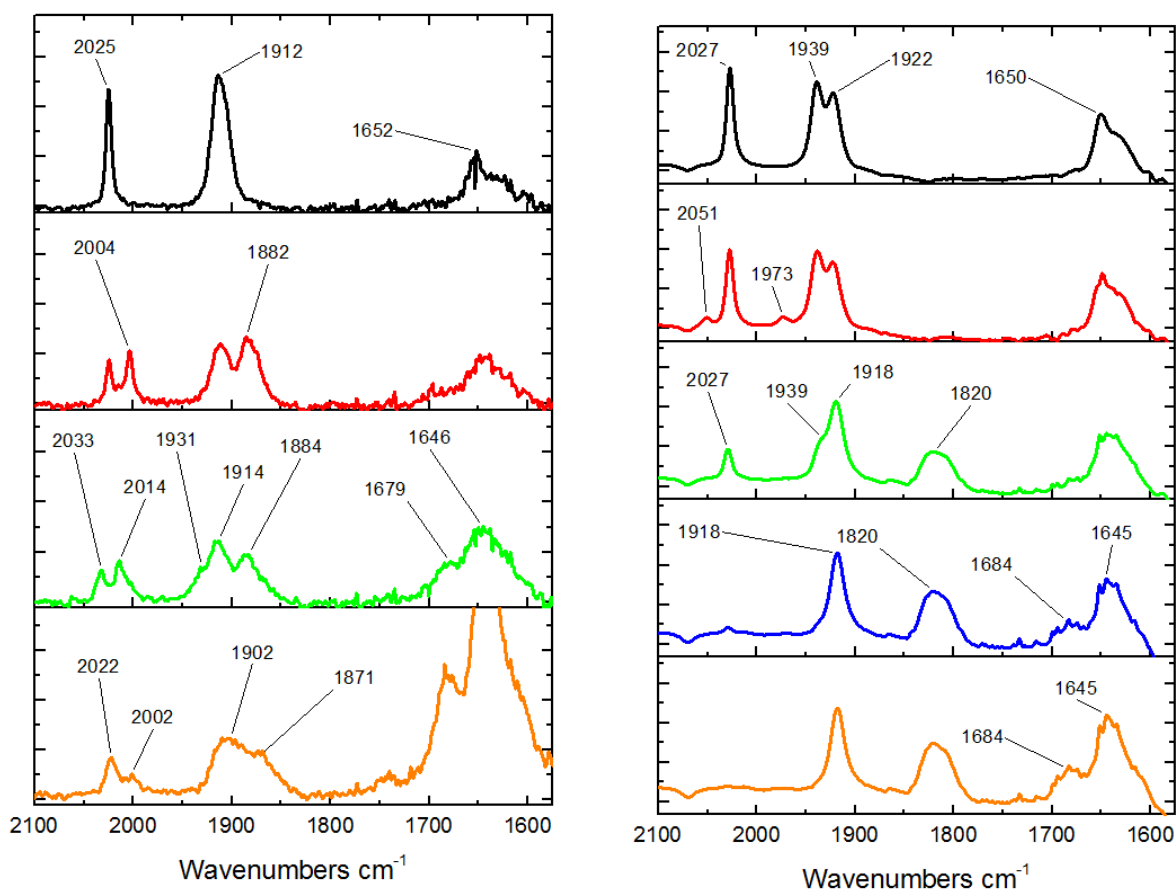
Figure 7.12 IR-SEC spectra of ReHPIB (left) and MnHPIB (right) under CO_2 performed in Grubbs dried acetonitrile in the presence of 0.3 M TBAPF$_6$.

ReHPIB under CO_2 forms the one electron reduced $[ReCl(CO)_3(HPIB)]^{\bullet-}$ complex which upon further reduction forms a CO_2 associated complex based on the band observed at 1679 cm^{-1}. The reaction mechanism followed after this point is not clear as no 5-coordinate anion is observed and the CO_2 coordinated bicarbonate species is observed. This is somewhat surprising as it was assumed that the alkyl chains would act to inhibit CO_2 association as was observed for MnHPIB, it may be however that the larger rhenium nucleus is able to more easily coordinate CO_2. Multiple peaks are observed in the spectra which migrate over time to lower wavenumbers, it seems probable from the observed results that there are to different CO_2 associated species which are most likely conformers.

7.4 Conclusions

We can conclude from these complexes that having such large sterically demanding groups in the ortho position does not act to inhibit CO_2 reduction. In addition the effects of the electron withdrawing carbonyl moiety do not prevent catalytic activity. Under CO_2 no 5-coordinate anion is observed with the rhenium complex indicating that the metal nucleus is much more accessible than is the case with the manganese analogue. The complexes have shown that electron withdrawing moieties close to the diimine and sterically demanding groups close to vacant coordination sites do not prevent

catalytic CO_2 reduction, this opens opportunities for many other complexes which may otherwise have been overlooked.

7.5 Further work

The HPIB project was unique in that it acted as the genesis for several other projects which at the time of writing are incomplete but in which the project has progressed to the point where by they are ready to start yielding results. The section will outline the status of the projects and the background to their development.

7.5.1 Photochemical degradation

As is discussed above the HPIB project was initially born out of an aim was to investigate whether changing the moieties on the bipyridine ligand would result in significant changes to the rate of photochemical degradation. To this end an experimental method for quantitatively measuring the rate of photodegradation was developed using a modified flash laser set up. A broad band Xe lamp would irradiate a sample of a manganese complex resulting in photodegradation and increased transparency of the MLCT band, as is shown in figure 7.13 Degradation was monitored by recording the increase in transparency of the MLCT band with a photon multiplier tube. Increased transparency results in a higher voltage being reported by the photon multiplier tube. The voltage could be measured at regular intervals and compared to 100 % transmission seen with DCM. The voltage is converted to differential absorption using equation 7.2, where Voltage t is the recorded voltage at the time t and C is the voltage of 100 % transmission, and normalised.

$$-\log(\text{Voltage t})/C \qquad\qquad 7.2$$

$$N(t) = N0\ e^{((-t)/\tau)} \qquad\qquad 7.3$$

From the differential absorption the lifetime can be calculated using equation 7.3, where N(t) is the differential absorption at time t, N0 is the initial differential absorption and τ is the observed lifetime, and using equation 7.4 the observed half-life can be calculated.

$$t_{1/2} = \tau\ \ln(2) \qquad\qquad 7.4$$
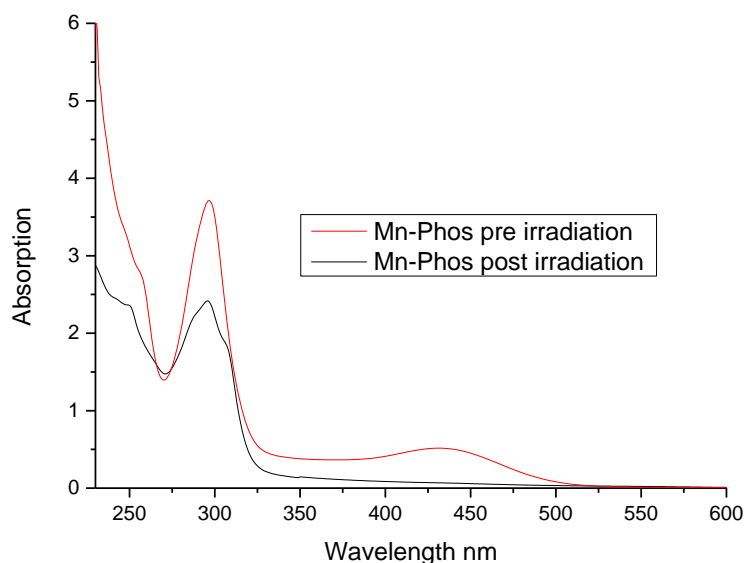
Figure 7.13 [MnBr(CO)₃(4,4'-methylphosphonate-diethyl-2,2'-bipyridine)] (Mn Phos) in DCM before and after broad band irradiation with a Xe lamp. As can be seen the intensity of the absorption at ca. 400-500 nm decreases substantially upon photodegradation.

In order to find the most suitable method to accomplish this several variations were investigated based upon changing the following factors: the cell type, the aperture size, the method of data recording and the use of filters.

7.5.1.1 Flow cell, no aperture, manual data recording, neutral density filter

The first method investigated involved using a flow cell with a 2 mm path length through which a solution of 1.7×10^{-5} mols of complex (0.0118 g of Mn phos and 0.0141 g of MnHPIB) dissolved in 20 cm^3 of DCM would be flowed. The beam was unfocussed and fitted with a neutral density filter for a measured power output 20 mW +/- 1mW). This method was used because we were concerned that diffusion in a static cell would result in inaccurate data, as such a flow cell was used in which the solution was cycled until no change in observed voltage was seen with voltage readings were taken every minute. This method was used to generate the data shown in table 7.4 and figure 7.14
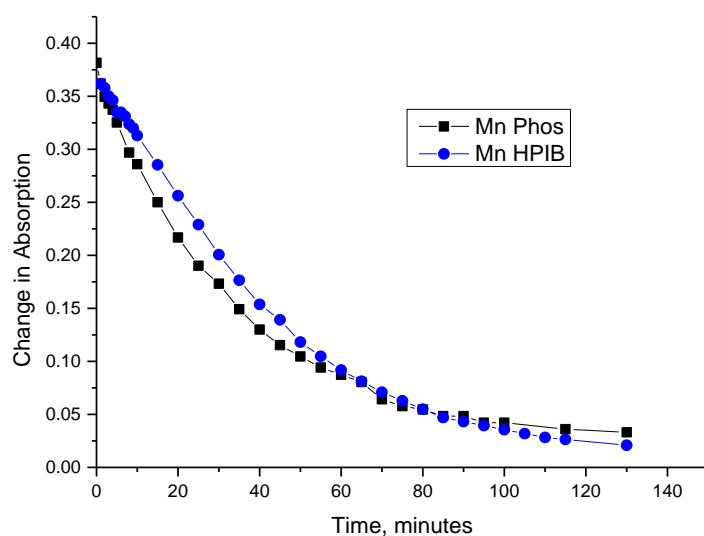
Figure 7.14 Decay traces of [MnBr(CO)₃(4,4'-methylphosphonate-diethyl-2,2'-bipyridine)] and MnHPIB in flow cell.

As can be seen in figure 7.14 the initial rate of decay of MnHPIB appears to be slower than Mn Phos. The half-lives shown in table 3 confirms that MnHPIB does have a slightly longer observed half-life than Mn Phosphonate. From this data we could regard HPIB to be a partial success; we have not prevented degradation though we have apparently inhibited it slightly.

Table 7.4 Observed kinetics of photochemical decay, flow cell in DCM

	τ -Observed lifetime minutes	$t_{1/2}$ – Observed half-life minutes
Mn Phosphonate	34.1 (+/- 0.6)	23.6
MnHPIB	47.9 (+/- 1.8)	33.2

7.5.1.2 Static cell

Flowing the solution was not the ideal method of conducting the experiment as the rate of diffusion in a 2 mm static cell should be very slow and if the solution is not being flowed then the timescale of the experiment could be shortened from tens of minutes to seconds and the diffusion of undecayed material into the path of the light would probably be negligible. Following on from this we needed to decide if it was better to have a beam focussed on a narrow area of solution (5mm or so) recording a decay trace in that spot or if it would be better expose the entire sample to light and collect a decay trace over the entire sample area. The advantage to using a focussed spot is that theoretically it should be more precise as the photon flux across the sample area should be constant which may not be true of an unfocussed beam. The advantage to the unfocussed beam is that there is less risk of diffusion and there is more light reaching the sample so the decays should be more rapid and easily observable.
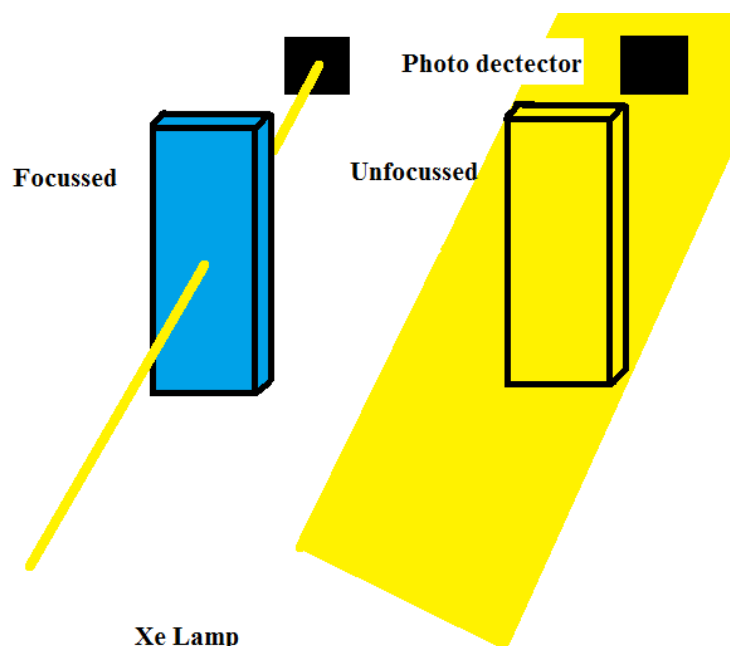
Figure 7.15 Representation of the two beam types explored in the degradation rate experiments.

The second question was should the light from the Xe lamp be passed through a filter or not? By using a filter with transmission in the 400 -500 nm region the bands being excited should be the MLCT and XLCT bands of the manganese complex[2] and we would know what transmission was occurring. Conversely that was a problem in itself, as was discussed in chapter 2 there is no evidence that the MLCT/XLCT transition is the one responsible for photodegradation. Further the power output of the Xe lamp will be further decreased.
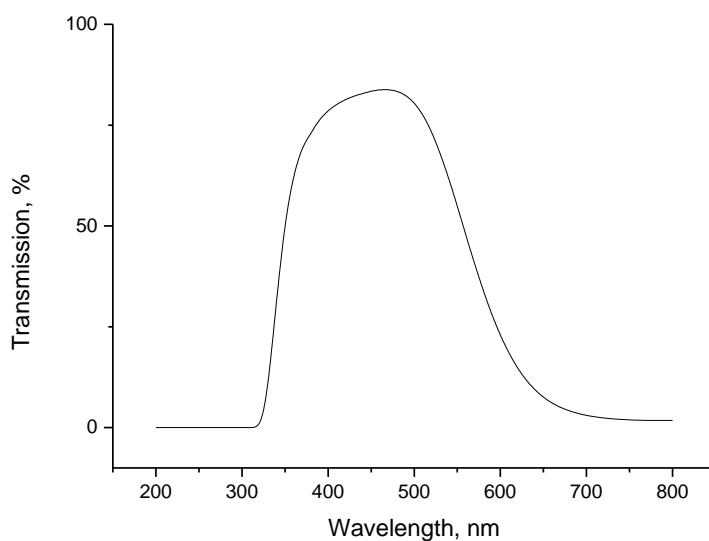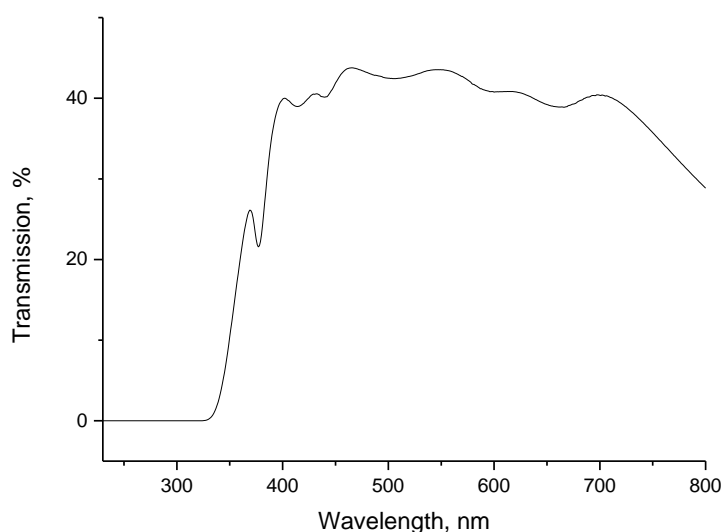
Figure 7.16 Transmission spectrum of the selective wavelength filter (top) and neutral density filter (bottom).

In order to test this solution of Mn-Phos in DCM (prepared as above) was subjected to degradation under the following conditions: with filter, unfocussed; with filter, focussed; no filter, unfocussed; no filter, focussed and with a neutral density filter, unfocussed. This last run was performed to compare the filtered and unfiltered kinetics at comparable power outputs. The change in voltage was recorded with a video camera and frames analysed individually to give a change in voltage measured in arbitrary units.

Table 7.5 Observed kinetics of photochemical decay, static cell in DCM

	τ -Observed lifetime seconds	$t_{1/2}$ – Observed half-life seconds
With filter, unfocussed	9.2	6.4
With filter, focussed	6.5	4.5
No filter, unfocussed	6	4.2
No filter, focussed	3.5	2.4
Neutral density filter, unfocussed	19	13.2

What can be seen from the results in table 7.5 is that experiments that were unfiltered resulted in the fastest observed rate degradation as did the experiments with a focussed beam. This is most probably due the greater photon flux arising from the unfiltered sample and the smaller quantity of material that must be decayed. The decay traces shown in figure 7.17 show the differences between the different experimental set ups, from this it appears that the unfiltered focussed beam provides the most complete degradation. Based on the results discussed in chapter 2 it is likely that use of the filter inhibits certain degradation pathways and so is not the ideal method for studying degradation.
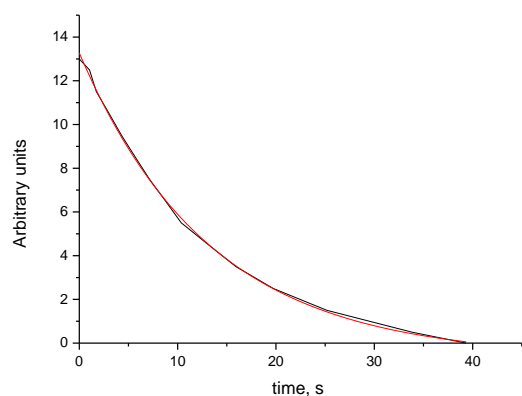
Filter, unfocussed
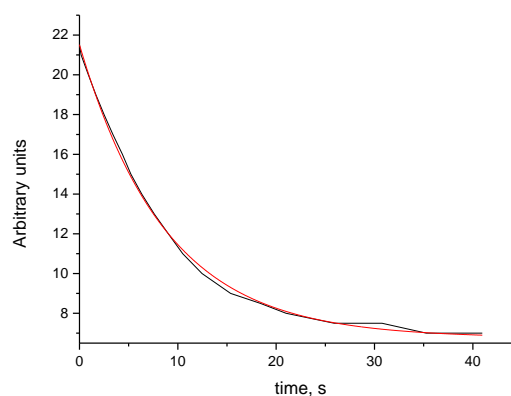
No filter, unfocussed
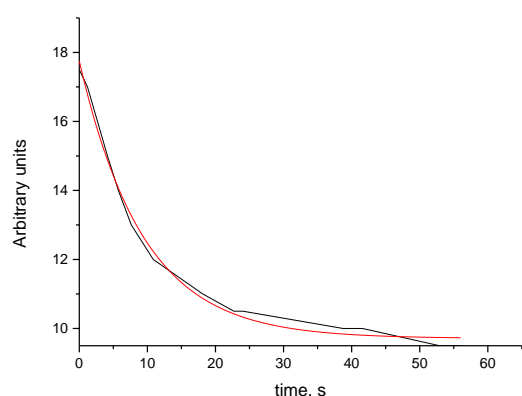
Filter, focussed
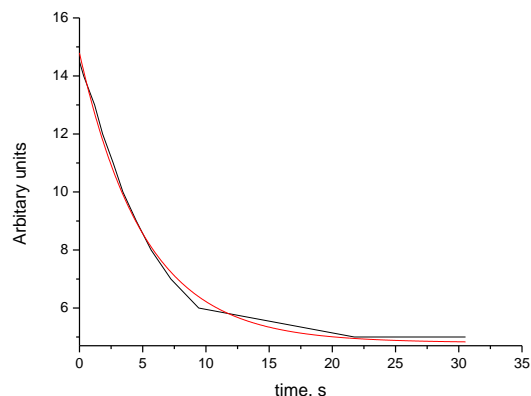
No filter, focussed
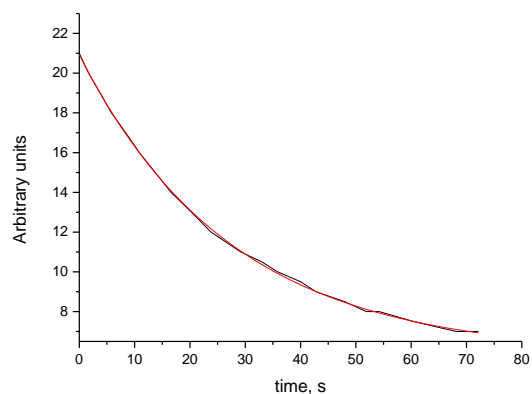
Neutral density filter, unfocussed

Figure 7.17 Decay traces of [MnBr(CO)₃(4,4'-methylphosphonate-diethyl-2,2'-bipyridine)] in static cell under different experimental conditions.

7.5.1.3 Conclusions and further development

From these results we have concluded that he optimal setup for this experiment uses a focussed beam of broad band light with no filter. From these results an experimental set up for comparing the rate of degradation of different manganese tricarbonyl α-diimines was devised which upon the initial

190

exposure to light uses a photodiode to trigger an oscilloscope which can record a decay trace in Δ volts. Using the formulas above (*vide supra*) this can be converted to differential absorption. The advantage to this method is that there no delay in recording data and no ambiguity in analysis. The experimental set up for this method is included as appendix 3 for the benefit of future group members who wish to replicate the experiment. This project is therefore at the stage of being ready to gather data, the complexes discussed in chapters 5 and 6 would be eminently suitable for investigating manganese tricarbonyl α-diimine decay as they offer the change to explore the effects electronic and steric variation has upon the rate of degradation.

7.5.2 Peptides as diimine ligands

The HPIB ligands had served as proof of concept that even attaching very large and bulky chains onto the bipyridine moiety would not necessarily inhibit catalysis and that adding electron withdrawing and donating groups in close proximity to one another wasn't inherently problematic. From this we were curious to see what the effect of attaching an entire peptide chain to the bipyridine would be and if this would be electrocatalytic. Proving that the peptide complex could exhibit catalytic behaviour would be a first step toward designer enzymes, although the complex described can in no way be described as an enzyme it was hoped to provide a step towards that ultimate goal. Peptide synthesis was conducted at the University of Sheffield and University of Birmingham by Liam Marshall.
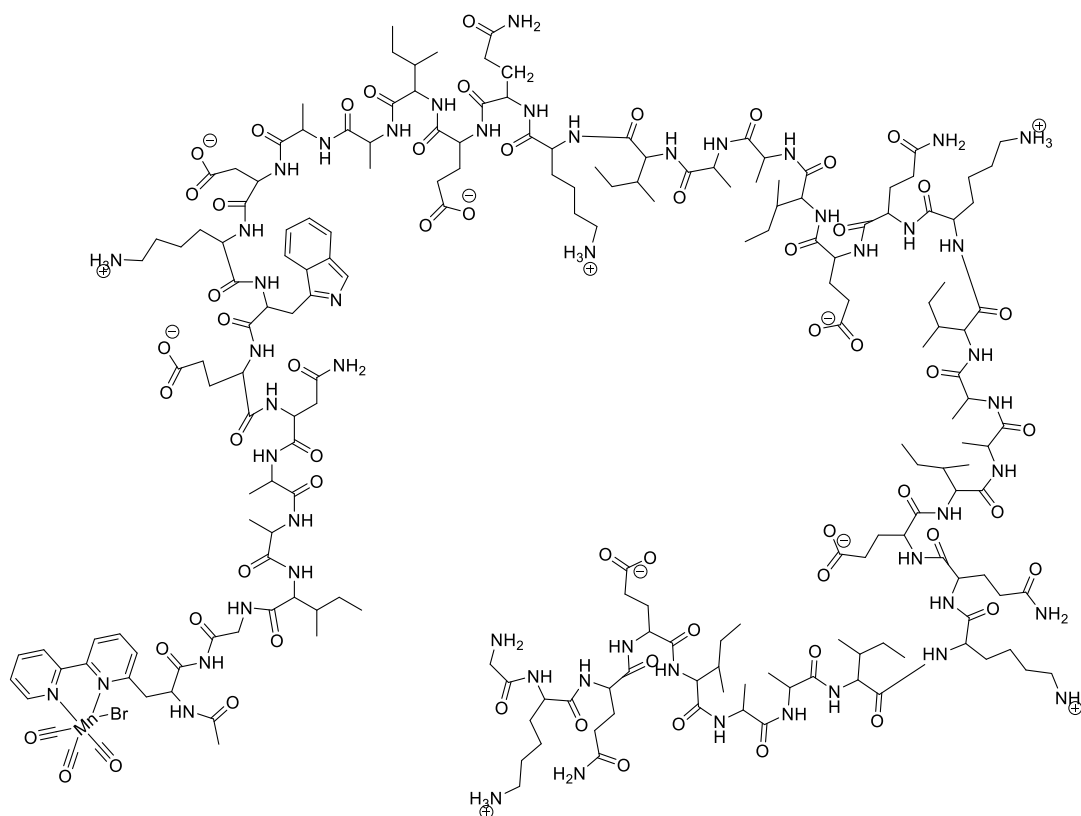
Figure 7.18 Target complex showing the peptide bound bipyridine complex synthesised by Liam Marshall complexed to manganese tricarbonyl bromide.

7.5.2.1 Synthesis of peptide complex

Because purification of the peptide complex was recognised to be a potential source of problems and also because of the likelihood that manganese may be able to bind in multiple locations it was important to accurately determine the reaction quantities of peptide and [MnBr(CO)$_5$]. A vial containing 0.1297 g of raw peptide were supplied by Liam Marshall from which a sample of $2.6.02 \times 10^{-4}$ g was taken which was dissolved in 25.5 ml of water and an absorption spectrum taken. Using an absorption coefficient provided by Liam Marshall of 17344 L mol^{-1} cm^{-1} the total concentration of peptide was determined to be 1.67×10^{-4} g or 64 % purity. The remaining weight was therefore determined to be 0.083 g of peptide (1.96×10^{-5} mols). This was combined in 10 ml of DMF with 0.00539 g of [MnBr(CO)$_5$] (1.96×10^{-5} mols) and stirred under reflux for 2 hours and a colour change to yellow was observed. This was then added dropwise into 2 vials of 35 ml of chilled diethyl ether to facilitate precipitation. These were then centrifuged for 10 minutes yielding 0.0937 g of peptide complex.

7.5.2.2 Analysis of the peptide complex

Analysis of the peptide complex proved to be extremely difficult due a variety of factors.

The large mass of the peptide ligand at 4447 Daltons meant that the use of NMR to characterise the complex was simply not practical as there are far too many carbon and proton environments to effectively assign, what is more the limited amount of peptide available meant that NMR was not a suitable technique for analysis.

The limited quantity of peptide complex available meant that mass spectrometry was the logical choice for analysis and samples were analysed using HPLC-MS with +ESI ionisation. Figure 7.19 shows the HPLC trace of the complex revealing that there appear to be at least two major components of the sample. The smaller peak in the region of 7.5 minutes retention time yielded mass fragments in the approximate range 890 to 4500 m/z which roughly corresponds to what would be the manganese peptide complex, looking at figure 7.18 though it becomes apparent that assigning the mass spectra is not a simple task due to the much larger contribution of the peptide to the total molecular weight than the manganese tricarbonyl bromide (4228 Daltons for the peptide and only 219 Daltons for the manganese tricarbonyl bromide) combined with many places where the peptide can easily fragment, lose or acquire protons mass spectrometry also has problems for characterisation.
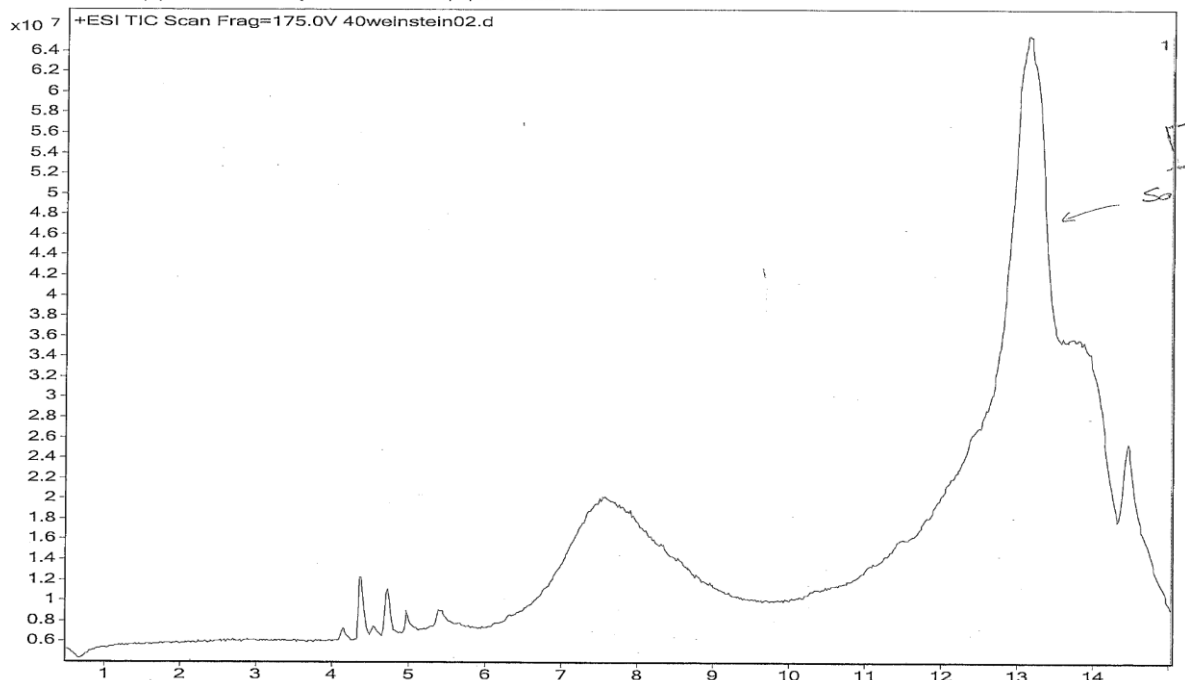
Figure 7.19 HPLC trace of the manganese peptide complex

In spite of the peak at 13 minutes retention time seen in figure 7.19 The complex was used as is for the following experiments due to problems with handling such as light sensitivity, the extremely sticky and viscous nature of the complex, lack of solubility in some solvents, solubility in water (which may facilitate hydrolysis of the bromide) and concerns about the stability of the peptide ligand on a column. The rationale behind continuing work with such little evidence for the formation of the complex was that since the characterisation and purification represented such a challenge it made more sense to use the limited material available to investigate if the complexes are capable of performing the chemistry we are interested in and if the results are promising use them as evidence for facilitating further research in the group in the future.

Several attempts were made to gather IR-SEC data with the intention of observing the growth of the bicarbonate and subordinate formate bands as evidence for the electrochemical reduction of CO_2 to CO. If such behaviour was observed this would serve as evidence for both the formation of the complex and its catalytic activity. All experiments were performed using a Princeton Applied Research VersaSTAT 3+ potentiostat and analysed using an optically transparent thin-layer spectroelectrochemical cell (OTTLE cell) equipped with Pt minigrid working electrodes, a Ag microwire psudoreference electrode and CaF_2 windows.

In the first attempt the intention was make up a 4 mmol dm^{-3} solution of the peptide complex in an acetonitrile solvent with 0.3 mol dm^{-3} of TBAPF$_6$. This proved to be impossible as the complex was

simply not soluble in the acetonitrile, however, several important lessons were learned from this, firstly the peptide complex is virtually impossible to weigh or handle accurately as it is simply too sticky and adheres readily to any surface. When the complex was added to the acetonitrile it retained its yellow colour suggesting that the complex was stable and had not degraded, additionally some small orange material was observed suggesting that unreacted manganese pentacarbonyl bromide was present.

Following this the experiment was repeated in dimethylformamide and this was successful in that the complex was soluble in DMF and a thin layer cyclic voltammogram under argon was collected, however, the IR window of DMF was not suitable to monitor reduction of the complex or CO_2 reduction in the carbonyl stretching region. Water also considered as a solvent, however, there was too much interference from the water to observe the free bicarbonate and subordinate formate bands to confirm CO_2 reduction.
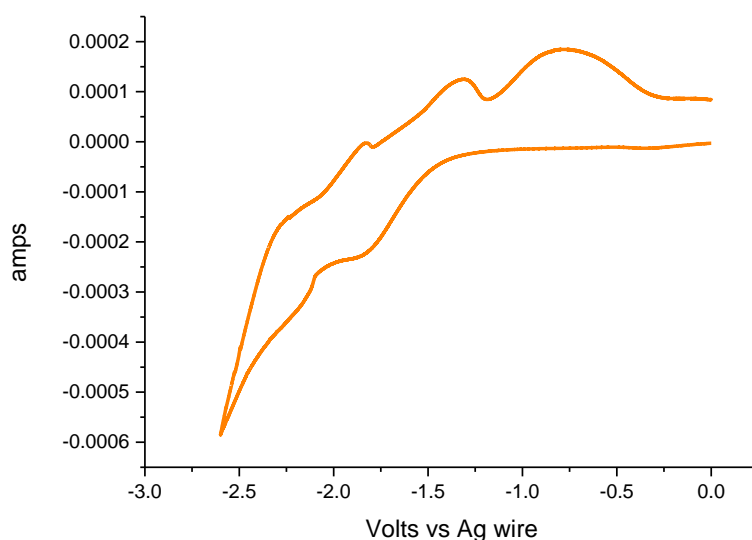
Figure 7.20 CV trace of the peptide complex in DMF under argon in the presence of 0.3 M TBAPF$_6$

7.5.2.3 Conclusions and further development

Further development should include synthesising a rhenium variant which would eliminate concerns over photodegradation as compared with the manganese variant. Ideally both complexes would be characterised with 2D NMR and crystal structures determined. Most importantly a suitable solvent for gathering IR-SEC traces must be found as at present it is not possible to explore the catalytic activity, without this information the value of the peptide bound complex cannot be discussed.

7.6 References

(1)   Rossenaar, B. D.; Kleverlaan, C. J.; Ven, M. C. E. van de; Stufkens, D. J.; Oskam, A.; Fraanje, J.; Goubitz, K. *J. Organomet. Chem.* **1995**, *493*, 153–162.

(2)   Rossenaar, B. D. Remarkable influence of L on the excited state and redox properties of M(L)(CO)3(alpha diimine)complexes (M= Mn, Re; L= Alkyl, halide, metal fragment), 1995.

(3)   Rossenaar, B. D.; George, M. W.; Johnson, F. P. A.; Stufkens, D. J.; Turner, J. J.; Vlcek, A. *J. Am. Chem. Soc.* **1995**, *117*, 11582–11583.

(4)   Rossenaar, B. D.; Hartl, F.; Stufkens, D. J.; Amatore, C.; Maisonhaute, E.; Verpeaux, J.-N. *Organometallics* **1997**, *16*, 4675–4685.

(5)   Rossenaar, B. D.; Stufkens, D. J.; Vlcek, A. J. *Inorg. Chem.* **1996**, *35*, 2902–2909.

(6)   Kirsanov, D. O.; Borisova, N. E. *Russ. Chem. ...* **2012**, *61* (4), 881–890.

(7)   Smieja, J. M.; Kubiak, C. P. *Inorg. Chem.* **2010**, *49* (20), 9283–9289.

(8)   Sampson, M. D.; Nguyen, A. D.; Grice, K. A.; Moore, C. E.; Rheingold, A. L.; Kubiak, C. P. *J. Am. Chem. Soc.* **2014**, *136* (14), 5460–5471.

(9)   Portenkirchner, E.; Fh, D. I.; Di, K. O. **2013**, *2*, 134–147.

(10)   Takeda, H.; Koike, K.; Inoue, H.; Ishitani, O. *J. Am. Chem. Soc.* **2008**, *130*, 6708–6716.

(11)   Yam, V. W.; Lau, V. C.; Cheung, K.; Chichester, H. **1996**, No. 1, 2749–2753.

(12)   Busby, M.; Matousek, P.; Towrie, M.; Clark, I. P.; Motevalli, M.; Hartl, F.; Vlcek, A. *Inorg. Chem.* **2004**, *43* (14), 4523–4530.

(13)   Rodriguez, A. M. B.; Gabrielsson, A.; Motevalli, M.; Matousek, P.; Towrie, M.; Jakub, S.; Zališ, S.; Vlček, A. *J. Phys. Chem. A* **2005**, *109*, 5016–5025.

(14)   Spall, S. J. P.; Keane, T.; Tory, J.; Cocker, D. C.; Adams, H.; Fowler, H.; Meijer, A. J. H. M.; Hartl, F.; Weinstein, J. A. *Inorg. Chem.* **2016**, *55* (24), 12568–12582.

(15)   Zeng, Q.; Tory, J.; Hartl, F. *Organometallics* **2014**, *33* (18), 5002–5008.

(16)   Bourrez, M.; Molton, F.; Chardon-Noblat, S.; Deronzier, A. *Angew. Chem. Int. Ed. Engl.* **2011**, *50* (42), 9903–9906.

(17)   Riplinger, C.; Sampson, M. D.; Ritzmann, A. M.; Kubiak, C. P.; Carter, E. A. *J. Am. Chem. Soc.* **2014**, *136*, 16285–16298.

(18)   Carter, E. a. *ACS Catal.* **2014**, *5*, 900–908.

(19)   Smieja, J. M.; Sampson, M. D.; Grice, K. A.; Benson, E. E.; Froehlich, J. D.; Kubiak, C. P. *Inorg. Chem.* **2013**, *52* (5), 2484–2491.

(20)   Artero, V.; Saveant, J.-M. *Energy Environ. Sci.* **2014**, *7*, 3808–3814.

(21)   Costentin, C.; Drouet, S.; Robert, M.; Save, J. *J. Am. Chem. Soc.* **2012**, *134*, 11235–11242.

(22)   Costentin, C.; Passard, G.; Robert, M.; Savéant, J.-M. *Proc. Natl. Acad. Sci.* **2014**, *111* (42), 14990–14994.

(23)   Costentin, C.; Passard, G.; Savéant, J.-M. *J. Am. Chem. Soc.* **2015**, *137* (16), 5461–5467.

(24)   Costentin, C.; Robert, M.; Savéant, J.-M. *Chem. Soc. Rev.* **2013**, *42* (6), 2423–2436.

(25) Costentin, C.; Robert, M.; Savéant, J.-M.; Tatin, A. *Proc. Natl. Acad. Sci.* **2015**, *112* (22), 6882–6886.

(26) Rountree, E. S.; McCarthy, B. D.; Eisenhart, T. T.; Dempsey, J. L. *Inorg. Chem.* **2014**, *53* (19), 9983–10002.

(27) Johnson, F. P. A.; George, M. W.; Hartl, F.; Turner, J. J. *Organometallics* **1996**, *15* (15), 3374–3387.

8. Attempting to quantify catalyst efficiency - an investigation of different techniques and the lessons to be learned from failure.

8.1.1 Introduction

The concerns over climate change and demands for greater energy security have resulted in increased interest in carbon capture and utilisation (CCU). This concept is similar to that of carbon capture and storage (CCS) in that carbon produced from combustion of organic material (typically coal or oil) is extracted from flue gases, resulting in a gas mixture with a much larger carbon dioxide concentration[1] as compared with untreated flue gas where carbon dioxide makes up only about 10% of the gas mixture.[2,3] Technologies for separation of the flue gas components include, but are not limited to, adsorption onto activated carbon[4] or polymers,[5,6] sequestration[7] in brine solution[8] and the currently commercially employed sequestration in amines.[9,10] Where CCU differs from CCS is that while with CCS, the resultant carbon dioxide gas is usually sequestered in salt water aquifers or depleted oil seams (often coupled with enhanced oil recovery), CCU instead aims to use this carbon source. Most of the commercial CCU processes are in the manufacture of polycarbonates and cyclic carbonates.

Carbon capture is currently employed commercially in several sites around the globe, which indicates that acceptably efficient processes for carbon capture exist. Therefore, the major impediment to the wider implementation of CCU technology comes from the lack of demand for the carbon dioxide. This is indeed the case, as carbon dioxide is currently regarded as a waste. If efficient catalysts are developed that would make conversion of carbon dioxide into higher value chemicals economically viable, then this would certainly spur development of CCU which would hopefully have the effect of reducing overall carbon emissions.

This desire has spurred the development of many catalysts for reduction of CO_2 to products containing carbon in various oxidation states, from carbonates to methane. The problem therefore arises is how does one determine the efficiency of an individual catalyst in order to determine if it can be commercially employed? With photocatalysts, this is simply a matter of counting the photons in over the amount of product out, and with electrocatalysts the matter is simplified further (due to the absence of sacrificial electron donors),[11] then it is a matter of techno economic analysis and lifecycle assessment to determine if the process is viable. However, acquiring valid numbers for valid metrics of comparison is no trivial task with many potential pitfalls and problems. In this chapter, I will discuss some of the problems and frustrations that arise trying gain meaningful kinetic data for the purpose of comparing the efficiency of different catalysts. This will be illustrated with some examples from our own work.

8.1.2 Aims

This chapter aims to discuss the challenges in gathering relevant kinetic data for the purposes of comparing and benchmarking catalyst performance in catalysts from both different families and from

the same family. The intention of this chapter is to bring to light some of the techniques attempted in our laboratory and to serve as a means for facilitating discussion of this challenging problem.

8.2 Background

One of the most significant issues facing the field of electrocatalytic CO_2 reduction is the problem of trying to gather accurate kinetic data or other quantitative indicators of performance. In particular values that can be meaningfully compared with values from other laboratories or set ups is extraordinarily challenging. Much of this arises from the nature of electrochemistry itself and an example of the challenges faced is outlined below.

If we take, for example, a chronoamperometric bulk electrolysis set up with a well-defined electrode surface area and accurately measured catalyst concentration, which is in turn coupled to a head space gas sampler that can accurately measure the concentration of CO in the head space, it would still not be possible to say with certainty what results were. Firstly, the performance of a catalyst is measured, in part, in relation to the current flowing through the cell set up. A simplified equation describing this situation (no catalyst or second substrate) is shown as equation 8.1 where i is current, A is the electrode area, F is the Faraday constant and j is the flux of substrate reaching the electrode surface area in moles cm^{-2} s^{-1}.

$$i = AFj \qquad\qquad 8.1$$

As such the current is directly related to the flux of substrate which is turn dependant on the concentration of the substrate (in this case CO_2) and rate of substrate migration to the electrode surface area, as per equation 8.2:

$$j = k[CO_2] \qquad\qquad 8.2$$

However, concentration of CO_2 in an acetonitrile water mixture is difficult to determine. This is because although Henry's constants should provide reasonable estimates CO_2 concentration the saturation of the solvent is not normally done in a sealed system and it is possible during the course of an experiment for the CO_2 concentration in the headspace to change, which will affect the solution phase – gas phase equilibrium in line with Henry's law (where H^{cp} is Henry's solubility defined via concentration, C_a is the concentration of the species in the aqueous phase and P is the partial pressure of the species in the gas phase .

$$H^{cp} = C_a/P \qquad\qquad 8.3$$

In addition during the course of catalysis water is required to act as a Brönsted acid changing the solvent composition and hence ability to solubilise CO_2. Much more importantly during the course of the electrolysis the temperature of solution will raise, and even if the solvent is stirred and surrounded by a cooling jacket local hot spots will still be created causing CO_2 to come out of solution. The natural variation of substrate concentration will also have a significant impact of the observed rate of reaction. As the CO_2 and H_2O are consumed in the reaction the production of CO will slow down and

if the reaction rate is calculated over this time it will appear slower that the rate of peak catalytic CO production. This raises the issue of comparability of the data obtained in different experiments, as one experiment may be run over seconds in a sealed system where as another may be run over hours in a poorly sealed system, such values cannot be compared.

With regard to performing electron counting, the situation is complicated as the presence of side reactions may contribute significantly to the total number of electrons transferred during the course of the experiment. Such reactions, for example, hydrolysis, may also result in reagents for CO_2 reduction being consumed. What has been noted in experiments in our laboratory is that after a period of time (varies depending on conditions of experiment but for a typical bulk electrolysis experiment with 20 ml solvent it was ca. 30 minutes) solutions containing manganese complexes will change from a coloured to a colourless solution, which we believe is due to reagents becoming depleted and subsequent electrolytic catalyst decomposition. Such decomposition, as was discovered in chapter 2, is highly likely to result in liberation of the carbonyl ligands giving a significant detector response, indeed due to the 3:1 molar ratio of CO to Mn manganese tricarbonyls are commonly employed as CO releasing molecules.[12,13,14]

Even if substrate concentration and temperature can be kept constant, catalyst degradation suppressed and detection is accurate and precise there is still the matter of calculating k values, turn over frequencies and turn over numbers. All of these values involve concentration of the catalyst, however, the bulk concentration of catalyst is not suitable for calculating these values because only a small percentage of the catalyst can be in contact with the electrode surface at any given time and using the bulk catalyst concentration will result in serious underestimation of catalyst performance. If the surface area of the electrode is known, it is possible to calculate the number of catalyst molecules that are theoretically in contact with the electrode and since electrolyte is present the charge diffusion layer should be supressed to the electrode surface. The solution however is not static (particularly if the solution is being stirred) and the catalyst molecules move to and from the electrode surface, this would result in overestimation of catalyst performance.

It is with this in mind that several attempts to gain catalytic data are discussed.

8.3.1 Efforts to develop Gas Chromatography techniques for CO quantification

When attempting to quantify the CO yield, the first method attempted was the analysis of head space gas samples taken using a gas tight needle from bulk electrolysis experiments. The gas was separated by gas chromatography using a Restek RT- Msieve 5A column, which utilises molecular sieves as the stationary phase for gas separation. This column is specially designed for the separation of permeant gases such as oxygen and carbon monoxide making it an ideal choice of column. The eluted gas was analysed with a thermal conductivity detector (TCD). The thermal conductivity detector was used because unlike a more common flame ionisation detector (FID), it is able to detect compounds that do not have carbon-hydrogen bonds, making it suitable for the measuring of CO. However, a

disadvantage of this technique is that it is less sensitive than a FID or other ionisation detection methods to the presence of lower concentrations of analyte. The thermal conductivity detector consists of an electrically heated filament in a temperature controlled cell in which the stable flow of heat from the filament to a detector is permitted. Under normal operation, with no analyte present, the gas effluent from the column other than the carrier gas (usually helium or hydrogen), the resistance from the filament to the detector is constant. When an analyte enters the cell, the thermal conductivity of the gas effluent is reduced causing the filament to heat up and the resistance to increase, resulting in a measurable change in voltage. The change in voltage that is measured can be used to determine the concentration of the analyte.

A more suitable detector may have been a discharge ionisation detector, which utilises a high voltage electric discharge to ionise helium atoms in the carrier gas resulting in an electrical current that can be measured as these are often used for atmospheric gas analysis. Alternative detectors were not explored, however, due to budget constraints which prohibited the testing and acquisition of new detectors.

8.3.1.1 Ramping method with H_2 carrier gas and calibration of TCD response

Initially the program used for the separation of gas samples involved a ramping method where the column was heated from 30 ^{O}C to 200 ^{O}C over a period of 11 minutes, resulting in good gas separation as shown in figure 8.1. Hydrogen was used as the carrier gas as this was the manufacturers recommended carrier gas due to the higher change in conductivity between hydrogen and typical analyte gases such as argon or CO.
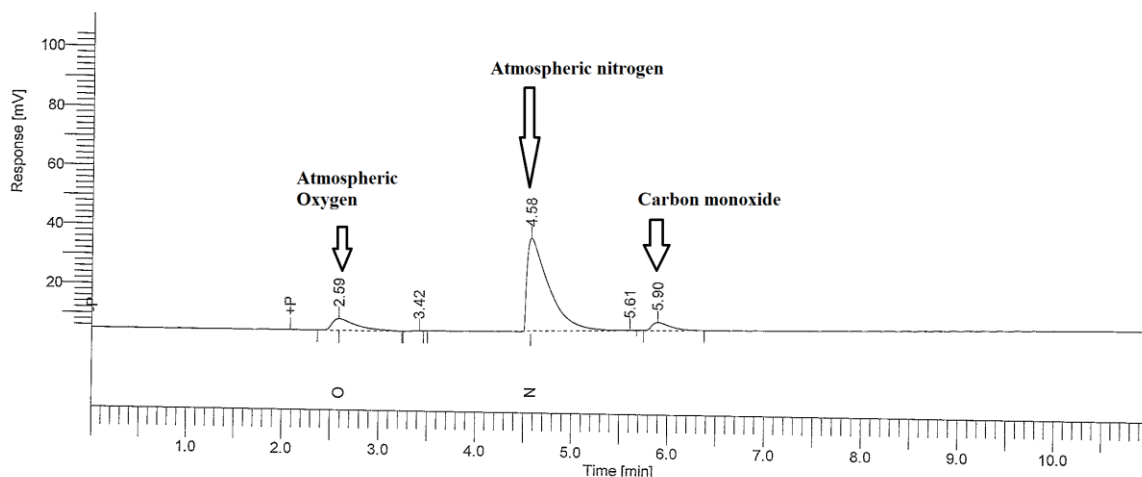
DEFAULT REPORT

Peak #	Time [min]	Area [µV·s]	Height [µV]	Area [%]	Norm. Area [%]	BL	Area/Height [s]
1	2.590	68357.29	3971.26	11.25	11.25	BB	17.2130
2	3.420	1302.97	172.80	0.21	0.21	BV	7.5404
3	4.575	497564.15	31353.31	81.88	81.88	VE	15.8696
4	5.606	2705.66	224.63	0.45	0.45	EV	12.0449
5	5.895	37732.21	2819.49	6.21	6.21	VB	13.3827
-	9.815	0.00	0.00	0.00	0.00		---------
		607662.27	38541.48	100.00	100.00		

Figure 8.1 Chromatogram showing N₂, O₂ and CO peaks using the initial ramping method.

The major issue with this method was the very long wait time inherent to the ramping procedure. In addition to the 11 minute run time of the chromatogram the oven also had to cool back down to 30 ^{O}C after the run and then the detector needed to equilibrate. This meant that the time between measurements in each experiment was approximately 20 minutes, preventing the use of this method for kinetic analysis as no meaningful increase could be observed. Figure 8.2 shows GC data on CO2 reduction with four "asymmetric" complexes, [MnBr(CO)$_3$(IminoPyridines)] [see chapters 5 & 6 for detail] and it is clear that even for the most active TBIEP complexes the first measurement after time = 0 s could only be recorded after ca. 20 minutes meaning that the rate of CO production when CO$_2$ and H$_2$O were at their maximum concentration (i.e. under ideal conditions) cannot be quantified, in most cases only two samples could be taken before peak CO evolution was reached.
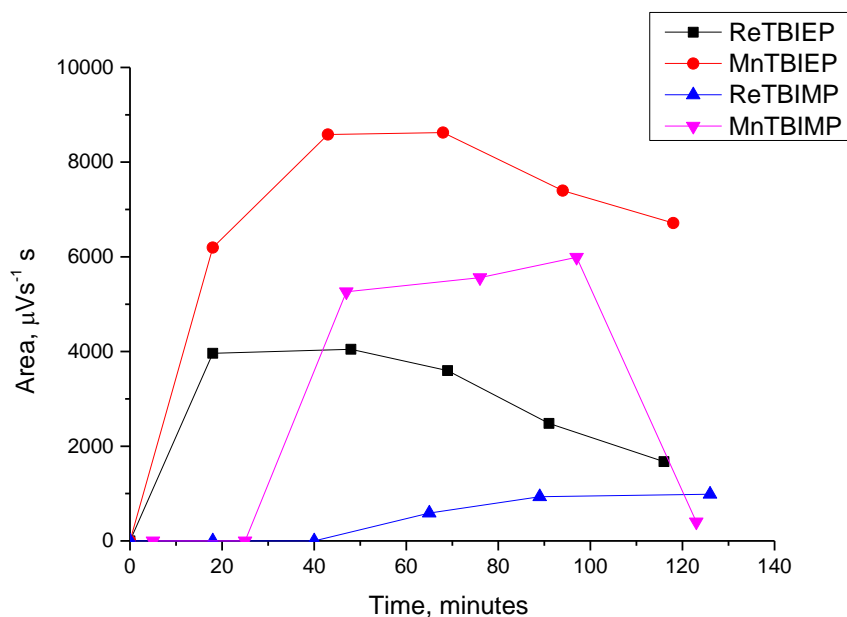
Figure 8.2 Termal conductivity detector response to CO in head space gas samples analysed by gas chromatography. 0.05 g of each complex dissolved in 60 cm^3 of a CO$_2$ saturated 9:1 acetonitrile/water solution in the presence of 0.2 M TBAPF$_6$

In order to attempt to quantify the CO yield from the experiments, Thomas Smith[15,16,] a PhD student in Dr. Michael Hippler's research group, prepared CO/air mixtures of known composition for calibration of the detector. The gas solutions were prepared in a vacuum cell with CO being added according to barometric readings and their CO concentration being confirmed by IR spectroscopy. The CO was analysed using the method outlined above with the voltage response shown in figure 8.3. These results show two important findings: firstly, that the response is highly linear ($R^2 = 1$) between 9 % and 2 % CObut that the linearality breaks down at lower CO concentrations and that the linear region does not bisect 0 µV s^{-1} at 0 % CO. Unfortunatly, the results shown in figure 8.2 give conductivities below those corresponding to even 0.34 % CO. As such it can be said that we are dealing with very low concentrations of CO and that the response is not in the linear detection region. Hence getting accurate data will not be possible with this set up.

% CO	Area $\mu V\ s^{-1}$
0.34	4643
0.41	5210.94
1.9	31447.31
4.2	92319.72
9.1	222840.73
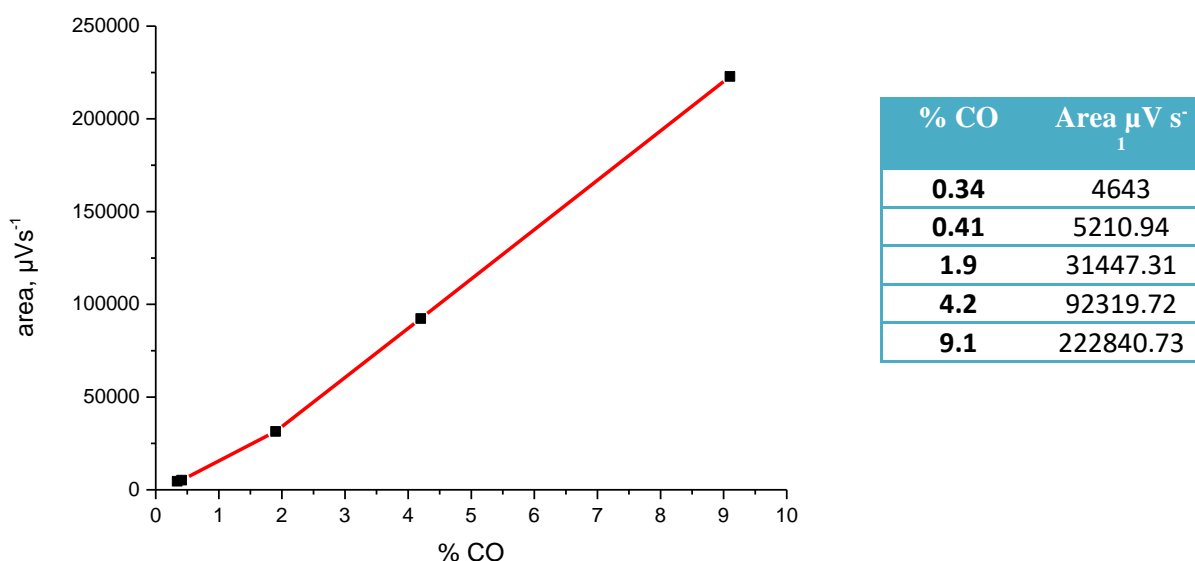
Figure 8.3 CO calibration curve of the response of the Thermal conductivity detector (GC)

Despite the drawbacks of this method, it was used in the analysis of head space gas taken from bulk electrolysis of some of the compounds discussed in chapters 2 and 4, and to look for evidence of CO formation during the photocatalytic tests on the Re mesBIAN complexes. This method was used because the good separation between peaks corresponding to different gases allowed for easy identification of CO and also because the method proved to be reliable with equipment failure being comparatively rare, which was an issue with some of the other methods explored. Importantly GC analysis was not used for the analysis of the compounds discussed in chapters 3, 6 and 7 because we believed there were simply too many drawbacks to the method and not enough information to be gained in order to justify the use of the method. In addition to the drawbacks already discussed above bulk electrolysis consumed large quantities of compound in a destructive technique and can only provide information that CO is in the headspace gas. The experiment does not tell us if hydrogen is formed, the faradaic efficiency or even if the CO observed is formed via the catalytic conversion of CO_2 in CO or if the CO arises from the degradation of the complex and the release of the carbonyl ligands as proved to be the case in the photocatalysis experiments discussed in chapter 2. While it is true that some of these issues could be resolved by simply conducting experiments in N_2 saturated solution and observing if CO formation occurs without having a quantitative method this would neither prove nor disprove catalytic CO formation. With this in mind characterisation of complexes such as those discussed in chapter 3, 6 and 7 did not involve head space GC analysis of bulk electrolysis experiments but rather relied on IR-SEC experiments to observe the formation of subordinate formate and free bicarbonate, which are characteristic of electrocatalytic CO formation.[17,18] We believe this to be a much more suitable method for confirming the electrocatalytic

formation of CO as it does not consume excessive amounts of sample material and also allows direct observation of the metal-carbonyl bands (confirming that the complex is not decaying) and the formation of new bands associated with CO formation. It was not our intent to use GC analysis on the complexes discussed in chapter 5, however, requests from reviewers to see GC data with time results meant we had to offer GC results. In order to do this an isothermal method was developed the rationale for which is discussed below.

8.3.1.2 Isothermal method

Before abandoning the use of GC for CO analysis in favour of more suitable spectroscopic methods attempts were made to address some of the drawbacks encountered with the ramping method: the long time between sampling intervals and the inability to detect hydrogen in the gas sample (due to its use as the carrier gas). In order to rectify these problems an isothermal method was developed and experiments with N_2 as the carrier gas were conducted. An isothermal method would have the advantage of not requiring the oven temperature to be changed during or after the sample run limiting the time between sampling to equilibration time (typically around 2 minutes) and the time the sample was in the column, this would result in a much shorter time between sampling intervals potentially allowing some measure of kinetic data to be gathered. Changing the carrier gas to N_2 would allow the observation of any H_2 that might be formed during the electrolysis.

During these initial experiments a gas solution provided by British Oxygen Company of 2 % CO and 2 % CH_4 was used and hence 4 peaks should be observed in each GC trace (O_2, N_2, CO and CH_4).

In order to compare the isothermal method with the ramping method two measurements were taken of the CO response in the gas solution using the original ramping method at the start of and the end of the experiment (in order to account for any leakage in the gas cell used or change in response of the detector). The CO peak has been observed at ca. 9 minutes time point in figure 8.4. The integrated signal has a value of 39,421.71 μVs^{-1} in the first run and 36,416.20 μVs^{-1} in the second run, which is consistent with the variation observed in prior experiments using the ramping method. As such for the method to be comparable a response of ca. 38,000 μVs^{-1} should be seen.

Peak #	Time [min]	Area [µV·s]	Height [µV]	Area [%]	Norm. Area [%]	BL	Area/Height [s]
1	2.619	12640.26	767.32	0.78	0.78	BB	16.4733
2	3.372	290.22	52.86	0.02	0.02	BB	5.4908
3	4.290	1523256.57	73611.48	94.31	94.31	BV	20.6932
-	4.623	0.00	0.00	0.00	0.00		----------
4	5.795	39496.16	2383.67	2.45	2.45	VB	16.5695
5	9.178	39421.71	4854.35	2.44	2.44	BB	8.1209
-	9.815	0.00	0.00	0.00	0.00		----------
		1615104.92	81669.67	100.00	100.00		

Peak #	Time [min]	Area [µV·s]	Height [µV]	Area [%]	Norm. Area [%]	BL	Area/Height [s]
1	2.675	25846.29	1572.66	1.60	1.60	BB	16.4348
2	3.636	880.90	124.83	0.05	0.05	BV	7.0570
3	4.390	1508992.15	72529.14	93.53	93.53	VV	20.8053
-	4.623	0.00	0.00	0.00	0.00		----------
4	5.885	41193.59	2058.28	2.55	2.55	VB	20.0136
5	9.260	36416.20	4363.61	2.26	2.26	BB	8.3454
-	9.815	0.00	0.00	0.00	0.00		----------
		1613329.13	80648.50	100.00	100.00		

Figure 8.4 GC traces and TCD response from the ramping method on the BOC supplied gas solutions taken at the start and end of the experiments.

The first method utilised an oven temperature of 70 °C with a run time of 7.8 minutes, the results are shown in figure 8.5. As can be seen the time taken for the CO to elute was reduced from 9 minutes to 6.7 minutes giving a total time between runs of 11 minutes with a TCD response of 29834.84 μVs^{-1}. These results are not satisfactory, therefore, the temperature was raised to 80 °C. The result of increasing the temperature was a much broader CO peak compared with the ramping method or the temperature at 70 °C. Importantly the results shown in figure 8.6 reveal that the TCD response from the isothermal method does not match that of the ramping method, as such calibration methods are not transferable between different methods.
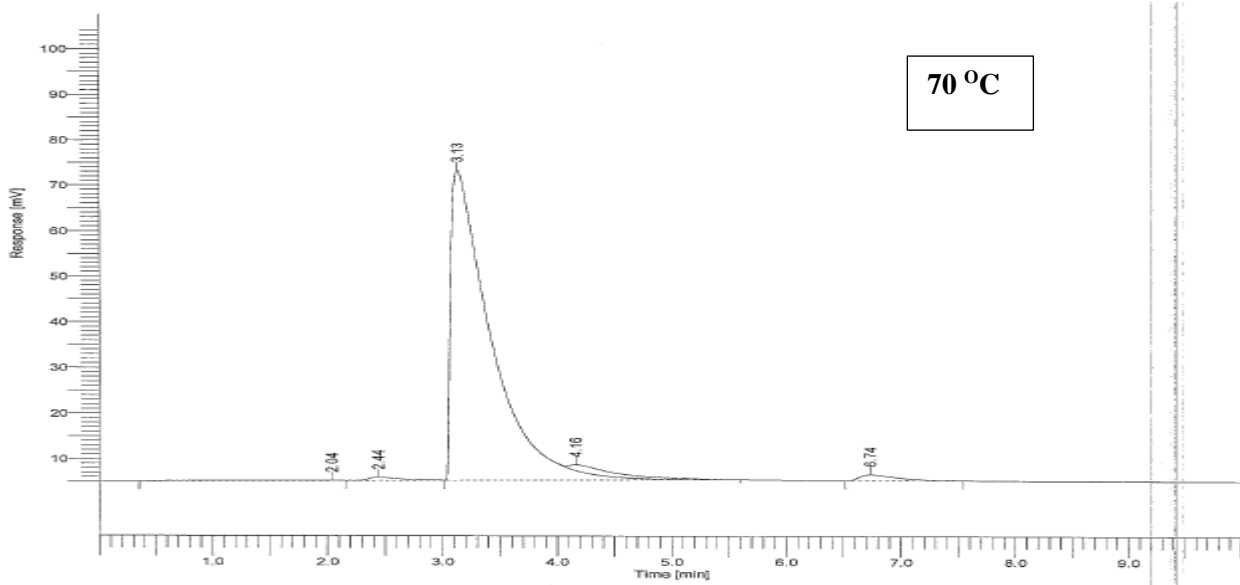
70 °C

DEFAULT REPORT

Peak #	Component Name	Time [min]	Area [uV*sec]	Height [uV]	Area [%]	Norm. Area [%]	Cal. Range	Volt Range	BL
1		2.041	9950.34	61.36	0.57	0.57			BV
2		2.441	14006.90	682.71	0.80	0.80			VV
3		3.133	1643037.47	68002.30	93.95	93.95			VE
4		4.162	51989.96	1258.89	2.97	2.97			EB
5		6.737	29834.84	1331.60	1.71	1.71			BB
			1748819.51	71336.86	100.00	100.00			

Figure 8.5 GC traces and TCD response from the isothermal method at 70 ºC on BOC supplied gas solution..

Figure 8.6 Results of isothermal method at 80 °C (bottom) and a comparison of the ramping and isothermal method.
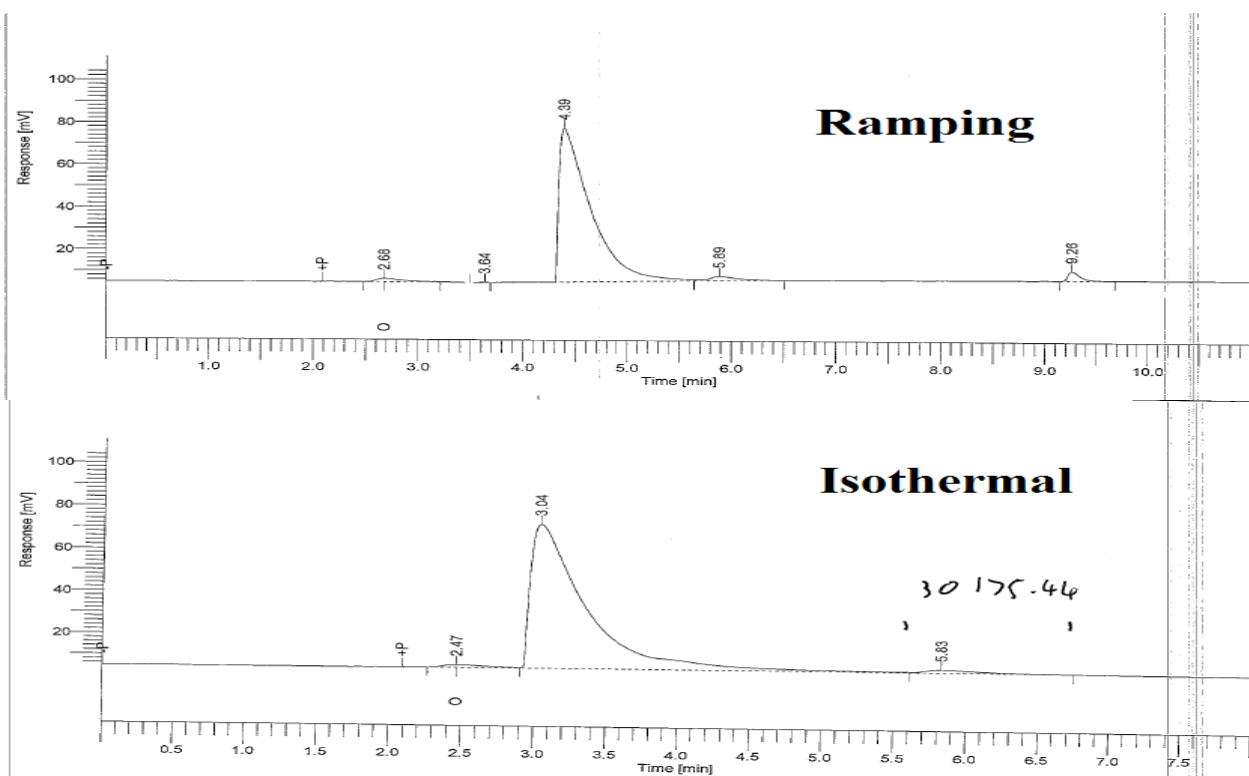
Isothermal run at 80 °C	Area μVs^{-1}
1	11239.52
2	30175.44
3	27894.68
4	33143.84

Further development of the isothermal method resulted in an oven temperature of 160 °C with H_2 carrier gas. As can be seen in figure 8.7, this method provided good separation of the peaks with a total run time of less than 3 minutes. As such it was possible to collect head space gas samples before the solution exhibited colour loss, meaning it is more likely that samples were being taken before the catalyst began to be destroyed. This was the method used in chapter 5 to compare the efficiency of CO_2 reduction to CO by asymmetric manganese complexes.
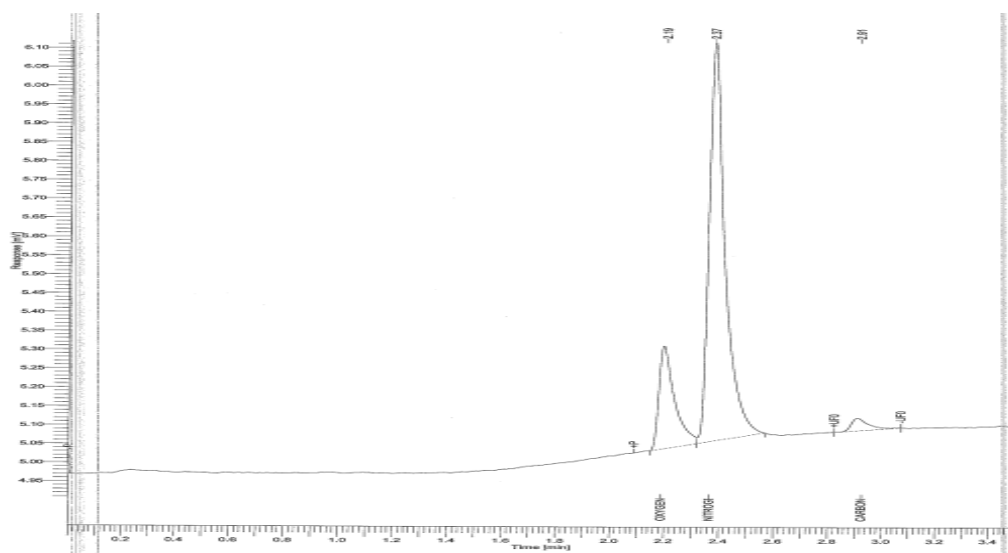
DEFAULT REPORT

Peak #	Time [min]	Area [μV·s]	Height [μV]	Area [%]	Norm. Area [%]	BL	Area/Height [s]
1	2.195	1089.70	274.02	19.65	19.65	BV	3.9766
2	2.372	4307.60	1058.96	77.66	77.66	VB	4.0678
3	2.907	149.64	34.10	2.70	2.70	MM	4.3884
		5546.94	1367.08	100.00	100.00		

Figure 8.7 Example of the results of final isothermal method at 160 ºC used in chapter 5.

8.3.1.3 Further discussion of GC methods

During the course of these investigations and the composition of this thesis several suggestions have been made and questions rose which will be addressed in this section. These topics are the carrier gas choice, the run time and the calibration.

As has been discussed above the carrier gas used in most of the experiments was H_2 as it provides good separation and a large change in TCD response when searching for CO. This however comes at the expense of the ability to detect H_2 that may be produced during the electrolysis. It has been suggested that He could be a suitable choice of carrier gas as it would allow for the detection of hydrogen, the use of He would result in diminished sensitivity toward CO detection but not to the same degree of N_2. It is possible that He would make a more suitable carrier gas and investigating the use of He would certainly be appropriate in the future.

It has been suggested that the run times used in the GC investigations are either too short (and hence the longer term performance of the catalyst cannot be properly understood) or too long (resulting in the degradation of the sample). These points are fair and ideally it would be best to perform a series of electrolysis's under differing conditions and for different durations both long and short in order to properly qualify the catalysts performance. This is though not entirely practicable and compromises have had to be made for the sake of time and resource constraints. One of the most significant restraints has been the electrode and cell set up. While several designs of cell set up have been made

for the preparative scale electrolysis work most were not successful and hence the bulk electrolysis cell with a large volume headspace has been used in all experiments. This has necessitated the use of a high surface area electrode designed for bulk electron counting in order to generate sufficient gas to occupy the head space. As such the CO_2 in solution is rapidly consumed leading to degradation of the catalysts. With better experimental design and more bespoke equipment better results should be possible, however, the author remains sceptical of the ability of these methods to provide meaningful insights.

Finally it has been discussed that the TCD should be linear even at very low concentrations and it may be advisable to run the calibration again in triplicate. It should be borne in mind though that even in the linear region the intersect did not pass through 0. An alternative method would be to inject pure CO (or a known dilution) into the GC at varying volumes. By varying the volume the total amount of CO being detected could be varied and a calibration curve constructed.

8.3.2.1 Cyclic Voltammetry

As has been outlined above, the use of bulk electrolysis for chronoamperometric analysis as a means to determine catalysts efficiency combined with the use of gas chromatography for quantification of the substrate leaves a lot to be desired. In particular given the large number and variety of catalysts for CO_2 reduction[19] combined with the problem that over potential and catalyst efficiency are all dependent upon: characteristics intrinsic to the molecule, cell design, transport factors and a host of other parameters means that the use of preparative scale electrolysis for systematic investigation presents a daunting task, especially due to the destructive nature of such electrolysis and the large amount of material that is often required. What is also significant is that, as shown in section 8.3.1, variation in the detection equipment used and the setup of the experiment can have a significant impact on the results of any quantitative analysis and as such strict parameters must be maintained to draw meaningful conclusions.[20] This is made even more complicated as not all researchers are familiar with performing preparative scale electrolysis experiments and so are likely to lack the skills and experience to perform these experiments with the rigor that is required.

In contrast it is quite likely that most researchers in this area will have some familiarity with cyclic voltammetry due to its ubiquity and common implementation as an experiment in undergraduate teaching labs[21] and what is more a wealth of information is available to those new to technique.[22,23] Cyclic voltammetry consumes significantly less material (according to Saveant *et al.* "in CV or related techniques about one-millionth of the substrate is consumed during each run, making these techniques non-destructive as opposed to bulk electrolysis"[24]) than preparative scale electrolysis and has been used for years to determine electrode reaction kinetics,[25] study multiple electron transfer[26] and investigate materials for solar cells,[27] however, due to the multicomponent, multistep, multielectron nature of electrocatalytic CO_2 reduction the use of cyclic voltammetry to provide meaningful kinetic parameters is challenging in this case.

Recently though a new method of using cyclic voltammetry data to obtain kinetic parameters has found increasing acceptance as a method to evaluate catalysts and overcome issues related to transport and side reactions phenomena. Although a full discussion of the mathematics and theory[28] of the molecular catalysis of electrochemical reactions is outside of the scope of this discussion (and readers are instead directed to the work of Jean-Michel Saveant who has published many thorough articles on this topic[29,30]) a brief overview is provided below but before this the benchmarks and definitions must be introduced.[31]

η - The overpotential is a thermodynamic parameter is the difference between the applied potential and the standard potential for the formation of a product from substrate.

k_{obs} - The observed rate constant describes the overall rate of catalysis observed in the system. k_{obs} has the same value as TOF_{max}.

TOF - The turnover frequency is a kinetic parameter that quantifies the catalytic activity. TOF is the moles of product produced per unit of time per mole of catalyst. (Note for homogeneous molecular catalysis TOF refers to the catalyst molecules contained in the reaction diffusion layer at the electrode).

TOF_0 - Is an extrapolated value for a TOF where the applied potential (E) is equal to the thermodynamic potential for the formation of a product from substrate $E^0_{A/B}$. It is used as an "intrinsic value" of catalytic activity.

8.3.2.1 Relationship between turnover frequency and over potential

The classical definition of a "good catalyst" is one that exhibits a high TOF and low η, however, this represents a vast over simplification of catalyst behaviour in terms of the kinetic and thermodynamic parameters of CO_2 reduction. Examining the equations for homogeneous[32] catalysis derived by Saveant *et al.* (where f is F/RT, k_s^{cat} is the electron transfer standard rate constant, E^0_{AC} is the standard potential of the substrate and product, E^0_{cat} is the standard potential of the catalyst couple and D_P is peak current density) it can be seen that the overpotential is an important parameter in producing the ultimate TOF.

$$\frac{1}{TOF} = \frac{exp(-f\eta)}{TOF_0} + \frac{\sqrt{2D_p}}{k_s^{cat}} \frac{exp\left(-\frac{f\eta}{\sqrt{2}}\right)}{TOF_0} + \frac{exp[-f(E^0_{AC} - E^0_{cat})]}{TOF_0} \qquad 8.4$$

This means that the TOF[33] reported widely in the literature could best be described as the potential dependent TOF as its value will change depending upon the applied potential. In contrast the value of TOF_0 does not include the η but rather is limited to constants, thermodynamic parameters and C^0_A (the bulk concentration of substrate) and represents the theoretical turnover rate at zero applied overpotential.

$$TOF_0 = kC^0_A exp[-f(E^0_{AC} - E^0_{cat})] \qquad 8.5$$

To this end Saveant *et al.* have proposed the use of a Tafel plot such as the one shown in figure 8.8[34] which allow a visual representation of the TOF of different catalysts at various overpotentials. The advantages of such comparisons are self-evident in that they allow the ideal catalyst to be developed for the desired voltage.
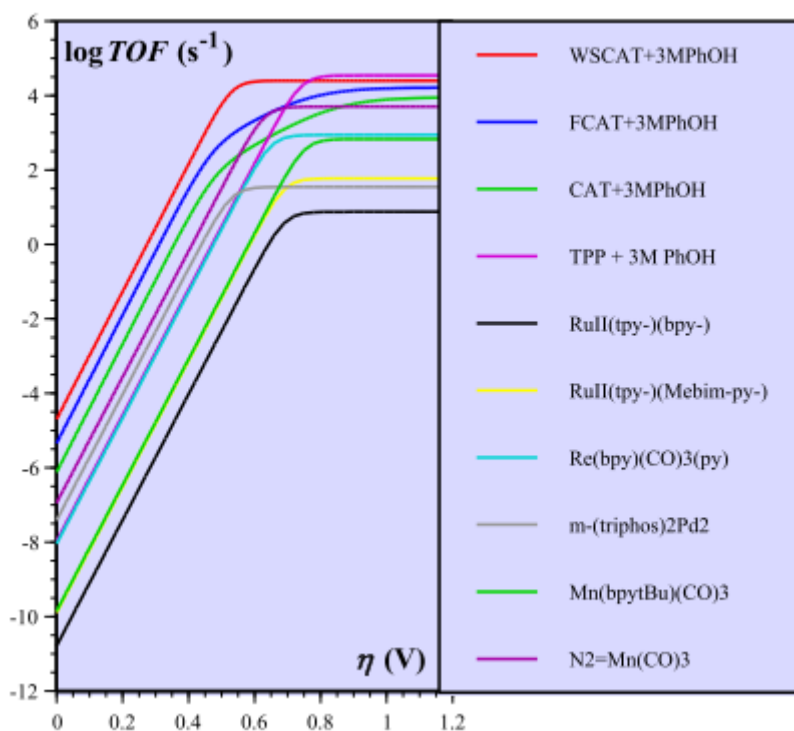
Figure 8.8 Tafel plot showing the comparative TOF of different catalyst types at varying overpotential.[34]

8.3.2.2 Catalytic responses in cyclic voltammetry

The cyclic voltammetry responses of catalysts can be summarised as being with one of several catalysis zones[35] shown in figure 8.9 Catalytic systems of interest have a large *k* value meaning the waveform will exist in the KT2, KT1, K or ideally KS[36] zones in which "pure kinetic conditions" are achieved, that is a steady state zone in which the area close to the electrode surface exists in a state of mutual compensation of catalytic reaction and catalyst diffusion.[37]
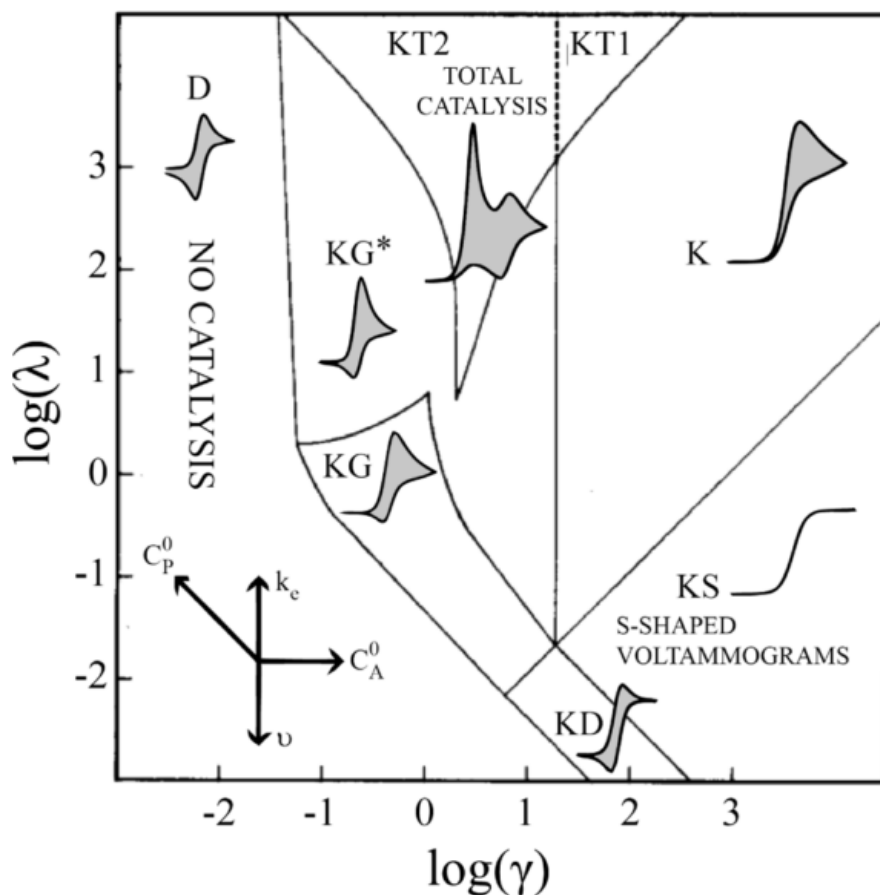
Figure 8.9 Kinetic zone diagram and simulated CV waveforms for the one-electron reduction of substrate A via redox catalyst mediator P, where λ is the kinetic parameter and γ is the excess factor. The compass rose visually depicts how catalysis may move between zones (C_P^0 is the initial concentration of the catalyst, C_A^0 is theinitial concentration of the substrate, υ is the scan rate, and k_e is the rate constant for homogeneous electron transfer from the reduced catalyst to the substrate). The CV waveforms follow the convention of negative potentials to the right and cathodic current upward. Scans are started from positive potentials.[29,31,38]

The idealised catalyst behaviour is exhibited in the KS zone (described by equation 8.6 where i is current and S is electrode surface area) where the result is independent of scan rate and the reverse trace is identical to the forward trace. These conditions correspond to prompt electron transfer from the electrode surface to the catalyst,[39] rapid catalytic activity and negligible consumption of substrate in the reaction-diffusion layer.[35]

$$\frac{i}{FS} = \frac{\sqrt{2kC_A^0 D_P C_P^0}}{1+exp\left[-f\left(E-E_{cat}^0\right)\right]} \qquad 8.6$$

This equation can be normalised to provide equation 8.7 where i_p^0 is the peak current under non catalytic conditions. Using equation 8.7 plotting $\frac{i}{i_p^0}$ against $1 + exp[E - E_{cat}^0]$ should yield a linear result that can be used to calculate the value of k.

$$\frac{i}{i_p^0} = \frac{2.24\sqrt{\dfrac{2kC_A^0}{fv}}}{1+exp\left[E-E_{cat}^0\right]} \qquad\qquad 8.7$$

Use of equation 8.6 and 8.7 to calculate values of k is effective provided the CV exhibits ideal KS conditions. However, using these equations to calculate values of k from voltammograms that do not exhibit this idealised behaviour, i.e. those with scan rate dependence or where the two waves do not overlap, will result in a nonlinear plot and calculation of k values with a scan rate dependence which will not yield the fundamental kinetic parameter TOF_0.
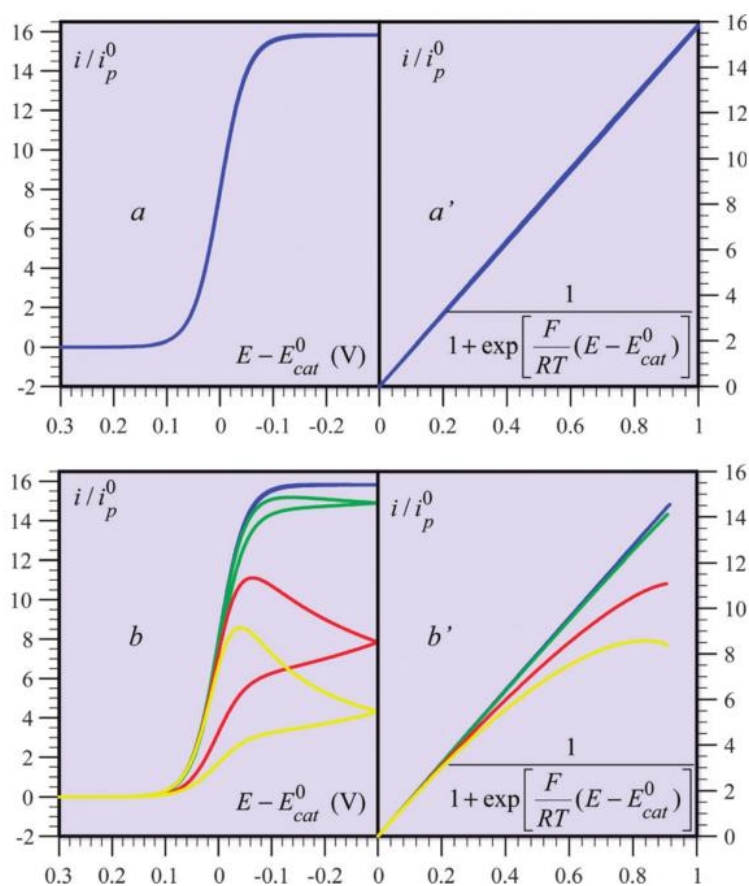
Figure 8.10 Catalytic cyclic voltammetry responses (left) and foot of the wave analyses (right) for a typical system showing the result when the waveform deviates from ideal behaviour. [24,35]

As discussed above the deviation from ideal behaviour most commonly arises from substrate consumption (as can be seen from the concentration parameters in equation 8.6) resulting in the non-linear plot, however, early in the voltammogram at the foot of the waveform the effect of side phenomena decreases and the slope becomes linear. It is from this principle that foot of the wave analysis is born. [24, 31,35,33]

8.3.2.3 Foot of the wave analysis

The above section should provide a reasonable outline to the rationale and mathematics of foot of the wave analysis allowing this to focus on the utilisation of this technique.

The ultimate form of the of the equation used in section 8.3.2.4 was the form shown in equation 8.8

$$\frac{i}{i_p^0} = \frac{2.24\sqrt{\frac{RT}{nFv}}\sqrt{n'k_{obs}}}{1+exp\left[\frac{nF}{RT}E-E_{cat}^0\right]}$$

8.8

which allows $\sqrt{n'k_{obs}}$ to be separated from the other parameters and allowing simple extraction of this value from the gradient of the slope. In the calculations n is the number of electrons transferred from the electrode to the active catalyst species (1) whereas n' is the number of electrons to convert CO_2 to CO (2).[40] From this a value of k_{obs} (TOF$_{max}$) can be calculated and used to obtain the potential dependent TOF which in turn can be used to produce a Tafel plot to allow comparison with other catalysts.[31,40]

$$TOF = \frac{2\,TOF_{max}}{1+exp\left[\frac{F}{RT}(E-E_{cat}^0)\right]exp\left(-\frac{F}{RT}\eta\right)}$$

8.9

8.3.2.4 Application of the foot of the wave analysis

From the sections above it is clear that foot of the wave analysis and the subsequent generation of fundamental kinetic parameters (TOF$_0$) and the ability to compare TOF to η in any number of catalytic systems has many advantages over almost any other method. CV's are simple to run and can be run with equipment available in almost any electrochemical lab. However, our attempts to use foot of the wave analysis have revealed some problems when it comes to performing the calculations. In this section calculations for the manganese phosphonate complex discussed in chapter 2 are shown.

Figure 8.11 shows the first attempt to generate the same graphs as those displayed in the bottom left and right of figure 8.10. As can be seen the results are not similar, although 8.11 (top) is not so dissimilar to what has been reported in the literature it is clear that there is no conversion between the two waves in figure 8.11 (middle). It appears that for the foot of the wave analysis (assuming we have used the formulas correctly) only one of the waves is actually used to calculate the resultant foot of the wave result and as such only the cathodic wave was used in when performing the foot of the wave analysis calculation.
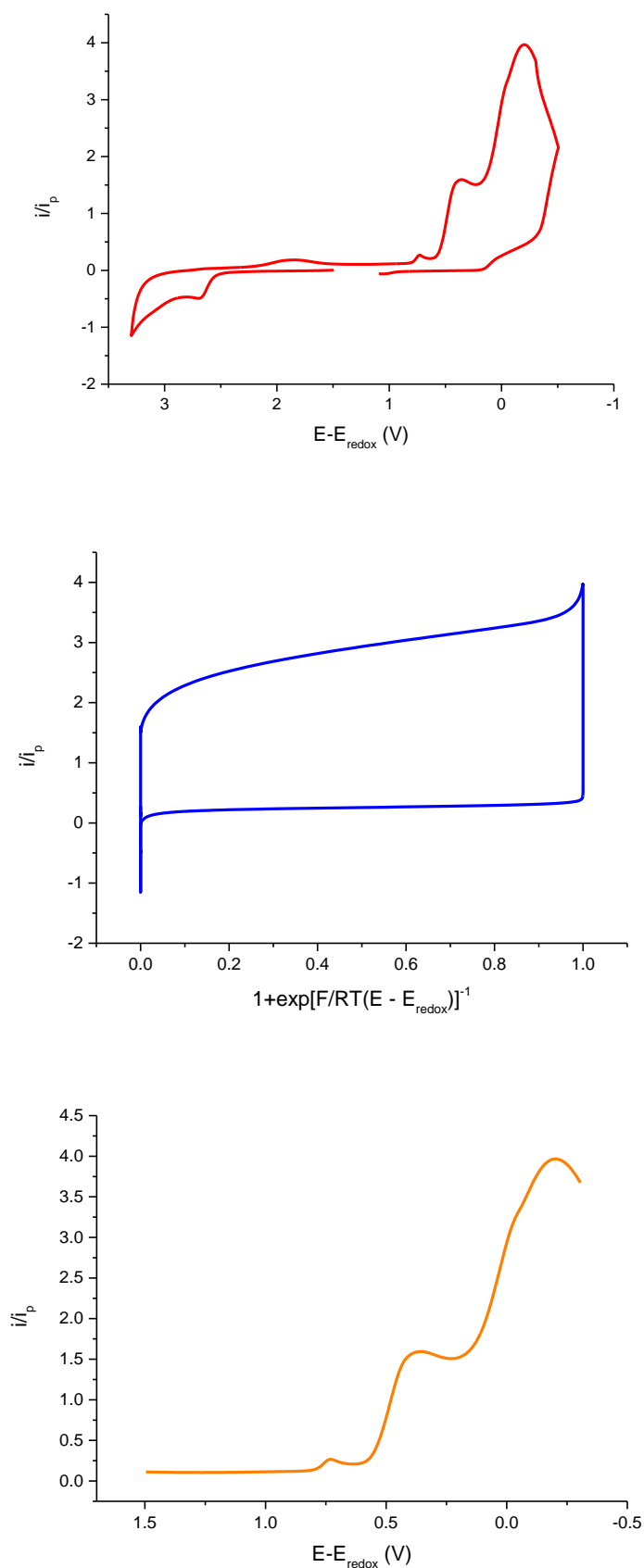
Figure 8.11 Full voltage range of catalytic cyclic voltammetry responses (top) and corresponding foot of the wave analyses (middle) with cathodic wave catalytic cyclic voltammetry response (bottom)
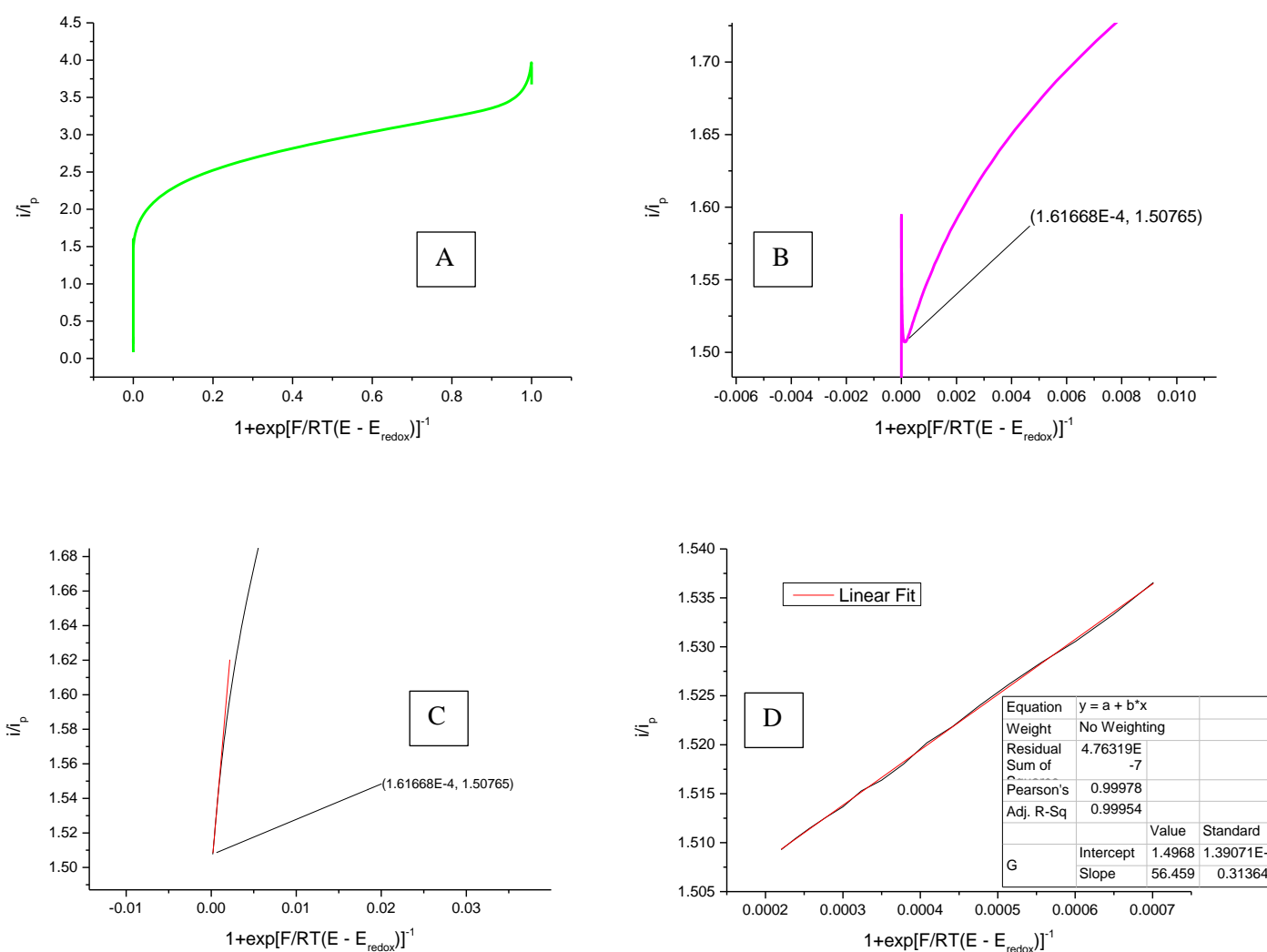
Figure 8.12 Foot of the wave analyses of the data shown in Figure 8.11 (bottom). From top left: (A) foot of the wave analyses plot of the cathodic wave in the range 0 to -2 V vs Ag/AgCl, (B) expansion of (A) searching for any area exhibiting linearity, (C) further expansion searching for any area exhibiting linearity, (D) Linear fit of the data in the initial, "linear" region.

From the voltammogram shown in figure 8.11 (bottom) the foot of the wave analyses shown in figure 8.12 the first issue becomes evident, the real lab results do not fit quite so easily as simulated data. In particular there is an enormous jump in current just after the zero point, followed by a swift decent before a curve begins to emerge. We have chosen to ignore these values; however, no mention is made of such phenomena in papers, more significantly the omission of a scale on the figures published make it unclear if our foot of the wave (amounting to a mere 16 data points) is sufficiently large to provide a k_{obs} value. The gradient of the linear fit yields a k_{obs} value 2474 which has been used to calculate potential dependent TOF and plotted in the form of a Tafel plot.
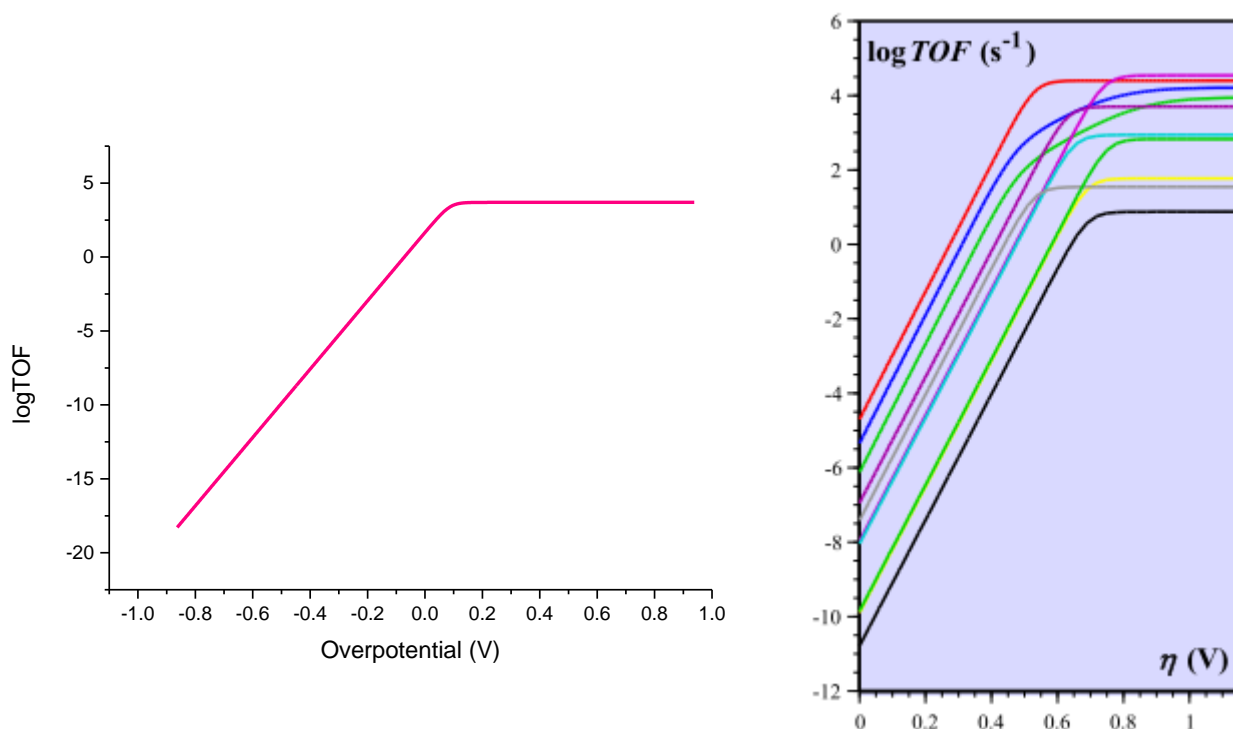
Figure 8.13 Tafel plot for the Mn-Phos complex (left) alongside Tafel plots reproduced from published sources[34]

As can be seen in figure 8.13, the general form of the Tafel plot for the Mn-Phos complex appears correct and the TOF values themselves also appear reasonable, however, the plot seems to be shifted compared to the other values giving very high turnovers at zero applied over potential (A value of - 0.650 V vs NHE was used).[40,41] Since this is the same value used by Kubiak *et al.* in their papers it seems strange that our over potential is so low. However, it appears that foot of the wave analysis can be used with some success. Our luck was not maintained when we attempted to apply foot of the wave analysis to the rhenium mesBIAN complexes in chapter 3, and figure 8.14 shows some of the graphs used in the effort to obtain a k_{obs} value. This mirrored efforts to use foot of the wave analysis on other complexes where we simply didn't know where to progress from; in this case we were unable to find a linear region of more than five data points which we felt was insufficient for analysis. The implications of this are discussed further in the conclusions.
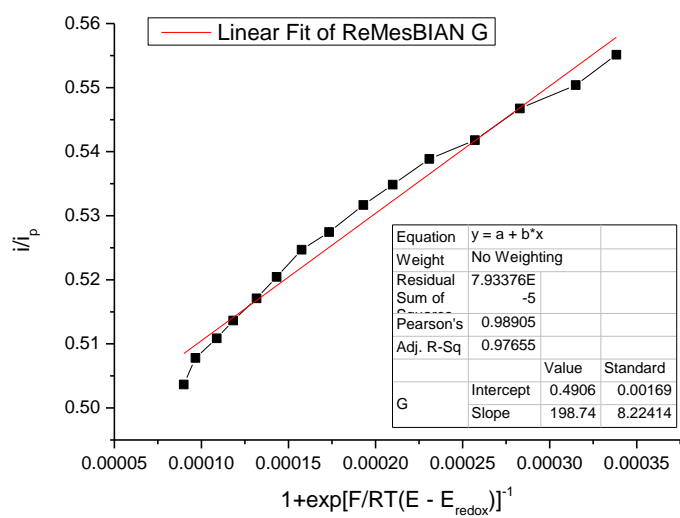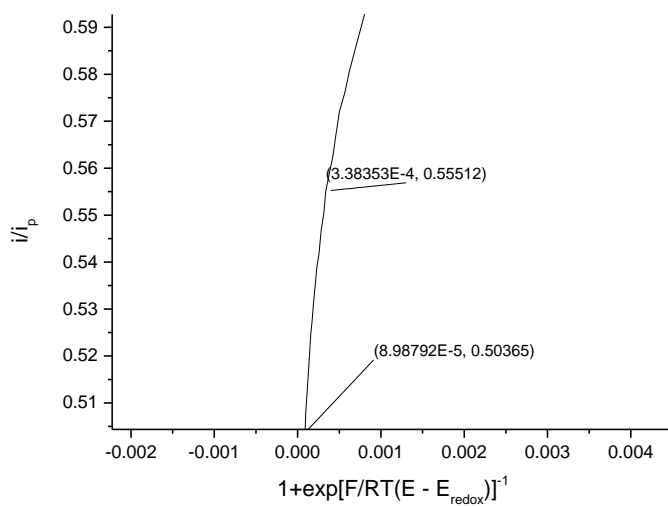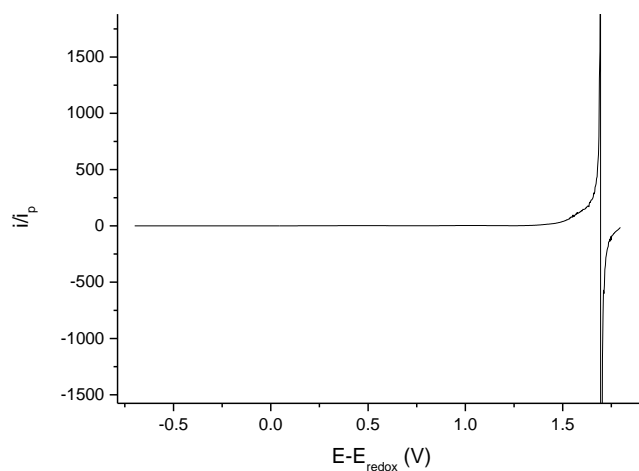
Figure 8.14 Attempting to apply foot of the wave analysis to Re mesBIAN

8.3.3 Myoglobin capture with concomitant UV spectroscopy

The limitations with other methods for determining the yields of CO I was curious see if a more suitable method could be developed. The three most significant issues that I see as the most problematic with current techniques are summarised below.

Firstly not all of the CO is released immediately into the gas phase upon formation. This results in the need for the solution phase to become saturated with CO before the release of CO into the gas phase becomes linear. Secondly certain techniques such as GC have long wait times between successive readings resulting in low precision. It is entirely conceivable that under certain circumstances the initial reaction rate, which as outlined in section 8.3.2.1 corresponds to the peak rate due to the maximum concentration of non-deactivated catalyst, highest concentrations of CO_2 and Brönsted acid and the lowest possible degree of electrode poisoning in the experiment, may be missed entirely using a technique with response times of even a minute or more. Finally the detection limit must be as low as possible and ideally with a linear relationship between CO concentration and detector response in order to make calculation of kinetic parameters simple.

Using what may be termed as a retro spectroscopic analysis an ideal method would therefore: capture all CO released while in the solution phase, be able to have measurements recorded instantaneously, have no wait time between successive measurements, have a very low detection limit and exhibit a linear response. The obvious choice is therefore IR or UV spectroscopy on a solution that contains a medium which captures the CO producing a new species with a characteristic spectroscopic response or myoglobin.

I wish at this point to acknowledge the enormous amount of support and practical assistance provided by Hannah Southam in the laboratory of Professor Robert Poole in the Department of Molecular Biology and Biotechnology, University of Sheffield in investigating this method.

8.3.3.1 Theory behind UV absorption spectroscopy and CO bound myoglobin

The use of myoglobin as means to detect CO or the use of CO to detect haem proteins in biological studies has been used for several decades due to the readily detected and pronounced change in the absorption spectrum of haem proteins upon binding of CO. As it is well known haem proteins exhibit preferential binding of CO over O_2 this technique is highly suitable for CO quantification.

CO binding is monitored by recording difference spectra of CO bound myoglobin – reduced myoglobin. The recorded spectra show characteristic features that depend on the spin-state of the iron and the haem type. Myoglobin is a b-type haem (the distinction being that the haem is not attached by covalent bonds from cysteine –SH groups across vinyl sidechains of b-type haem) which Fe center is present in a high spin configuration without CO coordinated, and low spin when bound to CO. Although the haem type has significance on the biological level (mostly regarding the location of the protein within the cell) the significance chemically is that low spin c-type haems exhibit different absorption bands as compared with c-type haems or haems in other spin states. A more thorough

explanation of the spectroscopic properties is outside of the scope of this background and the reader is directed to P. Woods 1984 review. It is important when carrying out experiments on myoglobin and other haem proteins to maintain a constant pH (in this case ca. pH 7) as changes in pH can alter the spin state which in turn will change the absorption spectra, for this reason all work was conducted in phosphate buffer solution.
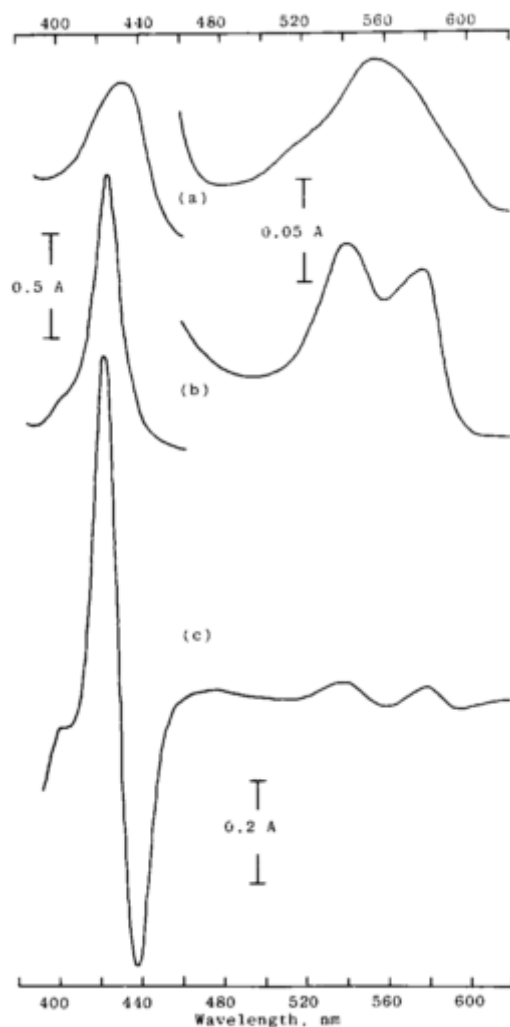
Figure 8.15 Spectra for myoglobin at pH 7: high-spin reduced state. Myoglobin from horse heart (Sigma, Poole, U.K.) dissolved in potassium phosphate buffer (pH 7.0). Final concentration was 6.7 μM. The solution was divided between two cuvettes, and both were reduced with dithionite. CO was bubbled into one cuvette for 15 s, and the cuvette was then stoppered. (a) Absolute spectrum for deoxymyoglobin at pH 7. (b) Absolute spectrum for the CO complex of myoglobin at pH 7. (c) Difference spectrum, reduced-plus-CO minus reduced. Image reproduced from ref [42].

Myoglobin (and other high spin reduced b-type haems) shows a broad absorption band in the region 430 to 435 nm referred to as the Soret band arising from π-π* transitions as well as a single broad combined α-β band in the region 550-560 nm[43]. Binding of CO forms a low spin complex resulting in blue shift of the Soret band and red shifted absorption for the α-β bands which become more clearly

resolved. As can be seen this shift in absorption allows a difference spectrum to be generated from which quantitative assaying can be performed.

$$A = \varepsilon cl \qquad\qquad 8.10$$

In order to gain quantitative values therefore the Beer -Lambert law is used, where the absorption value is taken as the peak of the Soret band minus the trough of the Soret band, the path length is kept as 1 cm and the absorption coefficient used is 177 mM^{-1} cm^{-1}. [44]

8.3.3.2 Method development

The use of myoglobin as a means for spectroscopic analysis of CO yield from electrocatalytic employment of Lehn type catalysts has many potential problems requiring innovative solutions; the following section explores our multiple attempts to develop a working method, the pitfalls that were encountered and our attempts to solve them.

The initial idea[45] for the employment of myoglobin would involve a simple modification to a UV spectroelectrochemical (UV-SEC) cell such as the one shown in figure 8.16.
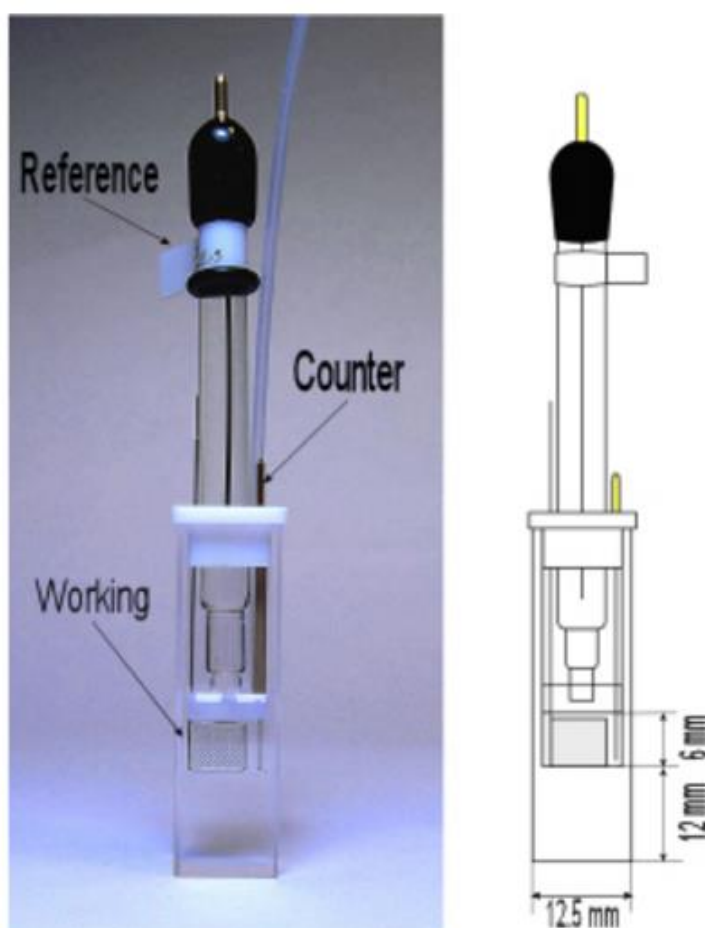
Figure 8.16 Example of a UV-SEC cell with a platinum gauze working electrode, platinum wire counter electrode and Ag/AgCl reference electrode. Image credit to http://www.ijcambria.com/SEC2000-3.html

In this experiment the reduced myoglobin would be in the CO_2 saturated solution alongside the catalyst and electrolyte. As the catalyst was reduced on the electrode CO would be catalytically formed and upon its release immediately bound[46] by the myoglobin before it is able to enter the gas phase, the addition of a small stirrer bar would result in a homogenous environment and prevent the reduction becoming diffusion controlled. This experimental set up would allow for tens of UV spectra to be recorded in situ during the course of the reduction. An important advantage of this set up is that it would not require a fully air tight and sealed system in order to be effective as the myoglobin present of the rate of binding by the myoglobin in solution is so rapid (although the rate[12] of CO binding is well studied we were confident in this conclusion due to empirical evidence from experiments conducted in the Department of Molecular Biology and Biotechnology on CO releasing molecules).[47,48,49]

Very quickly several problems were identified. Firstly the solvent[48] to be used would be acetonitrile which we were unsure would be suitable for the myoglobin; this would also necessitate the abandonment of the important phosphate buffer solution. Although we believed that the presence of the electrolyte necessary for the suppression of the charge diffusion layer at the electrode surface would probably have the same effect as the phosphate buffer it seemed unlikely that the myoglobin would perform identically in acetonitrile as it would in water due to the effect of water on protein folding.[50,51] Much more significantly it appears that the myoglobin would most likely be reduced by the working electrode at potentials much lower than those necessary for the reduction of the Lehn catalyst[45] which would result in either CO release from the myoglobin or in the destruction of the myoglobin on the electrode surface.

As a result of these issues it became apparent that an alternative technique would be required. Firstly it would be necessary to separate the myoglobin from the cell so as to allow the reduced myoglobin to be kept in the phosphate buffer solution and to prevent it from contacting the electrode surface. Preprepared solutions of reduced myoglobin in phosphate buffer (hereafter referred to as "myoglobin charges") would be made up and kept on ice during the experiment, samples of headspace gas would then be withdrawn and injected into the solution where the reduced myoglobin would be able to bind to the CO, tests conducted by Hannah Southam using existing and well-studied CO releasing molecules (CORMs)[12] confirmed that the concentration CO was being bound by the myoglobin was proportional to the CO being released by the CORMs meaning that this technique should be effective. Unfortunately this method would not have the advantages discussed above (not requiring a sealed system and not requiring saturation of the solvent) but would retain the advantage of relatively rapid sampling and low detection limits.

In order to determine if this technique would be effective for determining the efficiency of electrocatalytic CO_2 reduction with Lehn type catalysts a chronoamperometry experiment was carried out on a sample of $[MnBr(CO)_3(bpy)]$ in a single compartment cell. Gas samples extracted from the head space yielded no results for CO in the UV traces suggesting that at the concentration of catalyst

used there was insufficient CO in the head space to be detected. As a result of this the experimental setup was changed, the results from the GC experiments suggested that the build-up of CO in the headspace occurred over a period of tens of minutes and that during the initial phase of a reduction experiment most of the CO was retained in the solution phase. As such samples of 0.1 ml of the solution phase were extracted at regular time intervals and injected into the myoglobin charges where the CO in the solution phase could be bound to the myoglobin. The problem that now occurred was that the electrolyte used in the cell (tetrabutylammonium hexafluorophosphate) was not soluble in water (i.e. the phosphate buffer solution) this resulted in the solution becoming cloudy and scattering the UV light in the spectrophotometer. In order to counter this issue the solutions were centrifuged at 5500 rpm for 1 minute which caused the electrolyte to form a pellet and the supernatant could then be extracted and measurements taken on the spectrophotometer. Initial test results were promising with CO bound myoglobin being observed, however, it was apparent that CO bound myoglobin appeared to grow in far too rapidly to be sensible. Three experiments were then carried out on the asymmetric complexes discussed in chapter 5 one on MnIMP and two on MnTBIEP, the results in figure 8.17 show that the concentration of CO starts high and remains high and there is no consistent increase in CO concentration. Most significantly the CO concentration at 0 minutes is almost as high as at the end of the experiment, this strongly suggests that when the solution is added to the myoglobin charges the carbonyl ligands are being stripped from the manganese by the myoglobin. Unfortunately despite the potential this method could offer it does not seem to be usable under these conditions.
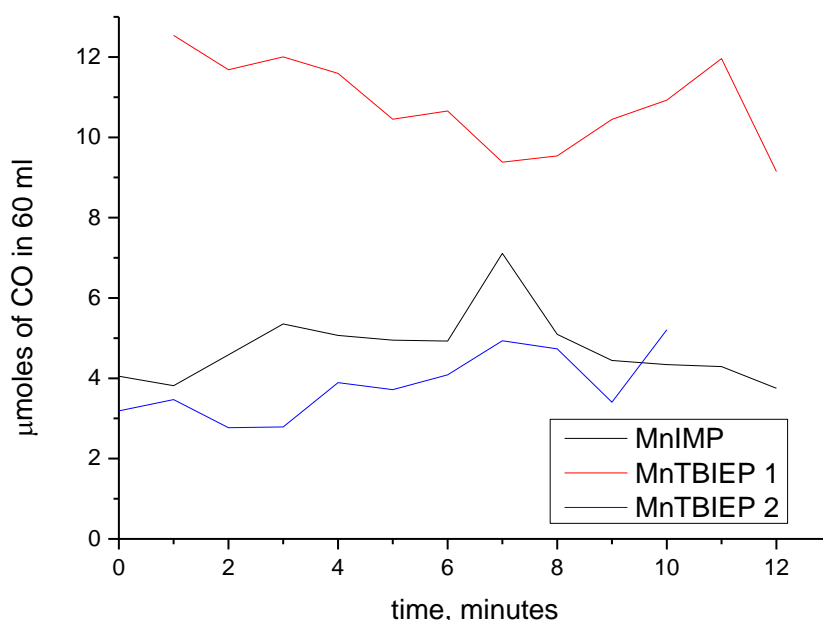
Figure 8.17 Moles of CO in the solution phase produced in the course of electrolysis of Mn-complexes (see legend) under CO$_2$ atmosphere in the presence of myoglobin, calculated from the changes in the absorbtion spectrum of myoglobin.

8.3.3.3 Experimental outline to Myoglobin capture

A concentrated stock solution of myoglobin (Mb) of 0.3 mM concentration was made up using 25.35 mg of Mb derived from horse heart[49] in 5 ml of phosphate buffer solution (PBS). The experimental capture solution was then made up by diluting 1.05 ml of the concentrated Mb stock solution into 47.95 ml of PBS to make a concentration of 10-15 µM, this was then reduced by adding a spatula tip of sodium dithionate and mixed gently for 2 minutes. The solution was then aliquoted 15 vials containing 3 ml of the reduced Mb solution.

The Mb solution was then quantified by baselining the spectrometer to PBS between 400 and 700 nm and recording a reduced Mb spectrum. The spectrometer is then baselined to the reduced Mb solution and the sample of the reduced Mb solution removed and bubbled with bottled CO for 2 minutes until a colour change was observed. A spectrum of this solution is taken and from the peak maxima and peak minima in the Soret region the Mb stock solution can be quantified using equation 8.11 as long as the Mb is in excess of CO this value can be used to determine the amount of CO released.[52]

$$\frac{peak\ maxima-peak\ minima}{177} = [Mb-CO]mM \qquad 8.11$$

8.4 Conclusions

It is the opinion of the author that foot of the wave analysis provides the best method of producing numerical values that can be used to compare catalyst efficiency, the experimental setup is simple and the technique of cyclic voltammetry highly robust and easy to repeat in other labs. In particular of all the techniques currently available from preparative scale electrolysis to rotating disk electrolysis[53] cyclic voltammetry is the most ubiquitous and has already been used for decades to investigate the kinetics of electrochemical systems.[54,55] What foot of the wave analysis offers in particular is the ability to compare in a meaningful way very different catalysts[56,57] in manner that is not dependent on the applied potential. This is certainly something that cannot be said of preparative scale electrolysis especially. This is not to say that preparative scale electrolysis does not have a place but it perhaps should be reserved only for certain kinds of experiments and not regarded as being so important. Additionally as with all things experiments could certainly benefit from some standardisation of equipment and procedures.

Given what has been discussed in section 8.3.2 it may come across as surprising that the author would hold this view given our failures to apply this technique to our own research, however, I believe this is more indicative of the relatively poor state of the dissemination of how to use this technique as it is perfectly probable our failure has arisen simply from misunderstanding. While there have been several excellent papers produced outlining the theory and rationale of foot of the wave analysis[24,28,31]

they are not readily accessible to the new reader and do not provide a step by step walk through leaving the implementation of the analysis up to the mind of the reader and this is no doubt in part responsible for the variety of equations seen in different papers. Indeed the closest thing in the authors opinion to a usable walk through of foot of the wave analysis is to be found in the supplementary information of Sampson, Kubiak *et al.* recent (2016 JACS) paper.[40] It is the opinion of the author that what would be most desirable to establish an easily repeatable method discussed in publications void of derivation and where nuance is discussed in its place. It is telling that when using foot of the wave analysis on manganese based Lehn catalysts we immediately reached an impasse in that there is no reversible redox potential from which to acquire an E_{cat}^0 value, never the less other manganese based Lehn catalysts had been discussed in the papers we were using as a guide. Ultimately I contacted Professor Cyrille Costentin who responded, "It is indeed a problem when the catalyst do not exhibit a reversible wave in absence of substrate. In such a case, raising the scan rate may be a way to get access to some reversibility and measure the standard potential. In the case of Mn(bpy)(CO)3Br, we used E1/2 as a approximate value for E°. This is not fully satisfactory but you may not have another option if you do not have possibility to get E°." This is the nuance that needs to be communicated most with the wider field and it is the authors sincere hope that a program of workshops and a series of more applied papers can be published in the future.

8.5 References

(1)   Chi, C.-C.; Lin, T.-H.; Huang, W.-C.; Hou, S.-S.; Wang, P.-Y. *Fuel* **2015**, *160*, 434–439.

(2)   Ji, M.-K.; Yun, H.-S.; Hwang, J.-H.; Salama, E.-S.; Jeon, B.-H.; Choi, J. *Environ. Technol.* **2016**, 10.1080/09593330.2016.1246145.

(3)   Osterloh, F. E. *ACS Energy Lett.* **2016**, *1*, 1060–1061.

(4)   Gibson, J. A. A.; Mangano, E.; Shiko, E.; Greenaway, A. G.; Gromov, A. V.; Lozinska, M. M.; Friedrich, D.; Campbell, E. E. B.; Wright, P. A.; Brandani, S. *Ind. Eng. Chem. Res.* **2016**, *55* (13), 3840–3851.

(5)   Xu, X.; Song, C.; Wincek, R.; Andresen, J. M.; Miller, B. G.; Scaroni, A. W. *ACS Div. Fuel Chem. Prepr.* **2003**, *48* (1), 162–163.

(6)   Girimonte, R.; Formisani, B.; Testa, F. *Powder Technol.* **2017**, *311*, 9–17.

(7)   Preetham, H. S.; Madhu, G. M.; Pai, K. V. K. *Eur. J. Chem.* **2016**, *7* (2), 176–181.

(8)   Ganjdanesh, R.; Pope, G. A.; Sepehrnoori, K. *Int. J. Greenh. Gas Control* **2015**, *34*, 97–105.

(9)   Liang, Z.; Fu, K.; Idem, R.; Tontiwachwuthikul, P. *Chinese J. Chem. Eng.* **2016**, *24* (2), 278–288.

(10)   Khakharia, P.; Mertens, J.; Huizinga, A.; De Vroey, S.; Sanchez Fernandez, E.; Srinivasan, S.; Vlugt, T. J. H.; Goetheer, E. *Ind. Eng. Chem. Res.* **2015**, *54* (19), 5336–5344.

(11)   Pal, U.; Ghosh, S.; Chatterjee, D. *Transit. Met. Chem.* **2012**, *37* (1), 93–96.

(12)   Mclean, S.; Mann, B. E.; Poole, R. K. *Anal. Biochem.* **2012**, *427* (1), 36–40.

(13)   Ruggi, A.; Zobi, F. *Dalt. Trans.* **2015**, *44* (24), 10928–10931.

(14)   Strinitz, F.; Trautner, P.; Pfeiffer, H.; Schatzschneider, U.; Burzlaff, N. *Tetrahedron* **2015**, *71* (19), 2951–2954.

(15)   Tinajero-Trejo, M.; Rana, N.; Nagel, C.; Jesse, H. E.; Smith, T. W.; Wareham, L. K.; Hippler, M.; Schatzschneider, U.; Poole, R. K. *Antioxid. Redox Signal.* **2016**, *24* (14), 765–780.

(16)   Smith, T. W.; Hippler, M. F. A. *Anal. Chem.* **2017**, acs.analchem.6b04924.

(17)   Vollmer, M. V.; Machan, C. W.; Clark, M. L.; Antholine, W. E.; Agarwal, J.; Schaefer, H. F.; Kubiak, C. P.; Walensky, J. R. *Organometallics* **2015**, *34* (1), 3–12.

(18)   Zeng, Q.; Tory, J.; Hartl, F. *Organometallics* **2014**, *33* (18), 5002–5008.

(19)   Bleys, G. (PUR patents). *TECHNOLOGY WATCH : Carbon Dioxide Conversion*; 2016.

(20)   McCrory, C. C. L.; Jung, S.; Ferrer, I. M.; Chatman, S.; Peters, J. C.; Jaramillo, T. F. *J. Am. Chem. Soc.* **2015**, *137*, 4347–4357.

(21)   Suroviec, A. H. *J. Lab. Chem. Educ.* **2013**, *1* (3), 45–48.

(22)   Nicholson, R. S.; Shain, I. *Anal. Chem.* **1964**, *36* (4), 706–723.

(23)   Heinze, J. *Angew. Chemie Int. Ed. English* **1984**, *23* (11), 831–847.

(24)   Costentin, C.; Drouet, S.; Robert, M.; Save, J. *J. Am. Chem. Soc.* **2012**, *134*, 11235–11242.

(25)   Nicholson, R. S.; Nicholso.Rs. *Anal. Chem.* **1965**, *37* (11), 1351–1355.

(26)   Bott, A. *Curr. Sep.* **1997**, *16* (2), 61–66.

(27)   Saji, V. S.; Lee, C.-W. *ChemSusChem* **2012**, *5* (7), 1146–1161.

(28)   Costentin, C.; Passard, G.; Savéant, J.-M. *J. Am. Chem. Soc.* **2015**, *137* (16), 5461–5467.

(29)   Savéant, J.-M. *Chem. Rev.* **2008**, *108* (7), 2348–2378.

(30)   Costentin, C.; Savéant, J.-M. *Phys. Chem. Chem. Phys.* **2015**, *17* (29), 19350–19359.

(31)   Rountree, E. S.; McCarthy, B. D.; Eisenhart, T. T.; Dempsey, J. L. *Inorg. Chem.* **2014**, *53* (19), 9983–10002.

(32)   Marcus, R. A. *J. Chem. Phys.* **1963**, *39* (7), 1734–1740.

(33)   Artero, V.; Saveant, J.-M. *Energy Environ. Sci.* **2014**, *7*, 3808–3814.

(34)   Costentin, C.; Robert, M.; Savéant, J.-M.; Tatin, A. *Proc. Natl. Acad. Sci.* **2015**, *112* (22), 6882–6886.

(35)   Costentin, C.; Robert, M.; Savéant, J.-M. *Chem. Soc. Rev.* **2013**, *42* (6), 2423–2436.

(36)   Costentin, C.; Passard, G.; Robert, M.; Savéant, J.-M. *Proc. Natl. Acad. Sci.* **2014**, *111* (42), 14990–14994.

(37)   Fourmond, V.; Jacques, P. A.; Fontecave, M.; Artero, V. *Inorg. Chem.* **2010**, *49* (22), 10338–10347.

(38)   Savéant, J.-M.; Su, K. B. *J. Electroanal. Chem.* **1984**, *171*, 341–349.

(39)   Sathrum, A. J.; Kubiak, C. P. *J. Phys. Chem. Lett.* **2011**, *2*, 2372–2379.

(40)   Sampson, M. D.; Kubiak, C. P. *J. Am. Chem. Soc.* **2016**, *138* (4), 1386–1393.

(41)   Costentin, C.; Drouet, S.; Robert, M.; Savéant, J.-M. *Science (80-.).* **2012**, *338*, 90–94.

(42)   Wood, P. M. *Biochim. Biophys. Acta.* **1984**, *768* (768), 293–317.

(43)   Gouterman, M. *The Porphyrins*; Academic Press: New York, 1978.

(44)   Antonini, E.; Brunori, M. *Haemoglobin and Myoglobin in their reaction with Ligands*; North-Holland, Amsterdam, 1971.

(45)   Chatterjee, S.; Sengupta, K.; Samanta, S.; Das, P. K.; Dey, A. *Inorg. Chem.* **2013**, *52* (17), 9897–9907.

(46)   Dowson, G. R. M.; Dimitriou, I.; Owen, R. E.; Reed, D. G.; Allen, R. W. K.; Styring, P. *Faraday Discuss.* **2015**, *183*, 47–65.

(47)   Matsuo, T.; Dejima, H.; Hirota, S.; Murata, D.; Sato, H.; Ikegami, T.; Hori, H.; Hisaeda, Y.; Hayashi, T. *J. Am. Chem. Soc.* **2004**, *126* (49), 16007–16017.

(48)   McKinnie, R. E.; Olson, J. S. *J. Biol. Chem.* **1981**, *256* (17), 8928–8932.

(49)   Bannister, J. V; Bannister, W. H. **1976**, *65* (3), 1–4.

(50)   Maruyama, Y.; Harano, Y. *Chem. Phys. Lett.* **2013**, *581*, 85–90.

(51)   Ben-Naim, A. *Eur. Phys. J. Spec. Top.* **2013**, *223* (5), 927–946.

(52)   Millar, S. J.; Moss, B. W.; Stevenson, M. H. *Meat Sci.* **1996**, *42* (3), 277–288.

(53)   Eggins, B. R.; Bennett, E. M.; McMullan, E. A. *J. Electroanal. Chem.* **1996**, *408*, 165–171.

(54)   Bolinger, C. M.; Sullivan, B. P.; Conrad, D.; Gilbert, J. A.; Story, N.; Meyer, T. J. *J. Chem. Soc, Chem. Commun.* **1985**, 796–797.

(55)   Perra, A.; Davies, E. S.; Hyde, J. R.; Wang, Q.; McMaster, J.; Schröder, M. *Chem. Commun. (Camb).* **2006**, *44* (10), 1103–1105.

(56)   Li, K.; Peng, B.; Peng, T. *ACS Catal.* **2016**, *6*, 7485–7527.

(57)   Li, X.; Yu, J.; Wageh, S.; Al-Ghamdi, A. A.; Xie, J. *Small* **2016**, *48*, 6640–6696.
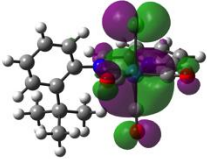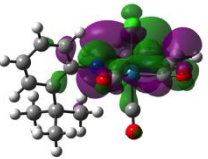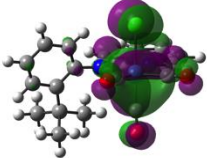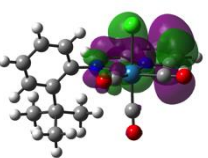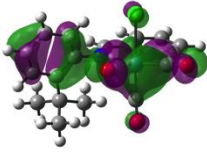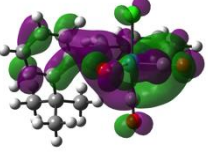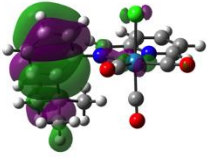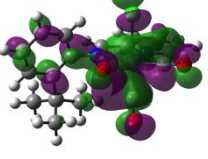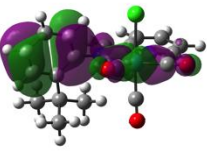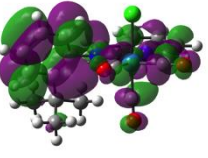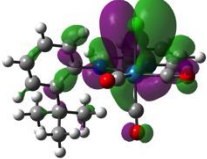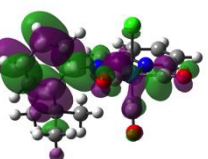
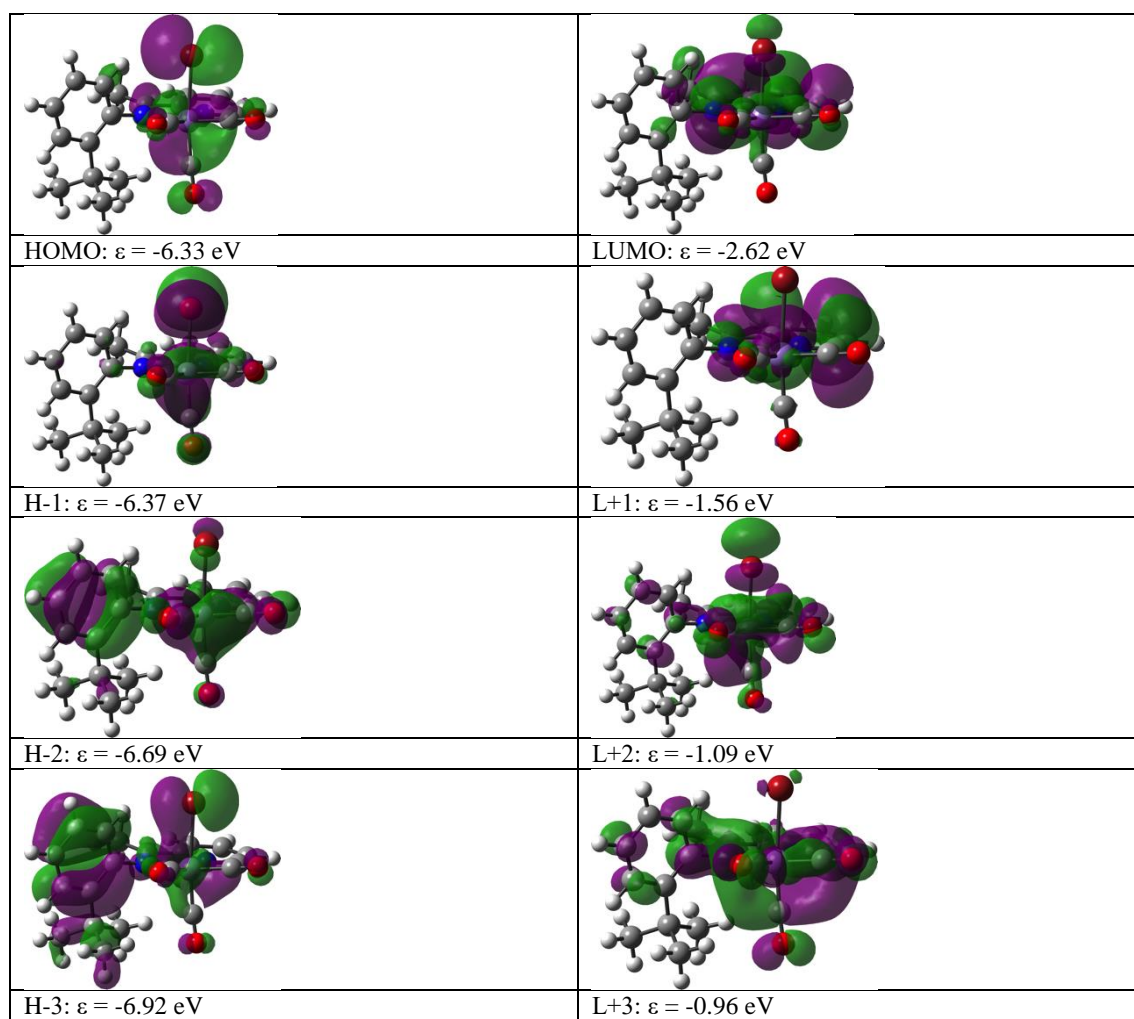|	
HOMO: ε = -6.35 eV	LUMO: ε = -3.05 eV
H-1: ε = -6.42 eV	L+1: ε = -1.76 eV
H-2: ε = -6.73 eV	L+2: ε = -1.07 eV
H-3: ε = -7.03 eV	L+3: ε = -0.94 eV
H-4: ε = -7.18 eV	L+4: ε = -0.63 eV
H-5: ε = -7.66 eV	L+5: ε = -0.52 eV

Figure A1.1 Frontier orbitals of [ReCl(CO)₃(TBIMP)] calculated at the B3LYP/SDD+6-311G(d,p)/IEFPCM level. Isovalue = 0.02 $\sqrt{e^-\,\text{bohr}^{-3}}$ for all orbitals.
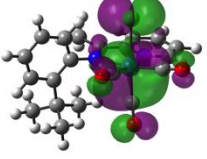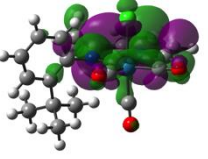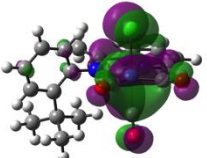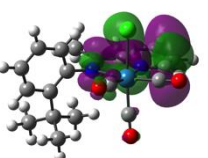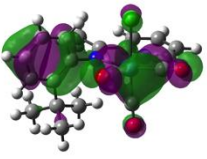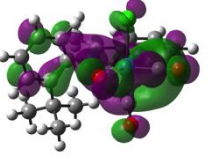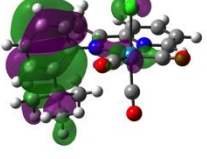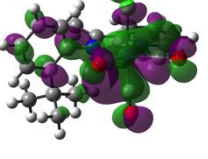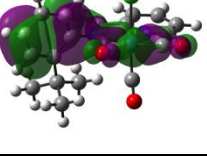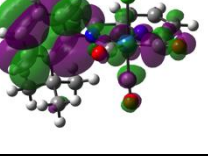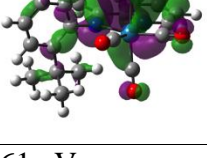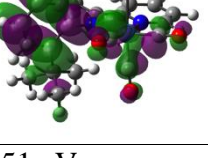
HOMO: ε = -6.30 eV	LUMO: ε = -2.87 eV
H-1: ε = -6.37 eV	L+1: ε = -1.75 eV
H-2: ε = -6.63 eV	L+2: ε = -1.00 eV
H-3: ε = -7.00 eV	L+3: ε = -0.89 eV
H-4: ε = -7.16 eV	L+4: ε = -0.60 eV
H-5: ε = -7.61 eV	L+5: ε = -0.51 eV

Figure A1.2 Frontier orbitals of [ReCl(CO)₃(TBIEP)] calculated at the B3LYP/SDD+6-311G(d,p)/IEFPCM level. Isovalue = 0.02 $\sqrt{e^-\ bohr^{-3}}$ for all orbitals.
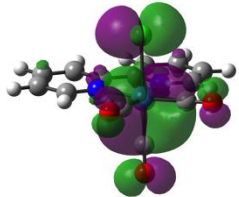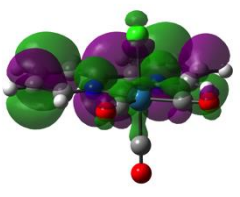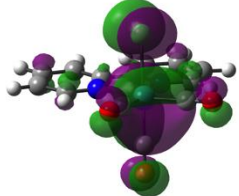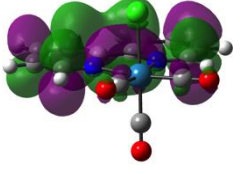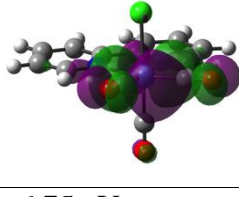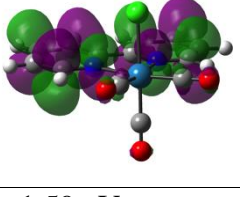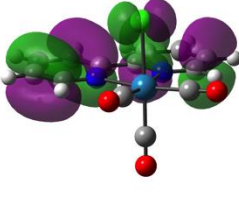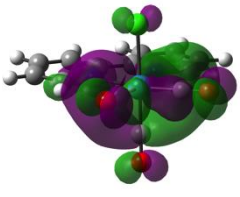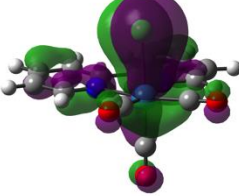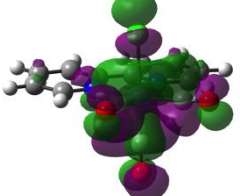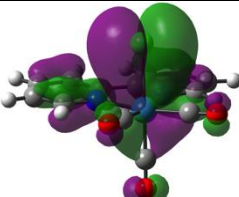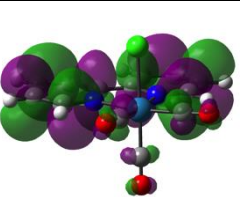
HOMO: ε = -6.26 eV	LUMO: ε = -2.72 eV
H-1: ε = -6.35 eV	L+1: ε = -1.78 eV
H-2: ε = -6.75 eV	L+2: ε = -1.59 eV
H-3: ε = -7.48 eV	L+3: ε = -0.98 eV
H-4: ε = -7.65 eV	L+4: ε = -0.82 eV
H-5: ε = -7.67 eV	L+5: ε = -0.29 eV

Figure A1.3 Frontier orbitals of [ReCl(CO)$_3$(bpy)] calculated at the B3LYP/SDD+6-311G(d,p)/IEFPCM level. Isovalue = 0.02 $\sqrt{\text{e}^-\ \text{bohr}^{-3}}$ for all orbitals.
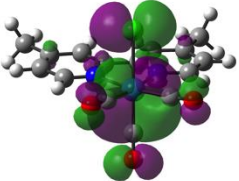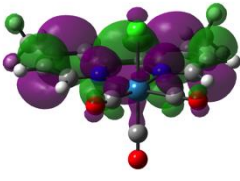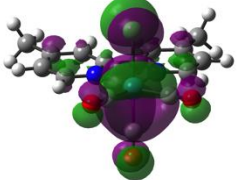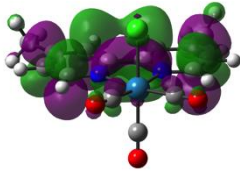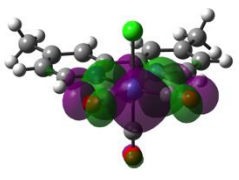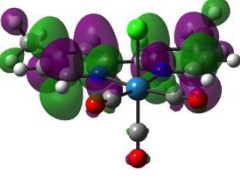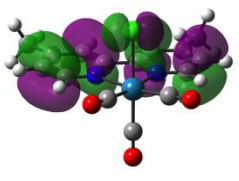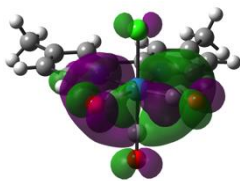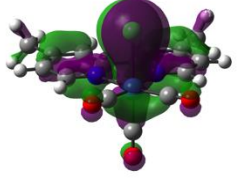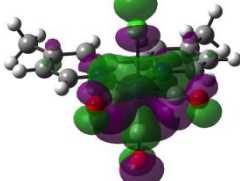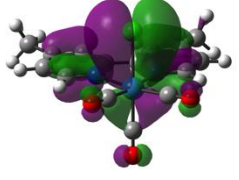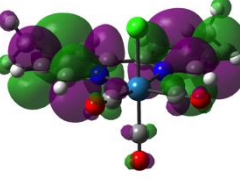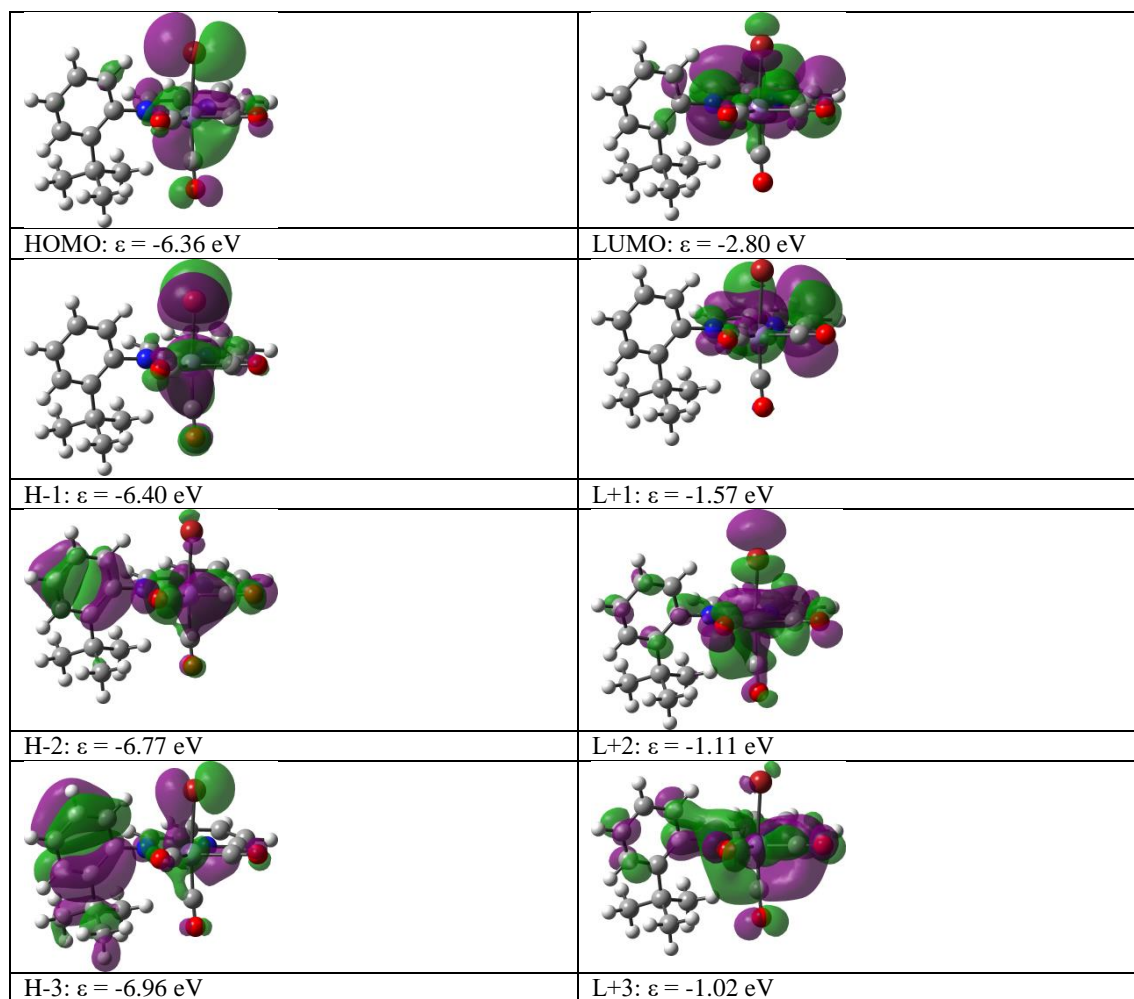
HOMO: ε = -6.21 eV	LUMO: ε = -2.62 eV
H-1: ε = -6.30 eV	L+1: ε = -1.63 eV
H-2: ε = -6.70 eV	L+2: ε = -1.41 eV
H-3: ε = -7.39 eV	L+3: ε = -0.93 eV
H-4: ε = -7.56 eV	L+4: ε = -0.78 eV
H-5: ε = -7.60 eV	L+5: ε = -0.25 eV

Figure A1.4 Frontier orbitals of [ReCl(CO)₃(TBIEP)] calculated at the B3LYP/SDD+6-311G(d,p)/IEFPCM level. Isovalue = 0.02 $\sqrt{\mathrm{e^- \, bohr^{-3}}}$ for all orbitals.
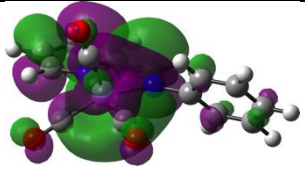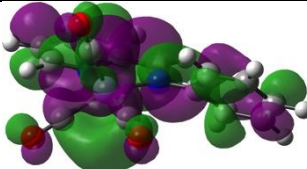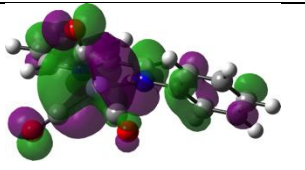
Calculated carbonyl stretching frequencies used in assignment of IR-SEC

ReTBIMP

Species	Peak postion / cm^{-1}
[ReCl(CO)$_3$(TBIMP)]	1904 1930 2030
[ReCl(CO)$_3$(TBIMP)]$^{\bullet-}$	1861 1885 2000
[Re(CO)$_3$(TBIMP)]$^-$	1826 1836 1947
[Re(CO)$_3$(TBIMP)(CH$_3$CN)]$^{\bullet}$	1897 1908 2016
[Re(CO)$_3$(CH$_3$CN)(TBIMP)]$^-$	not yet converged
[Re(CO)$_3$(TBIMP)]$_2$	1874 1878 1884 1888 1962 1985

Scaling factor: 0.978

ReTBIEP

Species	Peak postion / cm^{-1}
[ReCl(CO)$_3$(TBIEP)]	1900 1926 2028
[ReCl(CO)$_3$(TBIEP)]$^{\bullet-}$	1859 1882 1998
[Re(CO)$_3$(TBIEP)]$^-$	1821 1833 1943
[Re(CO)$_3$(TBIEP)(CH$_3$CN)]$^{\bullet}$	1893 1904 2013
[Re(CO)$_3$(TBIEP)(CH$_3$CN)]$^-$	not yet converged
[Re(CO)$_3$(TBIEP)]$_2$	1863 1868 1879 1881 1954 1979

Scaling factor: 0.978

Re NN

Species	Peak postion / cm^{-1}
[ReCl(CO)$_3$(bpy)]	1901
	1920
	2027
[ReClCO$_3$(dmbpy)]	1898
	1917
	2025

Scaling factor: 0.978

Appendix 2 Computational and electrochemical data for chapters 5 and 6
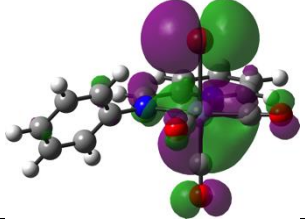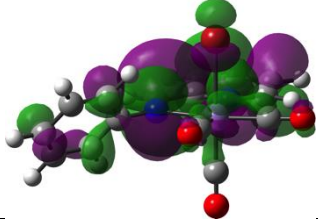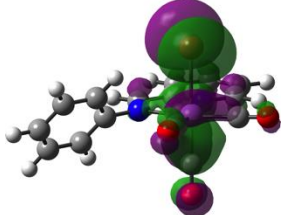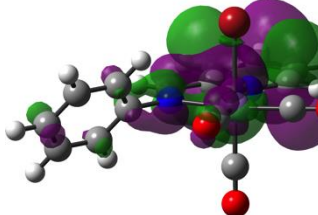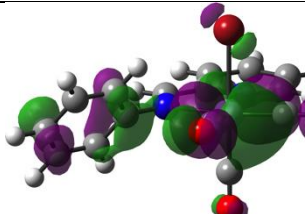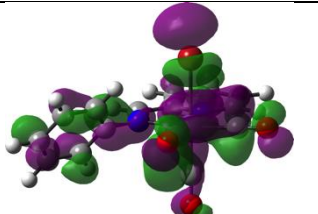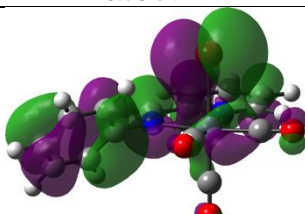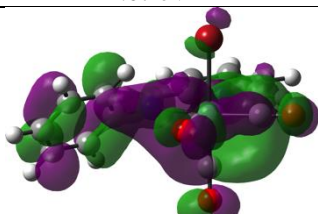
HOMO: ε = -6.31 eV	LUMO: ε = -2.84 eV
H-1: ε = -6.37 eV	L+1: ε = -1.57 eV
H-2: ε = -6.76 eV	L+2: ε = -1.07 eV
H-3: ε = -7.06 eV	L+3: ε = -1.01 eV

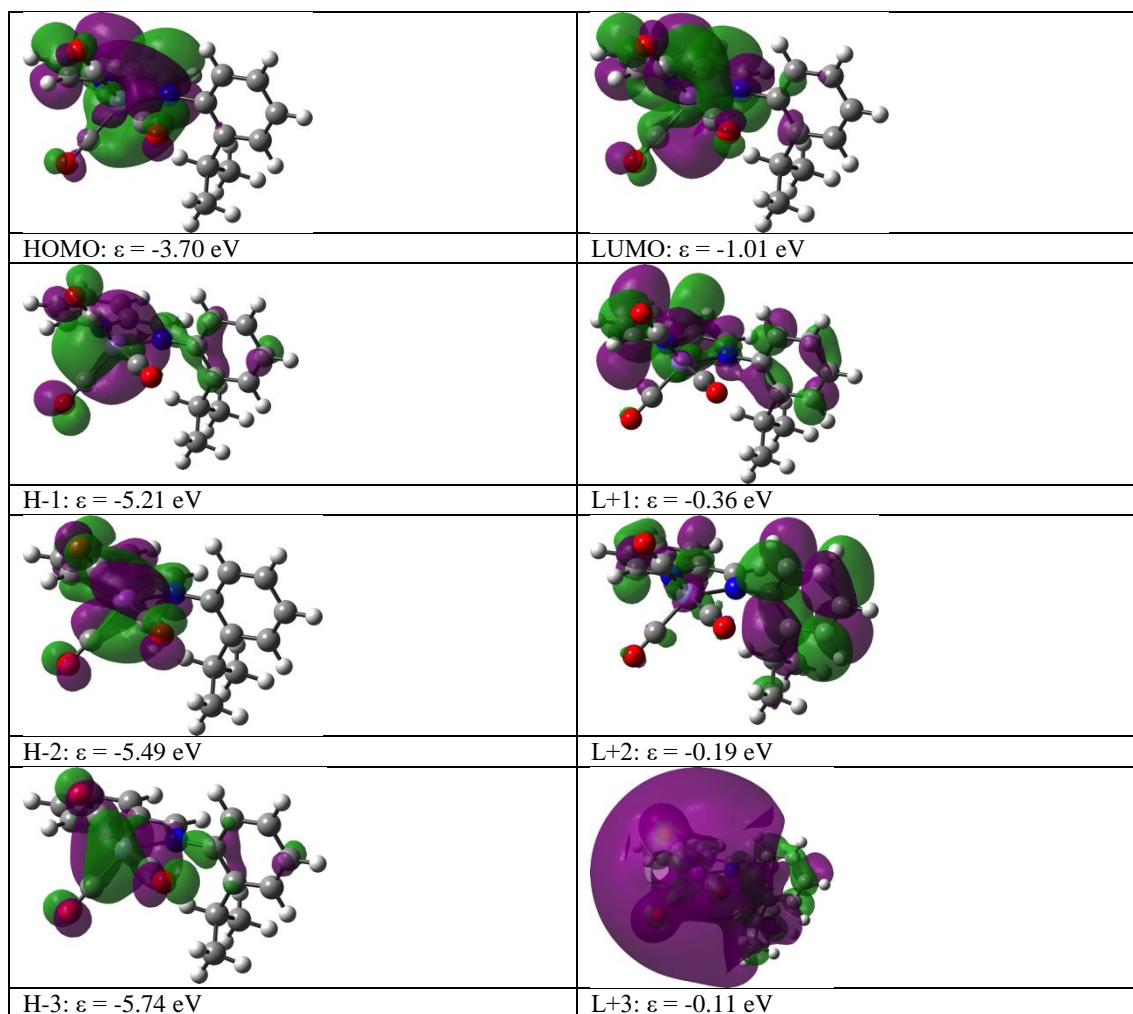**Figure A2.1 Frontier orbitals of [MnBr(CO)₃(IMP)] calculated at the B3LYP/SDD+6-311G(d,p)/IEFPCM level. Isovalue = 0.02 $\sqrt{e^-\ \mathbf{bohr^{-3}}}$ for all orbitals.**

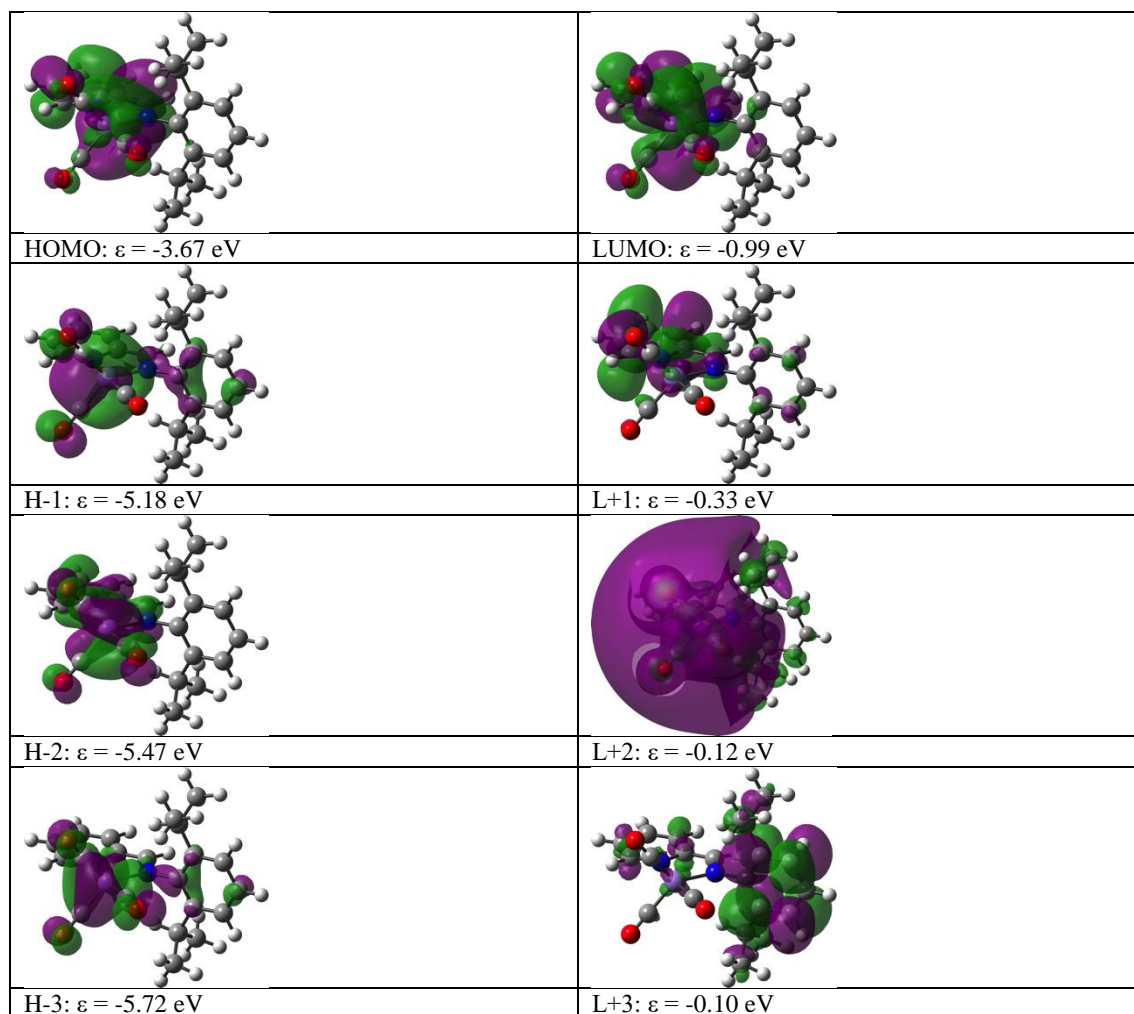|	
HOMO: ε = -6.33 eV	LUMO: ε = -2.81 eV
H-1: ε = -6.37 eV	L+1: ε = -1.56 eV
H-2: ε = -6.74 eV	L+2: ε = -1.07 eV
H-3: ε = -6.98 eV	L+3: ε = -0.98 eV
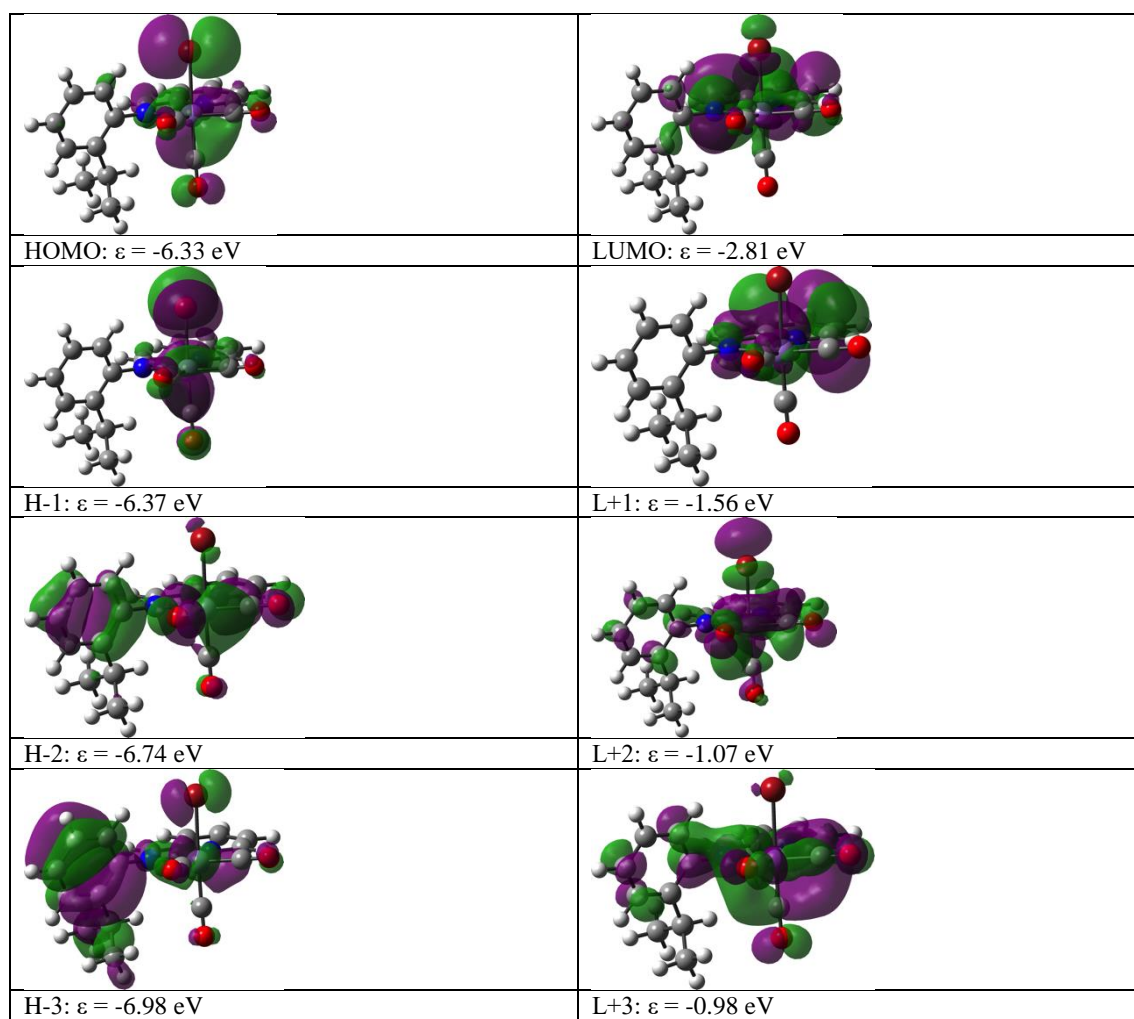
Figure A2.2 Frontier orbitals of [MnBr(CO)₃(IPIMP)] calculated at the B3LYP/SDD+6-311G(d,p)/IEFPCM level. Isovalue = 0.02 $\sqrt{\text{e}^-\ \text{bohr}^{-3}}$ for all orbitals.

HOMO: ε = -6.31 eV	LUMO: ε = -2.83 eV
H-1: ε = -6.42eV	L+1: ε = -1.57 eV
H-2: ε = -6.79 eV	L+2: ε = -1.12 eV
H-3: ε = -6.80 eV	L+3: ε = -1.03 eV
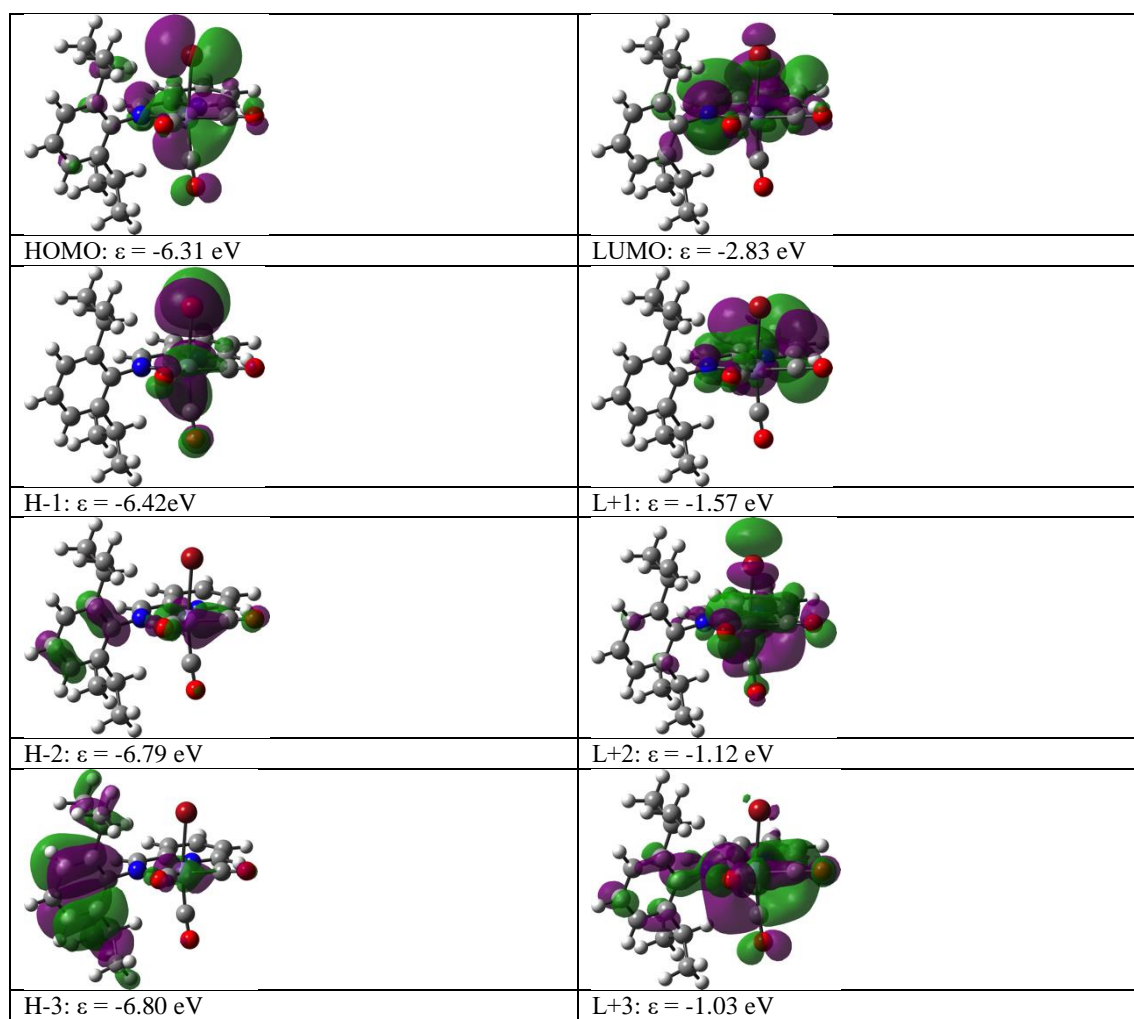
Figure A2.3 Frontier orbitals of [MnBr(CO)₃(DIPIMP)] calculated at the B3LYP/SDD+6-311G(d,p)/IEFPCM level. Isovalue = 0.02 $\sqrt{e^- \, bohr^{-3}}$ for all orbitals.

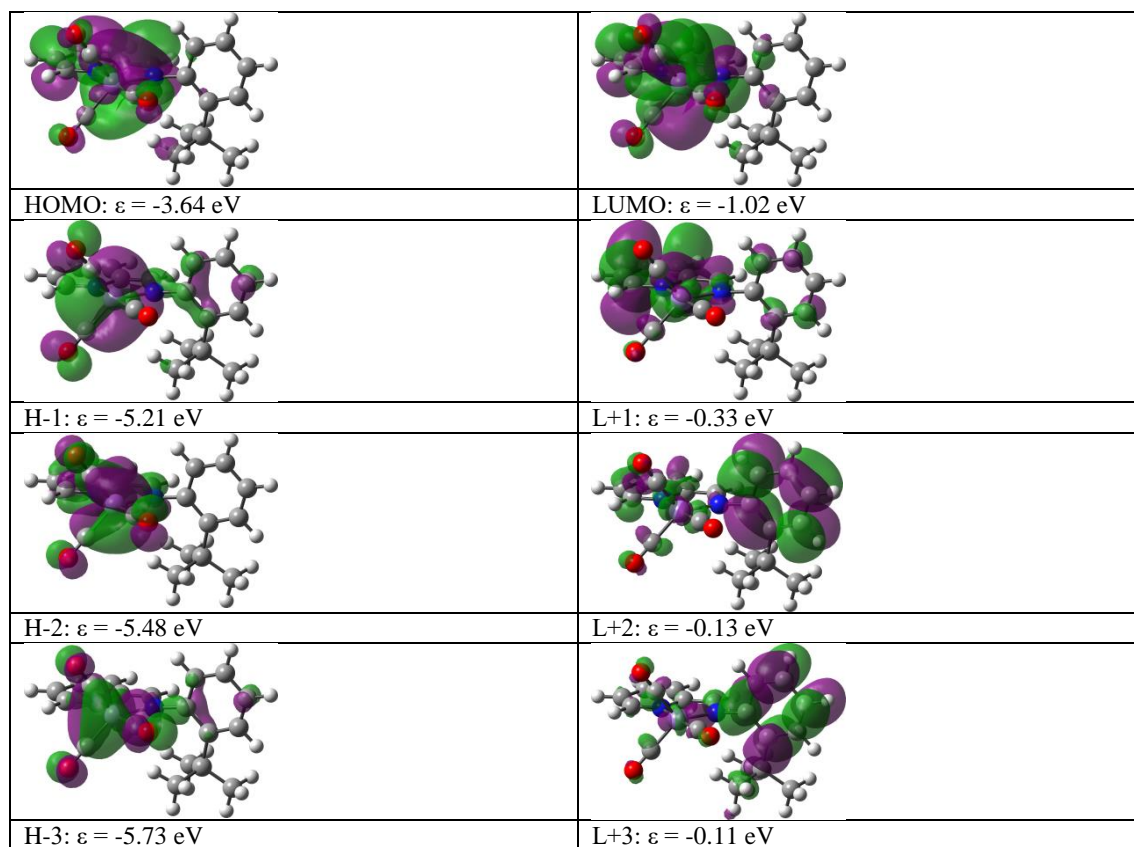|	
HOMO: ε = -6.33 eV	LUMO: ε = -2.62 eV
H-1: ε = -6.37 eV	L+1: ε = -1.56 eV
H-2: ε = -6.69 eV	L+2: ε = -1.09 eV
H-3: ε = -6.92 eV	L+3: ε = -0.96 eV

Figure A2.4 Frontier orbitals of [MnBr(CO)₃(TBIEP)] calculated at the B3LYP/SDD+6-311G(d,p)/IEFPCM level. Isovalue = 0.02 $\sqrt{\mathrm{e^-\ bohr^{-3}}}$ for all orbitals.

HOMO: ε = -6.36 eV	LUMO: ε = -2.80 eV
H-1: ε = -6.40 eV	L+1: ε = -1.57 eV
H-2: ε = -6.77 eV	L+2: ε = -1.11 eV
H-3: ε = -6.96 eV	L+3: ε = -1.02 eV

Figure A2.5 Frontier orbitals of [MnBr(CO)₃(TBIMP)] calculated at the B3LYP/SDD+6-311G(d,p)/IEFPCM level. Isovalue = 0.02 $\sqrt{e^-\ bohr^{-3}}$ for all orbitals.
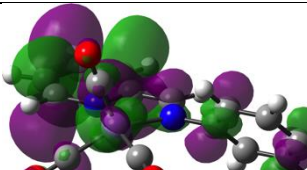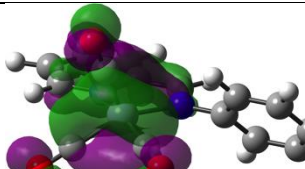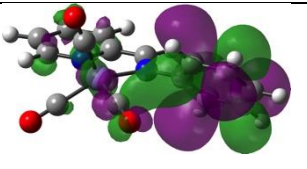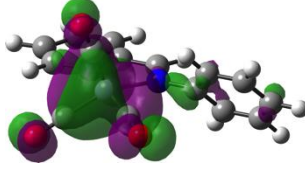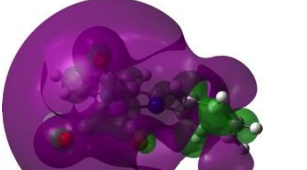
HOMO: ε = -3.67 eV	LUMO: ε = -1.18 eV
H-1: ε = -5.22 eV	L+1: ε = -0.36 eV
H-2: ε = -5.55 eV	L+2: ε = -0.30 eV
H-3: ε = -5.77 eV	L+3: ε = -0.06 eV

**Figure A2.6 Frontier orbitals of [Mn(CO)₃(IMP)]⁻ calculated at the B3LYP/SDD+6-311G(d,p)/IEFPCM level. Isovalue = 0.02 $\sqrt{e^- \, bohr^{-3}}$ for all orbitals apart from L+3, a Rydberg orbital, for which isovalue = 0.01 $\sqrt{e^- \, bohr^{-3}}$ is shown.**

HOMO: ε = -3.70 eV	LUMO: ε = -1.01 eV
H-1: ε = -5.21 eV	L+1: ε = -0.36 eV
H-2: ε = -5.49 eV	L+2: ε = -0.19 eV
H-3: ε = -5.74 eV	L+3: ε = -0.11 eV

Figure A2.7 Frontier orbitals of [Mn(CO)₃(IPIMP)]⁻ calculated at the B3LYP/SDD+6-311G(d,p)/IEFPCM level. Isovalue = 0.02 $\sqrt{e^- \ bohr^{-3}}$ for all orbitals apart from L+3, a Rydberg orbital, for which isovalue = 0.01 $\sqrt{e^- \ bohr^{-3}}$ is shown.

HOMO: ε = -3.67 eV	LUMO: ε = -0.99 eV
H-1: ε = -5.18 eV	L+1: ε = -0.33 eV
H-2: ε = -5.47 eV	L+2: ε = -0.12 eV
H-3: ε = -5.72 eV	L+3: ε = -0.10 eV

Figure A2.8 Frontier orbitals of [Mn(CO)$_3$(DIPIMP)]$^-$ calculated at the B3LYP/SDD+6-311G(d,p)/IEFPCM level. Isovalue = 0.02 $\sqrt{e^- \, bohr^{-3}}$ for all orbitals apart from L+2, a Rydberg orbital, for which isovalue = 0.01 $\sqrt{e^- \, bohr^{-3}}$ is shown.

HOMO: ε = -3.55 eV	LUMO: ε = -0.99 eV
H-1: ε = -5.11 eV	L+1: ε = -0.33 eV
H-2: ε = -5.41 eV	L+2: ε = -0.17 eV
H-3: ε = -5.63 eV	L+3: ε = -0.10 eV
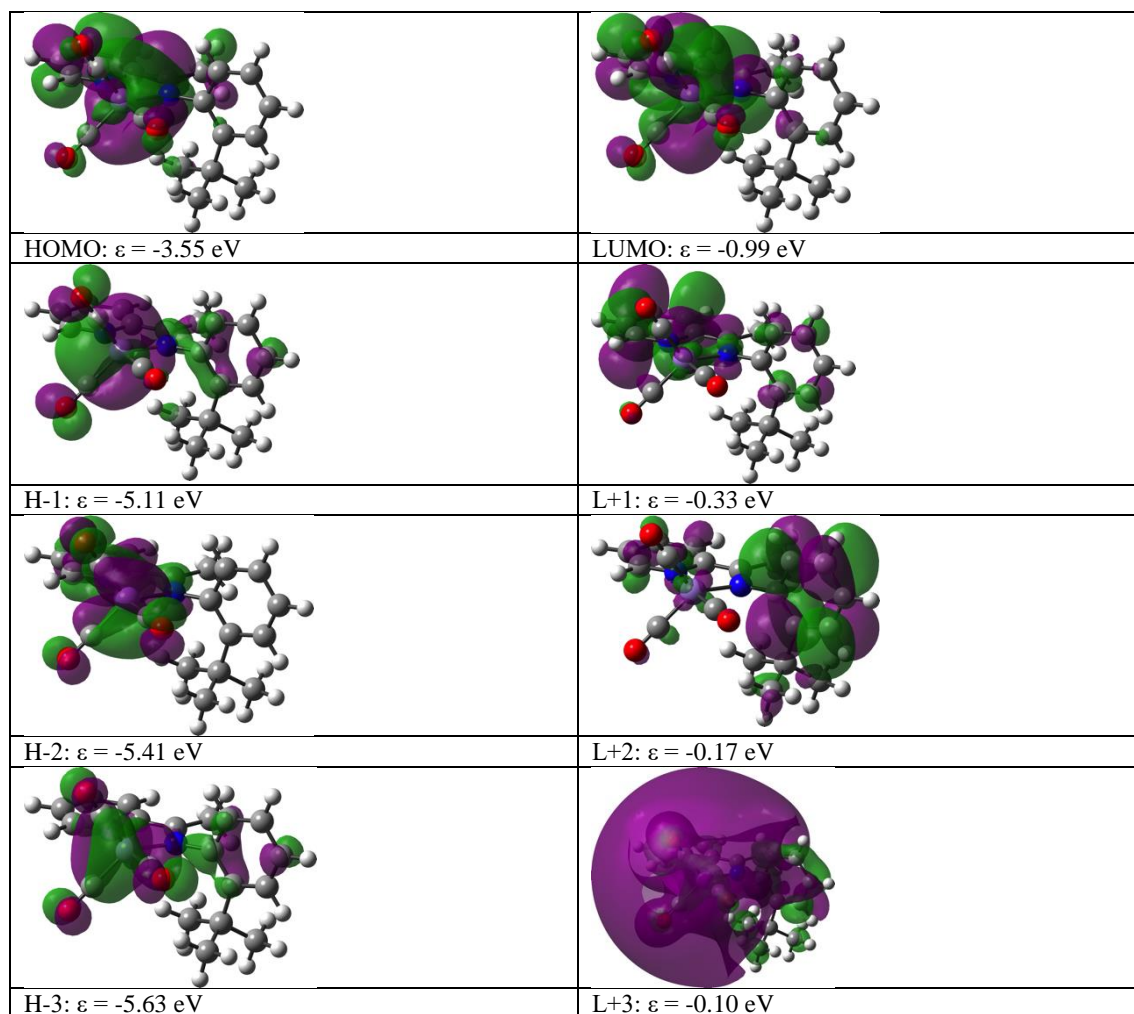
Figure A2. 9 Frontier orbitals of [Mn(CO)₃(TBIEP)]⁻ calculated at the B3LYP/SDD+6-311G(d,p)/IEFPCM level. Isovalue = 0.02 $\sqrt{e^-\ bohr^{-3}}$ for all orbitals apart from L+3, a Rydberg orbital, for which isovalue = 0.01 $\sqrt{e^-\ bohr^{-3}}$ is shown.

HOMO: ε = -3.64 eV	LUMO: ε = -1.02 eV
H-1: ε = -5.21 eV	L+1: ε = -0.33 eV
H-2: ε = -5.48 eV	L+2: ε = -0.13 eV
H-3: ε = -5.73 eV	L+3: ε = -0.11 eV

Figure A2.10 Frontier orbitals of [Mn(CO)₃(TBIMP)]⁻ calculated at the B3LYP/SDD+6-311G(d,p)/IEFPCM level. Isovalue = 0.02 $\sqrt{e^- \, bohr^{-3}}$ for all orbitals.
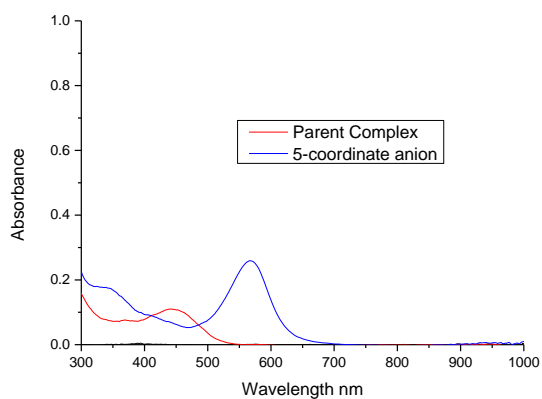
Figure A2.11 UV-SEC spectra of MnTBIEP showing no dimer absorption only the intense 5-coordinate absorption at ca. 569 nm.
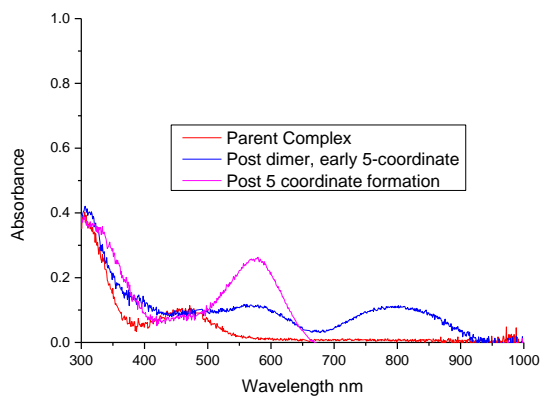
Figure A2.12 UV-SEC spectra of MnIMP showing characteristic broad dimer absorption at ca. 800 nm, which gives way to the intense 5-coordinate absorption at ca. 580 nm.
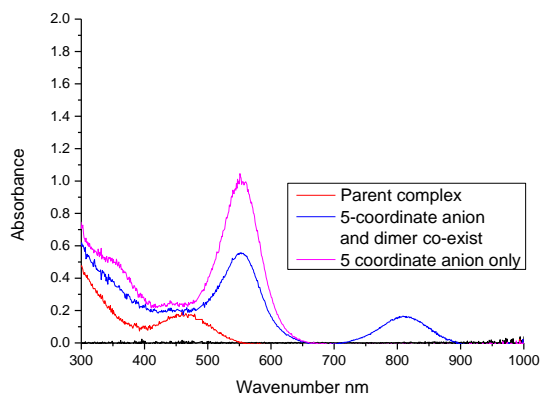
Figure A2.13 UV-SEC spectra of MnIPIMP showing characteristic broad dimer absorption at ca. 800 nm, along side the intense 5-coordinate absorption at ca. 550 nm.
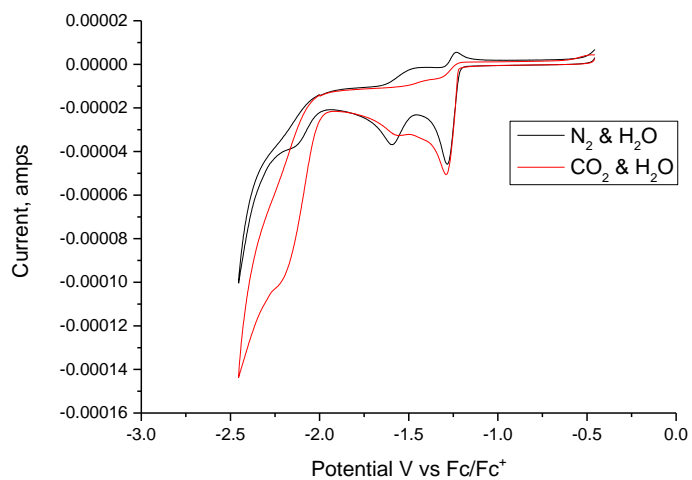
Figure A2.14 Cyclic voltammograms of 1 mM MnIMP in acetonitrile with 4.7% H2O, 0.2M [Bu4N][PF6], scan rate 0.1 Vs^{-1}. Under atmosphere of N$_2$ (black), and CO$_2$ (red).
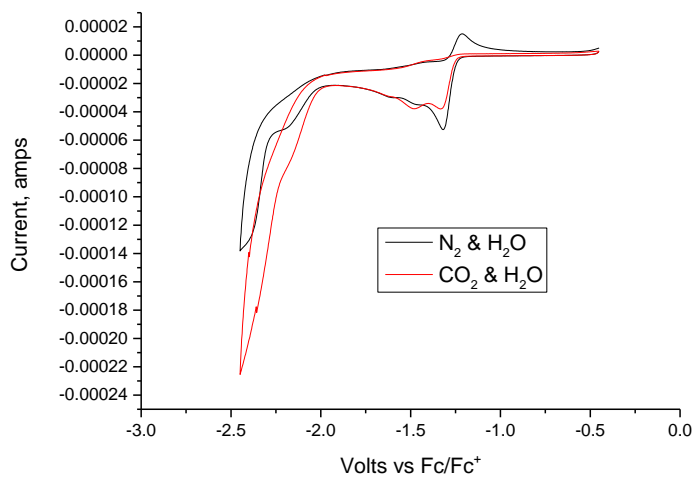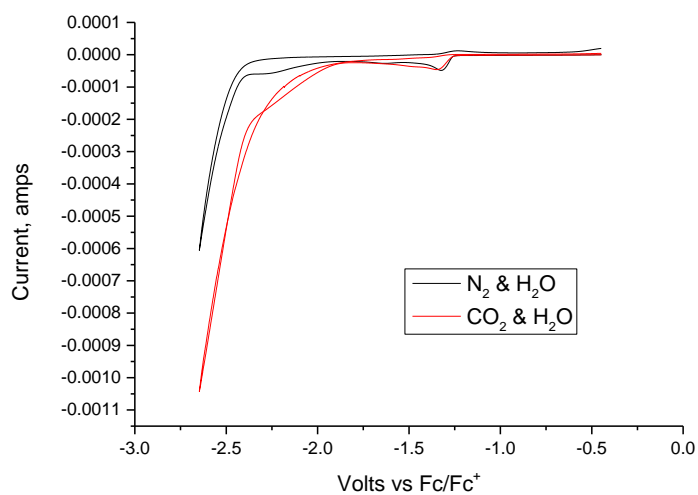

Figure A2.15 Cyclic voltammograms of 1 mM MnIPIMP in acetonitrile with 4.7% H2O, 0.2M [Bu4N][PF6], scan rate 0.1 Vs^{-1}. Under atmosphere of N$_2$ (black), and CO$_2$ (red).
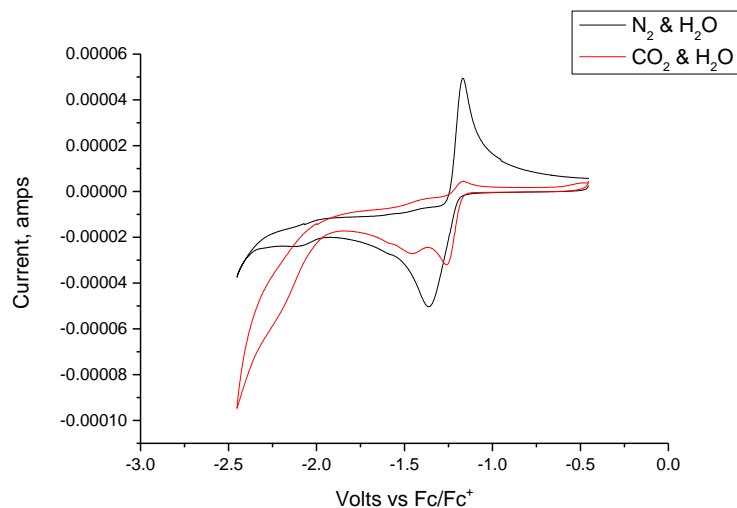
Figure A2.16 Cyclic voltammograms of 1 mM MnDIPIMP in acetonitrile with 4.7% H2O, 0.2M [Bu₄N][PF₆], scan rate 0.1 Vs⁻¹. Under atmosphere of N₂ (black), and CO₂ (red).
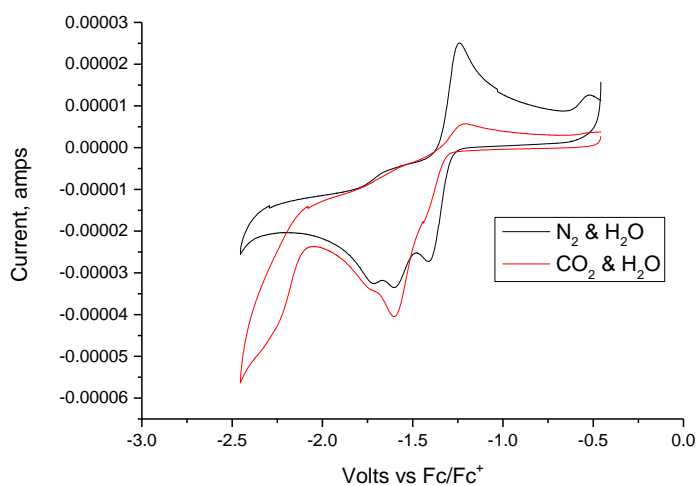
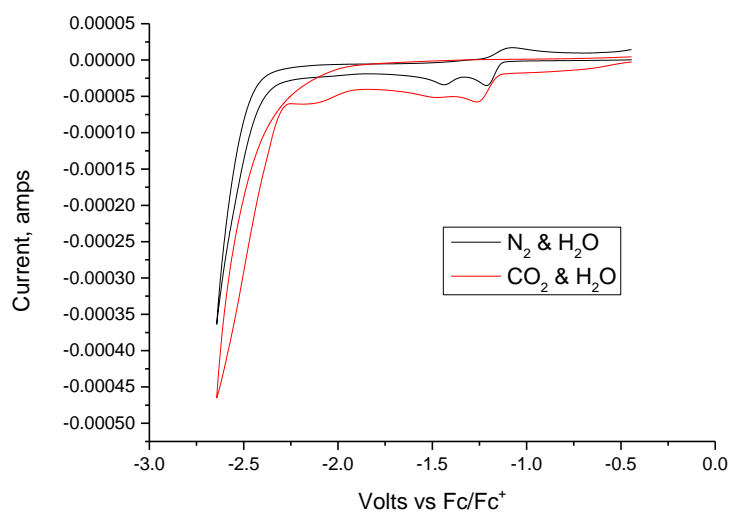**Figure A2.17 Cyclic voltammograms of 1 mM MnTBIEP in acetonitrile with 4.7% H2O, 0.2M [Bu₄N][PF₆], scan rate 0.1 Vs⁻¹. Under atmosphere of N₂ (black), and CO₂ (red).**
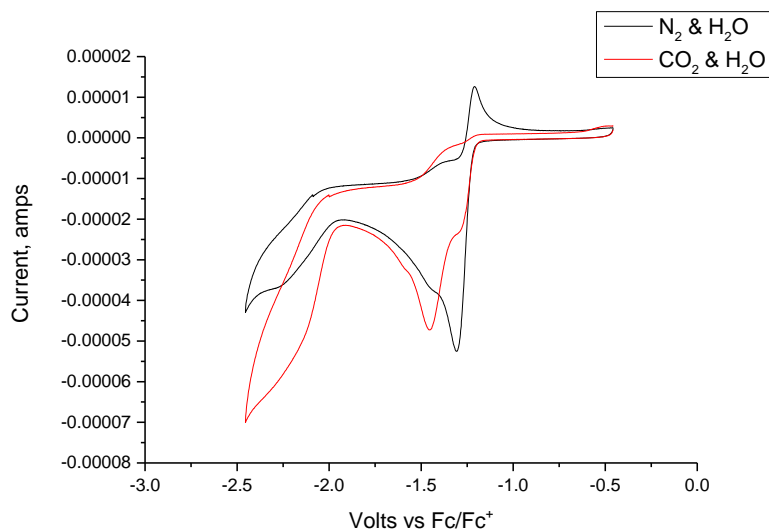
Figure A2.18 Cyclic voltammograms of 1 mM MnTBIMP in acetonitrile with 4.7% H2O, 0.2M [Bu$_4$N][PF$_6$], scan rate 0.1 Vs^{-1}. Under atmosphere of N$_2$ (black), and CO$_2$ (red).
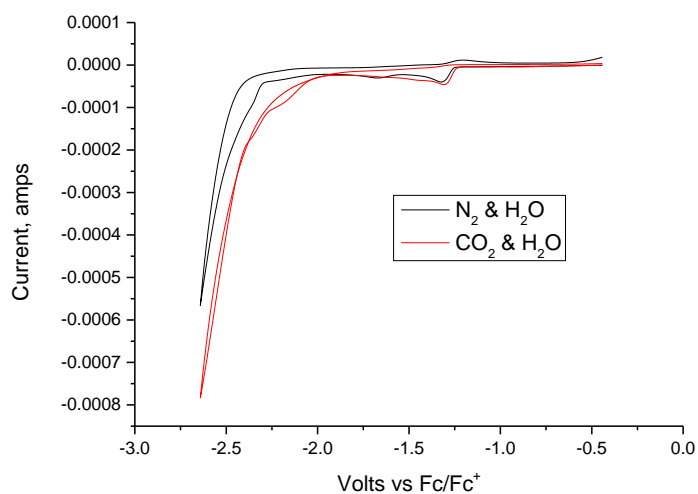
Figure A2.19 Cyclic voltammograms of 1 mM MnIMP-Me in acetonitrile with 4.7% H2O, 0.2M [Bu$_4$N][PF$_6$], scan rate 0.1 Vs^{-1}. Under atmosphere of N$_2$ (black), and CO$_2$ (red).

Figure A2.20 Cyclic voltammograms of 1 mM MnIMP-OMe in acetonitrile with 4.7% H2O, 0.2M [Bu₄N][PF₆], scan rate 0.1 Vs⁻¹. Under atmosphere of N₂ (black), and CO₂ (red).

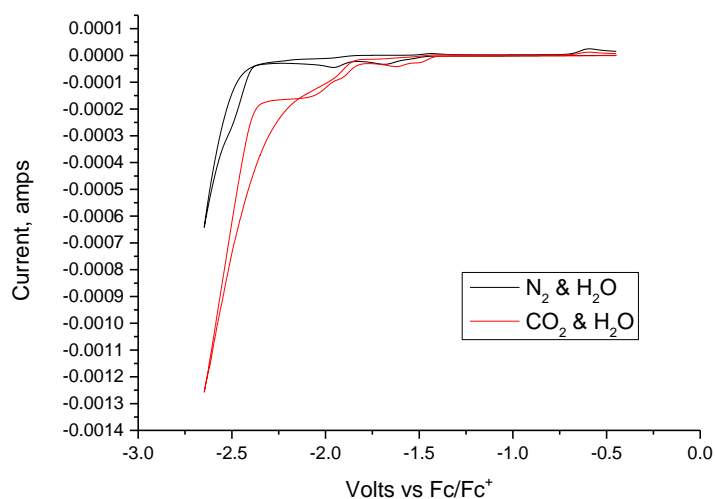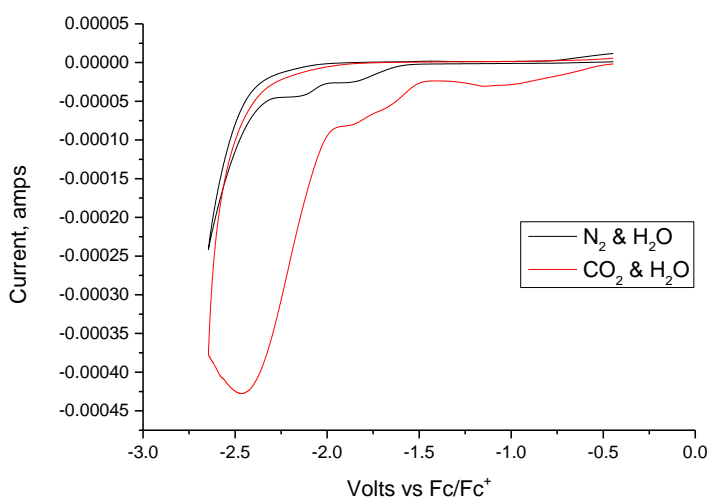**Figure A2.21 Cyclic voltammograms of 1 mM MnIMP-Br in acetonitrile with 4.7% H2O, 0.2M [Bu₄N][PF₆], scan rate 0.1 Vs⁻¹. Under atmosphere of N₂ (black), and CO₂ (red).**

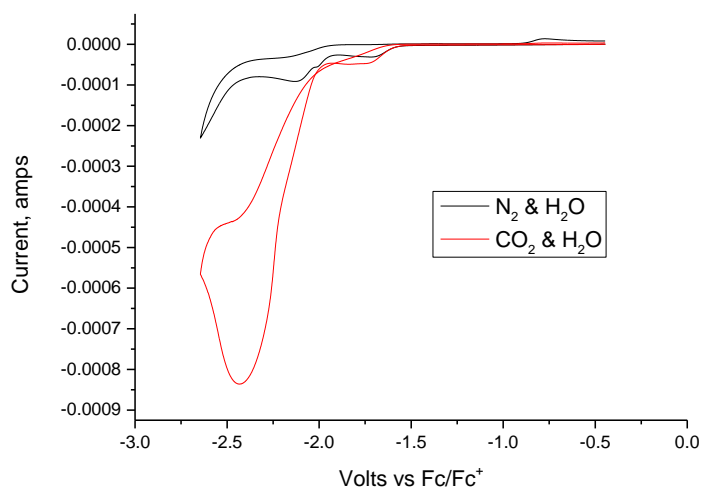**Figure A2.22 Cyclic voltammograms of 1 mM Mnbpy in acetonitrile with 4.7% H2O, 0.2M [Bu₄N][PF₆], scan rate 0.1 Vs⁻¹. Under atmosphere of N₂ (black), and CO₂ (red).**

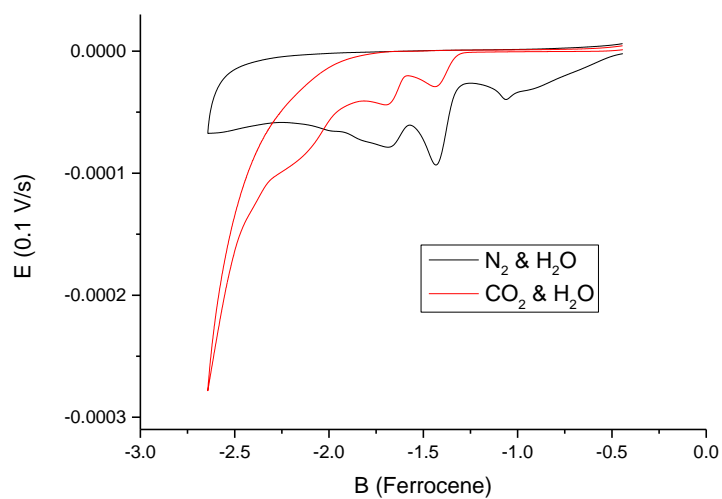**Figure A2.23 Cyclic voltammograms of 1 mM Mndmbpy in acetonitrile with 4.7% H2O, 0.2M [Bu₄N][PF₆], scan rate 0.1 Vs⁻¹. Under atmosphere of N₂ (black), and CO₂ (red).**

Figure A2.24 Cyclic voltammograms of 1 mM Mnbpy-OMe in acetonitrile with 4.7% H2O, 0.2M [Bu₄N][PF₆], scan rate 0.1 Vs⁻¹. Under atmosphere of N₂ (black), and CO₂ (red).

Figure A2.25 Cyclic voltammograms of 1 mM Mnbpy-Br in acetonitrile with 4.7% H2O, 0.2M [Bu₄N][PF₆], scan rate 0.1 Vs⁻¹. Under atmosphere of N₂ (black), and CO₂ (red).

Bibliography

(1)   Andersson, M. P.; Uvdal, P. *J. Phys. Chem. A* **2005**, *109*, 2937.

Appendix 3

Setting up the photodecomposition experiment

To set up the photodiode and oscilloscope

1. Turn on the Xe lamp
2. Set the photodiode to trigger
3. Connect the photodiode cable to channel 2 hole on the oscilloscope
4. Plug in the oscilloscope
5. Connect "crossover cable" between PC and oscilloscope
6. Set the aperture
7. Connect black cable from photon multiplier tube to channel 1 input on scope
8. Turn on the oscilloscope
9. Push "menu off" to proceed
10. Oscilloscope IP address = 192.168.1.1
11. Go to data
12. Format = spreadsheet
13. Turn on the photon multiplier tube, turn to 11 and allow to warm up
14. Turn on photodiode
15. Switch output on/off (20 V)
16. On oscilloscope push– Save recall > recall saved setup > setup 3

To record data

1. Prepare a curvette full of solvent
2. Set voltage to -1.03 V
3. Place cell in cell holder
4. On oscilloscope press- save recall > recall setup 3 > single sequence – Trig?
5. Expose sample to light triggering the photodiode, the horizontal scale adjusts seconds
6. Press "get " to get data
7. Repeat with sample

Turning off

1. Turn off output on/off on the photodiode
2. Turn off photodiode detector
3. Turn off photodiode
4. Turn voltage down on the photon multiplier tube
5. Turn off photon multiplier tube
6. Turn off oscilloscope

Trouble shoot = go to menu

Acquisition mode = sample

Trigger = Coupling DC
            Rising slope
            Type Edge